technische universität
dortmund

Revealing the Hidden Potential of Transition Metal Thiophosphates

Probing the Electronic Structure and Tunability of a New Class of 2D Magnets via Photoelectron Spectroscopy

Jonah Elias Nitschke
2025

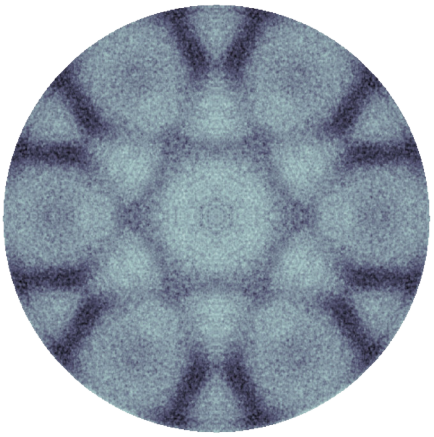

A document submitted in partial fulfilment of the requirements for the degree of
Doctor rerum naturalium
at
Fakultät Physik, Technische Universität Dortmund

Primary Examiner: Prof. Dr. Mirko Cinchetti
Secondary Examiner: Prof. Dr. Marc Aßmann

Accepted by the Faculty of Physics of the TU Dortmund University, Germany.
Day of the oral examination: October 30th, 2025.

Abstract

Magnetic order in low-dimensional materials offers exciting opportunities for spintronic, quantum, and next-generation information storage applications. Among layered magnetic crystals, the transition-metal thiophosphates (MPS_3, with M = Mn, Fe, Co, Ni) stand out for their air stability, chemical versatility, and diverse magnetic ground states, making them an ideal platform for studying the interplay between spin, charge, and lattice degrees of freedom. This thesis combines different photoemission spectroscopy techniques, including X-ray photoelectron spectroscopy (XPS), angle-resolved photoelectron spectroscopy (ARPES), and time-resolved ARPES (trARPES), with first-principles calculations to investigate the electronic structure, quasiparticle dynamics, and tunability of four representative MPS_3 compounds. In the first part, XPS and ARPES establish the intrinsic electronic properties, revealing complex valence-band structures with dispersive and flat bands, material-dependent orbital hybridisation, and momentum-dependent intensity variations. Using trARPES on $FePS_3$, we identify and characterise two distinct *d*-*d* transitions, determine their lifetimes and momentum fingerprints, and demonstrate the method's ability to follow local multiplet excitations in momentum space. In the second part, we explore tunability via molecular adsorption and alkali-metal intercalation. Photoemission orbital tomography on pentacene monolayers on $FePS_3$ and $NiPS_3$ reveals well-ordered, physisorbed layers, providing a baseline for studies with stronger donor-acceptor systems. Lithium and caesium intercalation show element-specific doping behaviour, oxidation-state changes, and orbital-selective band modifications, highlighting the potential for controlled band-structure engineering. Overall, this work presents a detailed study of the electronic ground state of four representative MPS_3 compounds, extends trARPES to multiplet excitations by investigating electron dynamics in $FePS_3$, and provides first insights into targeted modification through molecular adsorption and alkali-metal intercalation, demonstrating the versatility and potential of this material class.

Kurzfassung

Magnetische Ordnung in niedrigdimensionalen Materialien eröffnet vielversprechende Möglichkeiten für spintronische, Quanten- und neuartige Informationsspeicheranwendungen. Unter den geschichteten magnetischen Kristallen zeichnen sich die Übergangsmetall-Thiophosphate (MPS_3, mit M = Mn, Fe, Co, Ni) durch ihre Luftstabilität, chemische Vielseitigkeit und vielfältigen magnetischen Grundzustände aus und bieten damit eine ideale Plattform zur Untersuchung des Zusammenspiels von Spin-, Ladungs- und Gitterfreiheitsgraden. Diese Arbeit kombiniert verschiedene Photoemissionsspektroskopie-Techniken, einschließlich Röntgenphotoemissionsspektroskopie (XPS), winkelaufgelöster Photoemissionsspektroskopie (ARPES) und zeitaufgelöster ARPES (trARPES), mit ab-initio-Rechnungen, um die elektronische Struktur, Quasiteilchendynamik und Modifizierbarkeit von vier repräsentativen MPS_3-Verbindungen zu untersuchen. Im ersten Teil zeigen XPS- und ARPES-Messungen die intrinsischen elektronischen Eigenschaften, darunter komplexe Valenzbandstrukturen mit dispersiven und flachen Bändern, materialspezifische Orbitalhybridisierung und Impuls-abhängigen Intensitätsvariationen. Mit trARPES an $FePS_3$ identifizieren und charakterisieren wir zwei verschiedene *d*-*d*-Übergänge, bestimmen deren Lebensdauern und Impulsraumcharakter und demonstrieren die Fähigkeit der Methode, lokale Multiplett-Anregungen im Impulsraum zu verfolgen. Im zweiten Teil untersuchen wir die Modifizierbarkeit der elektronischen Eigenschaften durch Moleküladsorption und Alkali-Metall-Interkalation. Photoemissions-Orbitaltomographie an Pentacen-Monolagen auf $FePS_3$ und $NiPS_3$ zeigt gut geordnete, physisorbierte Molekülllagen und liefert eine Grundlage für Studien mit stärkeren Donor-Akzeptor-Systemen. Lithium- und Cäsium-Interkalation zeigen elementspezifisches Dotierungsverhalten, Änderungen des Oxidationszustands und orbitalselektive Bandmodifikationen, was das Potenzial für gezieltes Bandstruktur-Engineering unterstreicht. Zusammenfassend präsentiert diese Arbeit eine detaillierte Untersuchung des elektronischen Grundzustands von vier repräsentativen MPS_3-Verbindungen, erweitert die Anwendung von trARPES auf Multiplett-Anregungen durch die Untersuchung der Elektronendynamik in $FePS_3$ und liefert erste Einblicke in die gezielte Modifikation der elektronischen Eigenschaften durch Moleküladsorption und Alkali-Metall-Interkalation, was die Vielseitigkeit und das Potenzial dieser Materialklasse verdeutlicht.

Contents

Introduction **1**

1 Theoretical Background **7**
1.1 Photonic Excitations in Semiconductors . . . 7
1.1.1 Unoccupied and Transient States . . . 7
1.1.2 Coherent Lattice Vibrations . . . 8
1.1.3 Local Transitions Between *d*-Orbitals . . . 8
1.2 Transition Metal Phosphorus Trisulfides . . . 9
1.2.1 Structural Properties . . . 9
1.2.2 Electronic Properties . . . 10
1.2.3 Magnetic Properties . . . 12
1.2.4 Optical Properties . . . 13
1.3 Hybridisation at Molecular Interfaces . . . 14
1.3.1 Electronic Structure of Organic Molecules . . . 14
1.3.2 Interaction Regimes: Physisorption to Chemisorption . . . 15
1.3.3 Electronic Structure Effects at the ORG/SC Interface . . . 16

2 Experimental Methods **21**
2.1 Photoelectron Spectroscopy . . . 21
2.1.1 Angle-Resolved Photoelectron Spectroscopy . . . 21
2.1.2 Momentum Microscopy . . . 23
2.1.3 X-Ray Photoelectron Spectroscopy . . . 25
2.2 Time-Resolved ARPES . . . 27
2.2.1 Fundamental Principle . . . 27
2.2.2 High-Harmonic Generation . . . 28
2.2.3 Measuring Photonic Excitations with trARPES . . . 30
2.3 Experimental setups . . . 33
2.3.1 XPS . . . 33
2.3.2 KREIOS 150 MM . . . 34
2.3.3 METIS 1000 . . . 37
2.4 Sample Preparation . . . 41

Part I - Fundamental Properties **43**

3 Static Characterisation **45**
3.1 Core Level Spectroscopy . . . 46
3.2 Revealing the Valence Band Structure . . . 50
3.3 Investigation of the Orbital Character . . . 56
3.4 Conclusion . . . 59

4 Electron Dynamics in $FePS_3$ **63**
4.1 Unwanted (artificial) Dynamics in trARPES . . . 64
4.1.1 Static Space Charge Effects . . . 64
4.1.2 Pump-induced Space Charge Effects . . . 66
4.1.3 Laser Assisted Photoelectron Emission . . . 70
4.2 Introduction to Electron Dynamics in $FePS_3$ . . . 73
4.3 Resonant Excitation of the $^5T_{2g} \rightarrow {}^5E_g$ Transition . . . 74
4.4 Indirect Transitions by Above Band Gap Excitation . . . 76
4.5 Theoretical Description . . . 80
4.6 Conclusion . . . 83

Part II - Tunability **87**

5 Adsorption of Organic Molecules **89**
5.1 Sample Preparation . . . 90
5.2 Photoemission Orbital Tomography . . . 90
5.3 Pentacene Adsorption on $NiPS_3$ . . . 92
5.4 Pentacene Adsorption on $FePS_3$ . . . 95
5.5 Conclusion . . . 98

6 Targeted electron doping **101**
6.1 Sample Preparation . . . 102
6.2 Accessing the *d*-Orbital Occupation via XPS . . . 103
6.3 Modifications of the Valence Band Structure . . . 107
6.4 Conclusion . . . 114

7 Summary and Outlook **117**

List of publications and conference contributions **121**

List of Abbreviations **125**

A Appendix **127**
A.1 XPS Fits of MPS_3 M 2*p* and M 3*p* spectra . . . 127
A.2 XPS Fits of MPS_3 S and P 2*p* spectra . . . 130
A.3 Momentum Maps of Pentacene . . . 131
A.4 XPS spectra of Li/MPS_3 S and P 2*p* peaks . . . 132

Introduction

Magnetic order, and in particular the control of the electron's spin degree of freedom, forms the foundation of modern information storage technologies. Conventional electronics rely solely on charge transport, whereas spintronics exploits both charge and spin, enabling non-volatile memory elements, faster switching speeds, and reduced power consumption [1]. Magnetic materials are already integrated in various in devices ranging from hard-disk drives to magnetic random-access memory and racetrack memories, and are also considered promising platforms for novel information technologies [2–4]. However, most of these devices depend on three-dimensional bulk crystals or thin films, which face intrinsic limits in scalability, miniaturisation, and integration with low-dimensional material platforms [5].

The isolation of graphene in 2004 [6] marked the beginning of the two-dimensional (2D) materials era, revealing a vast landscape of layered van der Waals (vdW) crystals with exceptional physical properties [7, 8]. Atomically thin materials intrinsically offer extreme scaling potential, mechanical flexibility, and tuneable behaviour through external control parameters such as strain, doping, gating, stacking, and light-matter interaction [9–11]. Moreover, 2D semiconductors circumvent the surface-charge-scattering limitations faced by ultra-thin conventional semiconductors, as their surfaces are intrinsically passivated in the third dimension, preserving high carrier mobility even at atomic thickness [5]. Despite these advantages, most well-studied 2D materials, such as graphene, molybdenum disulphide, and hexagonal boron nitride, are intrinsically non-magnetic, restricting their direct applicability in spin-based technologies [12, 13].

The discovery of intrinsic magnetic order in truly two-dimensional crystals, such as CrI_3 [14] and $Cr_2Ge_2Te_6$ [15], demonstrated that long-range magnetism can persist down to the monolayer limit. This breakthrough overcame the restrictions imposed by the Mermin-Wagner theorem through the presence of magnetic anisotropy [16] and has opened up new prospects for 2D spintronic devices, where magnetic order can be tuned via electric fields, pressure, or interlayer engineering [17–20]. Despite this progress, many of the known 2D magnets suffer from practical limitations such as low magnetic ordering temperatures and limited air stability, posing significant challenges to their device integration [10, 21].

Among the various families of layered magnetic crystals, transition metal thiophosphates (MPS_3) stand out as particularly promising 2D magnets [22, 23]. Because of their antiferromagnetic ordering, they have zero net magnetic moment but are still internally magnetic [24]. This promises multiple advantages over ferromagnetic materials such as a higher robustness against external

fields, less dissipation and spin dynamics in the THz range [25, 26]. Furthermore, their van der Waals structure enables mechanical exfoliation down to the monolayer limit, while their chemical versatility allows systematic tuning of the magnetic ground state through the choice of transition metal (M = Mn, Fe, Co, Ni). This compositional flexibility gives rise to a wide range of magnetic behaviours, from Ising- to Heisenberg-type ordering, providing an ideal platform for studying the interplay between spin, charge, and lattice degrees of freedom [27]. Unlike many halide-based 2D magnets [28, 29], members of the MPS_3 family exhibit good air stability, simplifying device fabrication and enabling detailed investigations with surface-sensitive probes such as X-ray photoelectron spectroscopy (XPS) and angle-resolved photoelectron spectroscopy (ARPES). These attributes make MPS_3 compounds an exemplary model system for exploring how magnetism in 2D materials can be engineered and harnessed for next-generation technologies [30, 31].

The goal of this thesis is to investigate the intrinsic electronic properties and tunability of four representative members of the MPS_3 material class: $MnPS_3$, $FePS_3$, $CoPS_3$, and $NiPS_3$. While these compounds have been studied for decades, with early work focusing on their electronic and optical properties [32–38], the observation of long-range magnetic order in $FePS_3$ in 2016 [39] reignited interest in this material class, triggering a wave of recent optical studies and highlighting their potential for spintronic applications [31, 40]. Therefore, we will employ different state-of-the-art ARPES-based techniques, to explore both their intrinsic electronic properties and their tunability via different external modifications. Here, we will focus on room-temperature measurements, as the different compounds of the MPS_3 family are prone to charging effects when using PES based techniques at low temperature due to their wide-gap semiconducting character [41, 42].

Understanding the electronic structure and excitations in MPS_3 requires experimental techniques capable of probing the chemical environment, resolving the momentum-dependent band structure, and tracking transient states on ultrafast timescales. XPS provides element- and orbital-specific sensitivity, allowing precise determination of oxidation states, bonding configurations, and d-orbital occupations [43–45]. ARPES complements this by mapping the momentum-resolved valence band structure and identifying orbital contributions through direct comparison with density functional theory [46, 47]. The advent of high-energy ($> 20\,\mathrm{eV}$) and ultrafast ($< 100\,\mathrm{fs}$) light pulses has enabled time-resolved ARPES (trARPES), which extends these capabilities to the time domain, allowing direct observation of quasiparticle dynamics, coupling to phonons or magnons, and transient band-structure renormalisations inaccessible to static methods [48–51]. By integrating these three complementary approaches, this thesis aims to establish a comprehensive understanding of the ground-state properties, ultrafast dynamics, and tunability of MPS_3 compounds under controlled external perturbations.

To set the stage, the first two chapters introduce the theoretical and experimental foundations of this work. In **chapter 1**, the relevant physical properties of the MPS_3 family are described in detail, along with an introduction to relevant optical excitations in semiconductors and a summary of hybridisation processes at interfaces with organic molecules. Following, **chapter 2** describes the principles and implementation of the employed PES-based techniques, emphasising their capability to probe different aspects of the electronic structure and highlighting the advanced detector concepts used in this study.

The presentation of experimental results in this thesis is divided into two main parts.

In **Part I**, we want to establish a comprehensive understanding of the pristine MPS_3 compounds using photoelectron spectroscopy and computational modelling. First, we will present experimental data on the equilibrium properties of the MPS_3 material class, including information about the core level states as well as the electronic structure of the valence band region, necessary as a basis for assessing the tunability in later chapters. Second, we will investigate the electron dynamics observed in $FePS_3$, crucial as they dictate the behaviour in response to external stimuli like light, heat, or electric fields, and influence non-equilibrium properties and functionalities.

To start, **chapter 3** will present XPS and momentum microscopy (MM) measurements. XPS, using photons in the kiloelectronvolt range, probes the core-level s states, allowing assessment of sample quality and determination of oxidation states. Using advanced fitting routines based on theoretical analyses provides insights into the bonding environment and *d*-orbital occupation. Complementarily, momentum microscopy maps the valence-band structure across the first and neighbouring Brillouin zones. Combined with density functional theory (DFT), this enables an orbital-level assignment of spectral features and serves as a benchmark for computational models of the MPS_3 compounds, laying the foundation for later investigations of electron dynamics and tunability.

Afterwards, **chapter 4** presents experimental insights into the electron dynamics of $FePS_3$, building on the knowledge extracted from the static measurements in the preceding chapter. Here, the study is extended into the time domain using trARPES to understand how the electronic structure is perturbed by external stimulation via light. However, interpreting and analysing the time-resolved ARPES data is challenging, as multiple effects often overlap, including processes not intrinsic to the crystal. Therefore, the chapter first introduces three common artefacts that can influence the observed dynamics. These are illustrated with experimental data obtained from a single crystal of Au(111), providing detailed insights into the time-dependent characteristics of space-charge effects and laser-assisted photoelectron emission.

Afterwards, we will investigate a specific type of photonic excitation using trARPES, *d*-*d* transitions, which have not yet been observed with momentum resolved techniques before. Although *d*-*d* transitions are normally dipole-forbidden, they can become allowed through symmetry breaking or vibronic coupling, but remain weak in absorption spectra. However, in $FePS_3$ *d*-*d* transitions are particularly promising for future applications [52]. The lowest-lying *d*-*d* transition indirectly excites coherent lattice vibrations that couple to a magnonic resonance and can induce spin waves [53], an important mechanism for implementation in spintronic devices. Additionally, the resonance lies below the optical band-gap absorption threshold, thereby reducing thermal load under excitation. Using a pump–probe scheme with excitation both below and above the band gap, we investigate the different responses and aim to identify the characteristic momentum fingerprint of *d*-*d* transitions, opening a pathway towards a deeper understanding of their interplay with other quasiparticles.

In **Part II**, the focus shifts to the electronic tunability of the MPS_3 family. The ability to precisely tune magnetic material properties, such as magnetization, coercivity, Curie temperature, and magnetic anisotropy, is essential for optimising material performance in specific applications [54]. One of the most effective strategies for achieving such control is atomic-scale

engineering, which encompasses stacking different materials, alloying, intercalation, and functionalisation with molecules or heteroatoms [9].

Targeted tuning of material properties through stacking into vdW heterostructures has gained particular interest with the discovery of magnetic 2D materials. Owing to their atomically sharp interfaces, often realised by exfoliation and restacking of individual layers, it is possible to combine distinct functionalities of different components and introduce additional properties via proximity effects across interfaces. This approach offers a promising pathway for integration into memory devices, spin transistors, and other spintronic architectures [55]. Nevertheless, the reliance on exfoliation inherently limits large-scale production, as it constrains the achievable lateral size, throughput, and yield of high-quality thin films [56].

In contrast, alloying involves the incorporation of foreign elements into a host lattice, thereby altering the electronic structure and magnetic exchange interactions. For example, substituting non-magnetic atoms into ferromagnetic matrices can dilute magnetic order or tune magnetic anisotropy [57, 58], whereas introducing magnetic dopants into non-magnetic hosts can induce ferromagnetic or antiferromagnetic order [59, 60]. Similarly, intercalation refers to the insertion of atoms or molecules between the layers of 2D materials, such as transition metal dichalcogenides or graphene, offering a versatile means to manipulate interlayer coupling and magnetic ordering [61, 62]. Intercalated species can act as electron donors or acceptors, impose strain on the host lattice, or mediate indirect exchange interactions [63].

Finally, the functionalisation with molecules enables the design of hybrid materials whose magnetic properties can be tuned via the chemical nature, dipole moment, or spin state of the molecular species [64, 65]. Such systems hold promise for magnetoelectronics and quantum devices, owing to their potential for spin-dependent charge transport and long spin-coherence times [66, 67]. These approaches not only modify intrinsic magnetic parameters [68], but also provide control over emergent properties such as magnetoresistance [69], exchange bias [70], or spin textures [71, 72].

Recent studies on the MPS_3 family have demonstrated their high potential for targeted tuning using the techniques discussed above [73, 74]. For example, alloying through substitution of transition-metal cations can substantially modify exchange interactions [75]. Such modifications can induce changes in the magnetic ground state, including transitions between Néel, zigzag, ferrimagnetic, or even spin-glass configurations [76]. Furthermore, intercalation with molecular species or electrochemically inserted cations can shift the balance between direct and superexchange interactions, thereby driving phase transitions from antiferromagnetic to ferromagnetic or ferrimagnetic states [77]. In this context, the next two chapters will introduce two distinct pathways for tuning the properties of the MPS_3 family.

As a first method, **chapter 5** will address the modification of the electronic structure via adsorption of organic molecules. To track the changes occurring at the interface between the substrate and an ordered molecular overlayer, we employ photoemission orbital tomography (POT) [78]. This technique enables direct identification of molecular orbitals based on their unique momentum-space fingerprints, thereby allowing for the deconvolution of the energy-level alignment. As a prototypical molecular adsorbate, we use pentacene (5A), a well-studied, planar, conjugated molecule with an extended π-electron system, known for forming ordered layers and enabling strong yet tuneable interactions with surfaces in organic electronics. Employing POT

measurements, we will classify the interaction strength of $NiPS_3$ and $FePS_3$ with a monolayer of 5A, providing essential information about the self-assembly and energy level alignment, shining light on their potential for future device applications.

In **chapter 6**, we employ intercalation as a second method for targeted modification, using MM and XPS in combination with theoretical modelling to investigate the behaviour of the MPS_3 family under electron doping, with particular emphasis on how electron donation affects *d*-shell filling. The interplay between alkali metals and the MPS_3 family is already regarded as a promising pathway for future device implementation. Most existing works, however, have focused predominantly on magnetic properties, reporting phenomena such as reversible transitions between ferromagnetic and antiferromagnetic states [79, 80], a reduction of the magnetic ordering temperature in $FePS_3$ [81], and the emergence of ferrimagnetism in $NiPS_3$ [82]. In contrast, a comprehensive investigation of the electronic structure modifications and their potential for targeted control remains scarce. To address this knowledge gap, we employ XPS to determine how the additional electrons introduced by the alkali metal affect the orbitals of the different atomic species, including changes in oxidation state and electron localisation. Based on these results, we then use MM in combination with computational methods to investigate the modifications in the valence-band region and to assess the potential for controlled tuning of the electronic properties. As a model system for these studies, we use lithium atoms as electron donors and examine their influence on the electronic properties of four MPS_3 compounds: $MnPS_3$, $FePS_3$, $CoPS_3$, and $NiPS_3$.

Overall, this thesis integrates advanced spectroscopic methods with theoretical modelling to provide a detailed understanding of the electronic structure, quasiparticle dynamics, and tunability of MPS_3 compounds. This approach not only advances the fundamental knowledge of the 2D magnetic MPS_3 material class but also establishes a versatile platform for future investigations into their physical properties and potential device implementations.

1 | Theoretical Background

As a preparation for the experimental investigation, this chapter establishes the theoretical framework necessary to interpret the results presented later. The theoretical background is divided into three main components: a brief introduction to the most relevant optical excitations, an overview of the general properties of the MPS_3 material class, and a short description of the physical effects that occur at a hybridised interface with molecules.

1.1 Photonic Excitations in Semiconductors

The electronic band structure of a semiconductor can be well understood by starting with the periodic potential of a crystal lattice. When atoms are brought close to each other, their atomic orbitals hybridise and form bonding and antibonding states, separated by an energy gap due to the Pauli exclusion principle. As more atoms are arranged in a periodic crystal, these discrete molecular orbitals broaden into continuous bands. These bands define the dispersion relation $E(\vec{k})$ of electrons in the solid, describing how their energy depends on the crystal momentum $\vec{k}$ in the presence of the periodic potential formed by the nuclei.

1.1.1 Unoccupied and Transient States

In semiconductors, the highest occupied band at $T = 0\,\mathrm{K}$ is defined as the valence band (VB), while the lowest unoccupied band is referred to as the conduction band (CB). The energetic difference between these two bands is known as the band gap energy E_g, with typical values up to 3 eV in semiconducting materials. The nature of the band gap is determined by the relative positions of the CB minimum and the VB maximum in $\vec{k}$-space. In direct band gap materials, both extrema occur at the same $\vec{k}$-point (typically the Γ-point), allowing optical transitions to occur vertically in momentum space due to the negligible momentum of photons. In contrast, indirect band gap materials exhibit these extrema at different $\vec{k}$-points, requiring additional momentum transfer via phonons for interband transitions. As a result of the negligible photon momentum, optical excitations are typically vertical in $\vec{k}$-space and thus predominantly probe the smallest energy difference between the valence and conduction bands [83–85].

For many optical properties in semiconductors, the concept of excitons is of fundamental importance. Excitons are quasiparticles formed by optically excited electrons and holes, which are bound by their mutual Coulomb interaction, akin to a hydrogen-like system in semiconducting media. They play a central role in optoelectronic properties and typically manifest in absorp-

tion spectra as sharp peaks below the conduction band minimum, since the Coulomb attraction lowers the excitation energy.

In two-dimensional (2D) materials, excitonic effects are particularly pronounced due to two key reasons: (1) the enhanced Coulomb interaction resulting from weak dielectric screening in the out-of-plane direction, and (2) the strong spatial confinement of charge carriers [86]. As a consequence, 2D excitons exhibit binding energies on the order of several hundred meV, which is an order of magnitude larger than in their bulk counterparts, and in some cases remain stable even at room temperature [87–89].

This strong interaction regime also enables the formation of more complex bound states beyond neutral excitons. A single exciton may bind with an additional electron to form a trion, or with another exciton to form a biexciton [90]. Under suitable conditions, even more exotic composite quasiparticles such as quintons, bound states comprising a trion and an exciton, can emerge. These many-body excitonic complexes constitute a rich quasiparticle zoo that can be probed using high-resolution optical spectroscopy or time-resolved techniques [86].

1.1.2 Coherent Lattice Vibrations

Besides excitons, another type of quasiparticle that is crucial for understanding the electronic properties of semiconductors are phonons, quantized lattice vibrations resulting from the collective motion of atoms around their equilibrium positions. These quasiparticles come in two main types: acoustic phonons, which involve in-phase motion of atoms, and optical phonons, which arise from out-of-phase motion within the unit cell. Optical phonons and their interaction with electrons often play a central role in determining many material properties like thermal conductivity, charge carrier scattering, and optical response, and are mostly active in the infrared region [91].

Phonons can be investigated through a variety of optical methods, including infrared absorption, Raman spectroscopy, and ultrafast pump-probe techniques. These approaches enable the study of both coherent and incoherent phonon dynamics, anharmonic effects, and phonon coupling to electronic degrees of freedom [92, 93]. In two-dimensional (2D) materials, such as transition metal dichalcogenides (TMDs) or transition metal phosphorus trichalcogenides (MPS_3), phonons acquire particular significance. The reduced dimensionality in these systems leads to modified phonon dispersion relations and often results in enhanced electron-phonon coupling [94] or activates additional Raman modes [95], significantly influencing light-matter interaction in 2D materials [96]. This allows for direct optical access to coupled phenomena such as phonon-magnon and phonon-exciton interactions [53, 97].

1.1.3 Local Transitions Between d-Orbitals

The last optically active excitation introduced here are the so-called d-d transitions, which will play a fundamental role in chapter 4. As the name suggests, these transitions refer to electron excitations between the partially filled d-orbitals of transition metal ions. The theoretical description is based on crystal field theory (CFT), which explains the energetic splitting of d-orbitals due to the crystal field generated by surrounding ligands. According to CFT, this splitting can be deduced purely from geometric considerations: orbitals that point directly to-

ward ligand electron clouds experience increased repulsion and are raised in energy relative to those oriented between the ligands. The resulting energy difference is known as the crystal field splitting energy. For instance, in an octahedral coordination environment, the d-orbitals split into two groups: the t_{2g} orbitals (d_{xy}, d_{xz}, and d_{yz}), which experience less repulsion, and the e_g orbitals (d_{z^2} and $d_{x^2-y^2}$), which are more strongly repelled due to their orientation along the ligand axes.

In addition to crystal field effects, the full multiplet structure of transition metal ions also depends on interelectronic Coulomb interactions between the d-electrons, governed by Hund's rules and parameterized by Racah parameters. These interactions lead to a fine structure of the d-manifold, resulting in a series of spin- and orbital-multiplet states, which are crucial for understanding the observed optical transitions and their selection rules.

According to Laporte's selection rule, electronic transitions that do not involve a change in parity are forbidden in centrosymmetric environments (i.e., systems with an inversion centre) [98]. Consequently, d-d transitions are nominally dipole-forbidden. However, they may still appear as weak absorption features due to vibronic coupling or symmetry breaking, such as lattice distortions or ligand field asymmetry [52]. Despite their low oscillator strength, d-d transitions are essential for understanding localized electronic correlations, multiplet structure, and energy relaxation processes in transition-metal compounds. In $FePS_3$, for example, these transitions are crucial for achieving ultrafast optical control of magnetic properties [99]. Furthermore, they can be used to selectively generate magnons when excited below the band gap [53], thereby reducing the thermal load on the sample.

While many other phenomena contribute to the electronic and optical characteristics of crystalline materials, the dynamics associated with excitons, phonons, and d-d transitions are particularly relevant in the context of our investigation of $FePS_3$ using time- and angle-resolved photoelectron spectroscopy (trARPES). In subsection 2.2.3, we will examine how the first two of these excitations can be detected using trARPES, before ultimately aiming to capture the momentum-resolved fingerprint of d-d transitions in chapter 4.

1.2 Transition Metal Phosphorus Trisulfides

1.2.1 Structural Properties

Transition metal phosphorus trisulfides (MPS_3, where M represents a transition metal such as Mn, Fe, Co, or Ni) are layered van der Waals materials composed of transition metal ions arranged in a honeycomb lattice, with P_2S_6 clusters situated inside the hexagonal voids (Figure 1.1a). These P_2S_6 clusters consist of P-P pairs, where each P atom is tetrahedrally coordinated to three S atoms, forming a triangular sublattice (Figure 1.1b). Additionally, each S atom coordinates with two metal atoms, creating an octahedral environment around the transition metal ion that plays a crucial role in determining its electronic properties [23, 100].

As shown in Figure 1.1c, the bulk crystals consist of multiple layers stacked in an ABC-type sequence with a tilt along the c-axis (commonly referred to as the c^*-axis). This arrangement results in a monoclinic crystal structure with $C2/m$ space group symmetry, where the individual layers are held together by van der Waals forces. The stacking introduces a small trigonal distor-

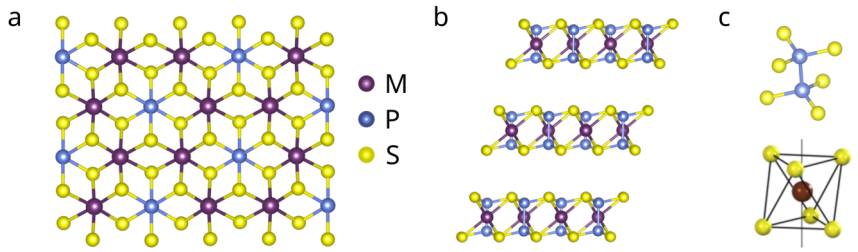

Figure 1.1: Structural, magnetic, and electronic properties of MPS3 compounds. (a) Crystal structure of MPS_3, illustrating the metal ions arranged in a honeycomb structure with the P_2S_6 clusters situated in the centre. (b) Shifted stacking of the individual layers parallel to the cleavage plane (left). (c) P_2S_6 cluster and the octahedral coordination of the transition-metal (M) ions by surrounding S atoms. Adapted from Ref [101].

tion in the crystal field of the sulphur atoms, which can vary depending on the transition metal ion, thereby leading to deviations from the intrinsic monolayer properties. The lattice constants of the MPS_3 compounds, as well as the monoclinic stacking angle β, and vdW-gap d are summarized in Table 1.1, showing only minor variations between the different metal cations.

Another notable property of MPS_3 is their high structural stability and ease of exfoliation. Calculated values for the cleavage energy, which quantify the feasibility of mechanical exfoliation, range between 0.1 and 0.3 $J\,m^{-2}$, which is lower than that of graphite (0.38 $J\,m^{-2}$) [102]. Furthermore, investigations of the phonon modes in $MnPS_3$ reveal no imaginary frequencies, which is interpreted as strong evidence for its dynamical stability and the potential to isolate free-standing monolayers [103]. This property is likely transferable to the other members of the MPS_3 material family.

Table 1.1: Lattice parameters for the investigated MPS_3 compounds

	a (Å)	b (Å)	c (Å)	β (°)	d (Å)
$MnPS_3$	6.077	10.524	6.796	107.35	3.21
$FePS_3$	5.947	10.300	6.722	107.16	3.19
$CoPS_3$	5.901	10.222	6.658	107.17	3.19
$NiPS_3$	5.812	10.070	6.632	106.98	3.21

1.2.2 Electronic Properties

Due to the various types of bonding present in MPS_3 materials, the key characteristics of their electronic structure were difficult to predict correctly for a long time. While band structure calculations based on the single-particle picture often suggested metallic behaviour [104], UV reflectivity and XAS measurements indicated semiconducting properties instead. To fully understand the nature of the electronic structure of this material class, it is essential to consider the contribution of different atomic orbitals. The observed semiconducting behaviour arises from strong Coulomb correlations among the $3d$ electrons. These interactions cause electron localization at the M^{2+} ions, thereby reducing their mobility. As a consequence, electrical conductivity is suppressed, and a band gap opens around the Fermi level [105]. The width of this

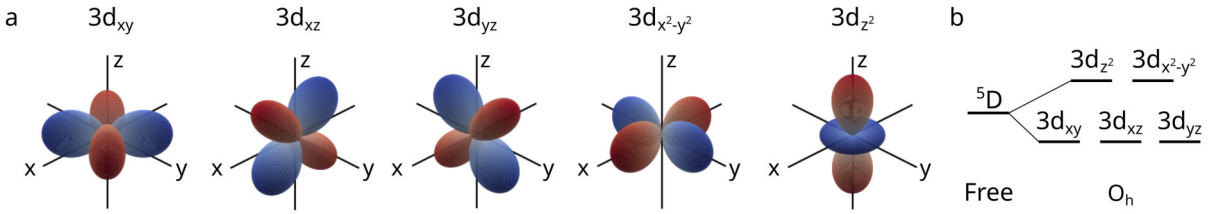

Figure 1.2: (a) Real space distribution of electron density for the 5 d-orbitals. (b) Energy splitting of the d-orbitals in an octahedral environment according to crystal field theory.

gap is governed by interionic excitations, specifically the energy required to transfer a $3d$ electron from one transition metal ion to another. A similar mechanism is well-known in transition metal oxides, which also exhibit insulating behaviour and have been studied extensively in this context [106, 107]. The following discussion is therefore based on this well-established behaviour and analogously applied to MPS_3.

The interaction between the transition metal atoms and the P_2S_6 clusters is predominantly ionic, with only weak covalent contributions. As a result, the metal atoms are present in a $+2$ oxidation state, with their $4s$ electrons transferred to the ligands, which are consequently in a -2 oxidation state. As noted previously, the transition metal ions reside in an octahedral (O_h) environment, which lifts the degeneracy of the $3d$ orbitals according to their magnetic quantum number m_l. This splitting can be understood within the one-electron approximation, where the surrounding ligands are treated as point charges interacting electrostatically with the $3d$ orbitals (illustrated in Figure 1.2a). Placing the ligands along the coordinate axes as point charges leads to different Coulomb interactions depending on the spatial orientation of the orbitals: the e_g orbitals (e.g. d_{z^2} and $d_{x^2+y^2}$), which point directly at the ligands, experience stronger repulsion and therefore increase in energy, while the t_{2g} orbitals (e.g. d_{xy}, d_{xz}, d_{yz}) point between the ligands and experience less repulsion, thus lowering in energy. The resulting energy difference between these levels is the crystal field splitting Δ_{CT} (see Figure 1.2b).

Table 1.2: Electronic structure of Mn-, Fe-, Co-, and $NiPS_3$.

	E_{gap}	d-electrons	spin configuration
$MnPS_3$	3.0	5	$e_g \uparrow\uparrow t_{2g}$ ($\uparrow\uparrow\uparrow$)
$FePS_3$	1.4	6	$e_g \uparrow\uparrow t_{2g}$ ($\uparrow\downarrow\uparrow\uparrow$)
$CoPS_3$	1.6	7	$e_g \uparrow\uparrow t_{2g}$ ($\uparrow\downarrow\uparrow\downarrow\uparrow$)
$NiPS_3$	1.4	8	$e_g \uparrow\uparrow t_{2g}$ ($\uparrow\downarrow\uparrow\downarrow\uparrow\downarrow$)

Table 1.2 shows the band gap energies, number of d-electrons, and their corresponding spin configurations. All four compounds exhibit a high-spin configuration, with the energetically higher-lying e_g orbitals always occupied by two spin-up electrons, while the t_{2g} occupation ranges from single occupancy of each orbital ($MnPS_3$) to full double occupancy ($FePS_3$) [23].

All MPS_3 compounds investigated in this thesis are semiconducting, with band gaps ranging between 1.2 and 3.5 eV, originating from interionic excitations, which also determine the magnitude of the gap. Generally, the different MPS_3 materials can be classified in terms of their semicon-

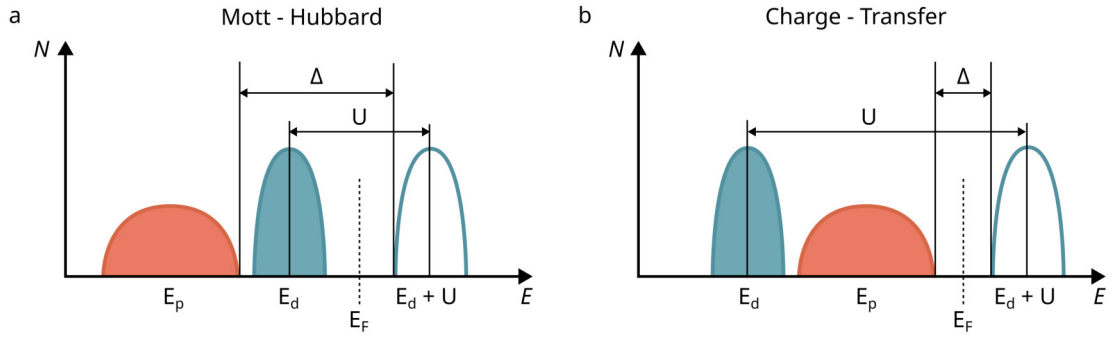

Figure 1.3: Energy diagram for the charge-transfer (CT) and Mott-Hubbard (MH) insulators. E_d and E_p mark the central energies for the metal ions d and the ligands p-bands. Adapted from Ref [110].

ducting behaviour using the Zaanen-Sawatzky-Allen (ZSA) formalism [108], which describes the dependence of the conductivity gap on the relative size of the on-site Coulomb interaction U and the charge-transfer energy Δ (see Figure 1.3). Figure 1.3 illustrates the typical relationship between these two parameters for Mott-Hubbard (MH) and charge-transfer (CT) insulators. In a Mott-Hubbard insulator, the energetic separation U between the $3d$ states is smaller than the charge-transfer energy Δ between the metal d-states and the ligand p-states. This classification applies to $MnPS_3$ and $FePS_3$. In contrast, CT insulators exhibit ligand p-states close to the Fermi level, resulting in electron transfer between metal and ligand orbitals; $NiPS_3$ falls into this category. $CoPS_3$ displays a mixed character where $U \approx \Delta$ [109].

1.2.3 Magnetic Properties

One of the most intriguing aspects of the different MPS_3 compounds is their inherent magnetic ordering. All MPS_3 compounds discussed above exhibit antiferromagnetic ordering at $T = 0\,\mathrm{K}$. As the temperature increases, thermal fluctuations progressively disrupt the long-range magnetic order. At the Néel temperature T_N, these fluctuations become sufficiently strong to destabilize the ordered ground state, leading to a transition into a paramagnetic phase. The magnetic moments, like the $3d$ electrons, are localized at the transition metal (TM^{2+}) ions. They originate from the interplay between crystal-field splitting and exchange interactions among individual spin moments. Due to the spatial confinement of the TM^{2+} ions between the $(P_2S_6)^{4-}$ complexes, hybridization of the transition metal orbitals is weak. As a result, the exchange interactions are primarily mediated indirectly through the surrounding sulphur and phosphorus atoms [104].

Depending on the specific transition metal ion, different types of magnetic ordering and properties emerge within this class of materials. The strength and orientation of the spin structure are influenced by several parameters that contribute to the inter- and intralayer exchange interactions, such as dipole-dipole interactions between magnetic moments, crystal field splitting, and spin-orbit coupling. For example, due to the orientation of all spins being perpendicular to the ab plane, $FePS_3$ is classified as an Ising-type antiferromagnet [39]. Additionally, the spins form a zigzag-type structure with antiferromagnetic coupling between the layers (see Figure 1.4). In contrast, $MnPS_3$ exhibits a Néel-type spin structure with ferromagnetic coupling between the

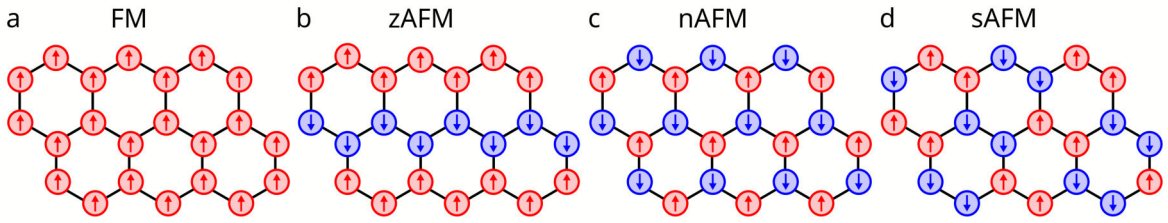

Figure 1.4: Different magnetic arrangement for hexagonally conformed materials for (a) ferromagnetic, (b) zigzag antiferromagnetic, (c) Néel-type antiferromagnetic, and (d) stripe like antiferromagnetic materials.

individual layers and spins canted with respect to the surface, as shown by neutron diffraction [111]. Lastly, both $NiPS_3$ and $CoPS_3$ also exhibit ferromagnetic interlayer coupling, but with in-plane spin orientation in a zigzag-type order. This diversity is one reason for the strong interest in these materials, as their varying spin arrangements allow a detailed study of different spin textures within a single material class [110].

Besides these differences in spin structure, the magnetic properties of MPS_3 compounds also exhibit intriguing variations. For instance, the Néel temperature spans a wide range: $MnPS_3$ shows the lowest value at only 78 K, while $NiPS_3$ has the highest at 155 K. $FePS_3$ and $CoPS_3$ lie in between with 118 K and 120 K, respectively. Moreover, while $FePS_3$, $CoPS_3$, and $MnPS_3$ retain their antiferromagnetic order down to the monolayer regime, with either no ($FePS_3$) or only minor variations ($CoPS_3$ and $MnPS_3$) in T_N, $NiPS_3$ appears not to preserve its magnetic order at the monolayer limit, exhibiting strong thickness-dependent variations of T_N [112, 113]. The observed stability of T_N in $FePS_3$ is generally attributed to the dominance of intralayer spin exchange interactions over the much weaker interlayer coupling, as well as the influence of spin-orbit coupling (SOC) [39, 113].

1.2.4 Optical Properties

As introduced in the previous chapter, all four MPS_3 materials exhibit optical band gaps in the near-infrared to visible range, governed by charge-transfer transitions involving phosphorus and sulphur states. Beyond the fundamental band-edge absorption, these compounds feature numerous sub-gap *d-d* transitions and excitonic resonances, often manifesting as sharp photoluminescence peaks or optical absorption features associated with localized ligand-field excitations. For instance, $NiPS_3$ displays exceptionally narrow photoluminescence peaks at 1.475 and 1.494 eV, attributed to spin-tangled and charge-transfer excitons with pronounced spectral anisotropy [114], closely linked to its zigzag antiferromagnetic order. $FePS_3$, on the other hand, exhibits giant optical linear dichroism associated with its zigzag spin texture, enabling optical detection of magnetic domains down to the monolayer limit [115]. Moreover, it hosts multiple *d-d* transitions, two of which lie below the onset of the band gap and can be used to excite magnons via strong magnon-phonon coupling [53]. Similarly, *d-d* transitions in $CoPS_3$ have been shown to effectively alter the orbital angular momentum of the M^{2+} ions, thereby launching coherent lattice vibrations in the THz regime [116]. The key optical resonances observed in the different MPS_3 compounds up to a maximum energy of 4 eV are summarized in Table 1.3.

Table 1.3: Lowest excitonic and *d*-*d* transition resonances in MPS_3 compounds up to 4 eV.

Compound	E_{d-d}	$E_{exciton}$	Additional Notes	Source
$MnPS_3$	1.91 eV	-	Three *d*-*d* transitions below gap	[22, 36, 37]
$FePS_3$	1.09 eV	-	Giant LD, magneto-optical coupling	[22, 37, 52, 115]
$CoPS_3$	0.94 eV	-	Crystal-field *d*-*d* absorption feature	[22, 34, 37]
$NiPS_3$	1.05 eV	1.475 eV	Strong electron-phonon coupling	[33, 114, 117–119]

1.3 Hybridisation at Molecular Interfaces

One of the techniques that we will employ later to explore the targeted modification of the electronic or magnetic properties of our samples is the functionalisation with molecular adsorption. Before experimentally investigating the interaction between a two-dimensional antiferromagnetic surface and a prototypical organic molecule, namely pentacene, it is essential to understand the physical processes that may occur at the interface and how they influence the electronic properties of both the substrate and the molecule.

1.3.1 Electronic Structure of Organic Molecules

The electronic structure of organic molecules is fundamentally determined by the arrangement and hybridization of atomic orbitals, particularly those of carbon, which typically adopts sp^2 or sp^3 hybridization states. Organic molecules consist of two major bonding frameworks: σ-bonds and π-bonds.

σ-bonds arise from head-on overlap of hybridized orbitals (e.g., sp^2–sp^2, sp^3–sp^3), forming the molecular skeleton. These bonds are localized, strong, and constitute the primary framework of the molecule. π-bonds, on the other hand, result from the lateral overlap of unhybridized p orbitals [120]. In conjugated systems, such as alkenes, aromatic rings, and polyenes, these π-orbitals can delocalize across multiple adjacent atoms. This delocalization gives rise to molecular orbitals (MOs) that extend over the entire conjugated segment. An illustrative example is shown in Figure 1.5, based on ethene (C_2H_4).

In linear conjugated systems (e.g., polyacetylene), alternating single and double bonds enable π-electron delocalization, which lowers the overall electronic energy and gives rise to semiconducting behaviour. In aromatic systems such as benzene, cyclic delocalization further stabilizes the molecule, fulfilling Hückel's $4n + 2$ π-electron rule. This is also the case for pentacene, an organic molecule consisting of five aromatic rings of carbon atoms, where the sp^2-hybridized carbon atoms form strong covalent σ-bonds in the molecular plane, while the remaining p_z orbitals lead to the formation of π-bonds.

The two most critical molecular orbitals in terms of chemical and electronic properties are the highest occupied molecular orbital (HOMO) and the lowest unoccupied molecular orbital (LUMO). The HOMO defines the topmost filled orbital, primarily determining the donor behaviour and ionization potential, while the LUMO corresponds to the lowest empty orbital, relevant for acceptor characteristics and electron affinity. The energy difference between HOMO and LUMO constitutes the fundamental electronic gap of the molecule. In conjugated organic

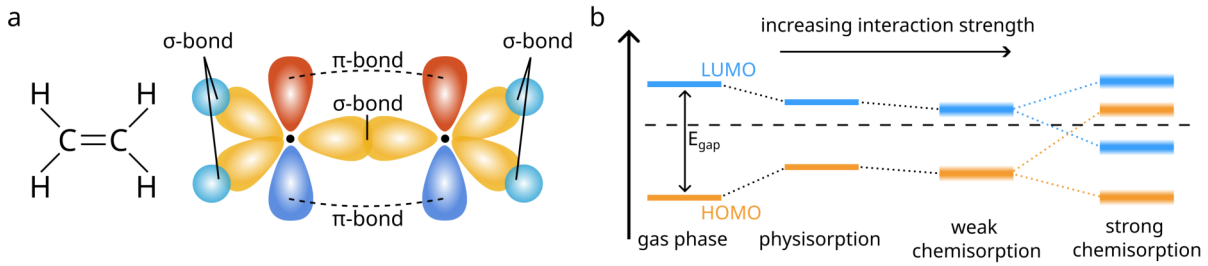

Figure 1.5: (a) The ethene molecule contains five σ-bonds. Four of them are due to the overlap of the C atoms sp^2 orbital with the hydrogen s orbital and one is between the two sp^2 orbitals in the centre. The side-by-side overlap of the two unhybridized orbitals then leads to the formation of two π-bonds below and above the plane of the σ-bonds. Adapted from [123].

molecules, this gap typically lies in the range of 1.5 eV to 3.5 eV, allowing photoexcitation and charge transport when integrated into optoelectronic devices [121].

In a simple conjugated system such as butadiene, the π-system forms bonding and antibonding molecular orbitals. The number of MOs equals the number of contributing p orbitals. For n conjugated atoms, there are n π-MOs arranged in increasing energy: the lower MOs are bonding (delocalized with constructive interference), while the higher MOs are antibonding (containing nodes and exhibiting destructive interference) [122].

Electronic excitations typically involve transitions from the HOMO to LUMO (or higher unoccupied orbitals), absorbing a photon whose energy matches the gap ($E_{\text{gap}} = E_{\text{LUMO}} - E_{\text{HOMO}}$). This defines the optical absorption edge. In organic semiconductors, both the orbital shapes and the degree of delocalization influence charge mobility and exciton binding energies.

1.3.2 Interaction Regimes: Physisorption to Chemisorption

As described in the previous chapter, the electronic structure of organic molecules consists of discrete molecular levels with well-defined energies. However, when these molecules are deposited on metallic or semiconducting surfaces, their electronic structure can undergo substantial modifications, ranging from simple energetic shifts to the formation of hybridized interface states that may split in energy. One key physical quantity used to characterize these regimes is the adsorption energy ΔE, defined as the energy required to remove an adsorbed molecule from the surface [124].

The interaction strength between molecular adsorbates and the substrate surface is commonly categorized into two regimes: physisorption and chemisorption. Chemisorption itself is often further divided into weak and strong chemisorption. Physisorption typically involves weak coupling at the interface, such as on surfaces without dangling bonds (e.g., many two-dimensional materials or inert/passivated surfaces), and is primarily governed by van der Waals forces, permanent molecular dipoles, and the Pauli exclusion principle. The latter interaction scales with the spatial overlap between substrate and molecule and therefore decays exponentially with distance. This weak interaction generally yields adsorption energies in the range of 0.1 to 1 eV and largely preserves the electronic structure of the molecule. The adsorbed species often retain their gas-phase character, exhibiting only minor modifications such as a reduced energy sepa-

ration between the LUMO and HOMO. Nevertheless, charge transfer may still occur through tunnelling processes [125].

On more reactive substrates, where chemical bonds and partial charge transfer occur at the interface, the interaction is described by the chemisorption regime, which can significantly modify the molecule's electronic structure. This includes the emergence of new hybridized states with mixed metal-molecule character, as well as shifts in energy levels. A widely used theoretical framework to rationalize these effects is the Newns-Anderson model [126, 127]. In this model, we need to consider another physical quantity in addition to the adsorption energy ΔE, namely the bandwidth W of the interacting substrate band. The ratio $W/\Delta E$ is commonly used to distinguish between weak and strong chemisorption.

In the weak chemisorption limit ($W/\Delta E \gg 1$), the molecule typically interacts with broad substrate bands, such as s and p bands, which have typical widths around $W \approx 10\,\mathrm{eV}$ [66]. Here, the hybridization results in a finite lifetime τ for molecular states, leading to Lorentzian broadening of sharp molecular orbitals, described by $\Gamma = \hbar/\tau$. Additionally, partial charge transfer between the substrate and molecule can occur, resulting in energy shifts and even partial occupation of previously unoccupied orbitals (e.g., LUMO+n) [128, 129].

In contrast, the strong chemisorption regime ($W/\Delta E \ll 1$) arises when the molecule interacts with narrow bands such as d or f bands, typically with $W \approx 1\,\mathrm{eV}$. In this regime, hybridization is so strong that the original molecular states may split into bonding and antibonding resonances, analogous to the formation of molecular orbitals from atomic orbitals. Depending on the energetic position of these hybrid states relative to the Fermi level, they can undergo electron backdonation (if the newly formed states fall below the Fermi level) or electron donation (if the initial molecular states lie above it), resulting in partial filling or depletion of molecular orbitals [66].

1.3.3 Electronic Structure Effects at the ORG/SC Interface

The nature of molecule-substrate interaction has profound implications for the interface electronic structure, influencing device-relevant parameters such as carrier mobility, charge separation, and optical response. These modifications can often be understood in terms of the energy level alignment at the surface, hereafter abbreviated as ELA, which refers to the relative position of the energy levels on both sides of the interface. The ELA determines the tunnelling properties across the interface, including the direction of charge transport [130], which is critical for many applications such as solar cells.

Figure 1.6 displays different types of alignment that can occur at the molecule-substrate interface. As key physical quantities relevant for the ELA, we consider the energetic positions of the valence band maximum (VBM) and conduction band minimum (CBM) of the semiconducting (SC) substrate, as well as the HOMO and LUMO of the adsorbed molecule. In the case of type I alignment (shown in Figure 1.6a), the material with the smaller band gap aligns entirely within the band gap of the other material, making it particularly suitable for energy transfer, as both holes and electrons will relax into the same material.

In contrast, type II interfaces exhibit staggered alignment of the CBM (LUMO) and VBM (HOMO), which provides an efficient pathway for electron-hole separation, as required in photo-

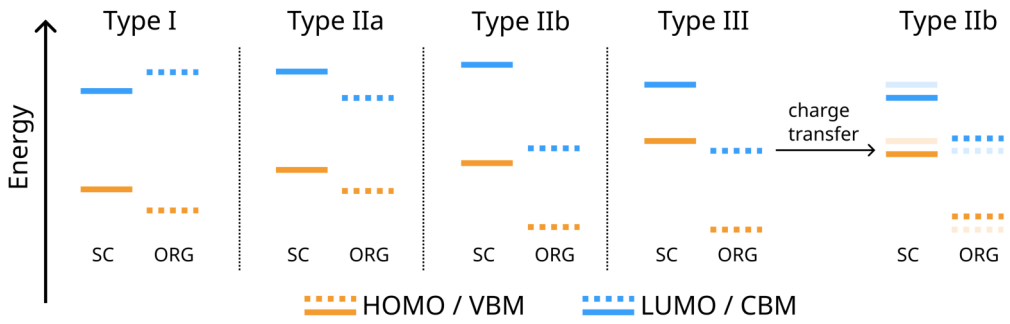

Figure 1.6: Different band structure alignments between the SC surface and the organic molecules (ORG). The roles of both components are reversible. The different types are characterized mainly by the relative positions of the VB and HOMO (orange) of component 1 with respect to the CB or LUMO (blue) of component 2. Type IIa and IIb are separated based on the barrier between the unoccupied and occupied levels. Adapted from [131].

voltaics and photodiodes. Depending on the relative energy spacing between the CBM (LUMO) and VBM (HOMO) of both materials, this class can be further divided into type IIa and type IIb. The last type of interface, type III, features the CBM (LUMO) of one material positioned below the VBM (HOMO) of the other. However, such a configuration is often unstable and can evolve into a type IIb ELA due to interface effects such as band bending, charge transfer, and, in some cases, chemical bond formation. The latter is itself influenced by the initial ELA, as, in a simplified picture, bond formation is driven by the hybridization of electronic states at similar energy levels [131].

In the situation depicted for a type III alignment in Figure 1.6, the contact between both materials leads to an electron transfer from the VBM of the semiconducting substrate into the LUMO of the adsorbed organic molecules. This local positive charge induces a rearrangement of the energy levels, resulting in a transformation of the ELA into a type II alignment. This effect enables targeted tuning of the ELA, leveraging the versatility of organic molecules, where factors such as molecular orientation, substitutional groups, and chain length all influence the molecule's electronic properties. For example, Greiner et al. [132] have shown that changes in the work function of transition metal oxides upon adsorption of organic molecules follow a universal trend, primarily governed by the ionization energy of the molecule and the initial work function of the substrate [120, 133–136].

A slightly different situation arises in the case of n-doped semiconducting substrates, where the LUMO of the adsorbed molecule lies below the Fermi energy of the substrate due to the molecule's electron affinity exceeding the substrate's work function [137, 138]. In this case, electrons are transferred from the substrate to the molecule, building up an interface dipole moment Δ_{CT}, which shifts the partially occupied LUMO to higher energies until it aligns with the Fermi energy. This interface dipole is generally divided into two contributions: one stemming from band bending (Δ_{BB}), and one from a surface dipole contribution (Δ_{SD}). The magnitude of each contribution can vary, with band bending often limited by defect states near the surface [138].

While many additional concepts are relevant for organic/metal interfaces, such as momentum-

selective orbital hybridization [139] or the IDIS model [140], these are primarily applicable to metallic substrates and are thus not central to the investigations presented in this thesis. Nevertheless, the effects discussed above already highlight that the ELA at organic/semiconducting interfaces provides essential insights into interface phenomena and is key to the targeted modification of a substrate's electronic structure. While conventional photoelectron spectroscopy already offers valuable information about the energetic alignment of molecular orbitals, we will see later in section 5.2 that a more advanced method, photoemission orbital tomography (POT), based on angle-resolved photoelectron spectroscopy, enables the direct identification of individual orbitals. This provides a more detailed picture of the ELA at the interface. Moreover, the development of time-resolved ARPES techniques offers further insight into the ultrafast electron dynamics at such interfaces. It enables the investigation of complex phenomena such as exciton formation, where a precise understanding of the ELA allows for disentangling contributions from different molecular and substrate orbitals [130, 141].

2 | Experimental Methods

This chapter provides an overview of all experimental methods employed in the research presented in this thesis. The first part introduces the theoretical principles of momentum microscopy, beginning with the fundamentals of angle-resolved photoelectron spectroscopy (ARPES) and a description of the two types of detectors used. In the second part, the focus extends to include the time domain. This section introduces the concept of time-resolved ARPES (trARPES), highlighting the central physical principles as well as the key quantum phenomena that can be investigated with this technique in semiconducting materials. The final two sections conclude the chapter by presenting the experimental setups in detail, along with a description of the sample preparation procedures.

2.1 Photoelectron Spectroscopy

The available literature on the fundamentals of the photoemission process is extensive. Therefore, this thesis will refrain from providing a comprehensive review of the various stages involved in photoemission or the distinctions between different theoretical models. Instead, we begin at a more application-oriented level by introducing the key experimental techniques used throughout this work - Momentum Microscopy (MM) and X-ray Photoelectron Spectroscopy (XPS). Following a brief overview of the general concept of angle-resolved photoemission, which forms the foundation of momentum microscopy, we will focus on the two types of detectors employed for the investigation of the MPS_3 material family. While both systems are based on the same physical principles, they differ significantly in terms of data acquisition and the subsequent data processing. This section concludes with an introduction to X-ray Photoelectron Spectroscopy, a technique that provides access to the atomic core levels and thus yields crucial information about chemical moieties, oxidation states, and the electronic configuration of specific orbitals. The presented explanations are based on the books by *Stefan Hüfner* [105] and *Shigesama Suga et al.* [142] as well as reviews by *Sobota et al.* [46], *Boschini et al.* [48], and *Na et al.* [49].

2.1.1 Angle-Resolved Photoelectron Spectroscopy

The basic principle of photoelectron spectroscopy (PES) is based on the photoelectric effect, in which electrons are emitted from the surface of a material upon irradiation with monochromatic light. By capturing these emitted electrons and measuring parameters such as their kinetic energy E_{kin} and emission angles (ϕ, θ), it is possible to extract detailed information about the electronic structure of the material. Depending on the photon energy used, different aspects

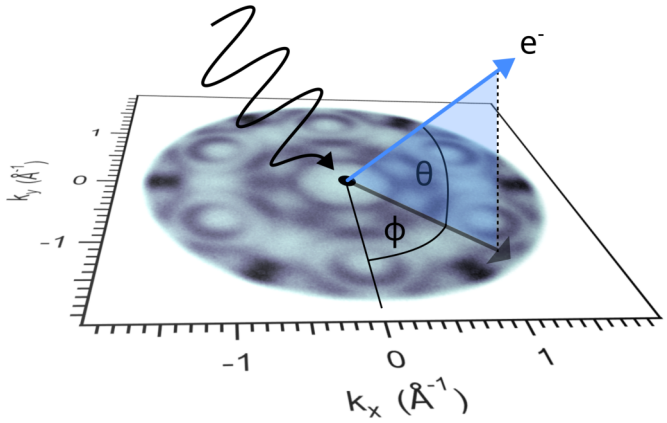

Figure 2.1: Schematic representation of the connection between the electron emission angles θ and ϕ and the parallel momentum components in k-space k_x and k_y. The black arrow stands for the incoming photon, subsequently leading to the emission of the electron (blue arrow). The underlying image is the momentum-dependent photoemission intensity at constant binding energy.

of the electronic structure can be probed. Photon energies in the range of a few hundred electronvolts are typically employed to investigate the valence band structure, whereas higher photon energies, in the range of several kiloelectronvolts, are used to access the core levels of specific elements.

In angle-resolved photoelectron spectroscopy (ARPES), measurements are typically performed using photon energies $h\nu$ in the range of a few tens of electronvolts. Based on energy and momentum conservation of the photoemitted electrons, it is possible to extract both the binding energy E_B and the parallel momentum component $k_{||}$ using the following relations:

$$E_{\text{kin}} = h\nu - \Phi - E_B \tag{2.1}$$

$$(k_{||,x}, k_{||,y})^\intercal = \frac{\sqrt{2m_e}}{\hbar}\sqrt{E_{\text{kin}}}\cos(\theta)\cdot(\sin(\phi), \cos(\phi)^\intercal \tag{2.2}$$

Here, Φ denotes the work function of the investigated material, and m_e is the electron mass. Together, these parameters allow for a detailed characterization of the electronic structure by mapping the emission intensity I as a function of E_B, k_x, and k_y. The resulting spectra can either be integrated over momentum, yielding the intensity solely as a function of binding energy (also referred to as energy distribution curves, or EDCs), or analysed in a momentum-resolved manner. In the latter case, two-dimensional cuts along specific directions in momentum space are typically used, often connecting high-symmetry points of the surface Brillouin zone.

Besides the maximum accessible momentum space, the ARPES intensity also depends strongly on the experimental geometry and the photon energy used. In a standard photoemission experiment, the ARPES intensity is described by

$$I(k,\omega) \propto |M^k_{f,i}|^2 A(k,\omega) f(\omega), \tag{2.3}$$

where $M^k_{f,i}$ is the photoemission matrix element, $A(k,\omega)$ denotes the one-electron removal spectral function, and $f(\omega)$ is the occupation function at a given temperature T (typically the Fermi-Dirac distribution in our case). The photoemission matrix element plays a critical role in the measured intensity and reflects the symmetry and polarization dependence of the photoemission process. It accounts for the polarization of the incoming photons as well as the symmetries of the initial and final states. As a result, it can significantly modulate the ARPES signal, occasionally even suppressing the contributions from specific orbitals entirely. For instance, the use of linearly polarized light can selectively enhance or suppress emission from particular d-orbitals: s-polarized light (polarized perpendicular to the plane of incidence) predominantly reveals contributions from the d_{yz} orbital, whereas p-polarized light (polarized within the plane of incidence) primarily probes the d_{xz} orbital [143]. However, spin-orbit coupling (SOC) can lead to a mixing of orbital contributions in the ARPES spectra, even when using linearly polarized light.

Equally important, the one-electron removal spectral function $A(k,\omega)$ encodes the intrinsic electronic structure and many-body interactions of the system. It is formally defined via the imaginary part of the retarded Green's function [46, 49]

$$A(k,\omega) = -\frac{1}{\pi}\mathbf{Im}G(k,\omega) = -\frac{1}{\pi}\mathbf{Im}[\frac{1}{\omega - \epsilon_k - \Sigma_k(\omega)}] \tag{2.4}$$

$$= \frac{-1}{\pi}\frac{\Sigma''_k(\omega)}{|\hbar\omega - \epsilon_k - \Sigma'_k(\omega)|^2 + |\Sigma''_k(\omega)|^2}. \tag{2.5}$$

Here, ϵ_k represents the bare-band dispersion describing the electronic structure in the non-interacting case, while $\Sigma_k(\omega)$ denotes the electron self-energy, introduced to account for perturbations based on the interacting system. As the formula indicates $\Sigma'_k(\omega)$ leads to an offset of the electron band energy ϵ_k and $\Sigma''_k(\omega)$ broadens the spectral peak [46]. This connection to the electron self-energy positions ARPES as a unique technique for understanding the electronic properties of solids [144].

2.1.2 Momentum Microscopy

Conventional electron energy analysers typically operate in a two-dimensional plane, allowing the simultaneous acquisition of photoelectrons only within a limited angular range, typically around 30° in one direction. As a result, mapping the full band dispersion across a broader range of parallel momenta requires mechanical rotation of either the sample or the detector to scan through different emission angles ϕ and θ. In recent years, a new technique has emerged that combines ARPES with imaging electron optics — momentum microscopy (MM). This method allows for the simultaneous capture of the full momentum space in a single-shot experiment. The key innovation is the use of a cathode immersion lens, also referred to as an extractor lens. A strong accelerating electric field is applied between the sample and the entrance lens, typically in the range of 5 kV to 30 kV. This field bends the trajectories of photoelectrons, even

those emitted at high angles, such that they all enter the lens system and are subsequently imaged. Since the accelerating field is oriented perpendicular to the sample surface and exhibits cylindrical symmetry, the parallel momentum component $k_{||}$ is conserved. However, the emission angle is reduced to a smaller effective angle θ' under which the electrons enter the lens. This reduced angle remains related to the parallel momentum through:

$$\sin(\theta') = k_{||} \frac{\hbar}{\sqrt{2m_e(eU_A + E_{\text{kin}})}} \tag{2.6}$$

An exemplary schematic of the cathode lens system, along with the trajectories of the electrons after emission from the surface, is shown in Figure 2.2a. When the acceleration voltage U_A is large compared to the kinetic energy of the emitted electrons, the resulting momentum distribution in the back focal plane (also referred to as the Fourier plane, in analogy to conventional optics) is linearly proportional to the parallel momentum $k_{||}$. Assuming that the cathode lens collects electrons emitted within an angular range of $\pm 90°$, the maximum accessible parallel momentum depends solely on the kinetic energy E_{kin} of the emitted electron and is given by:

$$k_{||}^{\text{max}} = \frac{\sqrt{2m_e E_{\text{kin}}}}{\hbar} \tag{2.7}$$

As an example, illuminating an Au(111) surface (with a work function of $\Phi = 5.31\,\text{eV}$) using photons with an energy of $h\nu = 21.22\,\text{eV}$ (corresponding to the He I α line of a helium discharge lamp) results in a maximum accessible parallel momentum of $k_{||}^{\text{max}} = 2.043\,\text{Å}^{-1}$. This value is sufficient to cover the entire first Brillouin zone (BZ). This relationship also explains why high-harmonic generation (HHG) sources are used in later experiments. For instance, a conventional laser pulse with $h\nu = 6\,\text{eV}$ would only yield an accessible $k_{||}^{\text{max}} \approx 0.725\,\text{Å}^{-1}$ for a sample with a typical work function of $\Phi = 4\,\text{eV}$.

Besides imaging the electrons in momentum space (where each pixel on the detector collects electrons leaving the sample surface under identical emission angles θ and ϕ), momentum microscopes also enable imaging in real space. In this mode, each detector pixel corresponds to a fixed lateral position on the sample surface, effectively forming a spatially resolved image. Switching between momentum and real-space imaging is achieved in the third stage of the lens column. By employing additional electron lenses, one can choose whether to project the momentum space (Fourier plane) or the real space (image plane) onto the CCD detector. This functionality allows for direct imaging of the sample surface, often performed using secondary electrons. Since the Fermi level is aligned to the detector through electrical grounding, the energetic position of the secondary onset of the emitted electrons varies depending on the material's work function (see Figure 2.2b, Materials 1 and 2). By selecting a kinetic energy where only electrons from a specific material contribute, high-contrast imaging of the sample is possible. While this is often done at low kinetic energies, higher energies can also be used, provided that the density of states (DOS) at the chosen energy differs significantly between materials, ensuring sufficient contrast (also illustrated in Figure 2.2b).

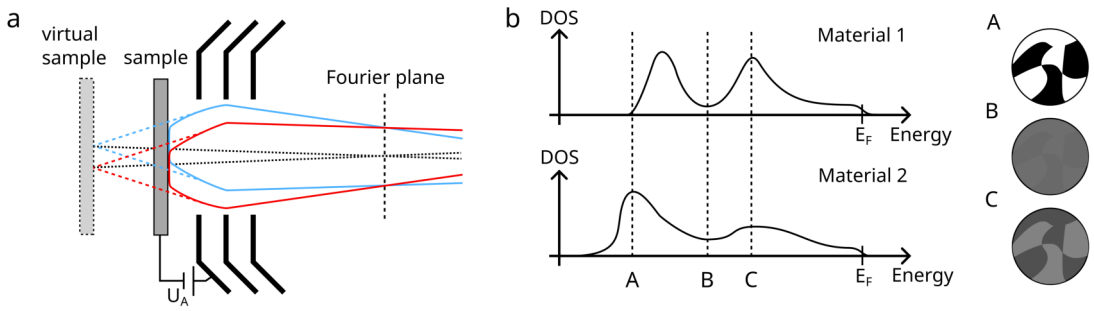

Figure 2.2: (a) General design of the immersion lens, projecting a virtual sample by bending the trajectories of electrons leaving the surface under high emission angles into the detector. The plane, where all electrons emitted under the same angle overlap is the Fourier plane (or momentum image plane). Adapted from [142]. (b) Obtainable PEEM real space image when measuring at different kinetic energies. Measuring close to the secondary onset of the material with the lower work function results in the image with highest contrast (A). Measuring at other energetic positions can lead to usable images depending on the difference in DOS, resulting in very bad contrasts at energies with a similar DOS (B) and detectable contrast for energies with stronger deviations (C).

Another important feature of the lens column includes the so-called field aperture and contrast aperture. As discussed, specific positions in the lens column contain either the real-space or momentum-space image. By inserting plates with variable hole diameters at these planes, the passage of electrons can be selectively restricted. The field aperture is placed at a real-space image plane, allowing selection of electrons originating from a defined region of interest (ROI) on the sample. This is particularly useful for studying small or fractured regions where only a limited area is suitable for measurement, or for avoiding contributions from the surrounding substrate. Similarly, the contrast aperture is positioned at a momentum-space plane and restricts electrons to a defined region in k-space. This allows targeting of specific parallel momentum values, for instance, by selecting electrons from a particular high-symmetry point in the Brillouin zone.

Momentum microscopes come in two primary configurations, differentiated by how they resolve the kinetic energy of photoemitted electrons: hemispherical analyzer-based systems and time-of-flight (ToF) based systems. Both types share the foundational lens system for momentum imaging introduced above, but differ significantly in their energy-dispersive mechanisms and data acquisition strategies. The specific implementations used in this work are described in detail in subsection 2.3.2 and subsection 2.3.3.

2.1.3 X-Ray Photoelectron Spectroscopy

While the momentum microscopy introduced in the previous section is primarily employed to investigate the valence band structure of different materials, it is also essential to examine the core levels, particularly in the context of alkali metal-induced changes discussed in section 6.2. This can be achieved using X-ray photoelectron spectroscopy (XPS). In contrast to valence band studies, XPS typically employs much higher photon energies to excite core-level electrons, most commonly around 1.5 keV (e.g., Al Kα: 1486.6 eV, Mg Kα: 1253.6 eV). Since each element

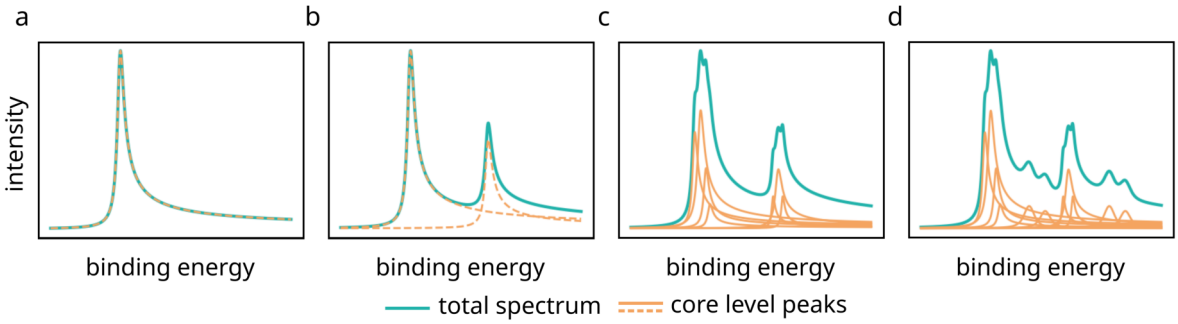

Figure 2.3: Schematic visualisation of the different features appearing in XPS spectra, depicting a XPS spectrum containing (a) a single core level spectrum, (b) spin-orbit coupling (SOC) split main peaks, (c) SOC split peaks including multiplet effects, and (d) all effects mentioned before plus additionally satellite features.

exhibits a unique set of core-level binding energies, XPS enables precise elemental identification as well as the detection of chemical shifts, which reveal changes in the local chemical environment and oxidation states. Despite the higher photon energies, XPS remains a surface-sensitive technique, with tunable information depth that can be adjusted by varying the angle between the analyzer and the sample surface.

For the analysis of XPS peaks, it is crucial to consider the various physical effects that influence the observed core-level line shapes [44]. These effects often lead to complex spectral features, where core-level signals do not appear as simple single peaks [43, 45]. The most important of these effects are discussed in the following and are graphically visualized in Figure 2.3.

One of the most prominent effects in XPS spectra is the presence of spin-orbit coupling (SOC) and the characteristic splitting it induces in core-level peaks. Due to SOC, the kinetic energy of a detected photoelectron depends on whether its spin vector is parallel ($j = l+1/2$) or antiparallel ($j = l - 1/2$) to the orbital angular momentum vector. This results in the appearance of spin-split core-level doublets: $p_{3/2}$–$p_{1/2}$, $d_{5/2}$–$d_{3/2}$, and $f_{7/2}$–$f_{5/2}$ (see Figure 2.3b). The intensity ratio of these doublets is determined by the degeneracy of the corresponding levels $(2j + 1)$, leading to a $2 : 1$ area ratio between the $p_{3/2}$ and $p_{1/2}$ peaks, which are the peaks analysed in section 6.2.

Another important phenomenon affects the detailed shape of the core-level peaks. While in many cases the spectral features can be adequately described using a pseudo-Voigt profile (i.e., a convolution of Gaussian and Lorentzian components), the core levels of transition metals (TMs) often exhibit more complex structures composed of multiple contributions (see Figure 2.3c) [145]. These arise in open-shell systems where the exchange interaction between valence electrons and the unpaired electron left behind in the core level after photoemission gives rise to a set of final states with slightly different energies [146–150]. For example, the emission of a $3s$ electron from Mn^{2+} ($3s^2\,3p^6\,3d^5$) results in a Mn^{3+} final state ($3s^1\,3p^6\,3d^5$), where the hole in the $3s$ level can couple either parallel or antiparallel to the spins in the $3d^5$ shell. This results in two multiplet components within the Mn $3s$ spectrum.

Besides the effects due to SOC and the multiplet structure, which primarily affect the main peaks,

several additional phenomena give rise to secondary features in XPS spectra, often referred to as satellites. These additional peaks can originate from different mechanisms, with the two most common being shake-up (or shake-off) satellites and Auger-related features [151]. Shake-up satellites typically appear a few eV higher in binding energy than the main peak (see Figure 2.3d). They are caused by inelastic interactions between the photoexcited core electron and valence electrons, where the latter are excited to higher energy levels, resulting in an energy loss of the emitted photoelectron [152–154]. Auger-related features, which are sometimes observed in XPS spectra, arise from Auger processes. In such events, the core hole left behind after photoemission is filled by an electron from a higher-energy valence orbital [155]. The energy released during this process can be dissipated either via X-ray fluorescence or by emission of an Auger electron. Since XPS only detects electrons, the latter mechanism contributes to the measured spectrum. These transitions involve three electronic levels, commonly denoted by spectroscopic notations such as K, L, or M. For instance, a KLL transition describes a process where the initial hole is created in the K shell, which is then refilled by an electron from the L shell, with the released energy used to eject another electron from a second L shell [43, 45].

The kinetic energy E_{kin} of the Auger electron is given by:

$$E_{kin,Auger} \approx E_{bin,K} - E_{bin,L_1} - E_{bin,L_2} \tag{2.8}$$

As one can easily see, the kinetic energy of the Auger electron is independent of the photon energy. Consequently, its apparent binding energy position in the spectrum shifts depending on the photon source used. This shift can lead to an overlap with specific core-level peaks, as will be discussed later for the Co $2p$ peak in section 6.2.

2.2 Time-Resolved ARPES

While ARPES and XPS already allow detailed investigations of many interactions in solid-state materials, various specialized adaptations of ARPES have emerged over the past years. These include enhancements in spatial resolution (micro-ARPES, nano-ARPES), the detection of spin-resolved signals (spin-ARPES), and, crucially, the extension into the time domain through time-resolved ARPES (trARPES). Time-resolved ARPES enables the study of non-equilibrium electronic dynamics with energy and momentum resolution. This method provides access to transient phenomena such as carrier relaxation, ultrafast phase transitions, or quasiparticle lifetimes. It is particularly powerful for disentangling intertwined interactions in the time domain by tracking their evolution in energy-momentum space. As trARPES forms the methodological backbone of the investigations in section 4.6, this section introduces its fundamental operating principles, key technological developments in modern table top laser systems, and the types of electronic excitations that can be studied using this technique.

2.2.1 Fundamental Principle

The basic principle of trARPES relies on a spectroscopic pump-probe technique, widely employed in other spectroscopic methods, including photoemission-based approaches such as two-photon photoemission. This technique utilizes two temporally separated laser pulses: the first pulse

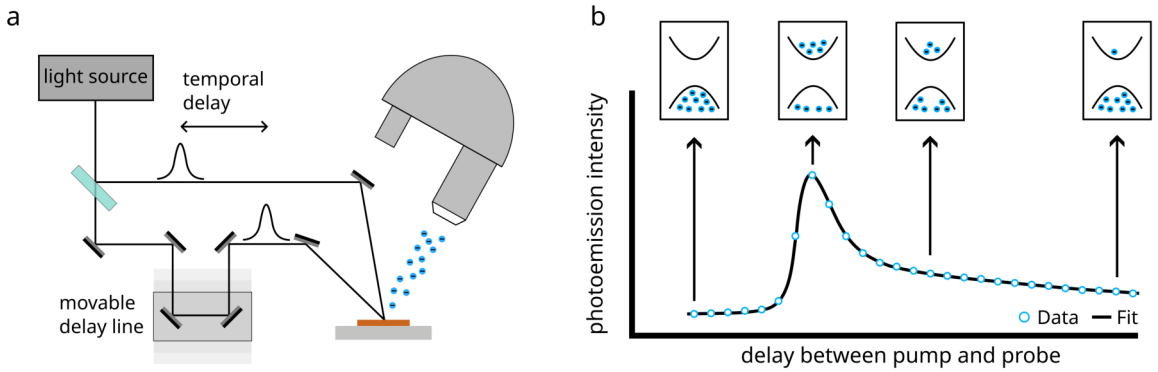

Figure 2.4: Experimental design behind time-resolved ARPES measurements. (a) Typical experimental setup for pump-probe photoemission experiments, consisting of two different pulses with variable delay with respect to each other, and an ARPES detector to detect the photoemitted electrons. (b) Schematic visualisation how a typical transient photoemission intensity curve corresponds to different "snapshots" of the induced dynamics.

(pump) excites the sample and triggers dynamical changes in the electronic structure, while the second pulse (probe) induces photoemission from the transiently excited state with controllable time delay (see Figure 2.4a). The photoemitted electrons are then detected and analysed, enabling access to the evolving out-of-equilibrium band structure. As illustrated in Figure 2.4b, by systematically varying the time delay between the pump and probe pulses and recording the corresponding photoemission intensity, one can reconstruct a time-resolved sequence of band structures. This effectively generates a movie of the electronic dynamics following optical excitation, providing deep insights into relaxation processes and transient phenomena.

Based on the complex fingerprint of electron dynamics typically investigated with trARPES, the laser pulses used must fulfil very specific requirements. First, to map a sufficiently large portion of the momentum space, high photon energies are usually required. While in some cases only dynamics near the Γ point are studied, for example in topological insulators such as Bi_2Te_3 [156], and photon energies around 6 eV are sufficient, many experimental scenarios require full access to the entire first Brillouin zone. As discussed in subsection 2.1.2, this typically necessitates photon energies of approximately 20 eV for most materials. The second key aspect is the time resolution. Many ultrafast processes, such as exciton generation, exciton recombination, or the formation of Floquet-Bloch states, occur on timescales of only a few picoseconds or even less. Therefore, resolving these non-equilibrium dynamics requires ultrashort optical pulses with durations of just tens or a few hundreds of femtoseconds.

2.2.2 High-Harmonic Generation

To meet the challenging requirements for the photon source, trARPES experiments are often based on pulses generated by high-harmonic generation (HHG). This technique is based on a nonlinear optical process, where high-energy photons are generated from a strong laser field interacting with a nonlinear medium, typically noble gases such as argon or neon. This process produces odd-numbered harmonics of the fundamental laser frequency and can therefore be used

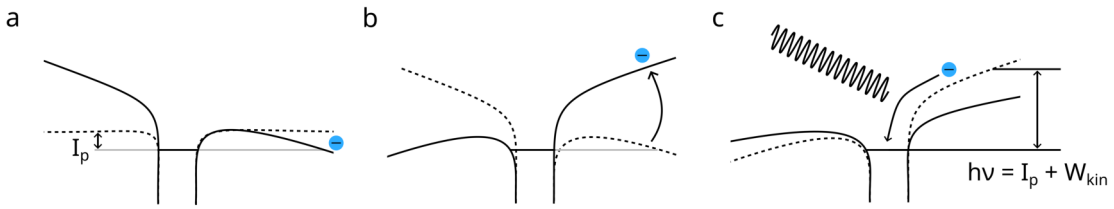

Figure 2.5: Visual depiction of the different steps in generation high harmonics. In the first step (a), the strong field of the laser pulses tilts the potential of the atomic nuclei, allowing the electron to escape. In the second step (b), the electron is accelerated away from the nucleus, before finally (c) recombining with the nucleus after field reversion under emission of a high energy photon. Adapted from [158].

to generate laser pulses with sufficient energy to map the full Brillouin zone of a material.

The process of generating these higher harmonics can be well understood within a semiclassical three-step model, visualized in Figure 2.5, and typically occurs when a high-intensity laser beam, around $1 \times 10^{15}\,\mathrm{W\,cm^{-2}}$, interacts strongly with the medium into which it is focused. In the first step, the electric field of the laser modifies the Coulomb potential of the atomic nucleus, effectively tilting the potential barrier. This leads to a finite tunnelling probability for bound electrons to escape from the atom (Figure 2.5a). In the second step, also known as propagation, the tunnelled electron is accelerated away from the ion by the oscillating field of the laser pulse. When the electric field reverses its sign, the electron is driven back toward the parent ion (Figure 2.5b), and in the final step, recombination of the electron with the atomic nucleus leads to the emission of Bremsstrahlung-like radiation (Figure 2.5c).

The spectrum of the emitted photons typically exhibits a plateau-like structure with several harmonics, terminating at a specific energy known as the cut-off energy. This maximum photon energy generated by HHG is given by:

$$E_{Ph} \leq I_p + 3.17U_q, \tag{2.9}$$

which includes the ionization potential I_p of the used medium and the ponderomotive energy U_p of the laser field [157]. As discussed previously, the emitted spectrum consists of multiple harmonics, which are generated at different times due to the frequency dependence on the ionization potential and the kinetic energy. For this reason, high-harmonic generation is typically followed by a dedicated filtering sequence that removes both the fundamental driving laser and undesired harmonic components. In conclusion, this method represents a table-top technique capable of producing pulses with narrow spectral linewidth and femtosecond time resolution.

However, there are also challenges in identifying an optimal set of parameters, as the pulse characteristics in high-harmonic generation are closely interdependent and typically involve trade-offs between photon energy, flux, and time resolution. Already at the level of the pump laser properties, a higher photon energy (corresponding to a shorter wavelength) results in lower HHG photon energies, but with significantly increased conversion efficiency [159]. Another important

requirement is the limitation of photon flux, as a high density of photoelectrons would lead to pronounced space charge effects arising from electrostatic repulsion. These effects strongly impact the energy resolution and cause broadening in the ARPES spectra, as well as blurring of the momentum maps (as will be shown in section 4.1). Furthermore, temporal and energy resolutions are inherently linked through the time-bandwidth uncertainty principle. This principle states that, in order to achieve a short temporal pulse duration, the pulse must span a broad energy range. This constraint leads to the so-called Fourier limit, which states that the product of the temporal and spectral width of a pulse cannot fall below 1800 meV fs [160]. In summary, HHG is a table-top technique capable of delivering narrow-bandwidth, femtosecond pulses, where a careful selection of experimental parameters is required based on the dynamical processes under investigation.

2.2.3 Measuring Photonic Excitations with trARPES

Many optical excitations that are typically observed with trARPES can also be detected using optical techniques such as photoluminescence measurements. However, due to the ability to resolve the momentum space and directly track the momentum of photoexcited electrons, a wide range of dynamical processes can be studied in greater detail. Moreover, trARPES allows access to specific dynamics that are not detectable using purely optical methods, as those are limited to vertical transitions and do not capture momentum-dependent processes (as illustrated in Figure 2.6). In the case of two-dimensional materials, for instance, enhanced Coulomb interactions can result in strong renormalization of the band gap and the single-particle band structure, pronounced many-body correlation effects, or an increased role of excitons during photoexcitation [48]. This section will therefore briefly outline the momentum-space signatures of different photoinduced excitations observed in trARPES, and highlight examples where these signatures have extended the range of accessible information beyond what standard optical techniques can provide.

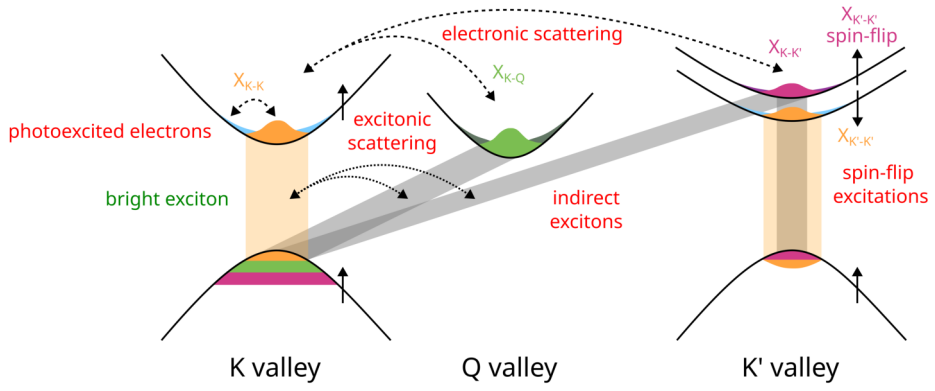

Figure 2.6: Schematic representation of different processes observable with time-resolved ARPES techniques, mostly hidden from standard optical techniques. While bright excitons are also optically accessible (green lettering), the other phenomena like indirect K-Q or K-K' excitons, mixing in different valleys or spin-flip excitons are hidden (red lettering) and can only be investigated in detail with trARPES techniques. Adapted from Ref [50].

Conduction band observation

One of the most fundamental applications of trARPES is the investigation of band gap dynamics in semiconductors. This often includes mapping of the unoccupied conduction bands [51], sometimes using varying pump energies to study intra- and intervalley scattering processes. For instance, the investigation of optical transitions in InSb with different pump energies enables the targeted excitation of specific transitions from selected bands, achieved by careful tuning of the pump wavelength. Additionally, by tracking the temporal evolution of photoemission intensity at distinct points in momentum space, it is possible to observe how electrons, initially excited in the Γ-valley with energies above the minimum of the L-valley, undergo intervalley scattering on timescales of only tens of fs before relaxing back into the Γ-valley [161]. Similarly, trARPES has provided critical insights into dynamical processes in two-dimensional materials such as MoS_2. In centrosymmetric transition metal dichalcogenides (TMDs), the bulk crystals typically exhibit an indirect bandgap between the Γ-point in the valence band and the K-point in the conduction band. However, in the monolayer limit, this shifts into a direct bandgap located at the K-point. By employing different pump photon energies, this change in the band gap character can be observed directly in momentum space. In this way, the direct bandgap of monolayer MoS_2 was measured to be $E = 1.95\,\mathrm{eV}$, a value that deviates significantly from those obtained using static ARPES methods, such as alkali metal doping [162].

Beyond static mapping of the conduction band, trARPES also allows the observation of transient modifications in the band gap energy and electronic relaxation processes. These include phenomena such as renormalization of the band gap, variation induced by the choice of substrate for exfoliation, or doping with foreign atoms [163]. For example, a monolayer of MoS_2 on graphene experiences a band gap renormalization of up to 400 meV [164], induced by the transient redistribution of photoexcited charge carriers that alters the screening potential [165]. The importance of substrate selection was further demonstrated by *Majchrzak et al.*, who characterized the quasiparticle band gaps of mono- and bilayer MoS_2 and WS_2 on graphene, Au(111), and Ag(111). Their results showed that the band gap of the 2D materials, as well as their relaxation dynamics, are strongly modulated by the choice of substrate [166, 167]. Extending these studies to 2D heterobilayers, trARPES has also provided access to intrinsic dynamics that reveal complex interlayer phenomena. These include not only band gap renormalization and charge carrier relaxation but also properties emerging from the relative twist angle between the layers, such as wavefunction localization within moiré patterns [159].

In addition to the mapping of conduction band structure and band gap modifications, trARPES has recently been used to study interactions of quasiparticles such as excitons and photons.

Excitonic excitations

Excitons, which are electron-hole pairs bound by Coulomb attraction, play a central role in defining the optical and transport properties of many semiconductors and insulators, particularly in low-dimensional and strongly correlated materials. In systems such as lead-halide perovskites, excitonic effects dominate the near-band-edge absorption and govern light emission even at room temperature. This behaviour results from their large binding energies and strong light–matter coupling [168]. In two-dimensional semiconductors such as monolayer transition-metal dichalcogenides, the reduced dielectric screening and quantum confinement lead to tightly

bound excitons with binding energies of several hundreds of meV, which determine nearly all optoelectronic behaviour [169].

As schematically visualised in Figure 2.6, many exciton dynamics are not accessible using standard optical techniques. In this context, trARPES substantially extends the range of experimentally observable phenomena. These include momentum-indirect excitons (also referred to as "dark excitons"), excitonic scattering processes, and spin-flip transitions. Following early theoretical work that sought to predict the photoemission fingerprint of excitonic states in ARPES [169, 170], the first direct observation of an excitonic signal using trARPES was reported by *Madéo et al.*, who studied a monolayer of WSe_2 exfoliated onto hexagonal boron nitride (hBN) [171]. By pumping the system well below its electronic band gap, excitonic features were revealed at the K-point of the surface Brillouin zone. More significantly, trARPES enabled the detection of a momentum-indirect dark exciton at the Q-valley. This state appeared with a delay of a few hundreds of fs and could not be detected using purely optical methods. The ability of trARPES to resolve photoemission signals in momentum space enabled the authors to independently analyse the relaxation dynamics at both valleys, including extraction of the scattering timescale between them. Building on these foundational results, the study of excitonic signatures using trARPES has advanced in several directions. These include the observation of excitonic resonances in moiré superlattices and the reconstruction of real-space wavefunctions associated with bound excitonic states [172, 173]. Most recently, trARPES has been applied to molecular layers, providing access to their complex orbital structure. In these systems, excitonic states originate from the coupling of electrons and holes located in different molecular energy levels, and their dynamics can now be studied in momentum space [130].

Light-driven phonons

The last class of quasi-particles relevant for the following discussions are phonons, which are collective vibrations of atoms around their equilibrium positions (see section 1.1). Phonons are often visible in trARPES experiments as oscillations either in the transient photoemission intensity of unoccupied states or in the binding energy of specific bands. In this way, trARPES allows one to investigate how phonons couple to the electronic bath, or more specifically, how they interact with other excitations such as excitons [48]. This interaction can typically be accessed through two different excitation schemes: resonant phonon pumping [174] and non-resonant excitation. The latter often involves displacive excitation mechanisms [53, 175] or Raman processes [176].

The detection of coherent oscillations in momentum space offers a more detailed understanding of the underlying dynamics. For instance, it enables the separation of surface and bulk responses [177] or the identification of mode-specific distortions, such as those found in Bi_2Te_3 and Bi_2Se_3 [178]. However, the detection of such oscillations requires probe pulses with both narrow bandwidth and high temporal resolution. This constraint limits the accessible phonon modes to those with lower frequencies, typically below 3-4 THz [48]. To overcome these limitations, a modified approach known as frequency-domain ARPES has recently been introduced. This method is based on applying a Fourier transformation to time-domain trARPES data and enables the direct extraction of off-diagonal electron-phonon matrix elements [179]. Frequency-domain ARPES allows for the identification of specific phonon modes and their influence on distinct electronic bands by analysing the FT bandstructure at selected oscillation frequen-

cies [180]. This provides access to otherwise hidden interactions and extends the information that can be obtained from time-resolved ARPES significantly.

In addition to the phonon-related phenomena discussed above, trARPES has been successfully applied to explore other ultrafast quantum phenomena such as Floquet-Bloch states [181–183] and charge density wave dynamics [184]. These examples already highlight the power and importance of this method, which in the last decade has yielded insights into processes that were previously either inaccessible or only partially understood with conventional optical techniques. Later in this thesis, we aim to extend the range of phenomena accessible with trARPES by analysing the momentum-resolved signature of *d-d* transition-related multiplet excitations in $FePS_3$.

2.3 Experimental setups

During the investigations presented in this thesis, different experimental setups were employed, each offering specific capabilities and advantages. For the analysis of core-level states, particularly the detection of alkali-metal-induced changes discussed in section 6.2, an X-ray photoelectron spectroscope (XPS) was utilized, as introduced in the first part of this section. To study modifications in the valence band electronic structure, two types of momentum microscopes were employed, each exploiting different detection principles. A hemispherical momentum microscope (MM) was used for the majority of the data acquisition, while a ToF-based MM was primarily used for the investigation of space-charge effects, as discussed in section 4.1.

2.3.1 XPS

XPS measurements were performed using a SPECS Phoibos 150 hemispherical analyzer (SPECS GmbH), in combination with a monochromatized Al Kα source operating at a photon energy of 1486.8 eV. The incident X-ray beam was focused to a spot size of approximately 2 mm on the sample surface. All spectra were recorded under consistent operating conditions, with an acceleration voltage of 12.1 kV and a fixed power setting of 111 W.

The analyzer consists of two concentric hemispheres between which a uniform electric field is applied, as depicted in Figure 2.7. As electrons pass through this field, they follow curved trajectories, with the radius of curvature depending on their kinetic energy. Only electrons with a specific kinetic energy, referred to as the pass energy, can exit the analyzer through the slit. This pass energy is experimentally adjustable to control the measurement resolution: lower values increase energy resolution, while higher values reduce it.

Since the kinetic energies of photoemitted electrons typically exceed the selected pass energy (commonly set to 20 eV or 50 eV), a retarding voltage is applied to decelerate the electrons before entering the analyzer. By tuning this retarding field, the instrument selectively transmits electrons of a chosen kinetic energy. After energy filtering, the transmitted electrons strike a phosphor screen, generating visible light that is subsequently detected by a CMOS camera, enabling image acquisition of the energy-resolved signal.

As the investigated materials are semiconducting and lack a well-defined Fermi edge, binding energy calibration was performed using the Fermi level of an Au(111) single crystal measured under

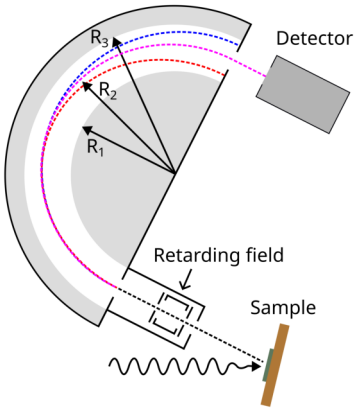

Figure 2.7: Schematic representation of the electron trajectories through the hemispherical analyzer used for energy discrimination. The retarding field changes the kinetic energy of the electrons, determining which electrons can pass through the exit slit of the analyzer. The different colours represent different energies of the electrons.

identical conditions. The acquired spectra were analysed using the XPS Tools (XPST) package for Igor Pro [185]. Spectral fitting was carried out using a pseudo-Voigt profile, constructed as a linear combination of Gaussian and Lorentzian components with a fixed mixing ratio of 0.3. A Shirley-type background was applied to account for inelastic scattering contributions.

2.3.2 KREIOS 150 MM

The experimental setup incorporating the KREIOS detector (SPECS GmbH) consists of two main components: the photon sources, comprising a helium discharge lamp connected to a monochromator and a high-harmonic generation (HHG) source producing light pulses with photon energies $> 20\,\mathrm{eV}$ and a temporal resolution $< 100\,\mathrm{fs}$, and the detection system, which includes the KREIOS 150 momentum microscope and a preparation chamber for molecular and alkali metal deposition. As the entire setup is described in detail in the work by *Schiller et al.* [186], the following section will emphasize only the most relevant aspects. A schematic overview of the full setup is shown in Figure 2.8.

The HHG generation system is custom-built and seeded by a carbide laser from Light Conversion with a variable repetition rate from 100 kHz to 1 MHz, generating infrared pulses at 1.2 eV with a pulse duration of 242 fs. These pulses are directed into a custom-built nonlinear pulse compression setup, initially guided through a combination of mode-matching optics. Subsequently, the pulses are reflected 32 times inside a Herriott-type multipass cell (MPC) [187], each time passing through a nonlinear medium (fused silica), resulting in spectral broadening. This broadened spectrum is then compressed by 12 reflections on dispersive mirrors with a negative group dispersion delay (GDD) of $-200\,\mathrm{fs}^2$, reducing the pulse duration to 41.7 fs. The setup also includes a flip mirror that allows switching between the compressed pulses and the uncompressed pulses, providing flexibility depending on whether higher time resolution or higher energy resolution is desired.

The compressed infrared pulses are then directed into a 0.5 mm thick beta-barium borate (BBO)

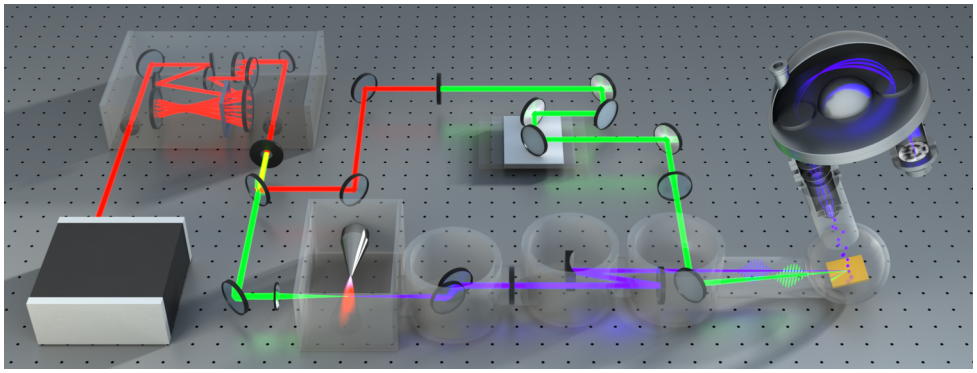

Figure 2.8: Experimental setup used for trARPES measurements with the KREIOS 150 MM detector. The setup consists of a primary light source, a beam separation into the pump and probe pulse beam path, with the latter employing high harmonic generation and a subsequent monochromator for creating pulses with energies above 20 eV. The pump pulse is guided through a delay line before both pulses impinge on the sample. The emitted electrons are then detected with the hemispherical MM. Image by Brad Baxley (Part to Whole).

crystal to generate the second harmonic at 2.4 eV, which increases the efficiency of the subsequent HHG. The fundamental wavelength is separated using a dichroic mirror, allowing the creation of separate pump and probe lines derived from the same laser pulse. For the HHG, the second harmonic pulses are focused into an argon gas jet within the XUV generation chamber, a vacuum-compatible module commercially provided by Active Fiber Systems GmbH.

Following generation, a set of grazing incidence plates separates the XUV pulses from the residual second harmonic, directing the latter into a beam dump. The XUV beam is filtered by a 0.2 µm thick aluminum foil, which removes harmonics below 20 eV. Subsequently, a monochromator selects the desired harmonic, typically 21.6 eV, 26.4 eV, or 31.3 eV. To maintain the UHV conditions required for photoemission measurements, the pressure in the generation chamber and monochromator is gradually reduced via multiple pumping stages, reaching a base pressure of 1×10^{-10} mbar.

After the first BBO crystal, the remaining fundamental laser pulse at 1.2 eV is directed into a separate optical path, where it is used as a pump pulse. An additional BBO crystal can be inserted into this path to generate the second harmonic, thereby allowing the experimenter to employ either 1.2 eV or 2.4 eV as the pump photon energy, as utilized for the investigation of electron dynamics in $FePS_3$ (see chapter 4). The pump pulse then propagates through a series of optical components including a delay stage (Newport DL125), which provides a maximum path difference of 250 mm. This enables the scanning of temporal delays between pump and probe pulses up to a maximum of 833.3 ps. After exiting the delay stage, the pump pulse is focused using a lens and redirected into the final chamber of the monochromator, where a motorized mirror permits precise alignment of the spatial overlap between the pump and probe pulses on the sample surface.

A second photon source, directly connected to the analyzer chamber, is a helium discharge lamp from SPECS GmbH, equipped with a monochromator to isolate specific emission lines. The helium lamp emits several spectral lines from the He I and He II series, the most commonly

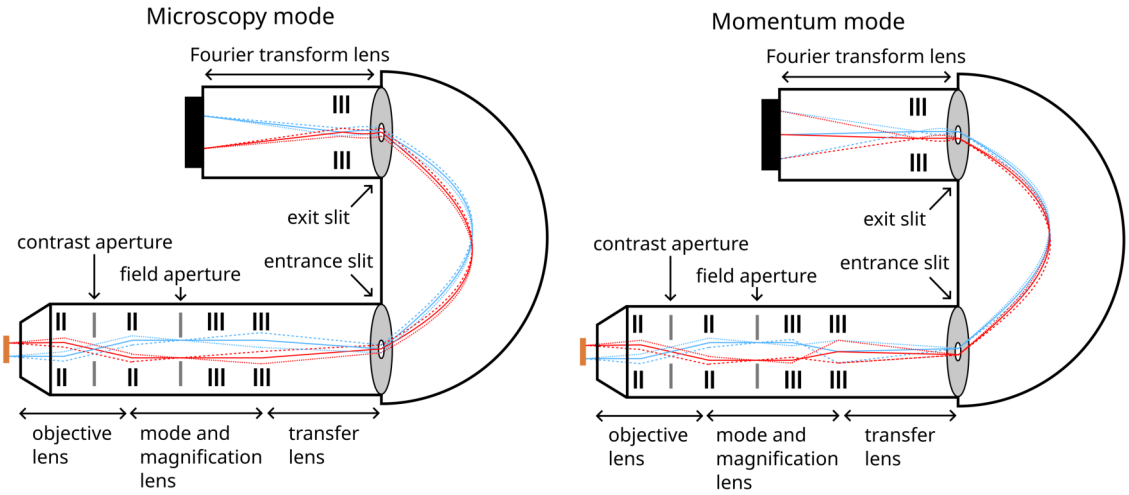

Figure 2.9: Beam trajectories are drawn according to Ref. [188]. The different colours represent different origins in real space, while the difference in style marks the different emission angles of the electrons. Therefore, planes where all beams with the same colour are focused on the same point correspond to the real space, while planes where all beams with same line style unite correspond to the momentum space. All beams depicted represent electrons with equal kinetic energy and do not display the energy dispersion introduced by the hemisphere. The work principle of the hemisphere is depicted in Figure 2.7.

used being the He I α line at 21.22 eV. A differential pumping stage follows the light source to maintain ultra-high vacuum conditions within the analysis chamber. The monochromatized light is then directed through a micro-focusing capillary, producing a beam spot size smaller than 1 mm on the sample surface.

A schematic representation of the electron trajectories through the KREIOS 150 momentum microscope is illustrated in Figure 2.9. In this section, we will concentrate on the components specific to a hemispherical momentum microscope, as the general aspects of such systems (including the extractor lens and the various apertures) were already introduced in subsection 2.1.2. In hemispherical analyzer-based momentum microscopes, electrons are energy-filtered by a hemispherical analyzer that disperses them according to their kinetic energy. The analyzer consists of two curved hemispherical electrodes, between which an electric field is applied. This field forces electrons with different kinetic energies to follow distinct trajectories. Only electrons with the correct kinetic energy, defined by the retarding voltage and the pass energy, follow the designated arc and reach the detector plane.

A fundamental aspect of the energy separation process is the usage of the Fourier-transformed image corresponding to the plane that will later be projected onto the detector. For instance, in momentum imaging mode, the real space image is first projected onto the entrance slit. While the electrons traverse the hemispherical analyzer, the image is distorted along the axis defined by the entrance and exit slit, due to the energy dispersion of the analyzer. However, assuming that the entrance angles of the electrons α are preserved throughout the analyzer, the Fourier lens placed after the exit slit reconstructs the correct momentum image on the

CMOS detector [189, 190]. This detector typically consists of a two-dimensional arrangement, including a multi-channel plate (MCP), a phosphorus screen, and a CCD camera, capturing the momentum-resolved electron distribution. The size of the exit slit determines the energy range that is projected onto the CCD. By sequentially scanning the retarding voltage, and hence adjusting the energy acceptance window, a series of 2D momentum images at different energies can be recorded. These images are then combined into a three-dimensional dataset: energy vs. (k_x, k_y). As discussed by Tonner [189], the resulting image is still susceptible to α^2-dependent aberration effects. These can be further minimized in advanced detector designs, for example by incorporating a second hemispherical analyzer [191] or an additional drift tube following the exit slit [192].

Two additional components that play a crucial role in determining the energy and momentum resolution of the detector are the entrance and exit apertures. In contrast to conventional hemispherical analysers, these apertures are not simple slits but rather circular holes. This distinction arises from the nature of the propagating electrons, which form a two-dimensional image with either (x, y) or (k_x, k_y) as axes, instead of a one-dimensional E_k versus $k_{||}$ projection. In a standard hemispherical analyzer, the energy resolution is typically adjusted by inserting rectangular slits of variable width along the direction of energy dispersion. In contrast, the entrance apertures in a momentum microscope are circular and available in different diameters. The two-dimensional image projected onto the entrance aperture is a Fourier-transformed representation of the image that will ultimately be projected onto the CCD camera. Reducing the diameter of the circular aperture limits the angular spread of the electrons that enter the analyzer. This restriction reduces spherical and chromatic aberrations, which results in improved energy resolution. However, this improvement comes with a significant trade-off. As the aperture becomes smaller, the number of electrons transmitted through the analyzer decreases substantially, leading to a reduced count rate. This intrinsic limitation of hemispherical analysers represents a central challenge when balancing energy resolution and acquisition time.

2.3.3 METIS 1000

The experimental setup used for the ToF-based analyzer is largely similar to the one introduced previously for the KREIOS 150 momentum microscope. However, as will be discussed later, energy discrimination in this type of analyzer relies on pulsed light sources. Therefore, this setup does not include a helium discharge lamp and is exclusively operated in conjunction with a high-harmonic generation (HHG) source.

A simplified schematic of the XUV setup employed together with the ToF detector is shown in Figure 2.10a. The setup, commercially obtained from Active Fiber Systems GmbH, is based on a Compressed Parametric Amplification laser that serves as the seed for the XUV generation. This laser incorporates a Ti:Sapphire light source with an output energy of 1.2 eV and a pulse duration $t_p \approx 262$ fs. The generated pulses are seeded into five Ytterbium-doped fiber resonators, which are combined through a collinear interferometric summation using two motorized mirrors, resulting in an initial output power of approximately 160 W. Subsequently, the laser beam is split into two paths. The transmitted portion is reserved for the generation of pump pulses, while the reflected portion is directed into an Argon-filled MPC. This cell functions similarly to the system introduced for the KREIOS setup, with one key difference. Whereas the KREIOS

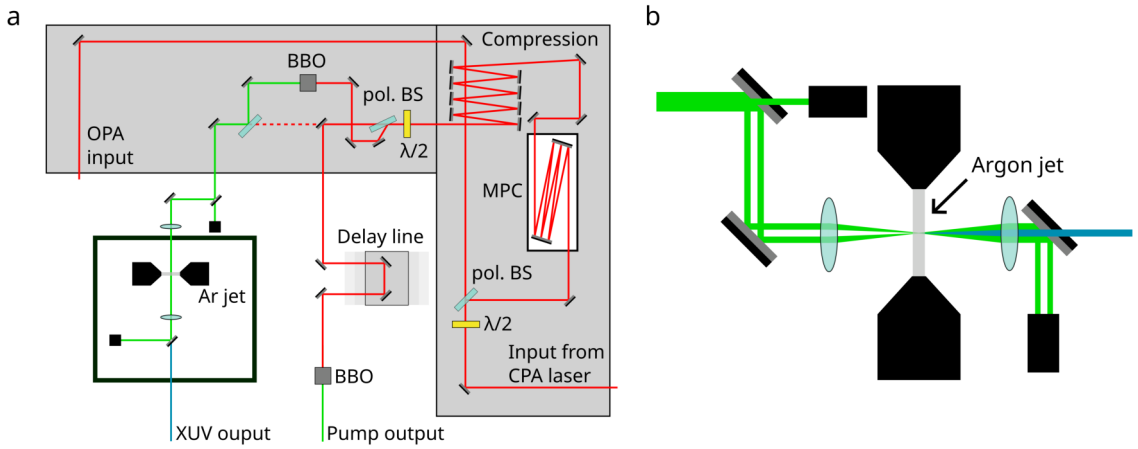

Figure 2.10: (a) Schematic drawing of the laser setup used for high harmonic generation coupled to the ToF-type MM. The output from the CPA laser passes through a MPC and 8 mirrors with negative GDD to compress the pulse down 50 fs. Passing through beam splitter, the reflected part of the pulse is guided into a BBO and the subsequent HHG chamber containing a gas jet based generation. Afterwards the desired harmonic is filtered out by an aluminum filter and a monochromator. The transmitted part of the beam after the previously mentioned beam splitter is guided through a delay line and an optional BBO and is used as a pump pulse for time-resolved experiments. Alternatively, the setup also contains an OPA, which was not employed for the measurements presented in this thesis. (b) Work principle of separating the Fundamental from the HHG using two holey mirrors. The first holey mirror reflects only the outer ring, generating a donut shaped intensity profile. Subsequently, the beam is focused into the Argon gas jet, generating the higher harmonics which are emitted along the optical axis. As the beam diverges again after the gas nozzle, a second holey mirror is placed to reflect the donut shaped intensity profile from the fundamental into a beam dump, while the HHG pulse is transmitted and guided into the monochromator.

system utilized a fused silica medium for nonlinear spectral broadening by self-phase modulation, the MPC in this setup employs Argon gas as the medium for spectral broadening. Following this step, the beam passes through a set of eight dispersive mirrors, each designed with a negative GDD of $-200\,\mathrm{fs}^2$. This compression process reduces the pulse duration to below 40 fs.

After the compression, the beam is separated into two distinct optical paths by a polarized beam splitter (BS). As the transmission and reflection coefficients depend on the polarization of the incoming light, the ratio of intensity directed into each path can be adjusted using a motorized $\lambda/2$-plate. While both beams can subsequently be guided into the HHG chamber, one of them is first focused into a BBO crystal, where the second harmonic is generated. This procedure allows the selection of the excitation energy used for the HHG process.

Although the generation scheme based on argon gas is conceptually similar to the system described earlier, the separation of the generated XUV pulses from the residual seed light follows a different approach, avoiding the use of a dichroic mirror. Instead, the fundamental beam is directed onto a mirror with a central aperture, which produces a donut-shaped intensity profile. Inside the generation chamber, the beam is focused into an argon gas jet, where the XUV pulses are generated near the beam axis. After generation, the pulses diverge and strike a second mirror with a central hole. The XUV radiation, emitted along the beam axis and exhibiting less

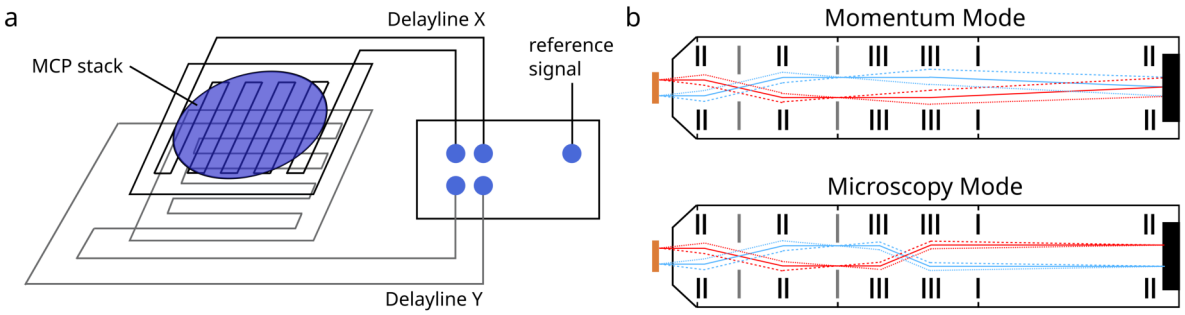

Figure 2.11: Schematic drawings of the main components of a ToF-type momentum microscope. (a) Configuration of the DLD mesh implemented as a detector in the ToF-MM, consisting of two delay line mashes rotated by 90° with respect to each other and a MCP stack on top. Reproduced from [193]. (b) General design of the detector showing the different lenses and apertures inside the microscope. Reproduced from [194] and [195].

divergence, passes through this hole, while the fundamental infrared pulses are reflected off-axis into a beam dump. A schematic visualization of this geometric separation scheme is shown in Figure 2.10b. Following the generation chamber, the XUV pulses pass through a 0.2 µm thick aluminum filter and a series of reflective optics housed inside a monochromator. This system isolates the specific harmonic that is selected for the photoemission experiments presented in this work.

As described earlier, one part of the laser beam is extracted before entering the MPC and is directed along a separate optical path. This pulse can be injected into an optical parametric amplifier (OPA), which is capable of generating tunable pulses over a broad energy range. However, the OPA was not used in the experiments presented in this thesis. Instead, the separated beam before the HHG chamber was employed directly as the pump pulse. Consequently, the working principles of the OPA will not be discussed further.

After discussing the functionality of XUV generation in this setup, we now turn to the implemented detection scheme. In this case, the momentum microscope is based on a ToF-type analyzer (METIS 1000 by SPECS GmbH), where energy discrimination is realized in a fundamentally different way compared to the hemispherical scheme used in the KREIOS 150 MM. Here, the kinetic energy of the electrons is not characterized by altering their trajectories, but instead by measuring the time required for them to traverse a field-free cylindrical drift tube, hence the term time-of-flight. The core element of this detection system is a delay line detector (DLD), which simultaneously captures the two-dimensional distribution of photoelectrons and the corresponding flight times. This functionality is achieved using two separate delay line layers, in combination with a multi-channel plate (MCP) in Chevron configuration, as schematically illustrated in Figure 2.11. Incoming electrons generate charge pulses upon striking the MCP, which are then recorded via capacitive coupling by the delay line layers. The timing and spatial information extracted from these signals allow for precise reconstruction of the electron's kinetic energy and momentum.

To determine the position of an event on the two-dimensional detector plane, a Time-to-Digital Converter (TDC) measures the signal propagation time across both ends of the delay line meshes.

For each spatial direction (X and Y), the DLD registers the arrival times t_1 and t_2, from which the position information is extracted by computing the time difference for each axis: $X \propto (t_{x1} - t_{x2})$ and $Y \propto (t_{y1} - t_{y2})$.

In addition to spatial resolution, the DLD also enables measurement of the electron time-of-flight. This is achieved by referencing the signal to an external trigger, which marks the moment of photon incidence (pump or probe pulse). Unlike the position, which is determined via time differences, the flight time is derived from the time *sum* of either pair (t_{x1}, t_{x2}) or (t_{y1}, t_{y2}), which both yield equivalent results. The relationship is given by:

$$t_{\text{sum}} = t_{x1} + t_{x2} = t_{\text{offset}} + 2 \cdot (t_{\text{hit}} - t_{\text{reference}}) \tag{2.10}$$

Here, t_{offset} is a device-dependent constant that accounts for delays introduced by cable lengths, electronics, and signal propagation. The term $(t_{\text{hit}} - t_{\text{reference}})$ corresponds to the actual time-of-flight of the detected electron. This detection principle constitutes a major advantage of time-of-flight analysers over hemispherical analysers. Since the flight time and thus the kinetic energy can be determined for each individual electron, the complete energy spectrum is acquired in parallel. In contrast, hemispherical analysers rely on stepwise acquisition by scanning over the energy range.

In contrast to the previously discussed hemispherical analyzer, the ToF detection scheme operates without an entrance slit, which eliminates transmission losses typically associated with slit-based analysers. This constitutes another major advantage of the ToF configuration. In this scheme, the energy resolution is governed by the drift energy E_D applied to the cylindrical drift tube and is directly linked to the time resolution of the detector. Lowering the drift energy increases the flight time of electrons, thereby enlarging the time difference between electrons of different kinetic energies and improving the energy resolution ΔE. In practice, the achievable energy resolution is limited by the detector's intrinsic time resolution $\Delta\tau$. For instance, assuming a time resolution of $\Delta\tau = 200\,\text{ps}$, a drift energy of $E_D = 5\,\text{eV}$ results in a ToF of approximately 800 ns and an energy resolution of $\Delta E = 20\,\text{meV}$. In contrast, increasing the drift energy to $E_D = 100\,\text{eV}$ shortens the ToF to 110 ns, but reduces the resolution to $\Delta E = 800\,\text{meV}$ [142].

Despite these advantages, the ToF detection method also presents several limitations. First, it requires a pulsed light source, rendering continuous illumination schemes incompatible. Given the additional need for photon energies high enough to access a large portion of momentum space, high-harmonic generation becomes the preferred excitation method. However, such systems are technologically more demanding than most conventional continuous-wave sources. A second drawback concerns aberrations introduced during the propagation of electrons with different energies through the detector's lens system. Since the electron optics are optimized for a specific kinetic energy, the resulting band structure images exhibit a finite energy window over which aberration-free mapping is possible. To mitigate this limitation, a field aperture is often placed along the electron trajectory. This aperture restricts the acceptance angle relative to the optical axis, thereby reducing off-axis aberrations and improving the spectral quality over a broader energy range. Nevertheless, this also limits the total electron count reaching the detector, which increases the required acquisition time to obtain adequate signal-to-noise ratios.

2.4 Sample Preparation

The MPS_3 crystals used in this thesis were grown via chemical vapour transport and commercially obtained from HQ Graphene. Between measurement periods, the crystals were stored in a desiccator under nitrogen atmosphere to prevent degradation. Representative images of $CoPS_3$ and $MnPS_3$, along with a schematic of the sample geometry used for the XPS and ARPES experiments, are shown in Figure 2.12. The as-grown crystals vary in lateral size from 2×2 to 7×7 mm, with a typical thickness of approximately 0.5 mm. At this size, the crystal surface is often uneven and exhibits multiple terraces. To reduce material loss during the cleaving process and to facilitate mounting, the crystals were trimmed into smaller flakes of typically 2×2 mm when necessary. The flakes were then mounted on top of copper dummy plates using EPO-TEK 21D silver epoxy adhesive, ensuring both mechanical stability and reliable electrical contact with the sample stage of the detector system. An exemplary image of a mounted $NiPS_3$ crystal is shown in Figure 2.12c.

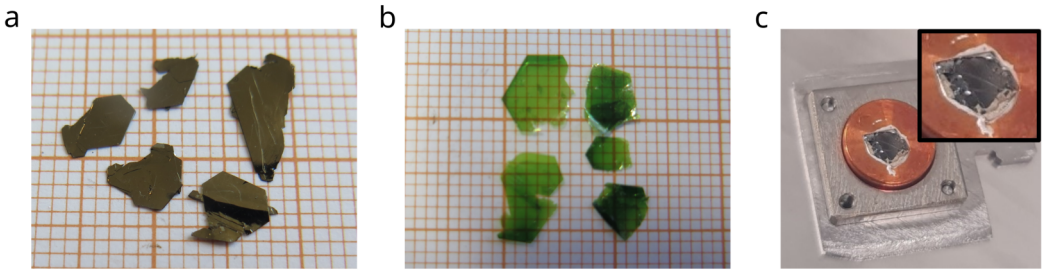

Figure 2.12: (a) and (b) present photos of $CoPS_3$ and $MnPS_3$, respectively. The lateral size as well as the thickness are not always homogeneous, as visible especially for $MnPS_3$, where the crystals show a clear gradient of transparency. The samples are cut in smaller pieces and subsequently glued onto our sample holder, as shown in (c). The silver glue sticking out under the sample will then be removed carefully with the tip of a knife to prevent any charging effects during the measurements.

Before utilization in our experiments, the crystals were cleaved multiple times using the standard scotch tape method, in which a strip of tape is applied to the surface and subsequently removed. By carefully repeating this procedure, we ensure the creation of a smooth, single-terrace surface suitable for our ARPES experiments. This preparation step is essential, as the laser spot size of up to 0.3×0.7 mm requires a sufficiently large and even surface to avoid photoemission contributions from sample edges. Additionally, our setup applies a high voltage of 10 kV between the sample and the detector, which may result in electrical discharge if the surface contains protruding structures acting as antennas. Once a smooth surface is achieved, a fresh adhesive strip is applied to the crystal with a small copper hook attached. The sample is then transferred into the UHV system, where the final cleaving is performed under base pressures of approximately 1×10^{-9} mbar for ARPES and 1×10^{-7} mbar for XPS. As confirmed by our XPS spectra presented in section 3.1, this procedure reliably produces clean surfaces that remain stable and free of significant contamination for several days inside the UHV environment. The preparation steps for the investigation of adsorbed organic molecules and alkali metals are described in section 5.1 and section 6.1, respectively.

Part I - Fundamental Properties

3 | Static Characterisation

Although antiferromagnetic MPS_3 compounds have attracted increasing attention due to their low-dimensional magnetism and van der Waals layered structure, combined theoretical and experimental studies of their electronic band structure remain limited in both number and scope. However, a comprehensive understanding of their electronic structure is essential for elucidating the microscopic mechanisms underlying their physical properties, including charge transport, magnetic ordering, and excitonic effects. Moreover, such insights are critical for evaluating the potential of MPS_3 materials in future applications ranging from spintronics and optoelectronics to energy storage and quantum information technologies.

In this first chapter, this knowledge gap is addressed through a detailed investigation of the ground-state electronic structure of MPS_3 compounds, with particular emphasis on $FePS_3$ in selected sections. A combination of X-ray photoelectron spectroscopy (XPS) and µ-angle-resolved photoelectron spectroscopy (µ-ARPES), together with theoretical modelling based on Hubbard-corrected density functional theory (DFT+U), is employed to probe both the core-level configuration and valence band structure of these materials. The µ-ARPES technique enables direct mapping of the valence band with high momentum and spatial resolution, granting access to fine features within the surface Brillouin zone. Our measurements reveal a rich and complex band structure, characterized by three principal energy regions populated by multiple overlapping bands. To interpret these features, we perform DFT+U calculations that yield a phenomenological value for the Hubbard U, consistent with previous theoretical estimates. Furthermore, the orbital-resolved electronic structure obtained from these calculations supports earlier interpretations of angle-integrated ultraviolet photoelectron spectroscopy (UPS) data reported in the literature [32, 109], confirming the dominant orbital character of the valence band features.

The results discussed in this chapter have been published previously in the following publications:

Jonah Elias Nitschke et al. “Valence band electronic structure of the van der Waals antiferromagnet FePS3”. In: *Materials Today Electronics* 6 (2023), p. 100061.
DOI: 10.1016/j.mtelec.2023.100061

Jonah Elias Nitschke et al. “Electronic structure reorganization in MPS3 via d-shell-selective alkali metal doping”. In: *arXiv, under Review in Advanced Science* (2025).
DOI: 10.48550/arxiv.2506.01527. eprint: 2506.01527

3.1 Core Level Spectroscopy

Figure 3.1a displays the survey scan for all four MPS_3 compounds investigated in this study, where contributions from the transition metal (M), phosphorus (P), and sulphur (S) atoms can be clearly identified. In contrast to the valence band spectra presented later, all XPS spectra are shown in binding energy, which was calibrated using a single crystal of Au(111) as a reference. This approach is necessary, as the MPS_3 compounds are semiconducting and therefore do not exhibit a Fermi edge, and as the contamination free composition of the sample surfaces does not allow a calibration of binding energy based on the carbon 1*s* peaks, which is another often used method. It is important to note that referencing against an external standard introduces certain uncertainties, particularly since semiconducting materials are susceptible to surface charging effects. However, throughout all measurements, no shifts in the kinetic energy of the photoemission peaks were observed. This allows us to assume that any charging effects are negligible. Consequently, referencing the binding energy scale to the Fermi edge of gold is considered justified. Returning to the survey scans, the peaks associated with the P and S atoms are located in the binding energy range of 100 - 250 eV, with no significant shifts observed across the different transition metal species. In contrast, the peaks corresponding to the transition metals appear in the regions between 0 - 100 eV and above 600 eV, the latter corresponding to the 2*p* core levels (exemplarily labelled for $NiPS_3$). Furthermore, the spectra confirm that cleaving the crystals under UHV conditions (10×10^{-7} mbar) does not lead to surface contamination, as evidenced by the absence of detectable carbon or oxygen signals (with the carbon region highlighted as a reference).

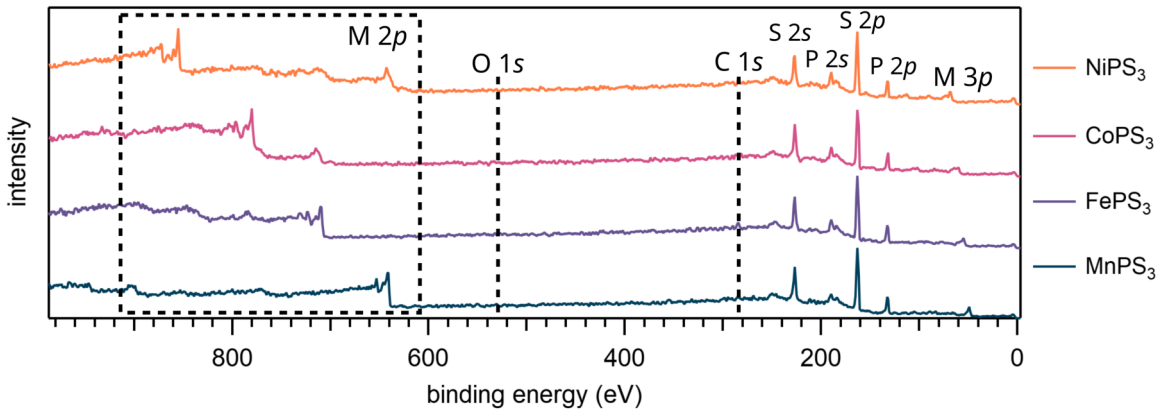

Figure 3.1: Survey spectra of the different MPS_3 compounds after cleaving the surface in 10×10^{-7} mbar. The peaks corresponding to the different atoms are marked accordingly. Additionally, the black dashed lines mark the position of the C 1*s* and O 1*s* core levels that are important to evaluate the contamination of the surface.

To extract information about the electronic configuration of the transition metal ion in the various MPS_3 compounds, we acquired the signals corresponding to the M 2*p* and 3*p* peaks. Figure 3.2 shows the M 2*p* spectra for the different MPS_3 compounds, including fitted components, which will be discussed in more detail later. Here, we first focus on the general features

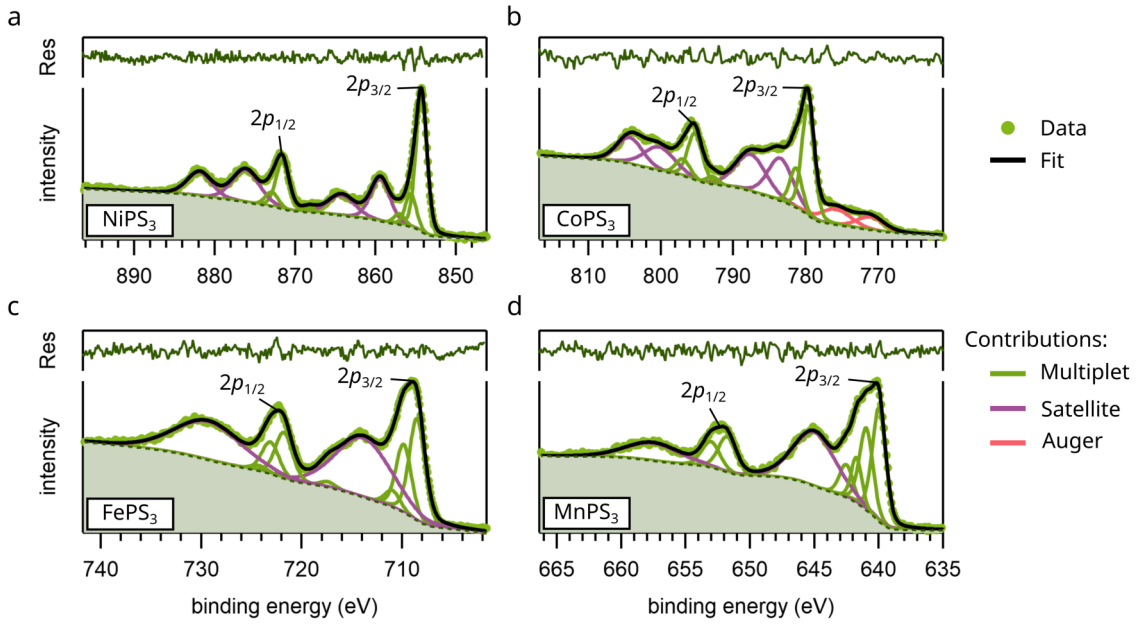

Figure 3.2: XPS spectrum of the (a) Ni $2p$, (b) Co $2p$, (c) Fe $2p$, and Mn $2p$ peaks. The fits consist of the $2p_{3/2}$ and $2p_{1/2}$ peaks including their multiplet structure (green curves, based on the Literature by *Gupta et al.* [146, 147]) and up to two satellites (violet curves). Additionally, the spectrum for CoPS3 shows an additional shoulder at lower binding energies stemming from the $L_2M_{23}M_{45}$ Auger transition (red curves). The extracted values (position and FWHM) for each peak are given in section A.1.

of the measured spectra. Beginning with the $NiPS_3$ $2p$ signal, two sharp peaks are observed, corresponding to the $2p_{3/2}$ and $2p_{1/2}$ spin-orbit components. Each of these is accompanied by prominent and clearly distinguishable satellite peaks, which exhibit comparable energetic separations relative to their respective main lines. Owing to the overall sharpness and energy position of these features, we attribute them to shake-up satellites arising from interactions between the outgoing photoelectrons and valence electrons. In this process, valence electrons are excited to higher energy states, thereby reducing the kinetic energy of the photoelectrons and resulting in satellite features at lower binding energies relative to the main peaks [197, 198]. Further insights into the ground-state electronic structure of $NiPS_3$ can be obtained by comparing the observed satellite structure with XPS data on $NiGa_2S_4$. While $NiPS_3$ is typically described as a charge-transfer insulator, XAS and XPS measurements suggest the presence of a so-called "self-doped negative charge-transfer (NCT) insulating state", in which electrons from ligand p orbitals are transferred to the transition metal d levels. This results in hole states on the ligands even in the absence of extrinsic doping [110, 199].

In contrast, the M $2p$ spectrum of $CoPS_3$ exhibits a more complex structure, as the features following the sharp $2p$ lines at 795.2 and 797.6 eV do not appear as well-defined pseudo-Voigt-shaped peaks. A fitting procedure guided by theoretical calculations from *Gupta et al.* [146, 147] suggests the presence of two satellite features, separated by approximately 4.6 eV. Additionally,

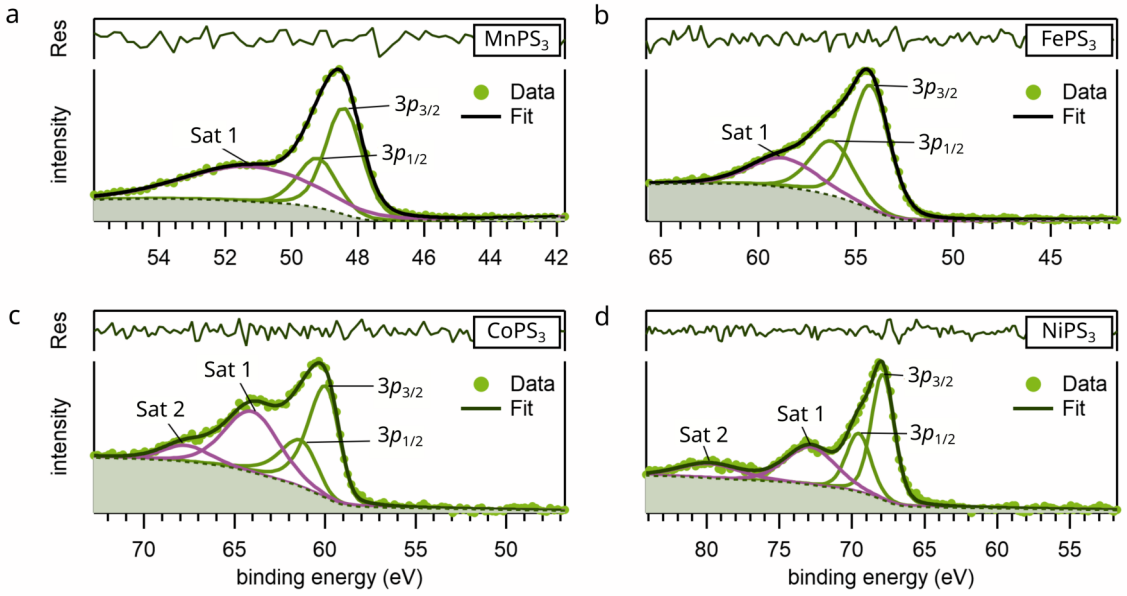

Figure 3.3: M 3p peaks, including fits for (a) Mn-, (b) Fe-, (c) Co-, and (d) NiPS3. The spectra contain the split $3p_{3/2}$ and $3p_{1/2}$ peaks (green curves) and one or two satellite features (violet curves). The residual from the fit is displayed at the top of each graph. The extracted values (position and FWHM) for each peak are given in section A.1.

the spectrum displays a broad shoulder at lower binding energies relative to the $2p_{3/2}$ peak, which can be attributed to the $L_2M_{23}M_{45}$ Auger transition. This feature appears near the Co $2p_{3/2}$ peak when using an Al $K\alpha$ excitation source at 1486.8 eV [200].

In contrast to the previously discussed materials, $FePS_3$ and $MnPS_3$ each exhibit only a single satellite feature, and their $2p_{3/2}$ and $2p_{1/2}$ peaks deviate from the shape of single pseudo-Voigt components. In general, interpretation of the M $2p$ main peaks for these compounds remains ambiguous and is frequently linked in the literature to the presence of different oxidation states (e.g., due to metal vacancies) or to multiplet splitting phenomena [146, 147, 201–203]. Since all samples were synthesized under identical laboratory conditions, and since the $CoPS_3$ and $NiPS_3$ spectra do not indicate the presence of mixed oxidation states, we attribute the observed spectral features in $FePS_3$ and $MnPS_3$ to multiplet splitting. While such multiplet splitting is also present in $CoPS_3$ and $NiPS_3$ (as shown in Figure 3.2a and b), it becomes significantly more pronounced in $MnPS_3$ and $FePS_3$ (Figure 3.2c and d). This trend correlates with the increasing number of unpaired electrons in the d-orbitals from Ni^{2+} ($3d^8$) to Mn^{2+} ($3d^5$), as multiplet splitting primarily arises from the Coulomb and exchange interactions between unpaired valence electrons [202, 204]. Consequently, the energetic separation between multiplet components increases across the series.

To identify the binding energies of the distinct spectral features, we reference the multiplet splitting values reported by Gupta et al. [146, 147]. Overall, the extracted binding energies of the main peaks and corresponding satellites (see Table 3.1) are in good agreement with existing data on comparable M^{2+} ions [110, 201, 205–209].

Table 3.1: Binding energies (E) and satellite shifts (ΔE) for the 2p and 3p core levels of MPS_3 compounds given in eV.

	$2p_{3/2}$	Sat1	Sat2	$2p_{1/2}$	Sat1	Sat2	$3p_{3/2}$	Sat1	Sat2	$3p_{1/2}$
	E	ΔE		E	ΔE		E	ΔE		E
$MnPS_3$	639.9	+5.0	-	651.7	+5.8	-	48.52	+2.74	-	49.22
$FePS_3$	708.5	+5.3	-	721.7	+6.6	-	54.24	+4.49	-	56.23
$CoPS_3$	779.6	+3.8	+ 6.9	795.2	+5.0	+9.0	60.07	+3.97	+7.59	61.48
$NiPS_3$	854.2	+5.1	+ 9.9	871.5	+4.6	+10.1	67.92	+5.14	+ 11.78	69.71

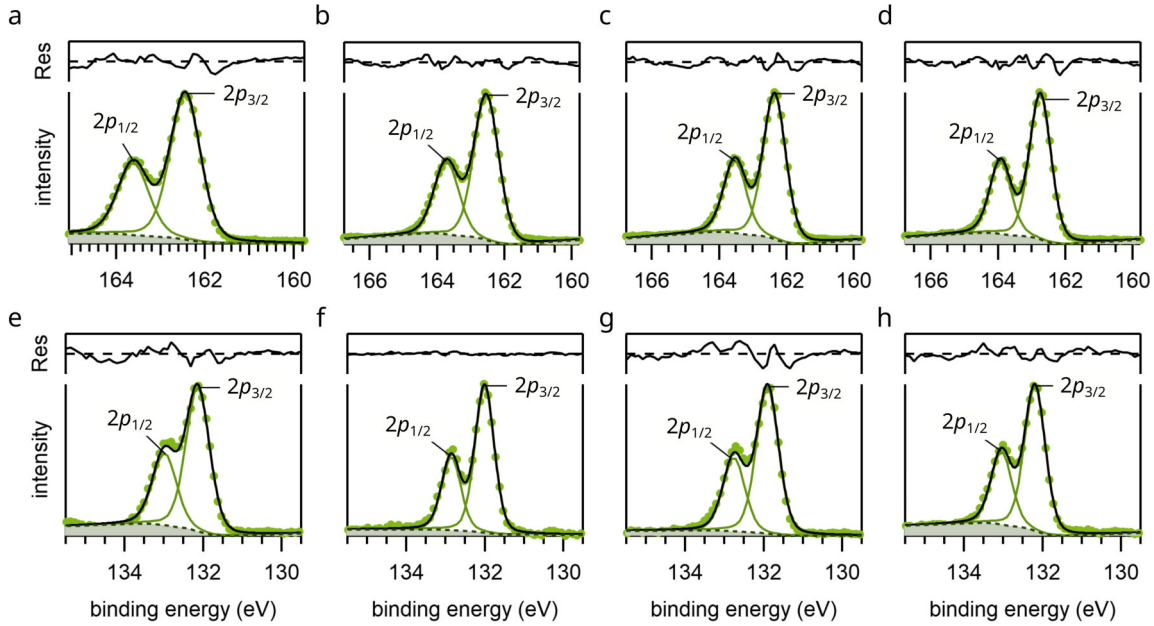

Figure 3.4: Fits of the experimentally obtained spectra for the S2p (top row) and P2p (bottom row) spectra, containing from left to right the intensity obtained for Mn-, Fe-, Co-, and $NiPS_3$. All spectra are fitted using a doublet structure accounting for the SOC split $2p_{3/2}$ and $2p_{1/2}$ peaks, with an area ratio of 2:1. For all fits, the residuum is displayed on top of each graph. The existence of only one doublet for all spectra indicates that all four MPS_3 compounds have only one oxidation state for the P_2S_6 cluster, in agreement with the fits performed on the M2p peaks in Figure 3.2. The extracted values (position and FWHM) for each peak are given in section A.2

Figure 3.3 presents the XPS spectra measured at the M 3p core levels. In contrast to the M 2p spectra, it is more challenging to energetically resolve the spin-orbit split $3p_{3/2}$ and $3p_{1/2}$ components, as well as the associated satellite features. Nevertheless, analogous to the 2p spectra, fitting procedures allow for the identification of the two spin-orbit split 3p peaks, accompanied by one satellite feature in the case of $MnPS_3$ and $FePS_3$, and two satellite features for $CoPS_3$ and $NiPS_3$. These findings are consistent with both the observations made for the M 2p spectra and with previous reports in the literature [33, 203]. Table 3.1 summarizes the binding energies of the identified peaks in the M 2p and 3p spectra. For the main peaks, we report the binding energy of the most intense multiplet component rather than listing all values extracted from the

fits. The complete set of fitted parameters is provided in section A.1. The extracted energetic separations between the satellite features and their corresponding main peaks are consistent across both core-level regions and are in reasonable agreement with values reported in the NIST XPS database.

In addition to the transition metal core levels, Figure 3.4 shows the XPS signals originating from the S $2p$ and P $2p$ levels, respectively. Both appear as doublet features, resulting from spin-orbit splitting into the $2p_{3/2}$ and $2p_{1/2}$ components. For all four compounds, only a single doublet is observed for each element, and the spectra can be accurately fitted using two pseudo-Voigt peaks with an area ratio of 2:1 (see section A.2). This indicates the presence of a single oxidation state for the $[P_2S_6]^{2-}$ clusters.

3.2 Revealing the Valence Band Structure

Following the investigation of the core-level states, we now turn to the valence band (VB) structure of the MPS_3 compounds. Figure 3.5 presents the energy distribution curves (EDCs) for the different materials, obtained by integrating over the entire accessible parallel momentum range. All measurements were performed using a high-harmonic generation (HHG) photon source with a photon energy of 21.7 eV. The energy axis is referenced to the Fermi level of a gold sample.

Overall, the EDCs exhibit strong similarities across all four compounds. The VB structure of each material reveals a pronounced segmentation, which can be approximately divided into three regions: a top section (from 0 eV to 2 eV below the valence band maximum (VBM)), a middle section (2 eV to 5.8 eV), and a bottom section (5.8 eV to 8 eV). While the spectral features below 2 eV display a nearly identical structure among all materials, the most significant differences appear in the topmost region near the VBM. $MnPS_3$ and $NiPS_3$ exhibit the narrowest upper VB features, with widths of approximately 1.3 eV and 1.6 eV, respectively. In contrast, $FePS_3$ shows a broader structure in this region, wider by nearly 700 meV. Despite this variation in width, the overall shape of the upper VB remains similar for these three compounds. $NiPS_3$, however, deviates more noticeably: instead of a distinct local minimum separating the top and middle sections, a step-like structure is observed, with features at 0.7 eV and 1.6 eV. Additionally, the middle region in $NiPS_3$ presents a pronounced shoulder at 2.4 eV.

As will be discussed in more detail in section 3.3, these differences in the upper VB are most likely related to varying contributions from the transition metal d states, whereas the middle and lower regions are dominated by sulphur and phosphorus states. This distinction likely accounts for the strong similarities observed in the lower parts of the VB across all four materials. Overall, the experimentally determined VB structures are in good agreement with prior studies [32, 33, 35, 210].

In addition to insights into the VB structure, ultraviolet photoelectron spectroscopy (UPS) also allows for the determination of the work function Φ of the investigated materials. This quantity can be extracted from the secondary electron cutoff of the spectra, which defines the total energy width E_{tot} of the photoemission signal. For metallic systems, the work function is related to the photon energy $h\nu_{\mathrm{ph}}$ via

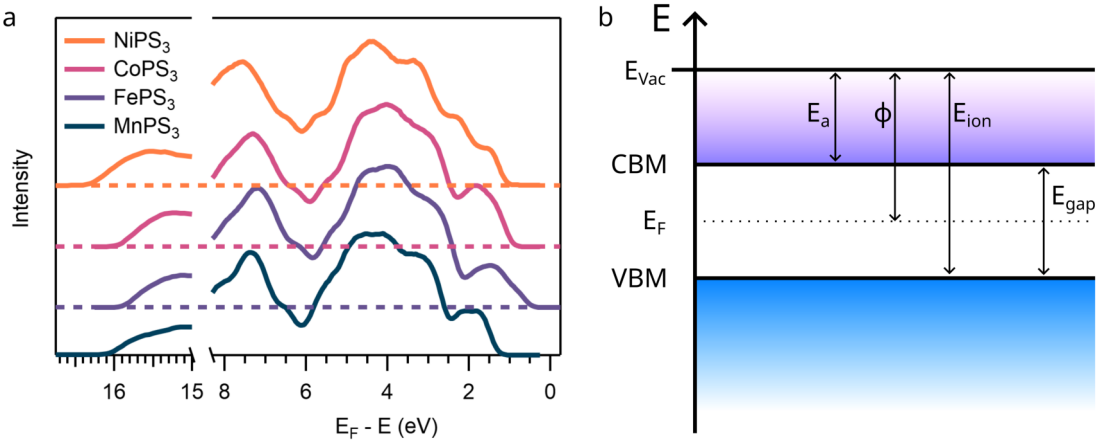

Figure 3.5: Electronic structure of the semiconducting MPS_3 class. (a) displays the full angle-integrated VB structure of all four MPS_3 materials, including the energy down to 9 eV below the VBM as well as the secondary onset at low kinetic energies. (b) displays a schematic representation of key physical quantities involved in the description of the electronic structure of a semiconducting material. Adapted from [211]

$$E_{\text{tot}} = h\nu_{\text{ph}} - \Phi\,. \tag{3.1}$$

This relation assumes that the Fermi level E_F lies within the conduction band and is thus detectable in the UPS spectrum. However, for semiconducting materials, E_F resides within the band gap and is not directly observable. As a result, E_{tot} overestimates the work function by the energy difference between the VBM and E_F. Instead, more relevant quantities for semiconductors are the ionization energy E_{ion}, the energy difference between the vacuum level and the VBM, and the electron affinity E_a, which is defined as the energy difference between the vacuum level and the conduction band minimum (CBM). Both quantities characterize the position of the electronic bands relative to vacuum. Despite these limitations, the concept of Fermi level pinning upon contact with a metallic detector enables the use of a reference material to estimate the work function. In our measurements (Figure 3.5), a gold reference was used to align the Fermi level. Therefore, the energy difference between the secondary electron cutoff and the Fermi level allows an estimation of the effective work function of the MPS_3 samples [212].

Table 3.2: Extracted energy values from the MPS_3 EDC curves denoting the total spectral width E_{tot}, the energetic position of the secondary electron cutoff E_{sec} and the work function Φ.

Material	E_{tot} (eV)	E_{sec} (eV)	Φ (eV)
$MnPS_3$	15.05	16.25	5.45
$FePS_3$	15.65	16.1	5.6
$CoPS_3$	15.25	16	5.7
$NiPS_3$	15.4	16.35	5.25

The extracted total spectral width E_{tot}, the energy of the secondary electron cutoff E_{sec}, and the corresponding work function Φ for the different MPS_3 compounds are summarized in Table 3.2. For $MnPS_3$, the obtained work function $\Phi_{\mathrm{Mn}} = 5.45\,\mathrm{eV}$ is in very good agreement with values reported in the literature [213]. In contrast, the extracted value for $FePS_3$ is significantly higher than that reported by Ramos et al. [214]. This discrepancy may stem from surface doping, which can shift the Fermi level within the band gap and thereby affect the measured work function. Nonetheless, the total spectral width remains comparable to previously published results [22]. For $NiPS_3$ and $CoPS_3$, no experimental work function values have been reported to date. However, for $CoPS_3$, the electron affinity has been experimentally determined to be approximately 4.84 eV [215]. Since the electron affinity is referenced to the conduction band minimum, the ionization energy E_{ion} should equal the sum of the band gap and electron affinity. Using a reported band gap of $E_{\mathrm{gap}} = 1.4\,\mathrm{eV}$ [41], the combined value $E_{\mathrm{gap}} + E_a = 6.24\,\mathrm{eV}$ agrees well with our extracted ionization energy of $E_{\mathrm{ion,CoPS_3}} = 6.35\,\mathrm{eV}$. Among all compounds, $NiPS_3$ exhibits the lowest work function, with $\Phi_{\mathrm{Ni}} = 5.25\,\mathrm{eV}$.

Due to the unavailability of the Au(111) Fermi-level reference in some measurements and the possible influence of charging effects on the spectral position, we will henceforth refer the energy scale to the VBM, using the convention $E = E_{\mathrm{VBM}} - E_{\mathrm{kin}}$. Having analysed the angle-integrated spectra, we now turn to momentum-resolved photoemission measurements. Figure 3.6 shows the momentum-resolved intensity map of $FePS_3$ recorded at a binding energy of $E = 5.15\,\mathrm{eV}$ below the VBM. The distribution reveals a hexagonally arranged pattern of high-intensity features corresponding to the $\overline{\mathrm{M}}$ points of the central and neighbouring surface-projected Brillouin zones (BZs). The outline of the first BZ is marked in red, while the high-symmetry points $\overline{\Gamma}$, $\overline{\mathrm{K}}$, and $\overline{\mathrm{M}}$ of the central BZ are indicated in green. This hexagonal symmetry is preserved across multiple binding energies, indicating the robustness of the observed features. At higher parallel momenta $k_{\parallel}$, additional features associated with the Γ points of adjacent BZs emerge. The contrast between the central and neighbouring BZs likely arises from the k_z-dispersion of states near the Γ point, an effect also observed in layered materials such as $ReSe_2$ and ReS_2 [216], as well as from matrix element effects in the photoemission process [217, 218].

Utilizing the previously established Brillouin zone structure, the electronic band dispersion along selected high-symmetry directions was extracted from the three-dimensional photoemission dataset $I(k_x, k_y, E)$. The momentum path $\overline{\Gamma_1} - \overline{\mathrm{M}} - \overline{\Gamma_0} - \overline{\mathrm{M}'} - \overline{\Gamma_1{}'}$, indicated by the black dashed line in Figure 3.6a, was selected for detailed analysis. Here, $\overline{\Gamma_0}$ denotes the centre of the first surface-projected BZ, while $\overline{\Gamma_1}$ and $\overline{\Gamma_1{}'}$ refer to the centre of a neighbouring BZ. The corresponding energy-momentum cut is shown in Figure 3.6b. The measured band structure exhibits three main energy regions, each characterized by multiple overlapping bands. These regions are separated by two narrow energy gaps, located approximately between 1.6 eV - 1.8 eV and 5.2 eV - 5.4 eV below the VBM. This subdivision of the VB is consistent with our earlier angle-integrated measurements. Notably, the angle-resolved data provide additional insights into the dispersion of individual bands: states near the VBM show flat, localized features, while bands at higher binding energies (from 1.8 eV to 8 eV) exhibit more pronounced dispersion.

Before comparing the VB structure of $FePS_3$ to those of the other MPS_3 compounds, we apply a symmetrisation procedure to the experimental data. This step, performed solely for visualization purposes, facilitates comparison with the calculated DFT+U band structures. The symmetrisation partially compensates for intensity modulations arising from photon polariza-

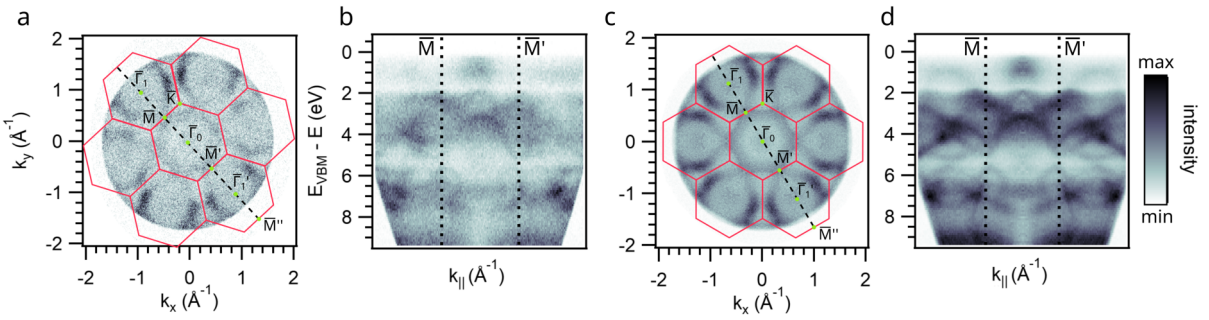

Figure 3.6: Experimental data directly after acquisition and after applying a symmetrising procedure. (a) displays the isoenergetic map extracted from the experimental data stack at 5.6 eV below the VBM for $FePS_3$. The first BZ can be identified based on the hexagonal symmetry of the pattern and is indicated with red hexagon (together with the border of the neighbouring BZs). Cutting along the indicated path in momentum space leads to the extracted band structure displayed in (b). (c) and (d) displays the same images as before after the symmetrisation procedure used to eliminate effects due to the polarization factor, enabling a better comparison between theory and experimental data.

tion and experimental geometry, which affect the momentum-dependent signal due to matrix element effects. It is based on the hexagonal symmetry of the BZ and involves rotating and mirroring the individual momentum maps at each energy before averaging them. The symmetrized momentum map at the same binding energy as before is shown in Figure 3.6b. The corresponding symmetrized energy-momentum cut along the same high-symmetry path is presented in Figure 3.6d.

Figure 3.7a, b, e, and f show the measured VB structures of $MnPS_3$, $FePS_3$, $CoPS_3$, and $NiPS_3$, respectively, along the high-symmetry path $\overline{K} - \overline{\Gamma} - \overline{M}$. As in $FePS_3$, all compounds exhibit a multi-region band structure separated by characteristic energy gaps. Notably, the 1.6 eV - 1.8 eV gap is absent in $NiPS_3$, which instead displays an additional feature around $\overline{\Gamma_0}$ in that range. While the overall band dispersions remain comparable across directions, differences emerge near 5 eV below the VBM: the extrema of two dispersive bands lie at $\overline{M}$ in $MnPS_3$, but shift toward $\overline{K}$ in the other materials. To support the experimental observations, we performed density functional theory (DFT) calculations in collaboration with Preeti Bhumla and Prof. Silvana Botti (Ruhr University Bochum). Full computational details are provided in Nitschke et al. [101]. The DFT+U calculations employed the *Vienna Ab initio Simulation Package* (VASP) [219, 220] using the PBE exchange-correlation functional [221] within the GGA framework. Structural relaxations were performed with the PBE+U approach [222], and the Hubbard U parameter was adjusted for each compound to match experimental spectra. The empirical U values used were 1.9 [196] (Fe), 5.0 eV [223] (Mn), and 4.5 and 4.6 for Ni and Co, respectively.

The calculated band structures are shown adjacent to their experimental counterparts in Figure 3.7, with the zero energy aligned to the VBM. While an exact one-to-one band correspondence is limited due to spectral overlap, the calculations reproduce the key features: separated energy regions, nearly flat bands near the VBM, and dispersive bands around $5 - 6$ eV below it. Interestingly, a parabolic band centered at $\overline{\Gamma}$ within this energy range appears in the DFT+U results but is not clearly visible in the primary experimental zone. However, closer inspection

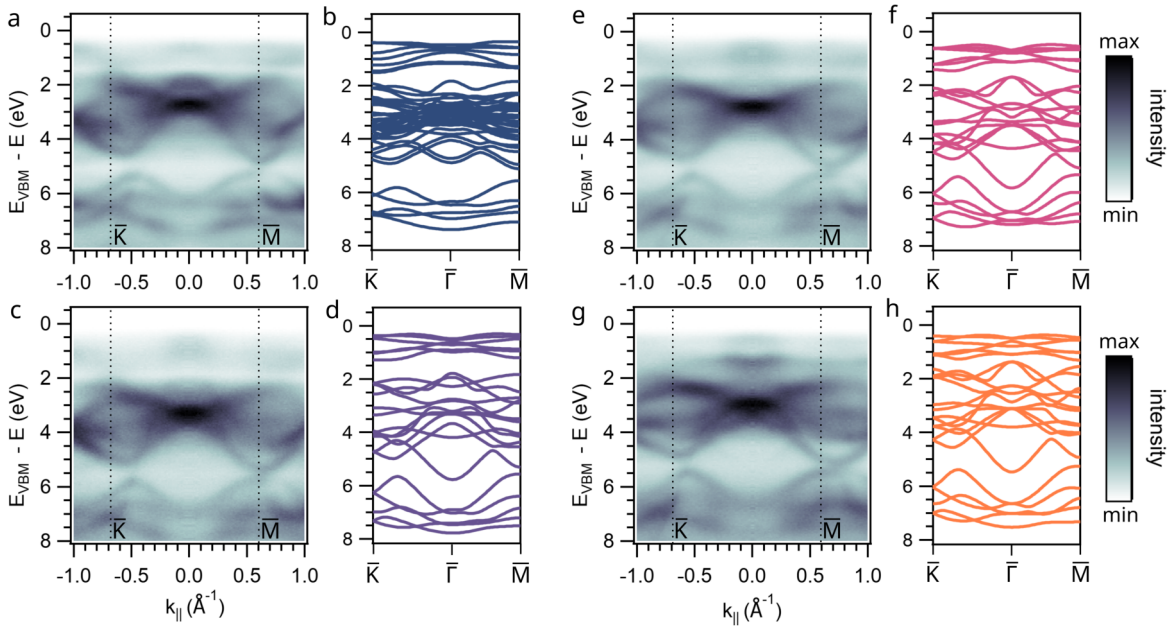

Figure 3.7: Comparison between the experimental and computational band structure. (a), (c), (e), and (g) show the experimental band structure extracted along the high symmetry points shown in Figure 3.6 for Mn-, Fe-, Co-, and $NiPS_3$, respectively. The panels (b), (d), (f), and (h) show the computational band structure extracted along the same high symmetry directions.

of neighbouring BZs reveals weak spectral features consistent with this predicted band.

As discussed previously, the high photon energy of 21.7 eV used in these measurements enables the investigation of photoemission from neighbouring BZs. Figure 3.8 presents a cut through the full momentum range accessible in our photoemission experiment, allowing a direct comparison of the band structure observed in the central BZ_0 ($\overline{M} - \overline{\Gamma_0} - \overline{M'}$) with that obtained from the neighbouring BZ_0 ($\overline{M'} - \overline{\Gamma_1}' - \overline{M''}$). The cut in intensity visible in all central panels originates from the photoemission horizon, as introduced in subsection 2.1.1. At lower kinetic energies of the photoemitted electrons, the available parallel momentum becomes increasingly restricted, which limits the observable k-space at higher binding energies. Despite this limitation, significant differences between the various regions of the band structure are observed. First, the bands near the VBM do not exhibit an intensity maximum at $\overline{\Gamma_1}'$ but instead show stronger intensity at the BZ edges, in contrast to the intensity distribution seen in the central BZ_0. Second, in the intermediate binding energy range, most bands show substantially weaker photoemission intensity, while one additional parabolic band between 4 and 5 eV binding energy emerges. This band is also present in the DFT+U calculations, further confirming the excellent agreement between experiment and theory. Finally, in the deeper energy region, a pronounced enhancement of intensity appears near the centre of the BZ, although the overall band dispersion remains largely unchanged. All these differences are attributed to variations in the photoemission matrix element, which affects the visibility of individual bands depending on their orbital character and the experimental geometry. Since the calculated electronic structure does not account for such matrix element effects, including light polarization, photon energy,

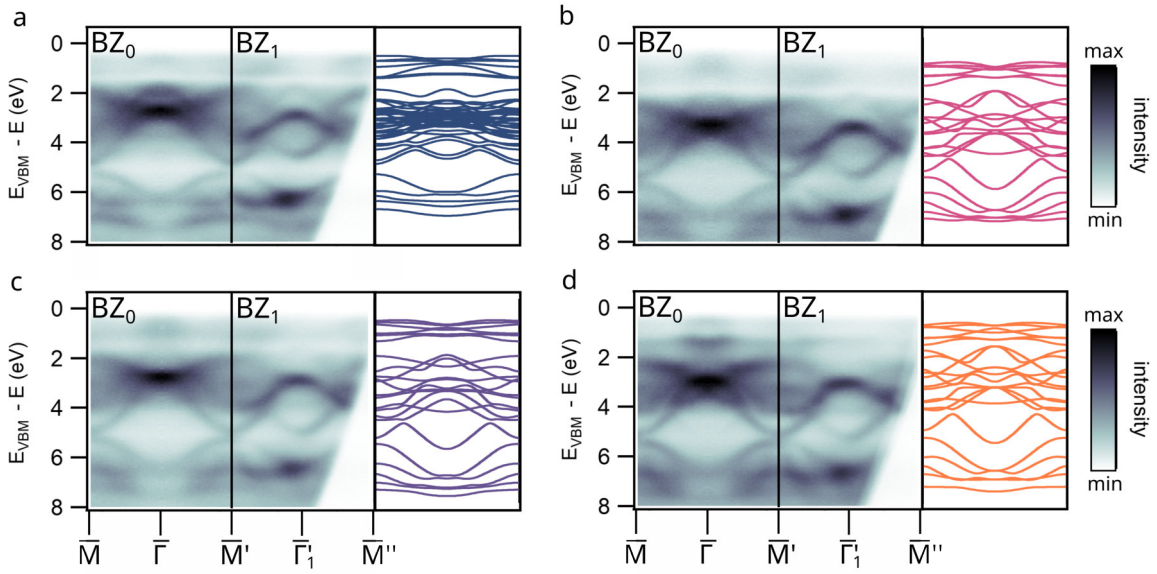

Figure 3.8: Comparison of the photoemission intensity obtained in the 1st and neighbouring BZ with computational data. (a), (b), (c), and (d) display the differences in photoemission intensity when measuring bands in the 1st or neighbouring BZ, marked as BZ_0 and BZ_1, respectively. A comparison with the computational band structure on the right side of each subfigure shows that a consideration of both BZ allows for a better comparison, as some bands are visible in only one of the two BZ due to differences in the matrix elements. This can be seen most prominent on the parabola shaped band around the $\overline{\Gamma}$-point for both BZ, energetically situated between 4 and 6 eV below the VBM.

and detection angle, accessing photoemission intensity from multiple BZs proves to be highly valuable for benchmarking theoretical predictions against experimental data.

In the case of $FePS_3$, the good agreement between DFT+U calculations and the experimentally observed band structure served as a foundation for computing the Fermi arcs, which can be directly compared to the measured momentum maps. These calculations were performed by Dorye L. Esteras and José Baldoví from the University of Valencia using the Wannier90 software and the WannierTools package [224, 225]. Full computational details are provided in the Reference [196]. Figure 3.9 displays both the experimentally obtained momentum maps and the corresponding calculated Fermi arcs at various binding energies below the VBM. In contrast to earlier figures, the momentum maps shown here are not symmetrized, as significant deviations from the expected symmetry are observed. While the experimental and theoretical patterns generally agree in terms of overall structure, notable discrepancies in symmetry remain. Figure 3.9a reveals a hexagonal symmetry that aligns with the symmetry assumptions used to process and symmetrize the raw data in previous band structure visualizations. However, in Figure 3.9b, the experimental map exhibits a rather tetragonal symmetry that is not reflected in the DFT+U-derived Fermi arcs. A similar observation holds for the uppermost part of the VB structure, where the experimental photoemission intensity reveals a pronounced twofold symmetry. This variability in symmetry is a general feature found across all investigated MPS_3 compounds and has also been reported in theoretical studies of related materials. For instance,

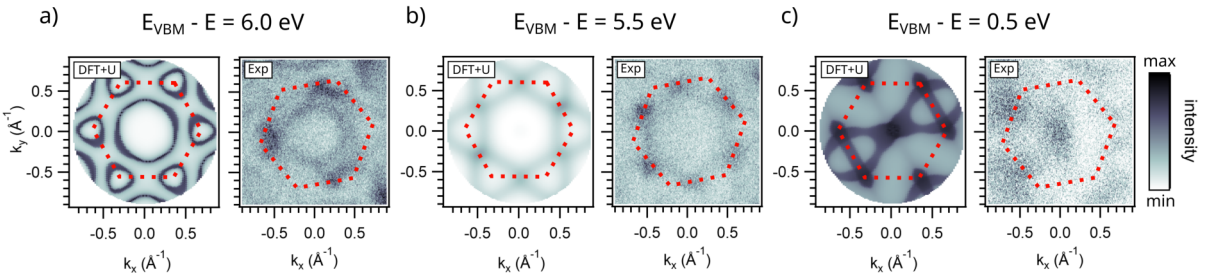

Figure 3.9: Comparison of experimental and computational momentum maps. (a), (c), and (e) display isoenergetic fermi-arcs extracted from the computational data at different energies below the VBM. The 1st BZ is marked by a red, dashed hexagon. The corresponding momentum maps extracted from the experimental ARPES measurements are shown in (b), (d), and (f). The displayed maps are not symmetrised and visualise the different symmetries observed in the experimental, reproduces also in the corresponding computational maps.

in the case of $CoPS_3$, *Voloshina et al.* propose a connection between the observed threefold symmetry and strong electron-electron correlations, in combination with fluctuations of the Co^{2+} magnetic moments [41]. Given the comparable electronic structures among the Mn-, Fe-, Co-, and $NiPS_3$ compounds, it is plausible that similar correlation effects and magnetic fluctuations are responsible for the symmetry variations observed in the experimental data.

To validate the results obtained from the WannierTools simulations, a detailed analysis of the surface states was carried out using a slab model consisting of eight atomic layers within the DFT+U framework. The electronic structure of this slab was subsequently computed using an extended Wannier basis set, incorporating the same orbital types as used in the original DFT calculations, namely, the Fe d orbitals along with the s and p orbitals of sulphur and phosphorus. This methodology enables a layer-resolved investigation of the electronic structure in the vicinity of the $\overline{\Gamma}$ point. The calculated band structure reveals distinct groupings of bands, each predominantly associated with specific atomic layers. In particular, surface states are clearly distinguished from bulk-like states by their confinement to the outermost layers, while the bands originating from the inner layers form an energy envelope around them. This stratified electronic arrangement underscores the significant role played by interlayer van der Waals interactions in shaping the electronic properties of the MPS_3 compounds. These findings suggest that the electronic band structure of this class of two-dimensional magnetic materials can be selectively modified through the intercalation of ions or molecules. This approach provides a tunable pathway to engineer the material's electronic structure and lays the groundwork for the targeted modifications explored in section 4.6 of this thesis.

3.3 Investigation of the Orbital Character

Based on the previous investigation of the electronic structure and the band structure reproduced by DFT+U, which shows overall strong agreement with the experimental data, we can now derive further insights into the orbital contributions to the observed spectra. To this end, the projected density of states (PDOS) was calculated for all four materials, focusing primarily on the M 3d

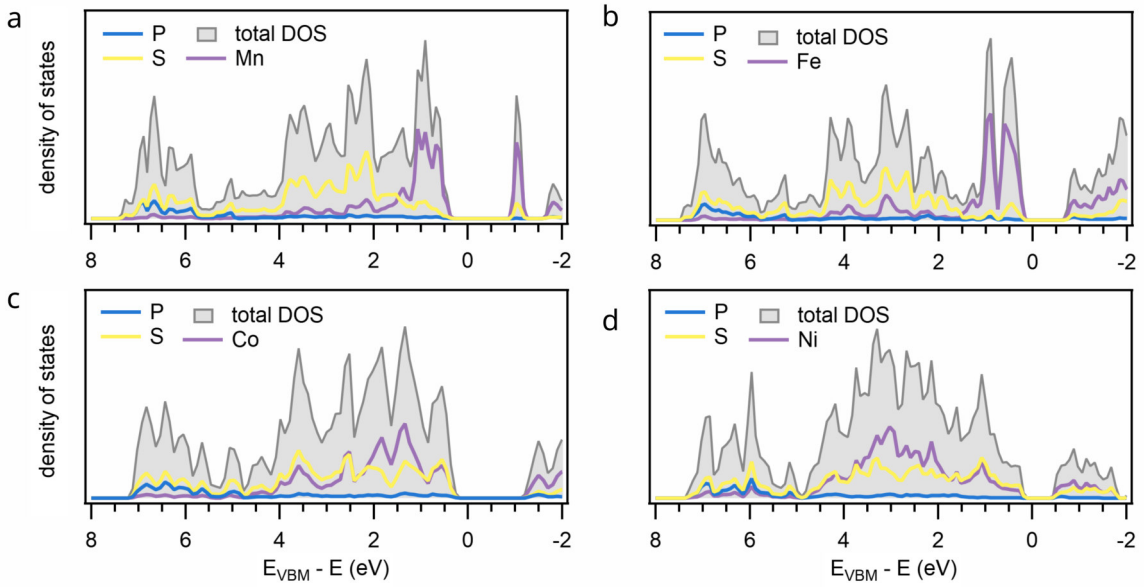

Figure 3.10: PDOS for different MPS3 materials. Projected density of states on the M 3*d*, S 3*p* and P 3*p* orbitals for (a) Mn- , (b) Fe-, (c) Co-, and (d) $NiPS_3$.

orbitals as well as the P and S 2*p* orbitals. Figure 3.10 presents the results for $MnPS_3$, $FePS_3$, $CoPS_3$, and $NiPS_3$.

For $MnPS_3$, the PDOS closely resembles the spectral structure observed in the experimental energy distribution curves (EDCs). The region closest to the VBM is dominated by Mn 3*d* orbital contributions, exhibiting three distinct peaks between 0.7 eV and 1.3 eV below the VBM. At higher binding energies, the Mn contribution gradually decreases. In contrast, the S 2*p* orbitals contribute across the full energy range, with maximum intensity observed between 2 eV and 4 eV below the VBM. A noticeable increase in Sr contribution is also observed in the lowest part of the spectrum. P orbitals contribute only marginally, except in the deeper VB region between approximately 5.5 eV and 7.5 eV. Overall, the projected DOS for $MnPS_3$ exhibits strong agreement with previous theoretical results reported by Strasdas et al. [213], further validating the reliability of our calculations.

Moving on to $FePS_3$, a qualitatively similar distribution of orbital weights is observed, with the Fe^{2+} 3*d* states again dominating the region closest to the VBM. In the literature, this feature is commonly associated with the ${}^6A_{1g}$ ground state of the high-spin d^5 configuration in approximately cubic ligand field symmetry [226]. In contrast to $MnPS_3$, however, the Fe^{2+} contribution does not exhibit a monotonic decrease but shows an additional small peak around 3 eV. The contributions from the P and S atoms closely resemble those seen in $MnPS_3$, with S 2*p* states spanning the entire VB and P 2*p* states contributing predominantly at binding energies between 5.5 eV and 7.5 eV.

While the near-VBM spectral features have also been confirmed experimentally by Koitzsch et al. [226] and Pestka et al. [227], other DFT+*U* studies report additional Fe $3d^5$ contributions

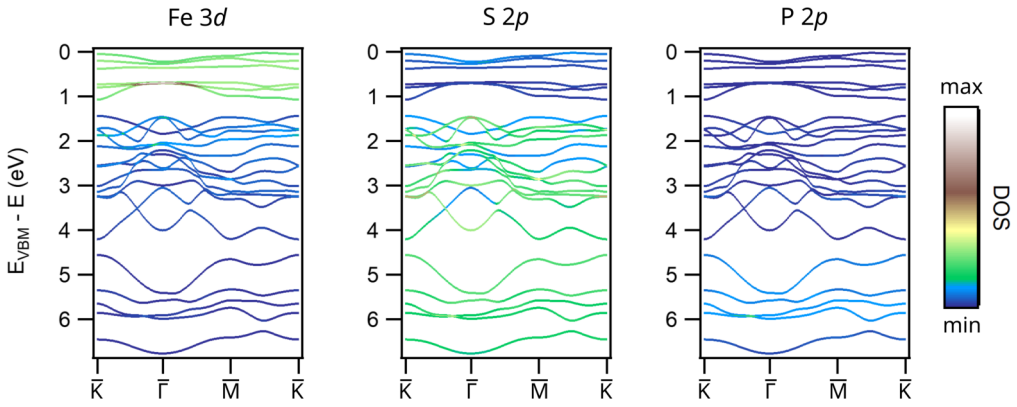

Figure 3.11: Relative contributions to the DOS for the different atmos. The three panels present the DOS projected onto the Fe 3*d*, S 2*p*, and P 2*p* orbitals, respectively. While the top region up to 2 eV seems to be dominated mostly by contributions from the Fe atoms, the rest of the bandstructure shows strong signatures from the S 2*p* orbitals with bands originating from the P 2*p* orbitals being present nearly only at regions more than 6 eV below the VBM.

in the range of 4.5 eV to 6 eV, reinforcing the classification of $FePS_3$ as a Mott insulator [228]. These states, strongly influenced by on-site Coulomb repulsion U_{dd}, show pronounced changes across the magnetic transition and shift in energy relative to the VBM upon entering the antiferromagnetic phase. The observed discrepancies in the reported PDOS between different publications may stem from variations in the orbital-projection schemes used in the calculations. For example, some studies project the Fe 3*d* states onto specific orbitals (d_{xy}, d_{xz}, d_{yz}, d_{z^2}, $d_{x^2-y^2}$), which highlight significant contributions from d_{z^2} and $d_{x^2-y^2}$. In our paramagnetic ground state model, however, we distributed the five *d* electrons across the d_{xy}, d_{xz}, and d_{yz} orbitals, which may explain the reduced weight at higher binding energies.

For $CoPS_3$ and $NiPS_3$, shown in Figure 3.10c and d, the PDOS reveals a qualitative change compared to $MnPS_3$ and $FePS_3$. In both cases, the M^{2+} 3*d* states do not dominate the region directly below the VBM; instead, their contributions are comparable to those from the S 2*p* orbitals. Notably, the maxima of the Co and Ni 3*d* PDOS are shifted to higher binding energies: around 1.5 eV for $CoPS_3$ and between 2 eV and 4 eV for $NiPS_3$. These trends are consistent with theoretical findings reported in Refs. [207, 208, 229], and they support the classification of $NiPS_3$ as a charge-transfer insulator with $U_{dd} > \Delta$, and $CoPS_3$ as an intermediate case where $U_{dd} \approx \Delta$. Here, U_{dd} denotes the Coulomb interaction strength within the 3*d* orbitals, while Δ represents the charge-transfer energy between the metal *d* states and the ligand *p* states [110].

In the case of $FePS_3$, we further extended the DFT+U and PDOS analysis by projecting the orbital contributions directly onto the calculated band structure. Figure 3.11 presents the orbital-resolved band dispersion along the $\overline{\mathrm{K}} - \overline{\Gamma} - \overline{\mathrm{M}} - \overline{\mathrm{K}}$ high-symmetry path. Focusing first on the Fe 3*d* contributions, we find that the largest weight is concentrated near the VBM, particularly around the $\overline{\Gamma}$ point, where the corresponding bands appear in brown. This agrees well with the previously discussed PDOS and reflects the dominant role of Fe 3*d* orbitals in shaping the top of the VB.

Turning to the S $2p$ contributions, we observe only minor weight in the uppermost VBs, while significantly stronger contributions are found in deeper bands, like the parabolic band centered at $\overline{\Gamma}$ around 1.5 eV, and the cluster of states between 3 eV and 4 eV. These bands exhibit a pronounced S $2p$ character and correlate with features seen in the experimental photoemission data. In particular, the same bands display the most prominent differences in spectral weight when comparing the central and neighbouring Brillouin zones in Figure 3.8. This variation may arise from the distinct orbital symmetries (p_x, p_y, p_z) of the S $2p$ states, which, due to photoemission matrix elements, couple differently to the light polarization and experimental geometry [217]. Consequently, some p-like states may be more visible in the central Brillouin zone, while others are preferentially detected in the second zone. Lastly, consistent with the PDOS analysis, the phosphorus $2p$ orbitals contribute only weakly to the overall VB structure. Their influence is almost exclusively limited to the lowest-energy bands in the valence manifold, suggesting minimal hybridization with the Fe $3d$ and S $2p$ states and reinforcing the localized nature of the P states in $FePS_3$.

3.4 Conclusion

In this chapter, we presented a comprehensive investigation of the electronic structure of four different MPS_3 compounds, combining XPS and detailed band structure studies using ARPES. Regarding the core-level analysis, we extended existing literature by implementing a rigid fitting procedure based on the known multiplet structure. This allowed us to extract precise information about the oxidation states and spin-orbit coupling-induced splitting in the $2p$ main peaks. The absence of oxygen and carbon contamination peaks, along with sharp sulphur and phosphorus features, confirms high sample quality with negligible surface degradation or defect states.

Our ARPES measurements revealed a rich and complex electronic band structure for all four compounds, characterized by a mixture of dispersive and flat bands as well as extensive overlap in energy and momentum. By analysing all materials in parallel, we identified three distinct energy regions within the valence band. Notably, the region within approximately 2 eV below the valence band maximum (VBM) showed the strongest material-dependent differences, while deeper energy regions were more consistent across all compounds.

In combination with DFT+U calculations, we found that the deeper energy levels (more than 2 eV below the VBM) are dominated by p-orbital contributions from sulphur and phosphorus. In contrast, the upper valence region is mainly formed by metal $3d$ states in $FePS_3$ and $MnPS_3$, while in $CoPS_3$ and $NiPS_3$, this region appears more hybridized with significant contributions from sulphur $2p$ orbitals. The comparison of central and neighbouring BZs revealed notable variations in photoemission intensity. While the central BZ shows a dominant intensity near $\overline{\Gamma_0}$, the neighbouring BZ features stronger contributions along the edges, and even reveals an additional parabolic band between 4 eV and 5 eV. This feature is well reproduced by DFT+U calculations, further corroborating the validity of our theoretical model. Furthermore, a momentum-resolved comparison between experimental data and theoretical Fermi arcs for $FePS_3$ confirmed the general agreement between simulation and measurement. However, distinct symmetry differences were observed in the experimental maps that were not captured by the calculations. Most notably, a tetragonal distortion in certain energy regions and a twofold symmetry near the top of the valence band. These deviations, also reported for other members of the MPS_3 family, may

be linked to strong electron correlations and local magnetic moment fluctuations [41].

As noted earlier, all experiments were performed in the paramagnetic phase, due to sample charging issues at low temperatures that restrict photoemission measurements in the antiferromagnetic regime [41, 226, 230, 231]. Although various experimental designs were attempted to circumvent this problem, including the exfoliation of gold-supported samples by our group reported in [232], we could not detect clear spectral differences across the Néel temperature. Recent literature, however, has reported signatures of magnetic ordering in $FePS_3$ [227], $NiPS_3$ [233, 234], and especially $MnPS_3$ [213], suggesting that further refinement of the low-temperature sample environment remains a crucial step toward exploring magnetic order-induced changes in the electronic structure.

However, the presented combined experimental and theoretical approach already significantly enhances our understanding of the electronic structure in the MPS_3 family and sets a firm foundation for subsequent chapters, including the study of electron dynamics in $FePS_3$ (chapter 4) and the targeted tuning of electronic properties through external modification (chapter 5 and chapter 6).

4 | Electron Dynamics in $FePS_3$

After characterising the static electronic properties of the MPS_3 family in the previous chapter, we now turn our attention to the electron dynamics, which are crucial for assessing their suitability for device applications. A powerful, yet relatively recent technique to investigate such dynamics is time- and angle-resolved photoelectron spectroscopy (trARPES), previously introduced in section 2.2. This method employs a pump-probe scheme to detect electrons from non-equilibrium distributions, enabling time-resolved imaging of the transient electronic structure. Over the past decade, trARPES has not only been used to observe ultrafast dynamics associated with conduction band occupations but has also proven instrumental in uncovering more complex many-body phenomena, such as exciton formation [171, 235], molecular orbital excitations [236], and the emergence of Floquet-Bloch states [181–183]. These achievements have positioned trARPES as a key method for studying non-equilibrium phenomena in energy and momentum space.

However, interpreting trARPES spectra is inherently complex due to the multitude of overlapping dynamical processes, some of which are unrelated to electronic properties intrinsic to the materials. Therefore, the first part of this chapter introduces three prototypical features commonly observed in trARPES data that do not carry information about the sample's intrinsic dynamics. These signatures typically emerge under high pump and/or probe fluence, commonly employed as the relevant transitions exhibit low cross sections and require enhanced excitation strength for visibility. Understanding these extrinsic photoemission effects is essential for disentangling them from genuine sample-related phenomena.

The second part of this chapter focuses on the electron dynamics in $FePS_3$, specifically on local *d*-*d* transitions within the Fe^{2+} ions. These involve excitations into higher multiplet states and have recently garnered attention due to their role in photo-induced magnon generation. Notably, resonant excitation below the charge-transfer gap has been shown to induce spin dynamics while avoiding the thermal load typically associated with above band-gap pumping. Our trARPES measurements extend the current understanding of such processes, revealing the spectroscopic fingerprint of local *d*-*d* excitations. These manifest as a replication of momentum dependent intensity profiles related to the transition metal *d*-states at elevated binding energies. Resonant excitation of the $^5T_{2g} \rightarrow {}^5E_g$ transition at 1.2 eV results in a fast response characterised by a single exponential decay, whereas above band-gap excitation preferentially addresses the $^5T_{2g} \rightarrow {}^3T_{1g}$ transition, producing a more complex temporal response. Both transitions exhibit distinct rise and decay times, with a clear temporal offset indicating a sequential excitation process. Complementary first-principles calculations corroborate our interpretation and enable unam-

biguous assignment of the observed dynamics to specific multiplet transitions. These results are partially published in the following publications:

Jonah Elias Nitschke et al. “Tracing the ultrafast buildup and decay of d-d transitions in FePS3”. In: *Newton* (2025), p. 100019.
DOI: 10.1016/j.newton.2025.100019

4.1 Unwanted (artificial) Dynamics in trARPES

While our primary interest in time-resolved photoemission lies in probing the intrinsic electron dynamics of materials, several phenomena observed in trARPES arise from extrinsic, sample-independent effects. These artefacts can significantly alter the measured spectra and must therefore be thoroughly understood and accounted for during data interpretation. In the following sections, we introduce three major non-intrinsic effects commonly encountered in trARPES experiments: static space charge (SC), pump-induced SC, and laser-assisted photoemission (LAPE), the latter also referred to as Volkov states.

4.1.1 Static Space Charge Effects

Space charge effects originate from the mutual Coulomb repulsion between photoemitted electrons when high-fluence laser pulses are used. These interactions can occur either directly at the sample surface or during electron transport through the spectrometer column, especially at focus points where electron density is locally high. The resulting effects manifest primarily in two ways, both governed by electrostatic repulsion: (i) an energy shift of the measured electrons due to electrostatic repulsion and (ii) a distortion of momentum distributions caused by changes in angular dispersion [238, 239]. While SC effects are also present in standard hemispherical analysers, they are significantly enhanced in momentum microscopy due to the electron lenses focussing the electrons in small confined spaces within the microscope [239], necessitating a proper understanding of their influence on the measured spectra.

Static SC refers specifically to effects induced by the probe pulse alone. Here, electrons excited by an intense, ultrashort probe pulse form a dense electron cloud in front of the sample surface. This cloud modifies the trajectories and energies of subsequently emitted electrons, resulting in distortions in both the energy and momentum distributions. Consequently, the experimental resolution, both in energy and angle, is severely affected. The main contribution to these probe-induced SC effects originates from secondary electrons, which are also a major factor in pump-induced SC (discussed later). Figure 4.1 presents exemplary data acquired on a Au(111) single crystal. Panel Figure 4.1a shows energy distribution curves (EDCs) around the Fermi level for three different probe fluences ($E_{probe} = 26.4\,\mathrm{eV}$), characterized by the count rates recorded on the delay line detector (DLD). When increasing the detector count rate from 50 000 counts per second (in the following written as 50 kcps) to 175 kcps, no significant changes are observed in the spectral shape. However, a further increase to 320 kcps results in two pronounced effects. First, the electron counts in the energy plateau between 0 eV and 1.5 eV binding energy increase relative to the Fermi edge. Second, additional spectral weight appears above the Fermi level. These signatures are characteristic of static SC: the electron cloud formed near the surface

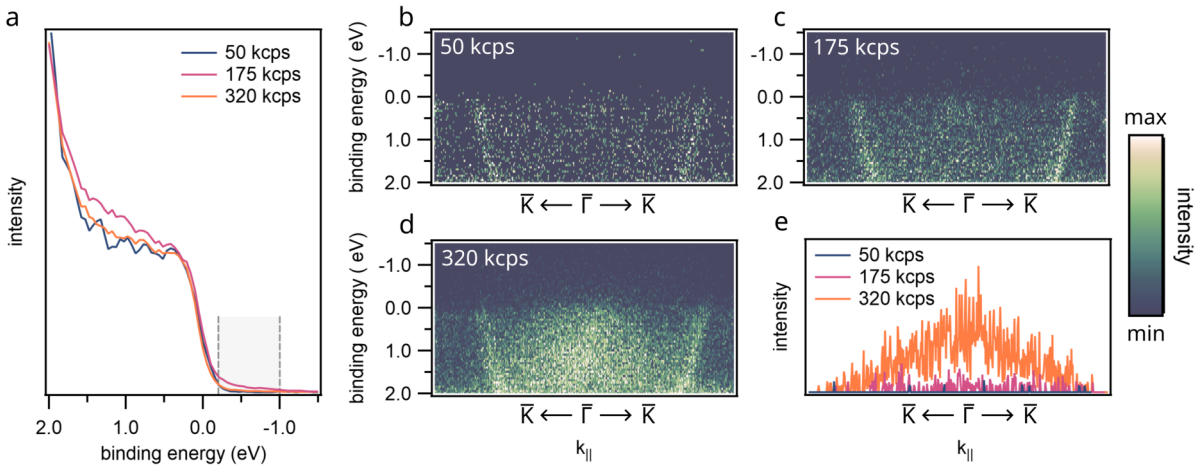

Figure 4.1: Influence of probe-induced SC on the electronic structure of Au(111). (a) EDC close to the Fermi edge for different probe fluences. The grey rectangle marks the energies used for integration in (e). (b), (c), (d) Cut along the $\overline{\mathrm{K}}-\overline{\Gamma}-\overline{\mathrm{K}}$ direction for different fluences. (e) Integrated counts in dependence of $k_{||}$ for three different count rates integrated over the energies marked by the grey area in (a), presenting a bell shaped intensity distribution for the highest fluence.

accelerates outgoing photoelectrons, shifting them to higher kinetic energies and artificially altering the spectral profile.

With the use of a momentum microscope, we are able to investigate not only energy-resolved, but also momentum-resolved consequences of static SC on the measured band structure. Figure 4.1b–d show energy-momentum cuts along the $\overline{\mathrm{K}}-\overline{\Gamma}-\overline{\mathrm{K}}$ path of the first BZ for the three different probe fluences presented previously in Figure 4.1a. All images were recorded using the same acquisition time and primarily reveal the bulk sp-band manifold up to the Fermi level, with the Au(111) surface state faintly visible at the $\overline{\Gamma}$ point. As the count rate increases from 50 kcps to 175 kcps, the quality of the spectrum improves significantly. In particular, the surface state near $\overline{\Gamma}$ becomes more distinct, reflecting enhanced signal-to-noise ratios due to increased photoelectron yield. However, a further increase to 320 kcps introduces strong distortions. These include a marked rise in background intensity as well as the appearance of spectral weight above the Fermi level, both clear indicators of SC effects. To analyse the spatial distribution of this additional intensity in more detail, we extract the momentum distribution curve (MDC) along the same high-symmetry path for different fluences(Figure 4.1e). The MDC is extracted by integrating the photoemission intensity over a binding energy range from -1 eV to -0.2 eV. At lower probe fluences, no significant signal is detected in this region. However, at 320 kcps, a bell-shaped distribution centered around the $\overline{\Gamma}$ point becomes visible, indicating a momentum-dependent redistribution of photoelectrons in energy.

These findings are consistent with previous reports by Schönhense et al. [240], who demonstrated that SC distortions exhibit pronounced momentum dependence, with the strongest effects occurring around the $\overline{\Gamma}$ point. Our data confirm this trend and highlight the importance of carefully managing probe fluence during ARPES measurements to avoid artefacts in both energy and momentum space.

4.1.2 Pump-induced Space Charge Effects

Pump-induced SC effects arise from the same fundamental mechanism as static SC, namely, the Coulomb interaction between dense clouds of photoemitted electrons, but with a different origin. In this case, the electron cloud near the sample surface is generated by electrons excited by the pump pulse rather than the probe. These electrons are typically created through multi-photon absorption processes, as the pump photon energy is often below the material's work function. As a consequence, the associated spectral distortions exhibit a pronounced time dependence. Depending on the relative timing between the pump and probe pulses, the photoelectrons can experience either an acceleration or deceleration, resulting in apparent energy shifts toward higher or lower kinetic energies. This is a significant distinction from static SC, where the effects are time-independent and solely governed by probe fluence. To accurately determine the temporal overlap of pump and probe pulses, often denoted as t_0, we utilize a well-established reference signal based on LAPE. This effect introduces a sharp, Gaussian-shaped feature centered at t_0, which serves as a reliable temporal marker for aligning the two pulses. The detailed physical origin and signature of the LAPE effect will be discussed in a subsequent section. The present discussion focuses exclusively on the pump-induced SC dynamics. Understanding these artefacts is essential for the correct interpretation of trARPES spectra, especially near the pump-probe overlap region, where the strongest SC distortions occur.

Figure 4.2a displays a typical delay map used to investigate time-dependent ARPES signals. It shows the angle-integrated photoemission intensity as a function of the pump-probe delay (x-axis) and binding energy (y-axis). For a better understanding of the occurring distortions, the angle-integrated spectra extracted from the delay map at selected time delays (marked by white dashed lines) are shown in Figure 4.2b. At $-250\,\mathrm{ps}$, the spectrum still closely resembles the equilibrium distribution, with intense feature between 3 eV and 4 eV in binding energy corresponding to the Au d-bands. Upon approaching temporal overlap, the spectrum undergoes significant broadening and a shift to higher energies by nearly 3 eV, reaching a maximum deviation around $-20\,\mathrm{ps}$. This shift results from the probe pulse arriving prior to the pump: the probe photoelectrons are already in flight when the pump pulse generates a secondary electron cloud at the sample surface. Due to Coulomb repulsion, this pump-induced electron cloud accelerates the probe photoelectrons, increasing their kinetic energy [241]. Subsequently, the signal shifts towards lower kinetic energies, induced by the pump pulse arriving before the probe pulse, leading to a repulsive interaction due to the electron cloud already existing at the surface. This effect reaches a maximum influence at approximately 16 ps, followed by a relaxation of the electron distribution to its equilibrium configuration.

This dynamic behaviour is further highlighted in Figure 4.2c, which plots the time-dependent photoemission intensity integrated near the Fermi edge. The signal exhibits a peak before and a dip after t_0, corresponding to energy shifts toward higher and lower kinetic energies, respectively. The dynamics begin around $-200\,\mathrm{ps}$, with a gradual increase in kinetic energy followed by a sharp decay just after t_0. The subsequent slower relaxation of the spectrum toward lower kinetic energy persists until the end of the observable delay window. These time-dependent spectral distortions, induced by pump-related SC effects, must be carefully accounted for when interpreting ultrafast electronic dynamics in trARPES measurements.

At t_0, however, the spectrum exhibits no apparent shift in binding energy; the corresponding

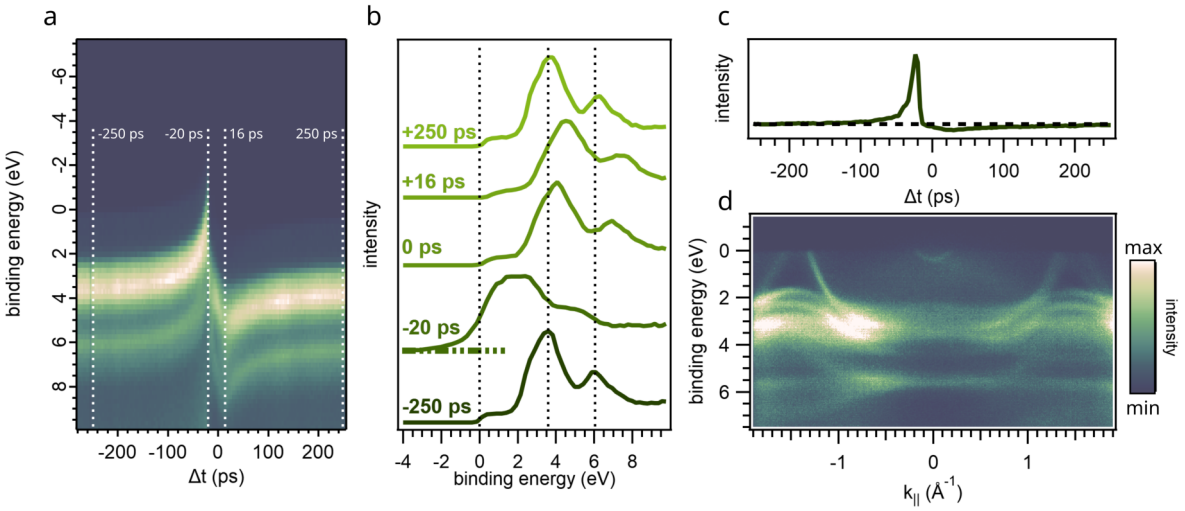

Figure 4.2: trARPES measurements on the band structure of Au(111) modulated by time-dependent SC. (a) Delay Map containing the photoemission intensity in dependence of binding energy for a total time-interval of 50 ps with a pump fluence of 1 mJ cm^{-2}. The white dashed lines mark different delays at which the EDC was extracted, presented in (b). (c) Momentum-integrated photoemission intensity around the Fermi edge exhibiting a peak before temporal overlap, followed by a steep decay and depletion before reaching equilibrium. (d) Band structure cut along $\overline{\mathrm{M}}-\overline{\Gamma}-\overline{\mathrm{M}}$ for an Au(111) single crystal in equilibrium.

EDC resembles the equilibrium one, albeit with a noticeable broadening of the main spectral features. In this configuration, the photoelectrons excited by both pump and probe pulses are emitted simultaneously and travel through the electron optics column together. As a result, their mutual Coulomb interactions are balanced and do not significantly shift the electrons in energy. After temporal overlap, the situation reverses: the pump pulse excites electrons first, generating a low-energy electron cloud at the sample surface. When the subsequent probe pulse arrives, its photoelectrons encounter this existing cloud. Initially, they are decelerated due to Coulomb repulsion. However, because probe-induced photoelectrons typically possess significantly higher kinetic energies, they eventually overtake the slower electrons from the pump and experience a slight acceleration as they exit the SC region. This leads to an overall weaker shift to lower kinetic energies (only around 1 eV compared to the larger shifts observed before t_0 [242]). At longer time delays, the spatial and temporal separation between the two photoelectron populations increases, diminishing their interaction. Consequently, the ARPES spectrum returns to its equilibrium shape, with the EDC again reflecting the unperturbed electronic structure of the sample.

Similar to the analysis of static SC effects, the experimental setup also allows for an investigation of how pump-induced space charge influences the electronic band structure of the Au(111) single crystal at various pump - probe delays. Figure 4.2d shows the measured band structure of Au(111), covering a binding energy range up to 9 eV, along the $\overline{\mathrm{M}}-\overline{\Gamma}-\overline{\mathrm{M}}$ path. Two distinct energetic regions are clearly visible: the dispersive sp-bands and surface state in the range from 0 eV to 2 eV, and the less dispersive bands originating from Au d-orbitals at higher binding

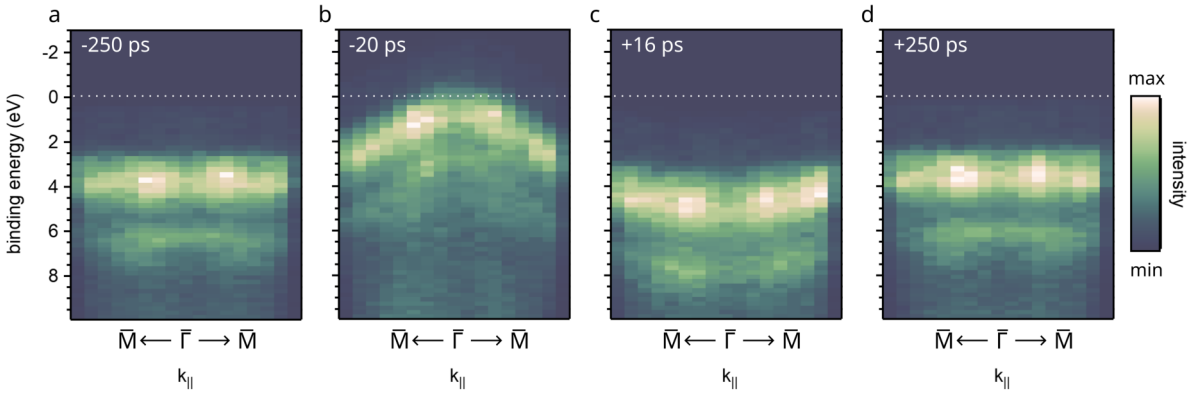

Figure 4.3: Distortion of the Au(111) band structure when pumping with $1\,\mathrm{mJ\,cm^{-2}}$.(a), (b), (c), and (d) display the band structure of Au(111) along the $\overline{\mathrm{M}}-\overline{\Gamma}-\overline{\mathrm{M}}$ at -250, -20, 16, and 250 ps with respect to temporal overlap, respectively. The white dashed line marks the Fermi level. Starting at equilibrium distribution in (a), the electrons are shifted first to higher kinetic energies (b) and then decelerated to lower kinetic energies (c), before shifting back in equilibrium position (d).

energies. The latter serve as a visual reference for monitoring distortions during time-resolved measurements. Figure 4.3a - d present the same band structure at different pump-probe delays. In contrast to Figure 4.2d, a broader $k_{||}$ integration range and stronger binning along $k_{||}$ have been applied, reducing the clarity of individual features in the band structure. A white dashed line marks the Fermi level. At the delay of -20 ps, corresponding to the maximum shift to higher kinetic energies, we observe a characteristic momentum-dependent bending of the band structure. The energy shift is strongest near $\overline{\Gamma}$ and weakens toward larger $k_{||}$ values, mirroring the behaviour observed for static SC effects. Similarly, at a delay of 16 ps after temporal overlap, the band structure bends downward, again showing the strongest shift at $\overline{\Gamma}$. At a longer delay of 250 ps, the interaction between photoelectrons from pump and probe pulses has fully dissipated, and the band structure returns to its equilibrium shape.

To better understand the origin of the pump-induced SC, we performed additional measurements using different pump polarizations and reduced fluences. Figure 4.4a presents the same time-dependent photoemission trace as shown in Figure 4.2b, this time comparing s- and p-polarized excitation. While the overall dynamics remain qualitatively similar, a markedly stronger shift is observed for s-polarized pumping, indicating a higher degree of SC effects. This enhancement can be attributed to an increased number of secondary electrons generated during the interaction of the s-polarized field with the sample surface. To gain insight into this effect, we conducted PEEM (photoemission electron microscopy) measurements on the Au(111) surface using only the pump pulses. Figure 4.4b and 4.4c show the resulting photoemission maps for p- and s-polarized light, respectively, over an area of approximately $800 \times 800\,\mu\mathrm{m}^2$. While the p-polarized pump produces a relatively homogeneous emission profile, the s-polarized pulse gives rise to more localized features with significantly higher intensity. These observations point to localized hot spot emission from surface impurities or inhomogeneities as the primary origin of the enhanced SC [243]. The stronger response under s-polarized excitation can be explained by the orientation of the electric field vector, which is parallel to the sample surface in this configuration. This alignment facilitates a stronger interaction with surface states and enhances

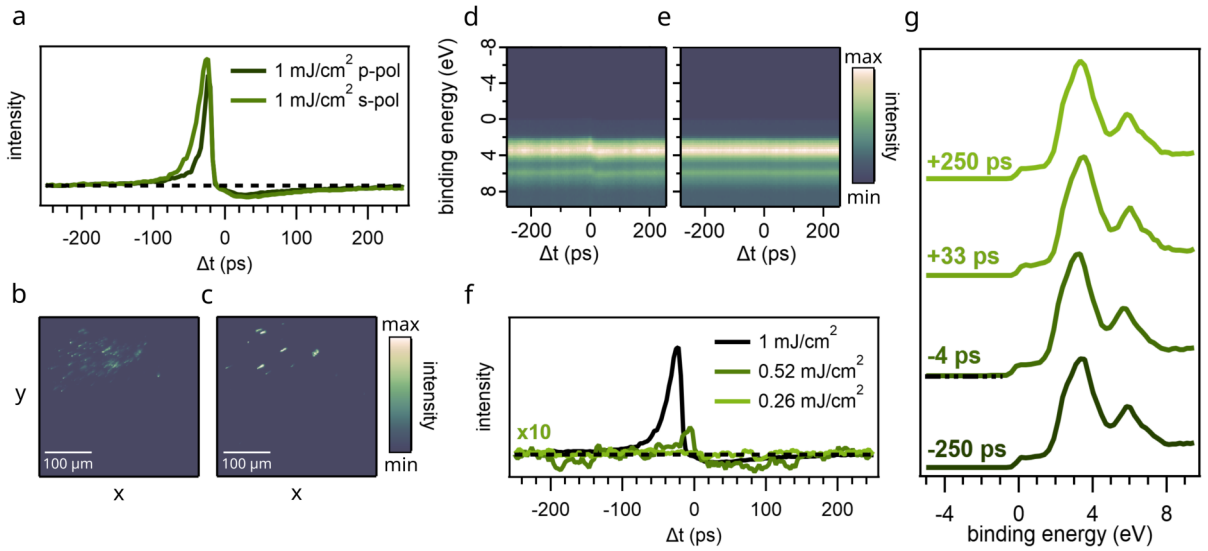

Figure 4.4: Fluence and Polarisation dependence of pump-induced SC. (a) Delay-dependent photoemission intensity for the same fluence as before with s and p-polarisation. (b), and (c) present PEEM measurements at low kinetic energies for p- and s-polarisation, respectively. (d), (e) Delay Maps as presented in Figure 4.2a for $0.52\,\mathrm{mJ\,cm^{-2}}$ and $0.26\,\mathrm{mJ\,cm^{-2}}$. (f) Corresponding photoemission intensity around the Fermi energy for different fluences in p-polarisation. (g) Distortion of the EDC at different delays under pumping with $0.52\,\mathrm{mJ\,cm^{-2}}$.

the local electric field at defect sites, thereby promoting multi-photon absorption and efficient secondary electron generation. This interpretation is consistent with earlier studies reporting enhanced multiphoton photoemission in nanostructured or impurity-rich regions under parallel-field excitation [244].

Additionally, we investigated the induced effects at different pump fluences. Figure 4.4d and e present delay maps analogous to those shown for the p-polarized pump with a fluence of $1\,\mathrm{mJ\,cm^{-2}}$ in Figure 4.2a, but now at half and one quarter of the original fluence, respectively. A prominent observation is the markedly reduced energy shift of the spectral features associated with the d-bands of the Au(111) surface. While Figure 4.4d still exhibits some residual band structure shifting near t_0, the lowest fluence case shows no apparent influence of the pump pulse within the investigated timescale (although later we will observe dynamics above the Fermi level). Figure 4.4f shows the extracted EDCs of the Au(111) surface at various delays. At $\pm 250\,\mathrm{ps}$, the spectra resemble the equilibrium signal for all fluences. Compared to the highest fluence, the EDC at $-4\,\mathrm{ps}$, corresponding to the delay with the maximal energy shift for the reduced fluence, reveals a substantially diminished shift, while preserving the overall shape of the EDC. Both the Fermi edge and the d-band features remain well resolved. Similarly, the EDC extracted at 33 ps confirms the reduced influence of SC induced by pump-photoexcited secondary electrons, as the observed energy shift is negligible.

Upon further reduction of the pump fluence to one quarter of the original value, the delay maps no longer show any visible pump-induced SC effects, with the EDC remaining effectively unchanged over the entire $\pm 250\,\mathrm{ps}$ delay window. Figure 4.4g presents the extracted time traces

for the same energy region across all three pump fluences used during the experiments. While the intermediate fluence trace still shows the characteristic peak and the less pronounced dip afterwards, the temporal evolution differs slightly from the higher fluence case. Both the peak and the maximum dip shift closer to t_0, and the Fermi edge relaxes back to equilibrium on shorter timescales. Thus, reducing the pump fluence not only decreases the maximum SC-induced energy shift from secondary electrons but also shortens the total timescale of the induced dynamics. For the lowest fluence, no visible time-dependent shift of the Fermi edge can be observed (note that the corresponding trace in Figure 4.4g is multiplied by a factor of 10). In conclusion, the reduction in SC intensity is not proportional to the reduction in pump fluence, reaffirming secondary electrons as the main source of this effect. Since photoexcitation by the pump pulse occurs via a multiphoton process (the pump photon energy of 1.2 eV is far below the work function of the Au(111) surface, $\Phi_{\mathrm{Au}} \approx 4.8\,\mathrm{eV}$ [245]), the nonlinear scaling of photoexcited electron yield with fluence leads to a strong reduction in secondary electron emission even upon halving the pump fluence.

4.1.3 Laser Assisted Photoelectron Emission

Another modulation of the electronic spectrum introduced by the development of high-intensity ultrashort laser pulses is laser-assisted photoelectron emission (commonly abbreviated as LAPE, and also referred to as Volkov states). In this process, the pump pulse modifies the emitted XUV photoelectron spectrum, producing sidebands adjacent to the main photoemission line. However, in contrast to Floquet-Bloch states, which correspond to a coherent modification of the electronic band structure [181, 183], the modifications introduced by LAPE affect only the final states of the photoelectrons and do not enable engineering of the material's intrinsic properties [246–248]. Consequently, LAPE is generally regarded as an undesired effect in trARPES experiments, as it can obscure the correct identification of other dynamical processes. Nonetheless, LAPE can be exploited to characterize the temporal resolution of a trARPES setup, since the measured time-dependent intensity reflects the cross-correlation of the pump and probe pulses.

In this thesis, LAPE was employed as a diagnostic tool to determine the temporal resolution of the TOF-based momentum microscopy setup. We selected the same Au(111) single crystal surface as in the preceding section, owing to its well-characterized behaviour in the LAPE regime. Measurements were performed using the same pulse parameters as for the SC investigations ($E_{\mathrm{pump}} = 1.2\,\mathrm{eV}$, $E_{\mathrm{probe}} = 26.4\,\mathrm{eV}$), with a pump fluence of $0.52\,\mathrm{mJ\,cm^{-2}}$ chosen to balance the detection of LAPE with pump-induced SC effects. Generally, the expected LAPE intensity strongly depends on the polarization of the pump pulse, with a more pronounced contribution for p-polarized light. For s-polarization, the LAPE intensity is completely suppressed if the in-plane electric field component E_{xy} at the sample surface is screened (i.e., $E_{xy} = 0$), which is typically the case for metallic samples. In cases where $E_{xy} \neq 0$, the LAPE contribution remains very weak, with only minor effects observed particularly at high parallel momentum $k_{||}$ [247].

Figure 4.5a displays the signal in a way comparable to previous chapters. However, here the displayed intensity is not the absolute value $I(E_B, t)$ but the difference to the intensity in an averaged region before temporal overlap $I(E_B)_{t<t_0}$. Additionally, to visually enhance the signal above the Fermi energy, the difference is also divided by $I(E_B)_{t<t_0}$:

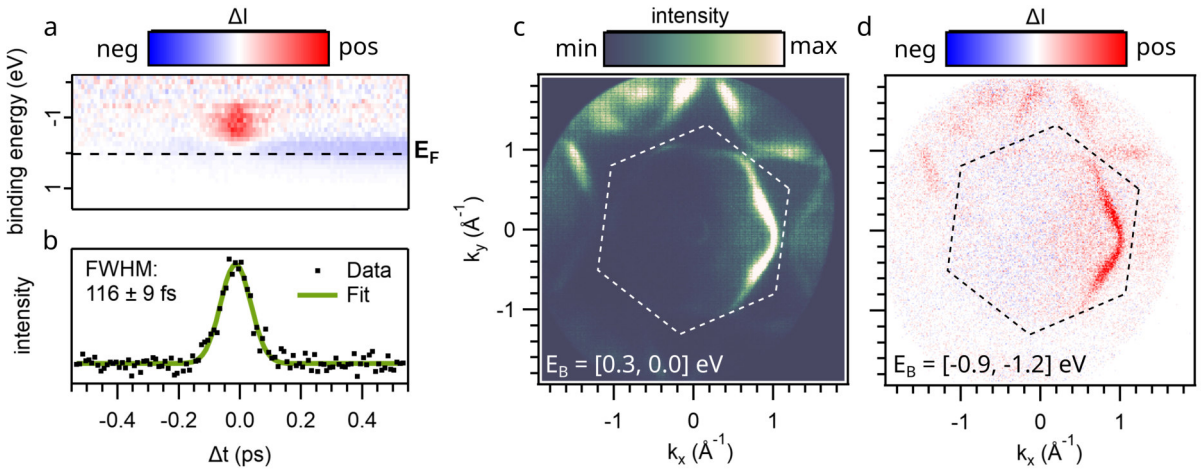

Figure 4.5: trARPES fingerprint of LAPE on Au(111). (a) Differential delay map for pumping with 1.2 eV, normed on the region more than 400 fs before temporal overlap. The red colour refers to additional intensity, while the blue colour refers to reduced photoemission intensity. The black line marks the Fermi level. (b) Time-dependent photoemission intensity integrated from −0.8 to −1 eV. (c) Momentum map extracted below the Fermi energy at temporal overlap. (d) Differential momentum map extracted between −0.9 and −1.2 eV, obtained by subtracting the signal before temporal overlap. The dashed hexagons mark the surface BZ of Au(111).

$$\Delta I(E_B, t) = \frac{I(E_B, t) - I(E_B)_{t<t_0}}{I(E_B)_{t<t_0}} \tag{4.1}$$

This differential angle-integrated non-equilibrium transient signal will be abbreviated in the following as the *differential delay map*, with a colour scale that displays increased and reduced intensity relative to the reference region as red and blue, respectively. In Figure 4.5a, two distinct dynamics can be visually identified. First, a prominent red feature appears around temporal overlap near the centre of the image, spanning from the Fermi edge up to approximately 1.2 eV above E_F. This signal originates from the previously introduced LAPE effect and will later be used to estimate the temporal resolution of the experimental setup. Second, a blue feature is particularly visible after temporal overlap around the Fermi energy. This feature is attributed to residual SC effects induced by the pump laser. As discussed in subsection 4.1.2, time-resolved SC leads to shifts of the spectrum as well as distortions in the EDCs. These distortions gradually relax over time and cause subtle differences in the shape of the Fermi edge, evolving linearly between −0.5 ps and 0.5 ps. As noted previously, the pump laser fluence is typically adjusted to avoid any influence from SC effects. However, the pump power here was chosen to match the fluence reported by *Keunecke et al.* [247], which is necessary to achieve a sufficient LAPE contribution. Nevertheless, this dynamic around the Fermi edge does not reflect any intrinsic dynamics of the electronic structure of the Au(111) surface.

Instead, we focus on the dynamics observed at the centre of the presented differential delay map. Integrating over an energy range from −0.8 eV to −1.0 eV yields the time trace shown in Figure 4.5b. As established, this curve corresponds to the cross-correlation of pump and probe pulses and is therefore expected to be symmetric around temporal overlap. Indeed, fitting the

observed signal with a Gaussian function reveals a symmetric shape with a full width at half maximum (FWHM) of (116 ± 9) fs, which is in agreement with the auto-correlation measured using an auto-correlator. To further confirm LAPE as the origin of this temporal evolution, we investigate the momentum-dependent intensity. As described previously, LAPE results in the dressing of the photoelectron after excitation, producing sidebands separated by the pump photon energy. Consequently, replicas of the band structure are expected to appear at energy intervals of 1.2 eV above and below the original band structure, which we will denote as the feature n_0.

For clarity, we focus our analysis on the energy range around E_F, where the first positive sideband n_1 (located at $E = E_F + 1.2\,\text{eV}$) appears at kinetic energies where no intensity is present before excitation. Figure 4.5c shows the momentum map extracted at temporal overlap in the energy range from 0 to 0.3 eV binding energy. It exhibits the characteristic star-like pattern of the Au(111) Fermi surface, including the surface state centred around $\overline{\Gamma}$. The uneven intensity distribution arises from residual SC effects, which introduce momentum-dependent distortions. We therefore expect similar distortions in the replicas induced by the LAPE effect. Figure 4.5d presents the signal extracted from -1.2 eV to -0.9 eV binding energy, exactly 1.2 eV above the range in Figure 4.5c. In contrast to the momentum map from the occupied states, this map shows the intensity difference between temporal overlap I_{t_0} and a pre-overlap region $I_{t<t_0}$ (similar to the differential delay map but without normalization):

$$\Delta I(k_x, k_y) = I_{t_0}(k_x, k_y) - I_{t<t_0}(k_x, k_y) \tag{4.2}$$

First, the dominant red colour confirms that the detected signal is indeed restricted to the temporal overlap of pump and probe pulses. Second, we observe the exact same (distorted) pattern as extracted from the occupied states, indicating that the intensity observed around temporal overlap originates from the dressing of the electronic states by the pump pulse. As a final verification to confirm LAPE as the source of this signal, we repeated the measurement under identical experimental conditions but using *s*-polarized pump light. In this case, no additional intensity was observed above the Fermi energy, unequivocally confirming that the previously described features arise solely from the LAPE effect.

In conclusion, LAPE is an important effects at high pump fluences that produces a replica of the occupied bandstructure. As the signal from this effect can mix with other phenomena (for example with bandstructure replication induced by Floquet-Bloch states [181]), special caution has to be taken when working with high pump fluences. As we will see in the next chapters, to exclude LAPE as the origin of observed modifications to the electronic band structure, it is important to bare in mind that the signal from LAPE contributions (i) does present as a symmetric, Gaussian-shaped feature around t_0 and (ii) is strongly suppressed in s-polarisation.

4.2 Introduction to Electron Dynamics in $FePS_3$

As previously mentioned, time- and angle-resolved photoelectron spectroscopy is a powerful method that enables direct observation of ultrafast electron dynamics and their manifestation in momentum space for crystalline solids. This makes trARPES an ideal tool for exploring the complex excitations present in the MPS_3 material family. Recent studies, for instance, have shown that in the XY-type antiferromagnet $NiPS_3$, optically driven *d-d* transitions can lead to the formation of electron-phonon bound states [249] and selectively excite low-energy magnon modes in the sub-THz regime [250]. In $FePS_3$, the excitation of a *d-d* transition within the Fe^{2+} multiplet has been demonstrated to launch coherent THz lattice vibrations and coupled phonon-magnon excitations [53], consistent with the strong interaction between antiferromagnetic magnons and optical phonons reported in other two-dimensional antiferromagnets [251–253].

Despite the significance of these findings, the ultrafast dynamics and lifetimes of *d-d* excitations in these materials remain insufficiently characterized. A detailed understanding of these processes is essential for leveraging *d-d* transitions as a means to manipulate the electronic, magnetic, and optical properties of 2D quantum materials. Early studies using optical absorption spectroscopy [37, 254] and X-ray photoelectron spectroscopy [32] have already revealed sub-band-gap spectral features in various $TMPS_3$ compounds (including $NiPS_3$, $FePS_3$, $ZnPS_3$, and $MnPS_3$), attributing these to intra-atomic *d-d* transitions within the transition-metal ions under octahedral coordination. These investigations enabled the extraction of key crystal-field parameters such as the splitting energy D_q and the Racah inter-electronic repulsion parameter B, classifying the $TMPS_3$ materials as ionic insulators with strongly localized *d*-states.

In the subsequent chapters, we will focus specifically on $FePS_3$ to determine whether *d-d* transitions exhibit momentum-resolved signatures in time-resolved ARPES, and to extract relevant information on their ultrafast electron dynamics. As outlined previously, the Fe^{2+} ions experience an octahedral ligand field due to the surrounding S atoms, leading to a crystal field splitting of the *d*-orbitals into two manifolds: the lower-energy t_{2g} orbitals (d_{xy}, d_{xz}, d_{yz}), and the higher-energy e_g orbitals (d_{z^2}, $d_{x^2-y^2}$). Within this field, the ground state $^5T_{2g}$ (t_{2g}^4 e_g^2) and the first excited multiplet state ^5E_g (t_{2g}^3 e_g^3) both arise from the high-spin ^5D term of the d^6 configuration. The optical transition from $^5T_{2g}$ to ^5E_g, hereafter referred to as *transition I*, corresponds to the only spin-allowed *d-d* excitation in the Fe^{2+} multiplet, involving charge redistribution from t_{2g} to e_g orbitals.

In contrast, other *d-d* excitations within the same multiplet, such as the lower-energy $^5T_{2g} \rightarrow {}^3T_{1g}$ transition (denoted *transition II*), are spin-forbidden and thus have remained less explored due to their inherently weak oscillator strength. Depending on their energy, these *d-d* transitions can appear in optical absorption spectra either as faint and broad absorption bands centered around approximately 1.1 eV, or be masked by the onset of strong interband absorption near the optical band gap at approximately 1.4 eV [37]. To investigate both of these transitions in $FePS_3$, we first employ near-resonant excitation at $E_{\mathrm{Pump}} = 1.2\,\mathrm{eV}$ to selectively probe transition I. We then proceed to investigate transition II by pumping the sample well above the band gap using photons with $E_{\mathrm{Pump}} = 2.4\,\mathrm{eV}$.

4.3 Resonant Excitation of the $^5T_{2g} \rightarrow {}^5E_g$ Transition

In the first part of our time-resolved ARPES study on $FePS_3$, we focus on the low-energy transition between the multiplet states $^5T_{2g}$ and ^5E_g. The sample is excited using pump pulses with a photon energy of 1.2 eV, which is close to the resonance of this spin-allowed *d-d* transition and lies below the material's band gap of approximately 1.5 eV.

In contrast to the measurements presented in the previous chapter, regarding space charge effects and LAPE, the following data were acquired using the KREIOS 150MM momentum microscope. Due to the work principle of the hemispherical analyser, this instrument requires a sequential acquisition of photoelectrons at different kinetic energies, rather than recording a full energy window in a single exposure. As a consequence, the accessible energy range in these measurements is typically narrower, and the energy resolution may be somewhat reduced.

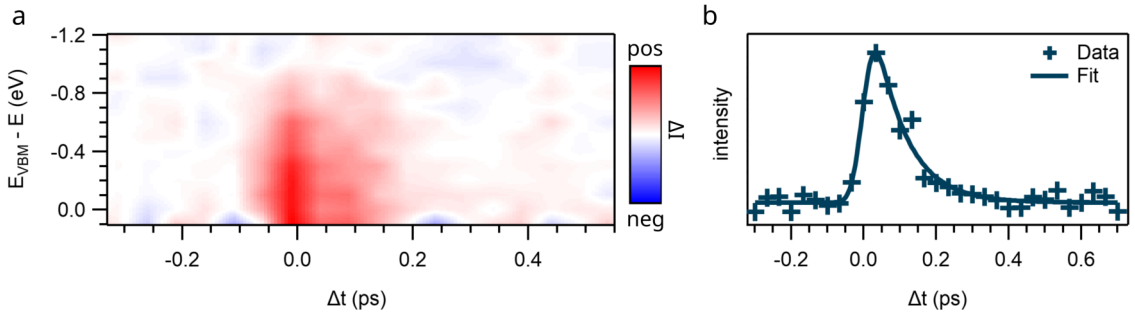

Figure 4.6: trARPES measurements on $FePS_3$ with $E_{Pump} = 1.2$ eV. (a) Differential delay map showing intensity variation in dependence of pump-probe delay, processes by bilinear interpolation to enhance the visualisation. The red signal displays additional intensity, revealing a strong signal up to 1.2 eV above the VBM. (b) Transient photoemission intensity extracted between 600 and 900 meV above the VBM.

The differential delay map corresponding to excitation with 1.2 eV pump photons is shown in Figure 4.6a. For consistency, the energy of the photoelectrons is referenced to the valence band maximum (VBM), as determined from static measurements, since $FePS_3$ is a semiconductor and does not possess a Fermi edge. The map reveals a pronounced resonance extending up to approximately -0.9 eV above the VBM. This feature exhibits consistent time-dependent characteristics across the entire energy window and decays within a few hundred femtoseconds. To improve the signal-to-noise ratio of the extracted time trace, we integrate the intensity in the energy range from -0.6 eV to -0.9 eV, as shown in Figure 4.6b. The resulting transient is fitted using a model function consisting of a Gaussian convoluted with an exponential decay, allowing the extraction of the decay time constant. This analysis yields a value of $\tau_I = (83 \pm 10)$ fs.

With the transient dynamics characterized, we now turn to the momentum-resolved ARPES pattern obtained at temporal overlap. Since the signal above the VBM is generally weak, and momentum-resolved measurements require high statistics, the momentum map was acquired for only three delay values. It is important to note that, despite the high harmonics being guided through a monochromator, there remains a non-negligible contribution from the next higher harmonic (on the order of 1 %). This higher harmonic is typically not visible in the occupied

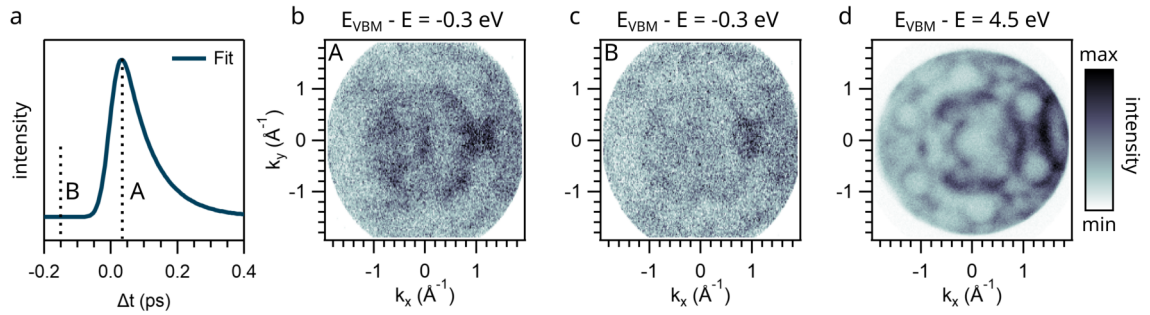

Figure 4.7: Momentum resolved transient intensity. (a) Schematic visualisation of the extracted transient with two vertical dashed lines marking the delays at which the momentum maps in (b) and (c) were extracted. (b) and (c) show momentum maps extracted 300 meV above the VBM at maximum transient intensity and before t_0, respectively. (d) Momentum maps extracted from static measurements, displaying the intensity distribution around 4.5 eV below the VBM.

states, but it introduces a substantial background when investigating the weak signals in the unoccupied states. To isolate the pump-induced dynamics, we subtract the momentum map acquired before temporal overlap. This removes the background contribution and results in a clean representation of the additional intensity stemming from the pump-induced electronic excitation.

This procedure for isolating the signal arising from pump-induced electron dynamics is illustrated in Figure 4.7. Panel (a) displays the raw momentum-resolved signal acquired at 300 meV above the VBM, featuring a structured pattern centered around $\overline{\Gamma_0}$ and extending into neighbouring Brillouin zones (BZs). However, as becomes evident when comparing this to the momentum map extracted before temporal overlap (shown in Figure 4.7b), a significant portion of the observed intensity originates from the leakage of higher harmonics, which is delay-independent. To verify the origin of this background signal, we compare it with static measurements taken at 4.5 eV below the VBM. Despite slight discrepancies due to differing probe photon energies (the leakage signal before t_0 would originate in the next higher harmonic with 4.8 eV higher photon energy), the resemblance in the momentum distribution confirms the higher harmonic contribution. To extract the pure pump-induced dynamics, we subtract the momentum map acquired before t_0 from the one recorded at temporal overlap; the resulting difference map is shown in Figure 4.8a. The dashed black hexagon outlines the central and adjacent BZs.

The resulting pattern exhibits a complex momentum-space fingerprint with pronounced intensity at the central $\overline{\Gamma_0}$ point and the $\overline{\mathrm{M}}$ points at the BZ boundaries. Interestingly, the pattern lacks a clear sixfold symmetry and instead displays a twofold anisotropy, consistent with static measurements at energies associated with Fe *d*-orbitals. This anisotropy arises from the stacking order of the individual $FePS_3$ layers (see chapter 3 for further details). Interpretation of the precise pattern is challenging due to the nature of *d*-*d* transitions, which cannot be captured within a simple single-particle band structure framework, as they involve the full multiplet manifold. Nevertheless, a striking observation is the strong resemblance between this non-equilibrium momentum map and the ground-state band structure. Figure 4.8b shows a static momentum map at 0.8 eV below the VBM, which closely resembles the observed non-equilibrium

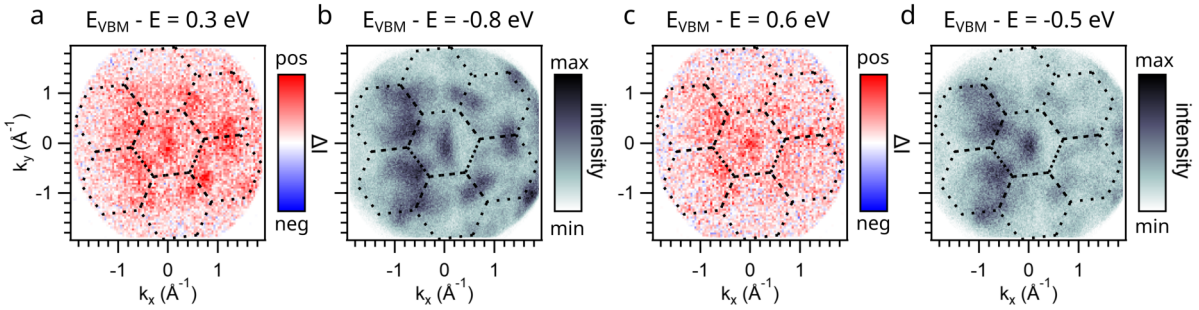

Figure 4.8: Transient momentum maps extracted at two different energies. (a) Differential momentum map at 300 meV above the VBM after background subtraction with red and blue indicating increased and reduced intensity, respectively. (b) MM extracted from static measurements around 800 meV below the VBM. (c) Same as (a) for $E_{VBM} - E = -600$ meV. (d) Same as (b) for $E_{VBM} - E = 500$ meV.

signal. Given that this energy range in the occupied states is dominated by Fe *d*-orbital character, and that the energy difference between both features is approximately 1.1 eV, matching the lowest *d*-*d* transition, we identify this fingerprint as indicative of the $^5T_{2g} \rightarrow {}^5E_g$ transition.

A second non-equilibrium momentum map, taken at 600 meV above the VBM and shown in Figure 4.8f, displays similar features. This again resembles the static momentum map taken at 500 meV below the VBM (see Figure 4.8g), with both maps being separated by exactly 1.1 eV in energy. Since this energy separation is close to the pump photon energy of 1.2 eV, we additionally performed control measurements using *s*-polarized pump pulses, in order to exclude contributions from LAPE effects (see subsection 4.1.3), which can also produce replicas of the band structure. These measurements showed identical temporal behaviour, but importantly, the dynamics lacked the symmetric temporal profile characteristic of LAPE. The asymmetry observed in the transient signal provides further evidence against a LAPE origin. Therefore, we attribute the observed momentum-resolved fingerprint to the $^5T_{2g} \rightarrow {}^5E_g$ transition, an assignment that will be further corroborated by theoretical modelling of the spectral function modifications across the multiplet manifold in section 4.5.

4.4 Indirect Transitions by Above Band Gap Excitation

After having investigated the excitation dynamics of the energetically lowest *d*-*d* transition using a pump photon energy below the band gap of $FePS_3$, we now turn to the electron dynamics induced by excitation with a photon energy of 2.4 eV, well above the band gap. The corresponding differential delay map is presented in Figure 4.9a and reveals a significantly more intricate structure compared to the previous experiment.

The left panel of Figure 4.9a shows the differential delay map, where red regions indicate additional photoemission intensity following excitation with the pump pulse. The map spans an energy range up to 2.3 eV above the valence band maximum (VBM), ensuring that all pump-induced dynamics within the accessible spectral window are captured by the detector. As a reference, we also mark the expected energy position of the conduction band minimum (CBM),

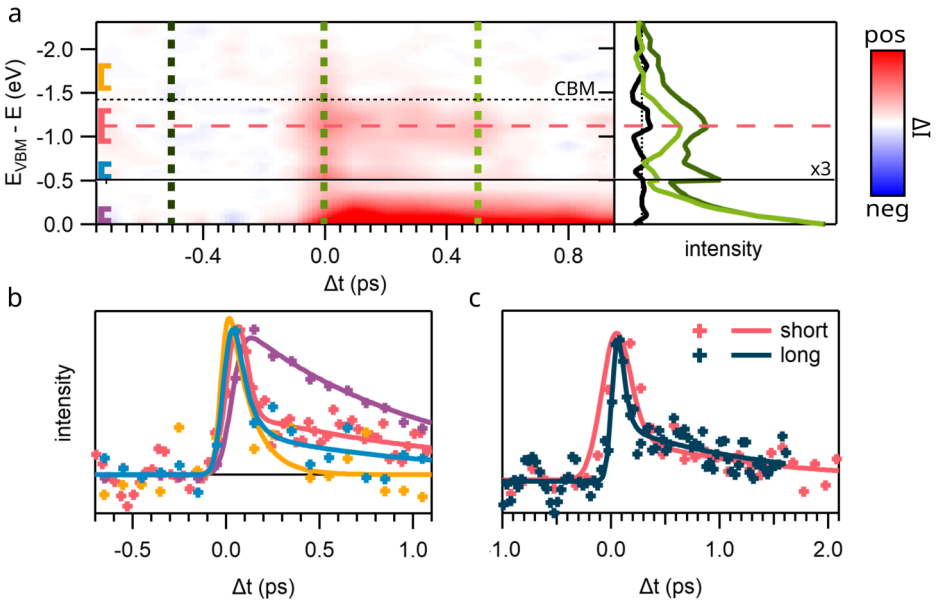

Figure 4.9: trARPES measurements under excitation with a 2.4 eV pump pulse. (a) Interpolated differential delay map displaying varying temporal behaviour in different energy regions above the VBM, marked by individual colours. The right panel displays the EDC in the previously unoccupied states at different delays, colour coded accordingly to the vertical dashed lines in the delay map. (b) Transient photoemission intensity extracted at the different energy ranges marked by the corresponding colours. (c) Comparison of the extracted transient signal around −1.1 eV for the uncompressed (long) and compressed (short) pulses, displaying a similar, double-exponential decay.

estimated to lie around 1.45 eV above the VBM based on optical measurements [52]. The map reveals a rich variety of transient features below the CBM, which are colour-coded to aid interpretation. Starting at the top of the energy window, in the region highlighted in yellow, we observe a rapidly decaying signal that can be well described by a single-exponential decay (see yellow curve in Figure 4.9b), yielding a decay constant of $\tau_{\mathrm{CBM}} = (115 \pm 100)$ fs. This ultrafast component is consistently observed throughout the energy range above the marked CBM, extending down to approximately 1.4 eV above the VBM. Just below the CBM, we identify a broad energy window of approximately 600 meV width, centred around 1.1 eV above the VBM (indicated by the red bracket), in which the transient response follows a double-exponential decay. This region contains the only long-lived component of the photoexcited signal, as seen in the right panel of Figure 4.9a. The three curves shown correspond to energy distribution curves (EDCs) extracted at distinct pump-probe delays, colour-coded consistently with the delay map. Notably, in the light green EDC taken at 500 fs after temporal overlap, a Gaussian-shaped component remains at 1.1 eV, clearly separated from the dynamics occurring near the VBM. This low-energy contribution will be discussed in more detail below.

To further investigate the origin of the long-lived, double-exponential decay observed in the previous measurement, we performed additional experiments with a threefold smaller temporal step size. The resulting transient (red line), plotted together with the other curves in Figure 4.9b, was fitted using the same model as before, consisting of a convolution of a Gaussian with a bi-

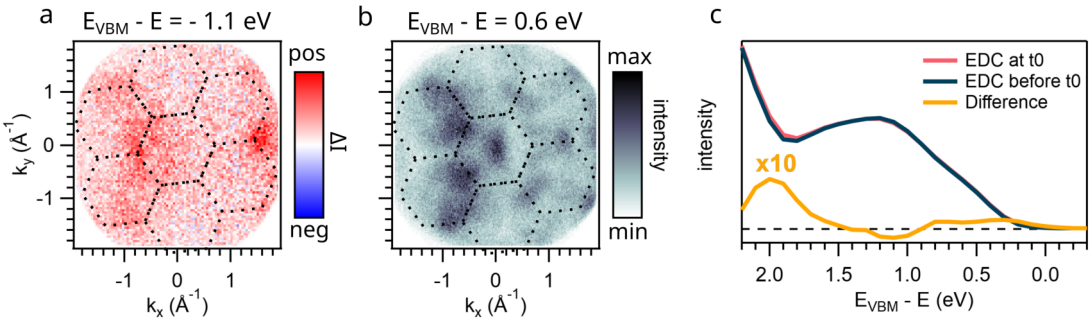

Figure 4.10: ARPES fingerprint of the $^5T_{2g} \rightarrow {}^3T_{1g}$ *d-d* transition. (a) Differential MM extracted around −1.1 eV above the VBM, displaying strong similarities to the momentum-resolved intensity distribution in static measurements obtained 0.6 eV below the VBM. (c) Comparison of the EDC before (blue) and around temporal overlap (red), revealing subtle variations in the difference signal (yellow).

exponential decay function. The fit reveals a fast decay constant of $\tau_{\parallel,\mathrm{a}} = (46 \pm 34)$ fs and a long-lived component of $\tau_{\parallel,\mathrm{b}} = (1273 \pm 268)$ fs. It is important to note that the shorter decay constant is close to the experimentally determined cross-correlation of the pump and probe pulses, which characterizes the time resolution of the setup and is approximately 40 fs [186]. To confirm the robustness of this observation, the same experiment was repeated in a different configuration, omitting the MPC. This setup yields a broader cross-correlation due to the longer pulse duration, thereby reducing temporal resolution. The corresponding transient is shown in Figure 4.9c. Despite the differing temporal resolutions, we again observe a clear double-exponential decay. In this configuration, the long-lived component is consistent with the previous result, yielding $\tau_{\parallel,\mathrm{b,\,long\,pulse}} = (1310 \pm 490)$ fs. The fast decay component is also again limited by the temporal resolution of the setup, with $\tau_{\parallel,\mathrm{a,\,long\,pulse}} = (110 \pm 49)$ fs, which closely matches the known cross-correlation of approximately 120 fs. These observations confirm the presence of a genuine long-lived relaxation process, while also indicating that the short decay constant is resolution-limited in both experimental configurations. As $\tau_{\parallel,\mathrm{a}}$ in the MPC-based setup matches the temporal resolution, we cannot conclusively determine whether this component reflects an intrinsic physical timescale or is constrained by the instrument response.

To gain deeper insight into the nature of the states involved in the observed dynamics around −1.1 eV, we again investigate the momentum-resolved photoemission pattern. Due to the relatively weak signal and long-lived nature of this feature, extended acquisition times over several days were necessary to obtain a sufficient signal-to-noise ratio. The resulting differential momentum map, extracted at the peak of the red transient approximately 50 fs after temporal overlap, is shown in Figure 4.10a. The map reveals a distinct momentum-dependent intensity distribution, with prominent features located at the borders of the central BZ. As observed previously in section 4.3, this pattern closely resembles the momentum maps extracted from static measurements in the ground state. Figure 4.10b displays such a static map acquired at an energy of 0.6 eV below the VBM, corresponding to an energetic offset of 1.7 eV relative to the transient signal. While the overall resemblance is evident, there are notable differences, particularly at the $\overline{\Gamma}$ point of the central BZ and the $\overline{\mathrm{K}}$ points located to the left and right. As will be discussed in more detail later, these differences in photoemission intensity are consistent with theoretical

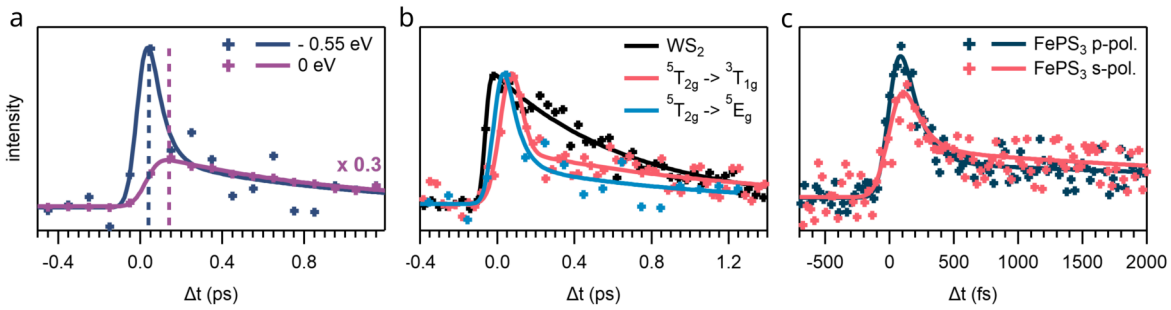

Figure 4.11: (a) Transient photoemission intensity around the VBM (violet) and at −0.55 eV (blue) including the fitted curves. (b) Comparison of the rising edge for the two extracted *d-d* transitions and reference measurement on a WS_2 sample for the population of the conduction band, assumed to be instantaneous. (c) Temporal dynamics around −1.1 eV measured for s- and p-polarisation of the pump-pulse to identify possible contributions from LAPE effects.

expectations when comparing the calculated spectral functions of the two involved multiplet states in the next-higher *d-d* transition, namely $^5T_{2g}$ and $^3T_{1g}$. Given that the energy of this transition is approximately 1.78 eV, closely matching the observed energetic separation between the static and transient momentum maps, we assign the observed photoemission pattern to be a fingerprint of the spin-forbidden $^5T_{2g} \rightarrow {}^3T_{1g}$ transition.

Before turning to the energy region marked by the blue bracket, we first examine the electron dynamics observed near the valence band maximum (VBM). By integrating a 200 meV broad energy window just above the VBM, we obtain the purple transient shown in Figure 4.9b. This signal is well described by a single exponential decay with a fitted decay constant of $\tau_{VBM} = (973 \pm 66)$ fs. We attribute the corresponding photoemission intensity to weak pump-induced thermal broadening, as previously discussed in the context of high-absorption under above-band-gap excitation conditions [255]. Figure 4.10c displays the energy distribution curves (EDCs) of the occupied states, extracted approximately 130 fs before and after temporal overlap. The differential spectrum (yellow curve) reveals an increase in intensity around the VBM as well as in the spectral range from 1.5 to 2.5 eV, along with a pronounced depletion near 1.1 eV below the VBM. These observations yield two important insights. First, the energetic separation between the emerging peaks in the differential signal and the pre-pump spectrum does not match the photon energy of the pump pulse. This provides strong evidence against any significant contribution from laser-assisted photoemission (LAPE), which would lead to replica bands appearing exactly 2.4 eV above the original valence band peaks [246]. Second, we performed Gaussian fits to the valence band structure at both time delays. A comparison of the full width at half maximum (FWHM) reveals a consistent post-excitation broadening, which supports our assignment of the observed dynamics to transient thermal effects. A similar analysis conducted for the below-band-gap excitation shows no significant broadening of the valence band, consistent with the absence of any persistent transient signal near the VBM in Figure 4.6a. This further confirms the interpretation that the observed broadening arises primarily from thermally induced effects, consistent with the stronger absorption in the case of above-band-gap excitation compared to sub-band-gap pumping [52].

After discussing the dynamics around the VBM, we now turn to the energy region indicated

by the blue bracket. This spectral window is of particular interest, as photoluminescence measurements suggest that excitation above the band gap can also trigger the lower-energy *d-d* transition [114]. Based on previous experiments, the energy range from approximately -0.5 to $-0.7\,\mathrm{eV}$ (blue brackets) was selected as the region where one would expect the signal associated with the $^5T_{2g} \rightarrow {}^5E_g$ transition. The corresponding transient signal is shown in Figure 4.11a (blue curve) and exhibits a bi-exponential decay. Fitting the data reveals a long-lived component that mirrors the VBM dynamics (purple curve), which is also shown in Figure 4.11a scaled by a factor of 0.3 to improve visual comparison. The short-lived component, with a decay constant of $\tau_{\mathrm{I,2.4eV}} = (66 \pm 128)\,\mathrm{fs}$, closely matches the decay constant observed for the 1.2 eV excitation, where we previously extracted $\tau_{\mathrm{I,1.2eV}} = (83 \pm 10)\,\mathrm{fs}$. We thus conclude that excitation above the band gap indeed leads to the activation of both transitions I and II, and that both are clearly observable in ARPES.

Beyond the shape of the observed transient signals, we can also compare their respective peak positions in time. Figure 4.11b presents the transient signals corresponding to both transitions observed under excitation with 2.4 eV, alongside a reference signal from the conduction band population in a WS_2 sample. The latter is assumed to occur quasi-instantaneously and was used by Schiller et al. [186] to determine the temporal resolution of the experimental setup. It therefore serves as a benchmark for evaluating the build-up times of the two observed transitions. This comparison reveals a distinct separation in the peak positions of the two transitions. Based on the extracted σ parameter from the previously introduced fitting procedure, we calculate the build-up time τ_b as the time difference between the signal reaching 10 % and 90 % of its maximum on the rising edge:

$$\tau_b = t_{90} - t_{10} = \sqrt{-2\sigma^2 \ln(0.9)} - \sqrt{-2\sigma^2 \ln(0.1)} \approx 1.68\sigma \tag{4.3}$$

Using this relation, we extract build-up times of $\tau_{b,I} = (47 \pm 15)\,\mathrm{fs}$ and $\tau_{b,II} = (79 \pm 18)\,\mathrm{fs}$ for transitions I and II, respectively. For comparison, the reference signal from the WS_2 sample yields $\tau_{b,\mathrm{ref}} = (34 \pm 13)\,\mathrm{fs}$. Consequently, the build-up time of transition I is consistent with an instantaneous process within experimental resolution, whereas transition II exhibits a measurable delay, indicating significantly slower population dynamics.

Similar to the below band-gap pumping, we again performed the measurements for s- and p-polarisation to exclude LAPE contributions, even though the energetic separation of 1.7 eV already discerns LAPE as origin of the replication, as this would necessitate a separation in order of the pump energy at 2.4 eV (see section 4.1). The two measurements with s- and p-polarisation under same conditions are presented in Figure 4.11c. Due to experimental limitations, these measurements were performed with the uncompressed pulse. However, it is directly apparent that both measurement show the same response under excitation with a double exponential decay. A fitting procedure of both signals results in the same decay constants, confirming again the reliability of our observation as well as the absence of LAPE induced dynamics.

4.5 Theoretical Description

For the investigation from a theoretical point of view, we refer to a simplified description for strongly correlated materials[256]. As the focus on this thesis is on the experimental investiga-

tion, we will introduce the theoretical framework only in a brief manner. The full theoretical background can be found in the supplementary information of our publication [237] that this chapter is based on. The calculations presented were performed by Prof. Dr. Frithjof Anders from the technical university of Dortmund.

We describe the Fe(II) 3d shell by a five-orbital model, where the Hamiltonian comprises the single-particle orbital terms and the spin-rotational invariant general Coulomb interaction, parameterized by the Hubbard energy U and the Hund's rule exchange interaction J. The single-orbital energies include the crystal electric field splitting (CEF) between the t_{2g} and e_g orbitals determined by the spectroscopic exchange energy of the lowest d-d transition ($\Delta E = 1.076\,\mathrm{eV}$)[37], adjusted so that the ground state contains six electrons. The local Mott excitation, $U_{eff} = U - 3J = 2.2\,\mathrm{eV}$, is taken from a recent LDA+U study[256] on $FePS_3$. To reproduce the experimentally observed $^5T_{2g} \rightarrow {}^3T_{1g}$ transition at $\Delta E = 1.796\,\mathrm{eV}$, the two Racah parameters are set to $U = 4.15\,\mathrm{eV}$ and $J = 0.65\,\mathrm{eV}$. Additionally, we use the total spin and total charge as conserved quantum numbers to construct the block-diagonal many-body Hamiltonian, and determine its spectrum and eigenstates through exact diagonalization of each block. Based on these results, we can now calculate the spectrum of the lesser Green's function, which describes the removal of an electron from a t_{2g} or e_g orbital of the 3d shell. In the following, we will use these spectra to explore, if the different d-d transitions can lead to the experimentally observed duplication of the band structure and if the varying similarity for both transitions is explainable in the simplified localized picture.

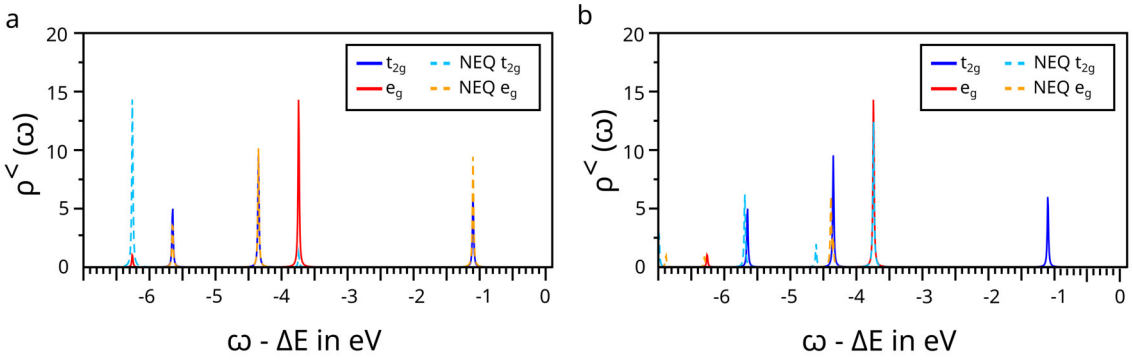

Figure 4.12: Lesser Green's function calculations in ground and excited state for transitions I and II. (a) The equilibrium spectra of the orbital-resolved lesser Green's function for the t_{2g} (blue) and e_g (red) orbitals. The corresponding non-equilibrium (NEQ) spectra after transition I is indicated by dashed lines of the same colours, shifted by the excitation energy $\Delta E = 1.0786\,\mathrm{eV}$. (b) The corresponding equilibrium and NEQ lesser Green's function spectra for this excitation (shifted by $\Delta E = 1.74\,\mathrm{eV}$) exhibit a slight shift in the orbital-resolved peaks. Notably, the lowest excitation peak is entirely absent in the NEQ spectrum, consistent with the spin-forbidden nature of the transition.

To interpret the experimental findings introduced in the chapters before, we start again with the lowest d-d transition at 1.1 eV that involves at spin allowed transition from the $^5T_{2g}$ into the ^5E_g multiplet structure. After photoemission from the excited ^5E_g spin multiplet, the system

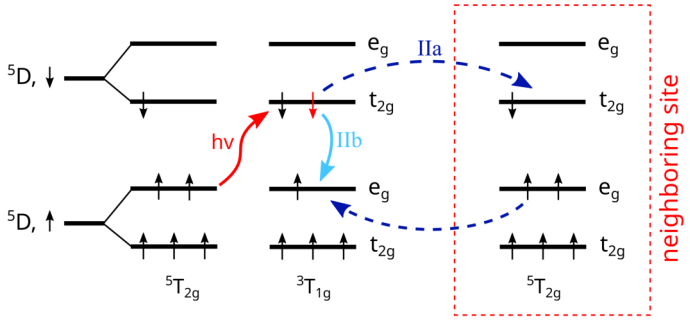

Figure 4.13: Schematic illustration of the multiplet structure of the Fe^{2+} ion in both the ground and excited states. In contrast to transition I, the second-lowest *d-d* excitation involves a spin-flip process: an electron from the spin-up t_{2g} orbital is excited into the spin-down t_{2g} orbital. This excitation may either propagate to a neighbouring site via virtual hopping (IIa) or relax through spin-orbit coupling (SOC), involving a spin-flip transition (IIb).

is left in a $3d^5$ configuration. The calculated spectra of both, the $^5T_{2g}$ ground state and the excited ^5E_g state are plotted in Figure 4.12a with different colours. Important to mention here is that the spectrum for the excited multiplet state is shifted to lower energies by exactly the excitation energy of the investigated *d-d* transition. This allows us to compare both spectra and see if the duplicated band structure we observed in the experiments are a result of the change in multiplet state. Indeed, we see that the energetic position of the different peaks overlap, with slight changes in the spectra width. Since the atomic Green's functions serve as the foundation for the lattice spectral functions [257], and the hybridization between orbitals is not significantly affected by the laser pulse to leading order, this result obtained in the localized Fe 3d framework can readily explain the notable similarities between the non-equilibrium momentum maps in Figure 4.7d and the equilibrium maps in Figure 4.7e.

This approach also enables us to interpret the data obtained under above-band-gap excitation. As previously noted, the non-equilibrium momentum maps measured at $-1.1\,\mathrm{eV}$ exhibit a marked resemblance to the momentum maps of occupied states at $0.6\,\mathrm{eV}$. Since this feature lies too low in energy to result from a population of the conduction band minimum (CBM), we attribute the transient state observed at $-1.1\,\mathrm{eV}$ to the spin-forbidden $^5T_{2g} \rightarrow {}^3T_{1g}$ transition of the Fe^{2+} multiplet. This transition is characterized by an energy difference of $1.7\,\mathrm{eV}$, matching the separation between the corresponding occupied and unoccupied momentum maps. Figure 4.12b presents a comparative analysis between the relevant equilibrium and non-equilibrium atomic spectra, again offset by the excitation energy of $\Delta E = 1.79\,\mathrm{eV}$. While both spectra share common features, the differences are more pronounced than in the previous case, consistent with the observation that the momentum maps in Figure 4.10a and b do not fully mirror each other.

Upon excitation of $FePS_3$ with $2.4\,\mathrm{eV}$ photons, our analysis revealed an initial population of the conduction band, followed by depopulation with a time constant of $\tau_{\mathrm{CBM}} = (115 \pm 100)\,\mathrm{fs}$. This is followed by the nearly instantaneous excitation of the $^5T_{2g} \rightarrow {}^5E_g$ transition ($\tau_{b,I} = (47 \pm 15)\,\mathrm{fs}$), and then by a delayed excitation of the spin-forbidden $^5T_{2g} \rightarrow {}^3T_{1g}$ transition, occurring within

$\tau_{b,II} = (79 \pm 18)$ fs. The latter exhibits a biexponential decay, indicating two independent relaxation channels back to the ground state, with decay constants of $\tau_{\mathrm{IIa}} = (46 \pm 34)$ fs (effectively instantaneous within our resolution) and $\tau_{\mathrm{IIb}} = (1273 \pm 268)$ fs. We associate these decay paths with virtual hopping between neighbouring sites (an exchange-driven mechanism) and spin-orbit-coupling (SOC)-mediated spin-flip processes, respectively. Figure 4.12 provides a visual representation of the excitation corresponding to the $^5\mathrm{T}_{2\mathrm{g}} \rightarrow {}^3\mathrm{T}_{1\mathrm{g}}$ transition and its subsequent relaxation to the ground state.

To further understand the SOC-mediated spin-flip timescale, we performed first-principles calculations including relativistic effects. Based on the electronic band structure of $FePS_3$ [196], we determined the SOC constant for Fe^{2+} to be $\lambda_{\mathrm{SOC}} = -113.24\,\mathrm{cm}^{-1}$ (14.04 meV), primarily arising from the Fe^{2+} 3d orbitals. The negative sign of λ_{SOC} reflects the more-than-half-filled shell of Fe^{2+}. Converting this SOC strength to a timescale ($\tau_{\mathrm{SOC}} = h/E \approx 300$ fs), we find reasonable agreement with the experimentally measured spin-flip time $\tau_{\mathrm{red},2} = (1273 \pm 268)$ fs. Additionally, in $NiPS_3$, an SOC value of $-280\,\mathrm{cm}^{-1}$ (34.7 meV) was found sufficient to mix the ${}^1E_g$ and ${}^3T_{2g}$ excited states [37], enabling the spin-forbidden ${}^3A_{2g} \rightarrow {}^1E_g$ transition. Given that the energy separation between SOC-mixed states in $NiPS_3$ is $7900\,\mathrm{cm}^{-1}$ (0.98 eV), a similar SOC-driven mixing between the $^5\mathrm{E}_{\mathrm{g}}$ and $^3\mathrm{T}_{1\mathrm{g}}$ states in $FePS_3$ appears plausible, especially since the energy difference in $FePS_3$ (0.72 meV) is even smaller than in $NiPS_3$.

4.6 Conclusion

In summary, we have successfully identified the momentum signature of two distinct *d-d* transitions in the antiferromagnetic van der Waals semiconductor $FePS_3$. By employing both resonant and non-resonant excitation of the $^5\mathrm{E}_{\mathrm{g}}$ and $^3\mathrm{T}_{1\mathrm{g}}$ states, we were able to extract their respective lifetimes and characterize the associated relaxation processes. Furthermore, we assigned specific momentum-dependent characteristics to both intra-ionic multiplet excitations, manifesting primarily in replication of the Fe^{2+} momentum fingerprint including a shift to higher kinetic energies. To test the reliability of our assignment as well as the observed features in momentum space, we performed calculations of the lesser Green function in ground state and after excitation as these spectra are the basis for further band structure calculations. Here, we obtained the same modifications of the spectral function, confirming our previous assignment, and suggested a first explanation for the two different decay channel observed when pumping above the band gap.

These findings demonstrate that time- and angle-resolved photoelectron spectroscopy, when combined with momentum microscopy, is capable of resolving the momentum-space signatures of *d-d* transitions. This work broadens the well-established scope of trARPES, already proficient in identifying quasiparticles such as excitons in molecular systems [236, 258] and light-induced quantum phenomena in two-dimensional materials [171, 235, 259], by introducing its applicability to the study of *d-d* transition dynamics. In this context, a systematic investigation of temperature-dependent changes in $FePS_3$ below the Néel temperature would be of considerable interest. Such a study could enable the observation of variations in relaxation rates associated with the onset of magnetic order, as well as interactions with phonons described by Mertens et al. [53] and Rao et al. [260], which only exhibit significant amplitude below the critical temperature.

Furthermore, other members of the MPS_3 family as well as completely new materials could be investigated to confirm the momentum dependent fingerprint of *d-d* transitions and to understand how these dynamics can vary between different materials. For example, it was shown recently that the combination of $NiPS_3$ and WS_2 significantly enhances *d-d* emission due to charge transfer in the formed type I heterostructure [118]. Here, trARPES would provide the perfect platform to follow the electron excitation and relaxation into the excited multiplet state. Additionally, as introduced in the beginning of this thesis, trARPES is also perfectly suited to investigate exciton formation. $NiPS_3$ would provide the perfect platform to study the interaction between excitons and *d-d* transitions, as it exhibits a rich plethora of both optical excitations [117].

In conclusion, this study of *d-d* transitions in $FePS_3$ showcases the potential of trARPES to provide fruitful insights into the diverse landscape of optical excitations in the family of MPS_3 materials, allowing for a better understanding of their fundamental electronic properties, but also opening up a promising way to follow how modifications can tune the electron dynamics in momentum space.

Part II - Tunability

5 | Adsorption of Organic Molecules

In the previous section, we have seen that the family of MPS_3 materials exhibits a rich and complex electronic character, with strong similarities in the overall band structure but also key differences in the atomic contributions to different parts of the density of states (DOS). While many of these properties already position these materials as promising candidates for various applications, targeted modification will be a crucial step to enhance their performance and adaptability. One of the most promising pathways to modify the electronic properties of a crystal surface is the adsorption of organic molecules. This approach is already widely employed in applications such as spin valves [261], magnetic tunnel junctions [262], and devices with negative magnetoresistance [263], and it holds great promise for further improving 2D materials, for example by increasing their susceptibility to external stimuli [264].

In this chapter, we investigate how an adsorbed layer of pentacene (5A) interacts with $NiPS_3$ and $FePS_3$, two MPS_3 materials that exhibit representative differences in the DOS contributions from the transition-metal ion near the valence-band maximum, and whether the molecules can be used to strategically tune their electronic and magnetic characteristics. 5A is chosen as a model system because it is a well-studied, planar conjugated molecule with a large π-electron system, known for forming ordered layers and enabling strong yet tunable interactions with surfaces in organic electronics. As described in section 1.3, understanding the energy-level alignment at the interface is essential to assess its potential for various applications. Therefore, we employ photoemission orbital tomography (POT) [78], a technique that enables direct identification of molecular orbitals based on their experimental fingerprints in ARPES. The basic principles of this relatively new method are briefly introduced in the first part of this chapter. For 5A adsorption on $NiPS_3$ and $FePS_3$, POT allows us to identify multiple molecular orbitals, confirming the formation of a self-assembled molecular layer with three different domains. Using POT, we unambiguously identify signals from multiple molecular orbitals, some well separated and others exhibiting significant overlap. The fact that all detected signatures originate from previously occupied orbitals (HOMO+n) confirms the absence of substantial charge transfer across the interface. Nevertheless, the observed formation of an ordered molecular layer in the physisorbed regime, combined with the preservation of pronounced free-molecule characteristics, establishes this interface as a promising platform for future studies.

5.1 Sample Preparation

The pristine $NiPS_3$ and $FePS_3$ crystals were prepared using the scotch tape exfoliation method, as described in section 2.4. The deposition of 5A thin films was carried out in the preparation chamber of the KREIOS-based photoemission setup, utilizing a Knudsen-cell-type evaporator loaded with pentacene powder of 99.99 % purity. To calibrate the optimal deposition rate and duration for achieving a 5 Å monolayer, the molecules were initially deposited on a Cu(100) surface in intervals of 3 minutes. By monitoring the evolution of the LEED pattern after each step and assessing the sharpness of the molecular diffraction spots, the optimal growth conditions were identified as a deposition time of 8 min at a temperature of 185 °C. Subsequently, the molecular thin films were grown on both MPS_3 substrates by positioning the crystal surfaces at an identical distance from the evaporator and applying the same deposition parameters.

5.2 Photoemission Orbital Tomography

While section 2.1 mainly discusses how photoelectron spectroscopy can be used to investigate crystalline solids, this section introduces how the technique can also provide substantial information about the adsorption of organic thin films on crystalline surfaces. Traditional analysis of the angle-integrated spectrum to identify molecular orbitals often suffers from complications arising from orbital broadening and the potential overlap of different orbitals. Here, the application of ARPES, referred to as photoemission orbital tomography (POT) [78] when applied to molecular layers, has proven to be a more insightful technique. It allows the identification of different molecular orbitals based on their momentum-dependent intensity distribution and thereby enables a detailed characterisation of the electronic structure of organic molecules adsorbed on a surface. Before applying this technique to the interface formed by 5A adsorbed on $FePS_3$ and $NiPS_3$, this chapter introduces the fundamental background of the method and explains how the momentum maps for the corresponding orbitals can be calculated.

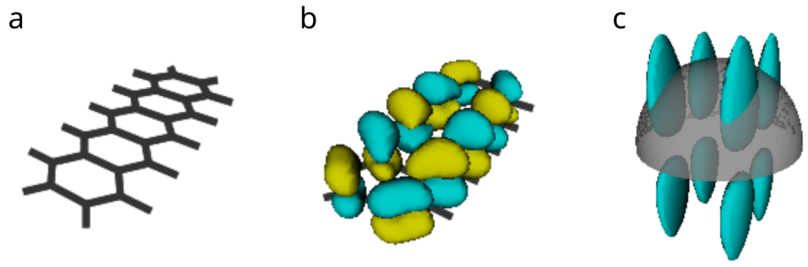

Figure 5.1: Different steps in calculating the photoemission signature of a molecular orbital. (a) presents the chemical structure of the 5A molecule, consisting of five aromatic rings connected on the long side. The corresponding electron density for the highest occupied orbital (HOMO) is depicted in (b), based on which the (c) Fourier Transformation for later extraction of the PE pattern at a specific kinetic energy can be calculated.

To calculate the characteristic fingerprint of a molecular orbital in photoemission, we start by considering the photoexcitation as a single coherent process from a molecular orbital to the final state. The intensity is then given by Fermi's golden rule as

$$I(\theta, \phi, E_{\text{kin}}) \propto \sum_i |\langle \Psi|_f (\theta, \phi, E_{\text{kin}})|\mathbf{A} \cdot \mathbf{p}|\Psi_i\rangle|^2 \times \delta\left(E_i + \Phi + E_{\text{kin}} - \hbar\omega\right) . \tag{5.1}$$

Similar to the introduction in section 2.1, the photocurrent I is given by a sum over all transitions from occupied initial states to final states (described by Ψ_i and Ψ_f, respectively). The δ function in the second part ensures energy conservation, including the sample work function Φ. Another important term is the transition matrix element, consisting of the momentum operator $\mathbf{p}$ and the vector potential $\mathbf{A}$ of the electromagnetic wave, which strongly influences the intensity distribution (and is often neglected, as we will see later). By approximating the final state as a plane wave, the above formula simplifies and leads to the photocurrent I being proportional to the Fourier transform (FT) $\tilde{\Psi}_i(\mathbf{k})$ of the initial-state wave function:

$$|\tilde{\Psi}_i(\mathbf{k})| \propto \frac{\sqrt{I_i(\theta, \phi)}}{|\mathbf{A} \cdot \mathbf{k}|} \tag{5.2}$$

Initially, this technique was widely believed to be unsuitable for the investigation and interpretation of ARPES data from oriented films of large polyatomic molecules. However, Puschnig *et al.* [78] demonstrated that, under specific conditions, the plane-wave (PW) approximation for the interpretation of ARPES data is indeed valid. These conditions are: (i) the emission should originate from π-orbitals of large planar molecules, (ii) the experimental geometry should involve a relatively small angle between the polarization vector $\mathbf{A}$ and the direction of the emitted electron $\mathbf{k}$, and (iii) the molecules should contain only light atoms such as hydrogen, carbon, nitrogen, or oxygen.

One of the first molecules for which this was demonstrated is pentacene, an organic molecule consisting of five linearly edge-fused phenyl rings (shown in Figure 5.1a), where the authors found exceptional agreement between the experimentally observed orbitals and computational predictions. Starting from the real-space orbital shown in Figure 5.1b, in this case the HOMO, one calculates the corresponding three-dimensional Fourier transform. As the experimental maps are evaluated at a constant binding energy, the corresponding computational momentum map is obtained by intersecting the 3D Fourier transform with a hemisphere of radius $k = \sqrt{(2m/\hbar^2)E_{\text{kin}}}$ (Figure 5.1c), yielding the momentum map for that energy.

A series of these computational maps, extracted at different kinetic energies in steps of 5 eV, is shown in Figure 5.2a–d. The kinetic energy of the electron originating from the molecular orbital under investigation (here the 5A HOMO) leads to slight differences in the observed signature. Therefore, it is important to match the computational maps closely with the experimentally observed patterns and to take the kinetic energy into account, as some patterns may exhibit the same features with only slightly different positions in momentum space (as, for example, the HOMO and HOMO−1 of 5A). During experimental investigations, this typically results in an iterative process in which a first identification of potential features is performed before matching them to the possible computational maps.

This technique has enabled a wide range of valuable experimental insights. By resolving more than 30 different molecular orbitals across an energy range exceeding 10 eV, *Haags et al.* [267] provided a detailed benchmark and validation for DFT calculations of molecular orbital energies.

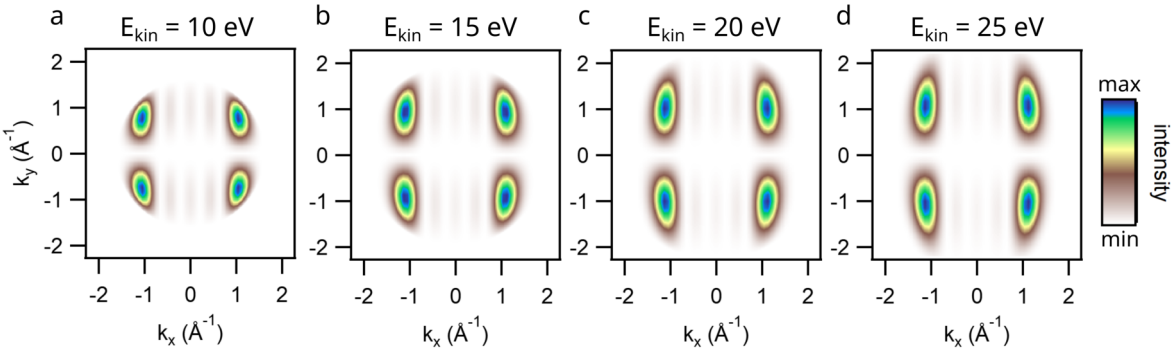

Figure 5.2: Isoenergetic patterns for different kinetic energies of the previously introduced 5A HOMO. The kinetic energy only slightly affects the position of the intensity maxima in $k_{||}$. Data taken from Ref [265] and [266].

Furthermore, recent findings by *Janas et al.* [268] have demonstrated that POT can be effectively employed to detect structural distortions of adsorbed molecules, even extending beyond the first molecular layer. In an approach inverse to the original computational derivation, *Bennecke et al.* [269] succeeded in reconstructing the full three-dimensional FT and thereby directly accessed the real-space electron density distribution by acquiring momentum maps at varying kinetic energies. Moreover, although originally developed for the study of π-orbitals, POT has also been successfully extended to probe σ-orbitals, opening new avenues for the investigation of surface chemical reactions, such as bond formation and dissociation processes [270].

Beyond these more static applications, the technique has also undergone significant advancements for the study of dynamic processes. For instance, POT can be employed to trace molecular orbitals on ultrafast timescales by imaging the unoccupied molecular orbitals of a PTCDA monolayer on Cu(001)-2O [236]. Similarly, the method has been adapted to interpret excitonic signatures in organic molecules, enabling the disentanglement of the individual orbital contributions to excitons formed in buckminsterfullerene [130].

These diverse applications collectively demonstrate that POT is now firmly established as a reliable technique for investigating the electronic structure of organic molecules on a variety of surfaces. In the following chapters, we will apply this method to explore whether the deposition of a 5A monolayer can be actively utilized to tailor the interfacial properties of MPS_3 crystals and to examine the energetic alignment of the associated molecular orbitals.

5.3 Pentacene Adsorption on $NiPS_3$

Figure 5.3 presents the energy distribution curves (EDCs) for both pristine $NiPS_3$ and the 5A-covered surfaces, obtained by integrating over the entire accessible momentum space. The dark-blue curve represents the pristine surface, which has already been introduced and discussed in detail in section 3.2. Upon deposition of the first 5A monolayer (1L), significant modifications are observed in the angle-integrated photoemission signal.

Focusing first on the energy region near the top of the valence band, a small Gaussian-shaped

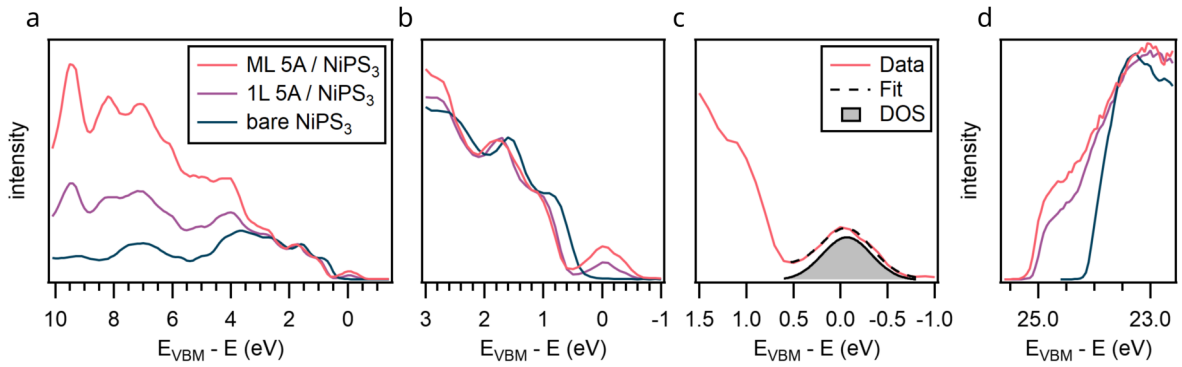

Figure 5.3: (a) and (b) Angle-integrated photoemission intensity for pristine $NiPS_3$ and 5A-covered samples. (c) Close-up of the valence-band maximum (VBM) region for the pristine surface, showing a Gaussian fit to the feature emerging after 5A adsorption. (d) Secondary cutoff (SEC) for all three spectra, revealing a 1 eV shift and a shoulder feature indicative of non-uniform molecular adsorption.

feature emerges around the valence-band maximum (VBM) of the pristine surface. This is accompanied by a shift of the substrate-related spectral structures toward higher binding energies. These changes are examined in more detail in section 3.2b, where all three spectra are normalized to the intensity of peaks located around $E_{\mathrm{VBM}} - E = 1.6\,\mathrm{eV}$. The observed 300 meV shift of the $NiPS_3$-related features is most plausibly attributed to the formation of an interface dipole [271], which can arise from Pauli push-back effects in physisorbed π-systems. Other possible contributions include changes in the local screening potential or band bending [138], the latter typically requiring interfacial charge transfer, which subsequent data suggests is negligible here. Less likely, though not entirely excluded, is that the adsorbed molecules modify the charging properties of $NiPS_3$, thereby enhancing photon-fluence-dependent effects. A conclusive determination of the dominant mechanism would require complementary investigations, such as density functional theory calculations.

To characterise the observed molecular feature, we apply a Gaussian fit to the obtained signal, resulting in a central energy of $-0.068\,\mathrm{eV}$ and a full width at half maximum (FWHM) of 0.367 eV. The central energy will be important later to compute the theoretical photoemission pattern of the orbital at the corresponding kinetic energy. At binding energies further below the VBM, a general increase in spectral intensity is observed, along with the emergence of distinct peak-like structures around 6.2 eV, 8.3 eV, and 9 eV. However, due to the inherently feature-rich EDC of the $NiPS_3$ substrate, an unambiguous identification of all molecular contributions remains challenging.

To gain a clearer understanding of the origin of the observed spectral features, the 5A coverage was further increased by depositing an additional 24 min on top of the existing monolayer, resulting in a total thickness of approximately four molecular layers. The corresponding EDCs are again shown in section 3.2a and b, exhibiting a further increase in intensity, particularly at energies more than 3 eV below the VBM. Additionally, the feature at the top of the valence band gains further intensity. The peaks attributed to molecular states are indicated by vertical dashed lines. However, apart from these changes, no further modifications of the EDC

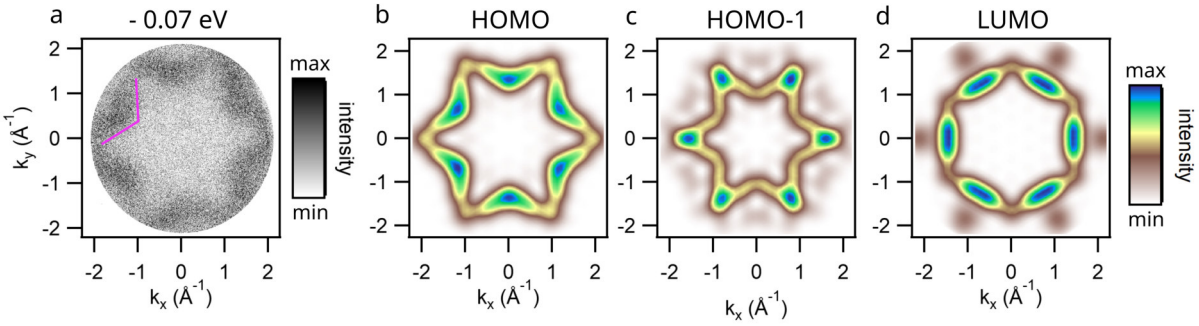

Figure 5.4: (a) Experimental momentum map at the central energy from the Gaussian fit in Figure 5.3, showing a star-shaped pattern with threefold symmetry. (b-d) Computational momentum maps for 5A's HOMO, HOMO−1, and LUMO, respectively. The close match between (a) and the HOMO map in (b) confirms the orbital assignment and supports the conclusion that the 5A layer remains electronically decoupled from the $NiPS_3$ substrate.

are observed when going from the mono- to the multilayer (ML) coverage. Returning to the original goal of this study, namely to examine whether the molecular layer can tune the surface properties, this observation indicates that no charge transfer occurs at the interface. If charge transfer were present, a shift of the molecular features toward either higher or lower binding energies would be expected, as everything beyond the first layer should have negligible interaction with the substrate and therefore resemble the gas-phase electronic structure of the molecular orbitals.

As a final part of the angle-integrated signal analysis, we investigate how the additional molecular layers influence the work function Φ of the surface. section 3.2d shows the secondary cutoff (SEC) at different molecular coverages. By quantifying the additional signal above the pristine VBM as well as below the pristine SEC, we estimate the total change in Φ associated with the interaction between molecules and surface. Including the additional signal from the HOMO, this amounts to a total work-function reduction of $\Phi_{\text{diff}} = -1.88\,\text{eV}$. However, this value may change under further coverage, as the general shape of the SEC indicates a non-uniform molecular coverage, evidenced by its shoulder-like feature that increases from mono- to multilayer.

While the reduction of the work function can be caused by multiple effects, the absence of considerable charge transfer between the molecular layer and substrate suggests two dominant mechanisms in this system. First, the observed HOMO lies above the VBM, which has been shown to cause a work-function reduction in similar systems where a 5A layer is deposited on TMDs [271]. Second, the so-called push-back effect describes the influence of the molecular electron-density distribution on the substrate. The interaction between both leads to a redistribution of electrons at the interface, creating an interfacial dipole layer that reduces the local electrostatic potential and subsequently lowers the work function by decreasing the vacuum level [271–273].

After investigating the angle-integrated signal, we now utilize the capabilities of our advanced detector to examine the momentum-resolved pattern in more detail. This analysis provides additional information about the general adsorption behaviour of the molecules, such as the

presence of different domains or whether 5A forms a self-assembled layer. We begin with the previously described feature around the VBM of the pristine surface. Figure 5.4a shows the raw signal acquired at this energy. It reveals a star-shaped pattern with high-intensity features arranged in a hexagonal symmetry. Each feature has a triangular shape with its tip pointing towards the centre (one feature is highlighted as an example). As shown in Figure 5.2, computational momentum maps of 5A typically display a twofold symmetry, reflecting the general shape of the molecule. Therefore, the observed threefold symmetry already indicates that the surface hosts multiple different azimuthal orientations of the 5A molecules. To match the experimentally deduced pattern with the corresponding molecular orbital, we apply a threefold rotational symmetry to the computational maps and compare different molecular orbitals. The best agreement is found with the HOMO, depicted in Figure 5.4b, which shows the same triangular high-intensity features at high momenta, located roughly $1\,\text{Å}^{-1}$ from the centre. For completeness, Figure 5.4c and Figure 5.4d present the HOMO-1 and LUMO, respectively. Both show clear differences compared to the HOMO, allowing an unambiguous assignment of the observed feature around the pristine VBM to the HOMO. Based on this assignment, and given the negligible changes observed upon deposition of additional 5A layers, we conclude that there is a complete absence of charge transfer between the 5A molecules and the $NiPS_3$ surface. Continuing the analysis of the angle-resolved intensities, we also conducted a momentum-resolved investigation of the molecular peaks at higher binding energies below the VBM (between 6 eV and 10 eV). However, even after extended integration times, none of these energies displayed a clear momentum-resolved pattern that could be associated with any of the computational momentum maps, down to the HOMO-10.

Having established the absence of significant interfacial charge transfer in the 5A/$NiPS_3$ system, we now turn to $FePS_3$ to examine whether its distinct electronic structure leads to a different adsorption behaviour and interfacial interaction.

5.4 Pentacene Adsorption on $FePS_3$

Similar to the previous chapter, Figure 5.5a and b present the EDCs for both pristine $FePS_3$ and the 5A-covered surfaces. The dark-blue curve represents the pristine surface, which has already been introduced and discussed previously. Upon deposition of the first 5A monolayer, we observe behaviour similar to that found for the 5A/$FePS_3$ interface. First, a small but noticeable peak appears around the VBM of the pristine surface, increasing in intensity upon deposition of the second layer. Second, the peak structure related to the MPS_3 substrate shifts towards lower kinetic energies by 600 meV for the first molecular layer and by an additional 200 meV for the second layer. This shift presents more significant in contrast to $NiPS_3$, where the first layer induced a shift of only 300 meV without further changes under the second layer. While we expect the same mechanism for both interfaces, the presented data does not allow to identify the specific reason and necessitate further investigation via density functional theory. Figure 5.5c display a gaussian fit of the new feature around the VBM, centered at 150 meV below the pristine VBM and a FWHM of 270 meV, similar to the same feature present for the 5A/$NiPS_3$ interface. Additionally, we see again a shift of the secondary onset by 1.2 eV upon deposition of the first layer, this time with a shoulder less structure. In contrast, deposition of the second layer leads to the emergence of the shoulder like structure also observed for deposition

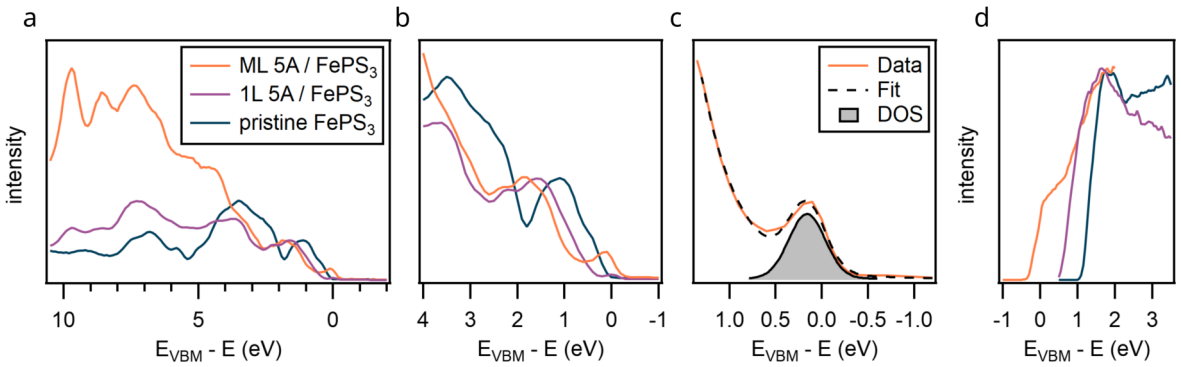

Figure 5.5: (a) and (b) Angle-integrated EDCs for pristine $FePS_3$ and two 5A coverages, with dashed lines marking peaks attributed to the molecular layer. (c) Gaussian fit of the peak nearest to the pristine VBM, later assigned to the HOMO. The greater number of molecular peaks compared to $NiPS_3$ indicates a broader set of detectable orbitals in the $FePS_3$ interface, enabling more complete mapping of the molecular electronic structure. (d) Similar to $NiPS_3$ the SEC for all three spectra, reveals a substantial shift and a shoulder feature indicative of non-uniform molecular adsorption.

on $NiPS_3$. This indicates that the initial doses of 5A on the Ni compounds eventually already accumulated to more than a single layer. This would explain the additional changes we observe for the 5A/$FePS_3$ interface, while $NiPS_3$ did not present any substantial additional changes with the higher 5A doses.

As presented for the 5A/$NiPS_3$ interface presented in the previous chapter, we proceed by obtaining angle-resolved momentum maps for each peak in the EDC that appears after molecular adsorption. The corresponding momentum maps are shown in Figure 5.6, sorted by their energetic position in the EDC. In contrast to the 5A/$NiPS_3$ system, we observe several symmetric features spanning an energy range up to 4 eV below the VBM of the pristine surface. Unlike the maps presented in the previous chapter, the images shown here are symmetrized according to the underlying symmetry of the molecular layer, which exhibits the same structural configuration with three different domains, each rotated by 120° with respect to one another. This symmetrisation allows for easier comparison between experimental and computational photoemission intensity patterns, as it removes inhomogeneities introduced by the polarization factor, which has a strong influence, particularly at higher binding energies below the VBM.

The first two peaks can be assigned unambiguously to the HOMO and HOMO−1 of 5A, both displaying a star-shaped pattern. The pattern presented in Figure 5.6c cannot be mapped to a single molecular orbital, but instead resembles a mixture of the HOMO−2 and HOMO−3, with an intensity ratio of 2:1. While the next peak in Figure 5.6d can again be assigned to the isolated HOMO−3, the last image presented shows the most complex composition, containing contributions from the HOMO−4, HOMO−5, and HOMO−6 with relative contributions of 2:5:10. The isolated momentum maps for each molecular orbital are provided in section A.3.

To precisely determine the energetic positions of the different orbitals and their relative contributions to the individual peaks observed in the EDC, a full deconvolution of the experimental data with computational molecular momentum maps would be required. However, this is not

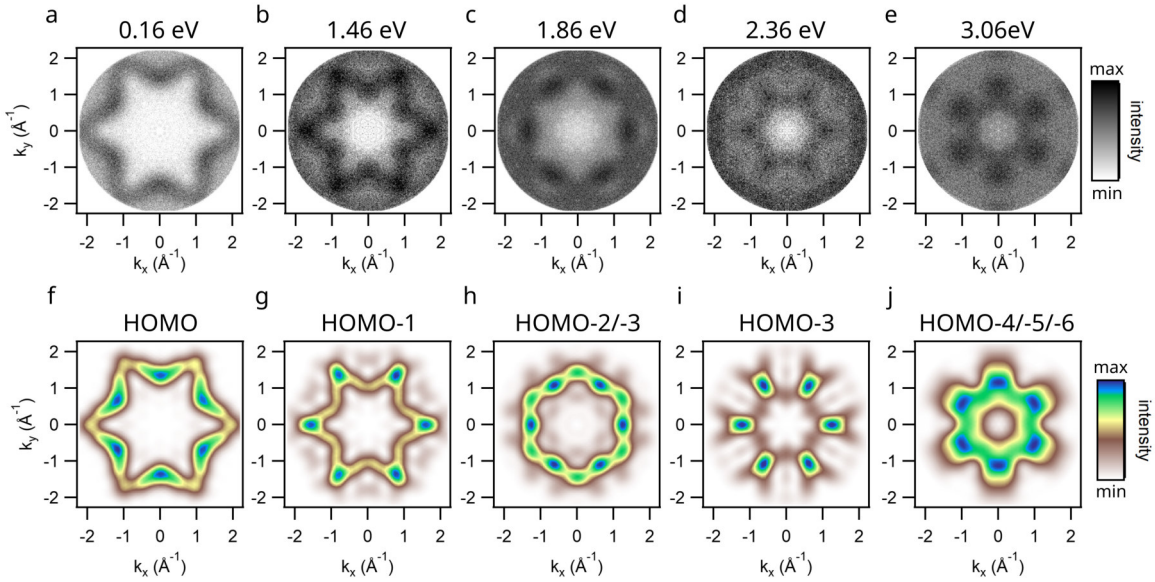

Figure 5.6: Top row: Experimental momentum maps at energies corresponding to peaks in the EDC that appear after 5A adsorption. Bottom row: Computational momentum maps showing the best match to the experimental data. (f), (g), and (i) correspond to isolated HOMO, HOMO−1, and HOMO−3 orbitals, while (h) and (j) are combinations of HOMO−2/HOMO−3 and HOMO−4/HOMO−5/HOMO−6, respectively. The need for mixed-orbital assignments reflects the close energetic spacing of higher-lying molecular orbitals, while the good agreement between experimental and computational patterns supports the interpretation of a physisorbed, electronically decoupled molecular layer.

feasible for the present data set, as the quality of the molecular film would necessitate a total integration time exceeding the lifetime of the sample surface, which degrades under irradiation with the high-energy XUV pulses used during the experiment. Nevertheless, as the observed orbitals indicate a decoupled molecular layer with negligible interaction between the molecules and the sample surface, we can compare the observed peaks with gas-phase calculations for 5A.

Table 5.1 presents the computed energetic differences of the HOMO$-n$ orbitals with respect to the HOMO, together with the energetic differences observed for the various peaks in the EDC, referenced to the isolated HOMO close to the VBM of the pristine surface. While the momentum maps have already shown that the peaks cannot always be assigned to specific orbitals in an isolated manner, the energies listed are sorted according to their appearance in the EDC for the two-layer sample. We observe a striking similarity for the first five orbitals following the HOMO. Together with the negligible shift of the HOMO after deposition of a second molecular layer and the strong agreement with the gas-phase momentum maps used for orbital identification, this indicates that there is no strong interaction between the $FePS_3$ substrate and the adsorbed molecular layer.

In comparison to the 5A/$NiPS_3$ system, where only the HOMO could be clearly identified, the richer set of assignable orbitals in the 5A/$FePS_3$ interface further highlights the weaker substrate

Table 5.1: Comparison of the gas-phase energies of various 5A molecular orbitals with respect to the HOMO and the observed molecular peaks in the EDC up to a maximum energy of 4 eV.

Orbital	HOMO-1	HOMO-2	HOMO-3	HOMO-4	HOMO-5
$\Delta_{E,Theo}$ (eV)	1.297	1.822	2.419	2.917	3.269
$\Delta_{E,Exp}$ (eV)	1.3	1.7	2.2	2.9	3.3

influence and the predominantly gas-phase-like character of the molecular electronic structure in both systems.

5.5 Conclusion

In this chapter, we investigated the adsorption of organic molecules, namely pentacene, on two different MPS_3 compounds. The original aim was to achieve hybridisation at the interface in order to create a system suitable for electronic modulation via light pulses, solely by creating excitations at the interface. Additionally, we sought to gain insights into possible modifications of the substrate's electronic structure induced by the presence of organic molecules.

Using photoemission orbital tomography, we successfully isolated the momentum-dependent photoemission intensity of various orbitals after adsorption on the surface. First, this confirms that on both surfaces, pentacene forms a well-defined, self-assembled monolayer with three different domains, rotated by 120° with respect to each other. Second, the occupation of pentacene's highest occupied orbital for both substrates, together with the absence of energetic shifts when moving from monolayer to multilayer coverage, suggests that no significant charge transfer occurs at the interface. In the case of $FePS_3$, this is further confirmed by comparison of the observed molecular peaks with the energetic differences between the molecular orbitals of gas-phase pentacene, which show striking agreement. While this confirms the absence of considerable hybridisation at the interface, the assembly of a well ordered 5A layer in the physisorption regime establishes this interface as a promising platform for further investigation, possibly introducing modifications of electronic properties such as exciton formation and charge-carrier density. For example, in the case of small aromatic molecules adsorbed on TMDs [274], it has been shown that the molecular layer can tune the charge-carrier concentration at the interface even in the physisorbed regime, thereby affecting exciton dynamics and, consequently, key electronic properties of the substrate.

In general, to achieve significant hybridisation between any of the discussed MPS_3 materials and a molecular layer, it may be necessary to employ organic molecules that are stronger donors or acceptors compared to pentacene. Promising candidates include highly polar molecules such as hydrazine, benzene, and TCNQ, which have been previously employed for chemical doping on TMDs [274]. The latter has also been used together with C_{60} in initial experiments on $FePS_3$, although no visible ordering was observed after deposition, rendering them unsuitable for the application of POT. However, as will be discussed in chapter 6, it could be promising to repeat the experiments on another member of the MPS_3 family. Intercalation with alkali metals has shown that $CoPS_3$ exhibits the most prominent modifications under electron doping, nearly an order of magnitude stronger than those observed for $FePS_3$. Since TCNQ is also a strong electron donor, the results obtained from alkali-metal intercalation suggest that its deposition

on $CoPS_3$ could result in stronger interactions, including charge transfer at the interface.

Overall, our results demonstrate that pentacene adsorption on both $NiPS_3$ and $FePS_3$ leads to well-ordered, physisorbed molecular layers without significant charge transfer or hybridisation at the interface, preserving the free-molecule character. While this limits the potential for direct electronic modulation via interfacial coupling, it provides an attractive basis for further investigations.

6 | Targeted electron doping

While the previous chapter focused on modifying the electronic structure of MPS_3 through the adsorption of organic molecules, this chapter introduces another well-established approach, alkali metal doping. Alkali metal doping is a widely used strategy for introducing additional electrons via the deposition of caesium, potassium, or lithium. Such doping can induce a variety of effects, including the emergence of superconductivity [275], the occupation of additional electronic states and corresponding shifts of the entire band structure [276, 277], as well as the population of higher-lying orbitals when combined with organic molecules [278].

In the following sections, we investigate the changes induced by lithium and caesium deposition on the surfaces of various MPS_3 materials. To date, scientific publications addressing the influence of alkali metal doping on the electronic structure of MPS_3 remain scarce, with most studies concentrating on magnetic properties. Nevertheless, these works already highlight the considerable potential of alkali metal intercalation in MPS_3, reporting phenomena such as a reversible transition between ferromagnetic (FM) and antiferromagnetic (AFM) states [79, 80], a reduction of the magnetic ordering temperature [81] in $FePS_3$, and the emergence of ferrimagnetism in $NiPS_3$ [82].

A key aspect of tuning the electronic and magnetic behaviour through alkali metal intercalation lies in controlling the *d*-shell filling. Whether by charge donation or local substitution of transition-metal ions, modifications to the *d*-orbital occupation strongly influence magnetic ordering. Despite notable progress, a comprehensive understanding of how *d*-shell filling governs the competition between exchange interactions, and thus the emergence of novel magnetic and electronic phases, remains elusive, yet is essential for enabling future device applications.

Therefore, the following chapter will place a particular focus on the changes induced in the *d*-shell occupation, presenting a detailed investigation of MPS_3 surfaces under electron doping by two different experimental approaches. First, Section 6.2 will present XPS measurements of the four different compounds, providing information on the oxidation state of the constituent atoms as well as the distribution of the additional electrons introduced by lithium and caesium deposition. This analysis reveals fundamental differences in the doping mechanism: for $FePS_3$, $CoPS_3$, and $NiPS_3$, a change in the oxidation state of the transition-metal ion is observed, whereas in $MnPS_3$ the additional electrons predominantly occupy ligand states. Furthermore, a comparison of the splitting between the M $2p_{3/2}$ and $2p_{1/2}$ core-level peaks indicates that the additional electrons also modify the occupation of the metal ions' *d*-orbitals.

Subsequently, Section 6.3 will focus on ARPES and MM measurements to reveal changes in the

work function and valence band structure. Here, two materials stand out in particular: $MnPS_3$ exhibits negligible changes in response to the additional charge, while $CoPS_3$ shows a pronounced modulation of the states closest to the VBM, previously assigned to transition-metal-derived states (see chapter 3), with the rest of the bandstructure being unperturbed. Additionally, new dispersive states appear above the pristine VBM of $CoPS_3$, indicating a reorganisation of the electronic structure. Complementary DFT calculations corroborate the experimentally observed differences between the compounds and provide a more detailed view of the charge redistribution, ultimately suggesting an increased conductivity in $CoPS_3$.

In conclusion, these results demonstrate that alkali metal doping offers a powerful and controllable approach for modulating the electronic structure of two-dimensional antiferromagnets. The capability to tune the band structure and charge distribution in compounds with a less energetically stable *d*-shell opens new opportunities for engineering the spin and electronic properties of ionically bonded 2D materials, paving the way for their integration into future spintronic and quantum technologies [5, 30].

The data presented in this chapter were previously published in the following publication:

Jonah Elias Nitschke et al. “Electronic structure reorganization in MPS3 via d-shell-selective alkali metal doping”. In: *arXiv, under Review in Advanced Science* (2025).
DOI: 10.48550/arxiv.2506.01527. eprint: 2506.01527

6.1 Sample Preparation

The bare crystals used in the experiments were prepared as described in section 2.4. Alkali metal deposition was carried out either in a dedicated chamber or in the load lock after bakeout, with the base pressure stabilised at approximately 1×10^{-9} mbar. For the deposition process, we employed alkali metal dispensers (AMD) from SAES GETTER [REF], which enable consistent and reproducible alkali metal release with low gas emission and precise control over the deposition rate.

A schematic of the alkali metal dispenser and the deposition process is shown in Figure 6.1. The dispenser (Figure 6.1a) consists of a central container holding the alkali metal (AM) bound in a salt of chromic acid (AM_2CrO_4, AM = Li, Cs), together with a reducing agent composed of an alloy containing 84 % zirconium (Zr) and 16 % aluminium (Al). The container has a trapezoidal cross section with a slit on the wider side through which the alkali metal vapour exits. This slit is partially obstructed by a thin wire, preventing the undesired loss of particles.

The release of alkali metals from the container is facilitated by heating the dispenser to a specific temperature at which a reduction reaction between the chromate and the reducing agent is initiated, thereby releasing the AM vapour. To ensure homogeneous heating of the entire container, the AMD is equipped with two side terminals for the application of an electric current, which enables precise control of the deposition rate. In addition, the ZrAl alloy acts as a getter by adsorbing all gaseous by-products generated during the reaction, thus preventing contamination of the sample surface.

The AMD is mounted on a feedthrough using copper wire to ensure electrical conductivity and

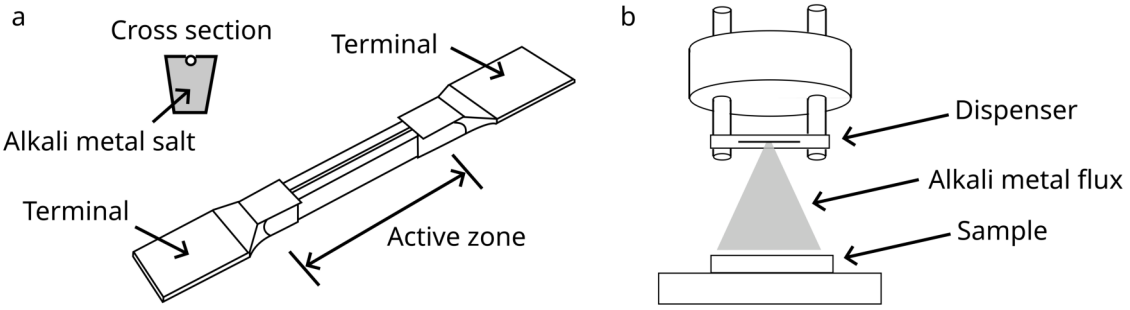

Figure 6.1: (a) Schematic of the alkali metal dispense by SAES Getters [279]. The central bridge contains the bound alkali metals that are released upon thermal heating. (b) Sample configuration during deposition of the alkali metals.

is subsequently baked together with the chamber at 150 °C for up to three days to achieve the required UHV conditions for clean deposition. Before the actual deposition, the dispenser was degassed by gradually increasing the applied current in steps until reaching the value used in the experiment. Whenever possible, the deposition rate was monitored using a quartz crystal microbalance to determine the exact rate for each current setting. During alkali metal deposition, the chamber pressure was maintained below 5×10^{-8} mbar at a current of 7.5 A.

Figure 6.1b illustrates the geometry of the sample and dispenser during deposition. The sample was positioned approximately 15 cm from the AMD and oriented away from the dispenser both before and after deposition. For the XPS experiments, alkali metal deposition was performed at a low rate in 10 min steps to track the evolution of changes induced by electron doping (as discussed in the next section). For ARPES measurements, a single 30 min deposition was used for each sample to achieve a comparable doping level.

6.2 Accessing the *d*-Orbital Occupation via XPS

A powerful technique to investigate how alkali metal adsorption influences the electronic structure of MPS_3 is X-ray photoelectron spectroscopy. As introduced previously, XPS provides direct access to the core levels of a material and thus enables the determination of how the additional electrons introduced by lithium and caesium doping modify the electronic configuration of specific orbitals. This approach not only yields information about the oxidation state of the different atomic species, but also reveals which orbitals are occupied by the additional electrons and how these changes affect electronic transitions within the band structure.

As a starting point, Figure 6.2 presents the XPS survey spectra for each material after lithium deposition. While the spectra shown here correspond to the final lithium coverage, measurements were also acquired after each deposition step to monitor the step-by-step evolution of the various peaks, as will be discussed later for the M $2p$ peaks as an example. Focusing on $FePS_3$ in the top panel of Figure 6.2a, the characteristic core-level peaks are labelled accordingly. In addition, the binding energies corresponding to the chromium (Cr) $3d$ peaks are marked. As discussed in the previous section, the alkali metal dispensers contain the alkali metals in the form of a chromate salt, which releases lithium upon heating above a specific temperature threshold. XPS

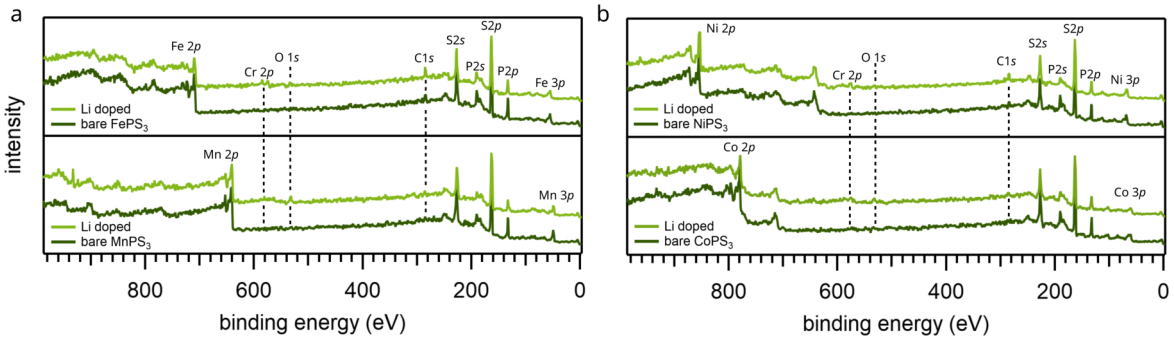

Figure 6.2: XPS survey scans for Mn-, Fe-, (a) Co-, and $NiPS_3$ (b) before (dark green) and after lithium deposition (bright green). The most important core level peaks are marked according to their origin. The generally mostly negligible intensity of the C 1*s* and O 1*s* peaks confirm that a clean deposition of lithium was achieved.

measurements, however, reveal a slight chromium contamination of the surface, which increases with the operational lifetime of the AMD. In the case of $FePS_3$, this contamination is particularly pronounced and may influence the intrinsic electronic structure of the MPS_3 crystal. Therefore, in the following analysis we focus only on those samples where no significant Cr contamination is detected. Besides the chromium peaks, the positions of the C 1*s* and O 1*s* orbitals are also indicated. No oxygen-related signal is observed, whereas $FePS_3$ and $NiPS_3$ exhibit weak signatures of additional carbon. However, the carbon intensity is negligible compared to the dominant MPS_3 core levels. Overall, the XPS survey spectra confirm that the alkali metal deposition was performed under largely clean, contamination-free conditions, ensuring that the observed spectral changes indeed reflect the intrinsic interaction of the MPS_3 substrates with the additional electrons introduced by the deposited alkali metal atoms.

Moving forward, we first investigate the changes to the M 3*p* peaks. The detected energy range was chosen to also include the Li 1*s* peak, allowing us to monitor the amount of deposited lithium atoms. Starting with $MnPS_3$ in Figure 6.3a, the dotted line represents the Mn 3*p* spectrum of the pristine surface. After lithium deposition, a new peak emerges at a binding energy of 56 eV, while the remainder of the spectrum remains largely unchanged except for a slight broadening of the main peak at 47 eV. Since the changes induced by the additional electron can be complex, potentially affecting both the main peaks (e.g., new chemical environments of the metal atoms) and the satellite structure (due to changes in orbital occupation), we refrain here from an exact fitting of the post-deposition spectrum. Instead, we take a phenomenological approach to confirm the successful deposition of lithium. A more detailed analysis of the induced changes in the electronic structure will be carried out later based on the M 2*p* spectra.

For Li-doped $FePS_3$, the additional Li 1*s* signal is less pronounced, as the peak is now situated on the shoulder of the main features. Nevertheless, a new peak is clearly visible at the same binding energy as for $MnPS_3$, accompanied by a slight broadening of the rising edge around 52 eV. In contrast, $CoPS_3$ exhibits a much stronger response to lithium adsorption (Figure 6.3c). The Li 1*s* peak is well resolved, and substantial modifications in the satellite structure are observed: the original peak at 56.9 eV disappears entirely, and the main peak exhibits significant broadening with a shoulder-like feature shifted toward lower binding energies relative to the $3p_{3/2}$ peak.

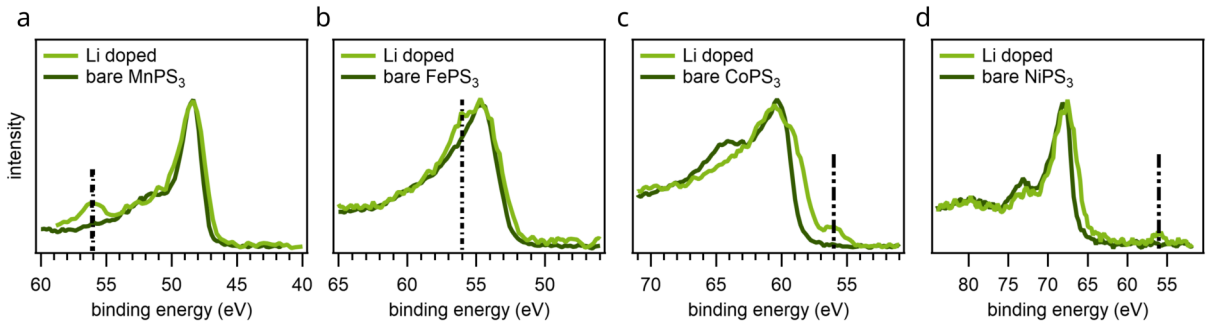

Figure 6.3: M 3*p* peaks for the different MPS_3 compounds. A comparison of the spectra before (dark green) and after lithium deposition (bright green) reveals the additional peaks due to the Li 1*s* orbital (black dashed line) as well an additional shoulder at lower binding energy visible most prominent in the spectrum of $CoPS_3$.

This behaviour provides a first indication that the oxidation state of the Co^{2+} ion may be reduced, as such a change is typically accompanied by the appearance of new peaks at lower binding energies [280]. The modification of the satellite structure further suggests changes in the valence band, since these satellites were previously assigned to shake-up features originating from interactions between the photoemitted electron and valence-band states. As will be shown later in section 6.3, this pronounced response of $CoPS_3$ to lithium adsorption is also clearly reflected in our ARPES measurements.

Lastly, $NiPS_3$ represents an intermediate case. Here, the main 3*p* features exhibit clear broadening, while the satellite peaks display a more moderate response: their intensity is reduced, but they remain discernible.

To gain a more detailed understanding of the modifications to the electronic structure, we also measured the M 2*p* core-level spectra. Figure 6.4 presents the effect of lithium adsorption on the M 2*p* states for the different MPS_3 compounds, as well as the step-by-step evolution for $NiPS_3$ and $MnPS_3$ as representative cases. Overall, the changes observed in the M 2*p* spectra can be grouped into two distinct categories: (i) $MnPS_3$, and (ii) $FePS_3$, $CoPS_3$, and $NiPS_3$.

For $MnPS_3$ (Figure 6.4a), the adsorption of lithium has only a minimal effect on the M 2*p* states. The $2p_{3/2}$ and $2p_{1/2}$ peaks show no measurable shift in binding energy and only exhibit slight broadening. The satellite peaks at higher binding energies are reduced in intensity but remain clearly visible. In contrast, $FePS_3$, $CoPS_3$, and $NiPS_3$ exhibit a markedly different response (Figure 6.4b–d). Lithium deposition results in the emergence of additional peaks at lower binding energies for both the $2p_{3/2}$ and $2p_{1/2}$ components. This behaviour indicates a change in the oxidation state of the transition-metal ions, as the new features correspond to the appearance of distinct species rather than a simple chemical shift of the existing peaks. This interpretation is further supported by the gradual spectral evolution with increasing lithium coverage, as shown exemplarily for $NiPS_3$ in Figure 6.4f.

The measured binding-energy shifts for the various 2*p* peaks are summarised in Table 6.1. A particularly informative quantity here is the energy separation between the $2p_{3/2}$ and $2p_{1/2}$ peaks, which decreases for all three compounds after lithium adsorption. Since spin–orbit splitting is

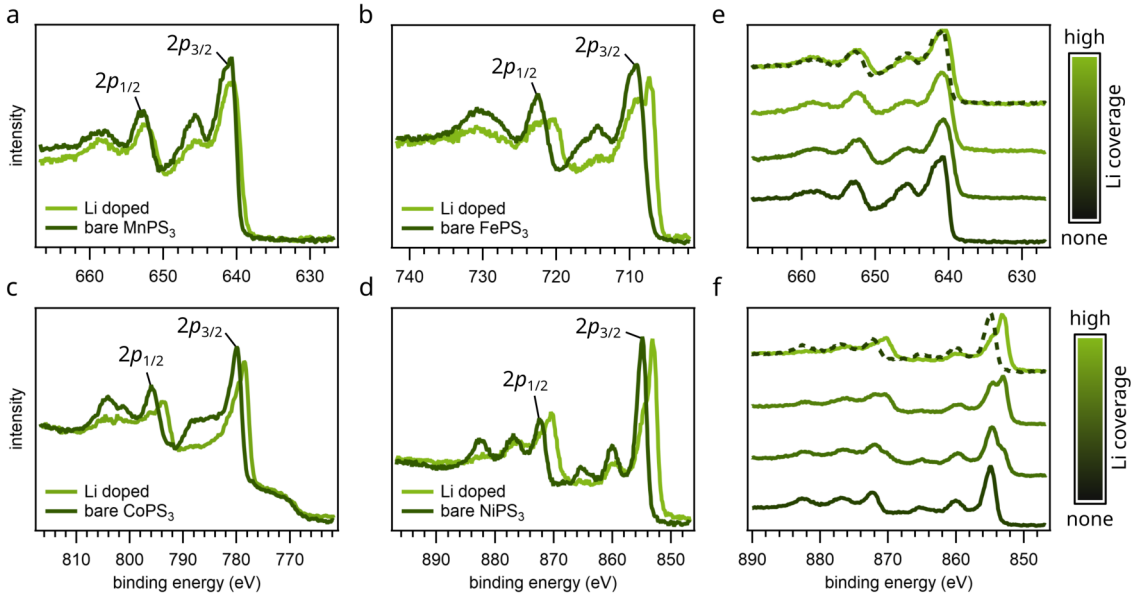

Figure 6.4: M $2p$ spectra after alkali metal deposition. (a) - (d) display the differences in the M $2p$ spectra after lithium deposition. While $MnPS_3$ (a) exhibits now changes besides a slight broadening, the other three materials undergo significant modification such as the appearance of a new feature at lower binding energy, a reduction in splitting between the $2p_{3/2}$ and $2p_{1/2}$ peaks and partial vanishing of the satellite features. The M $2p$ spectra in (e) and (f) for $MnPS_3$ and $NiPS_3$ elucidate the step by step evolution of these modifications.

generally expected to decrease with a lower number of unpaired electrons [148, 206, 281], this separation provides an indirect probe of the orbital population changes induced by alkali-metal doping. For example, Co^{2+} in $CoPS_3$ adopts a high-spin [Ar] $3d^7$ configuration with three unpaired electrons, consistent with the $2p$ splitting of 16 eV observed for the pristine surface and in agreement with the value reported by *Frost et al.* [282] for other high-spin $3d^7$ systems. After lithium deposition, the splitting is reduced to 15 eV, a decrease of 1 eV. *Frost et al.* reported similar reduced splitting for low-spin $3d^7$ configurations with a total spin $S = 1/2$. Given the known instability of the Co^{2+} oxidation state, we interpret this as a reduction to metallic Co^0 with a [Ar] $3d^9$ configuration, which also yields $S = 1/2$ (analogous to the low-spin $3d^7$ case) [148] . A comparable trend, though less pronounced, is also observed for $NiPS_3$ and $FePS_3$, both showing a measurable but smaller reduction in spin–orbit splitting after lithium adsorption.

Table 6.1: Extracted binding energies of the $2p_{3/2}$ and $2p_{1/2}$ peaks and their shift relative to the pristine surface, as well as the extracted differences for the pristine Δ_{bare} and doped surfaces Δ_{doped}. All values are given in eV.

	$2p_{3/2}$	Shift	$2p_{1/2}$	Shift	Δ_{doped}	Δ_{bare}
$FePS_3$	707.2	-1.7	720.2	-2.1	13	13.4
$CoPS_3$	778.4	-1.3	793.4	-2.3	15	16
$NiPS_3$	853.2	-1.1	870.3	-1.3	17.1	17.3

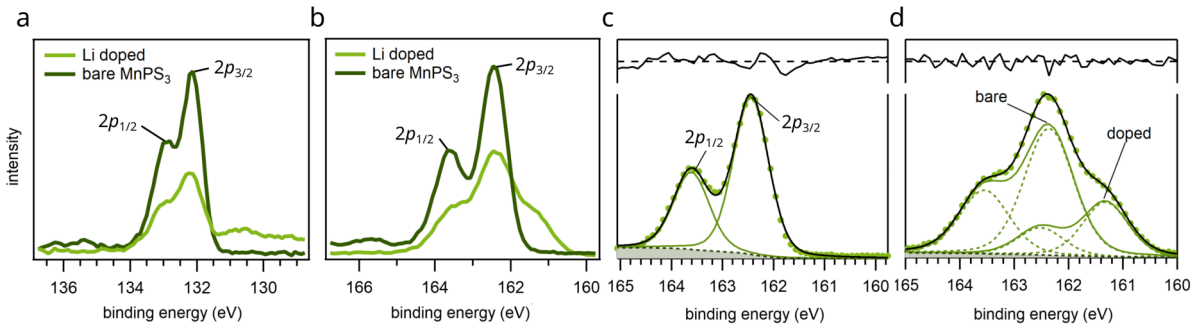

Figure 6.5: (a) and (b) display the P and S $2p$ spectra, showing the doublet split peak into the $2p_{3/2}$ and $2p_{1/2}$ peaks. (c) presents a fit of the S $2p$ spectrum using a doublet, confirming the existence of a singular oxidation state before lithium deposition. Fitting the spectrum after lithium deposition (d) results in a second doublet shifted by 2.1 eV to lower binding energies.

In addition to the reduced oxidation state, we observe a pronounced modification of the satellite structure across all three materials. For example, while $NiPS_3$ exhibits two distinct satellites for both spin-orbit split $2p$ peaks, the satellites located approximately 10 eV above the main peaks (labelled Sat1 and Sat2 in Table 3.1) disappear entirely upon lithium doping. Satellite features are often attributed to ligand-to-metal charge-transfer processes [197], involving either spin-flip interactions within the $3d$ orbitals of the transition-metal ion [283] or interactions with excited states. The observed changes in satellite structure may therefore reflect modifications in the final states of the transition-metal ions. The remaining satellites exhibit energy shifts corresponding to the spin-orbit splitting of the main peaks.

Investigation of the XPS signal originating from the phosphorus and sulphur atoms, specifically the P $2p$ and S $2p$ peaks, reveals no significant changes for $FePS_3$, $CoPS_3$, and $NiPS_3$ (see section A.4). The same holds true for the P $2p$ peak of $MnPS_3$ (Figure 6.5a and b). However, in the case of $MnPS_3$, the S $2p$ spectrum undergoes a notable transformation upon lithium adsorption. As shown in Figure 6.5c, the S $2p$ peak for the bare surface exhibits the typical $2p_{3/2}$ and $2p_{1/2}$ components, which are not fully separated due to the limited energy resolution of the chosen measurement settings. After Li deposition, the overall peak intensity decreases, and an additional shoulder appears at lower binding energies. Figure 6.5g and h present the S $2p$ spectra for the bare and Li-doped $MnPS_3$ surface, respectively. While the bare surface shows a clear double-peak structure corresponding to the $2p_{3/2}$ and $2p_{1/2}$ contributions, fitting the spectrum of the Li-doped surface reveals the presence of two distinct sulphur moieties. One doublet remains at the same energetic position as in the pristine sample, whereas the other is shifted to lower binding energies. This observation indicates that, in the case of $MnPS_3$, the additional electrons predominantly dope the ligand (sulphur) atoms rather than the transition-metal ion.

6.3 Modifications of the Valence Band Structure

After employing XPS to identify key differences under alkali metal adsorption and to classify the four materials into two groups, we now turn to ARPES to examine how lithium influences

the valence band structure. Interestingly, the classification based on XPS does not necessarily hold here, as Fe-, Co-, and $NiPS_3$ display marked differences from each other.

Figure 6.6 shows the energy distribution curves (EDCs) before (dark green) and after lithium adsorption (bright green) for all four MPS_3 compounds. For $MnPS_3$, only negligible changes are observed apart from a general broadening of the main features and the disappearance of the small gap at 1.5 eV below the VBM. The relative intensities of the peaks at 3 and 6.5 eV below the VBM remain unchanged, indicating a clean deposition process without noticeable contamination. In contrast, for $FePS_3$, lithium adsorption modifies the intensity between 2 and 4 eV below the VBM and, more importantly, introduces additional spectral weight above the pristine VBM, extending up to -1 eV with a small plateau followed by an exponential decay. As the VBM is dominated by Fe d states, this suggests a modification of the $3d$-orbital occupation, consistent with the XPS results in section 6.2. This behaviour differs from that typically reported for similar systems, where electron doping populates higher-lying bands and shifts the entire spectrum toward higher binding energies (due to the Fermi level being fixed to the detector) [276]. Notably, such a rigid shift is absent in all four samples investigated here.

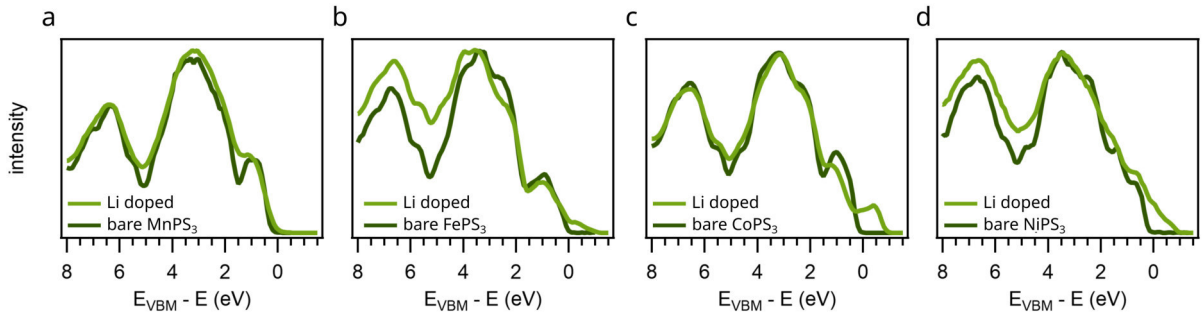

Figure 6.6: Energy distribution curves (EDCs) before (dark green) and after Li doping (bright green) of (a) $MnPS_3$, (b) $FePS_3$, (c) $CoPS_3$, and (d) $NiPS_3$. $MnPS_3$ shows no significant modifications apart from slight broadening, whereas the other three materials display additional intensity above the pristine VBM. $CoPS_3$ exhibits the most pronounced changes, with a new peak-like feature extending well above the pristine VBM and a shift of the valence band maximum relative to deeper-lying states.

The strongest and most structured response is observed in the valence band of $CoPS_3$. Similar to $MnPS_3$, this sample shows no change in the relative intensity of the two lowest-energy main features, indicating a clean and well-controlled deposition of the lithium atoms. However, in contrast to $FePS_3$, the modifications near the VBM are more pronounced. Again, additional intensity appears above the pristine VBM, structured with a distinct peak at -0.6 eV. Moreover, the lithium-induced electrons also modify the upper part of the valence band: the previously well-separated feature with a peak around 1 eV shifts to higher energies and transforms into a more shoulder-like structure. As will be shown later in the angle-resolved measurements, these changes are indeed related to modifications of the bands near the VBM, induced by the altered occupation of the Co $3d$ orbitals.

Finally, the EDC of Li-doped $NiPS_3$, shown in Figure 6.6d, also exhibits significant additional

Table 6.2: Changes in the work function Φ after Li deposition for all four MPS_3 compounds.

	$MnPS_3$	$FePS_3$	$CoPS_3$	$NiPS_3$
Φ_{bare} (eV)	5.45	5.6	5.7	5.25
Φ_{Li} (eV)	5.05	4.77	4.49	3.81

intensity extending up to 1 eV above the pristine VBM. However, the overall spectral shape appears more washed out after lithium deposition and does not display distinct features in this energy range. The resulting spectrum resembles that reported by Cao *et al.* [233] for potassium-doped $NiPS_3$, where the extra intensity was assigned to alkali defect states and the occupied conduction band. Nevertheless, as will be shown in the ARPES data presented later, the momentum-resolved spectra reveal no discernible bands or momentum-dependent features in this energy range, in contrast to $FePS_3$ and $CoPS_3$.

Based on the total energy width of the spectra for the different bare and doped compounds, we can also evaluate the change in work function induced by electron doping. The energetic differences vary strongly between the different transition-metal ions, ranging from the smallest variation for $MnPS_3$ to the largest for $NiPS_3$. The extracted work function values before (Φ_{bare}) and after lithium doping (Φ_{Li}) are listed in Table 6.2. This change in work-function is mediated by the positively charge alkali metal ion and the induced mirror charge on the surface, forming a dipole that subsequently lowers the work function [284].

The observations described above are corroborated by PDOS calculations performed using the parameters from the benchmark on the clean surfaces presented in section 3.3. The DFT calculations are again performed in collaboration with the Ruhr University of Bochum by Preeti Bhumla and Prof. Silvana Botti. Figure 6.7a-d show the PDOS for the bare (top) and lithium-doped (bottom) samples. Consistent with the experimental results, lithium intercalation in $MnPS_3$ leads to no major changes apart from a general broadening. Additionally, the absence of energetic shifts in the spectrum suggests that the oxidation state of Mn remains unchanged, in agreement with the XPS results. This stability can be attributed to the half-filled $3d^5$ configuration, which is particularly stable due to its electronic symmetry. In $FePS_3$, $CoPS_3$, and $NiPS_3$, the PDOS retains its general shape but exhibits an overall energy shift after lithium adsorption, confirming the oxidation state changes detected by XPS. Furthermore, $CoPS_3$ undergoes a pronounced modifications in its PDOS upon Li doping. As shown in Figure 6.7d, new states appear near the VBM, originating predominantly from Co d and S p hybridized orbitals, which shift slightly to lower energies due to Coulomb interactions with the extra electrons donated by Li. These features are not localized impurity states from Li itself but rather reflect a reorganization of the $CoPS_3$ electronic structure induced by doping. This suggests that Li alters the covalent Co-S interaction, potentially influencing both electronic dispersion and magnetic exchange interactions.

Additionally, the signal near the VBM, which has strong contributions from the Co $3d$ states, undergoes a pronounced shift to higher binding energy, with the main Co $3d$ contributions now located approximately 1.8 eV deeper in binding energy. This shift indicates a change in the oxidation state of the Co atoms, consistent with the modifications observed in the Co $2p$ core-level spectra. A similar shift is observed experimentally, though to a lesser extent. We attribute

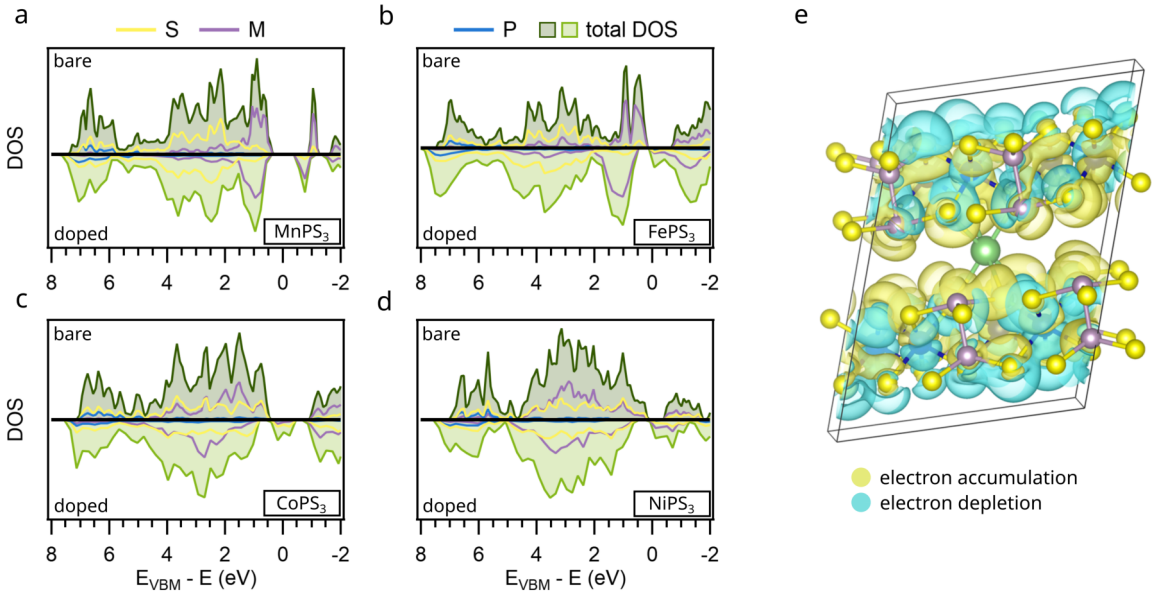

Figure 6.7: Computational results for Li-doped systems. (a)-(d) Comparison of the calculated EDCs for the bare and Li-doped Mn-, Fe-, Co-, and $NiPS_3$ surfaces, respectively. In agreement with the experimental observations, $MnPS_3$ shows no significant changes after Li deposition. In contrast, the other three compounds display a shift of the entire band structure, consistent with the previously discussed changes in oxidation state. $CoPS_3$ additionally exhibits a redistribution of the metal-ion contributions and the emergence of new in-gap states near the pristine VBM. (e) Charge density difference for Li-doped $CoPS_3$, with yellow and cyan regions indicating electron accumulation and depletion after doping, respectively.

this discrepancy to the theoretical assumption of a full electron donation per unit cell, whereas in the experiment the actual number of donated electrons per unit cell is unknown but likely less than one. To test this hypothesis, we performed a similar experiment using caesium atoms instead of lithium, where the expected electron donation per unit cell should be smaller due to the larger atomic size of caesium. This experiment will be discussed later together with the angle-resolved measurements.

To gain insights into the charge transfer upon doping, we plotted the charge density difference of the Li-doped system in Figure 6.7e, calculated as:

$$\Delta\rho = \rho_{Li/CoPS_3} - \rho_{CoPS_3} - \rho_{Li} \tag{6.1}$$

where $\rho_{Li/CoPS_3}$, ρ_{CoPS_3}, and ρ_{Li} are the charge densities of the Li-doped CoPS3 system, pristine $CoPS_3$, and isolated Li atom, respectively. In the plot, yellow and cyan regions represent electron accumulation and depletion, respectively. The Li atom donates its charge to the $CoPS_3$ lattice, and the resulting electron density is redistributed, particularly toward Co and S atoms. This confirms charge transfer and the interaction between Li and the host lattice. To quantify the charge transferred from the Li atom, we performed a Bader charge analysis. The results show that Li donates approximately 0.89 e^-, which is gained by the $CoPS_3$ lattice. Most of this

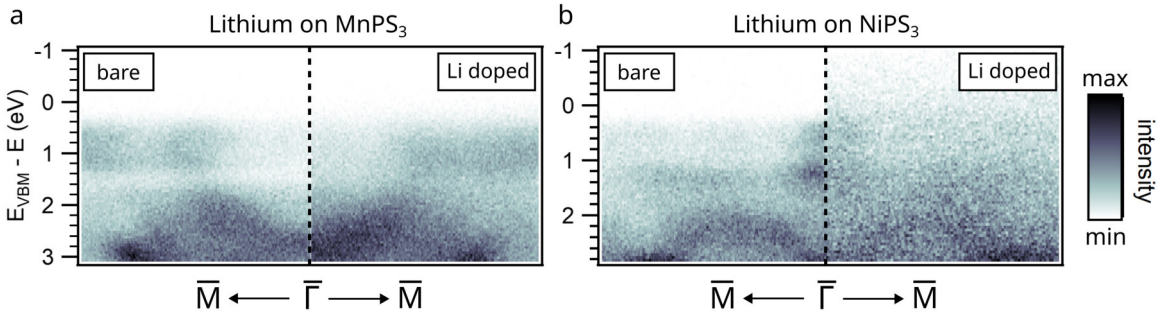

Figure 6.8: Extracted band structures from ARPES measurements of bare and Li-doped (a) $MnPS_3$ and (b) $NiPS_3$ along the $\overline{M}$ - $\overline{\Gamma}$ - $\overline{M}$ path. $MnPS_3$ shows no significant modification of the band structure, apart from minor broadening and a closing of the gap around 1.5 eV. In contrast, $NiPS_3$ exhibits additional photoemission intensity above the pristine VBM, extending up to -1 eV after doping.

charge is delocalized over the neighbouring Co and S atoms, indicating a strong interaction and redistribution of electron density within the lattice.

After identifying the alkali-metal-induced changes in the angle-integrated spectra, supported by PDOS calculations, momentum microscopy provides further insight into the band structure along specific high-symmetry directions. Figure 6.8 presents two cuts along the $\overline{M}$ - $\overline{\Gamma}$ - $\overline{M}$ path for the bare and Li-covered surfaces of $MnPS_3$ and $NiPS_3$ in an energy range up to 2 eV below the VBM.

For $MnPS_3$ (Figure 6.8a), no substantial modifications to the band structure are observed, aside from a general broadening that closes the gap around 1.4 eV. The overall band dispersion in the examined energy range remains unchanged. In contrast, the comparison for $NiPS_3$ (Figure 6.8b) reveals pronounced differences. Consistent with earlier observations, a strong increase in intensity is detected up to 1 eV above the pristine surface's VBM. However, this additional signal lacks any discernible structure in either the EDCs or the momentum-resolved band dispersion. The $NiPS_3$ bands themselves do not exhibit measurable shifts or structural changes, but rather appear more diffuse. Furthermore, momentum-resolved maps at various energies above the VBM show no clear patterns.

While a previous study on potassium-doped $NiPS_3$ [233] attributed similar features to alkali-related defect states and the occupied conduction band, our data do not allow us to draw the same conclusion. This discrepancy may be related to the higher purity of our AMD source. As will be shown in the following section for $CoPS_3$ and $FePS_3$, momentum-dependent features can indeed be observed under comparable conditions. The exact origin of the additional intensity in Li-doped $NiPS_3$ therefore remains inconclusive.

A different situation occurs for $FePS_3$ and $CoPS_3$, presented in Figure 6.9 in the same format as for the other two compounds, together with momentum maps extracted at selected energies. Figure 6.9a reveals two notable modifications for Li-doped $CoPS_3$. First, the feature located near $\overline{\Gamma}$ between 0.2 and 1.2 eV for the pristine surface (highlighted in pink) appears to shift to higher binding energy by approximately 400 meV. Interestingly, this shift is not observed for

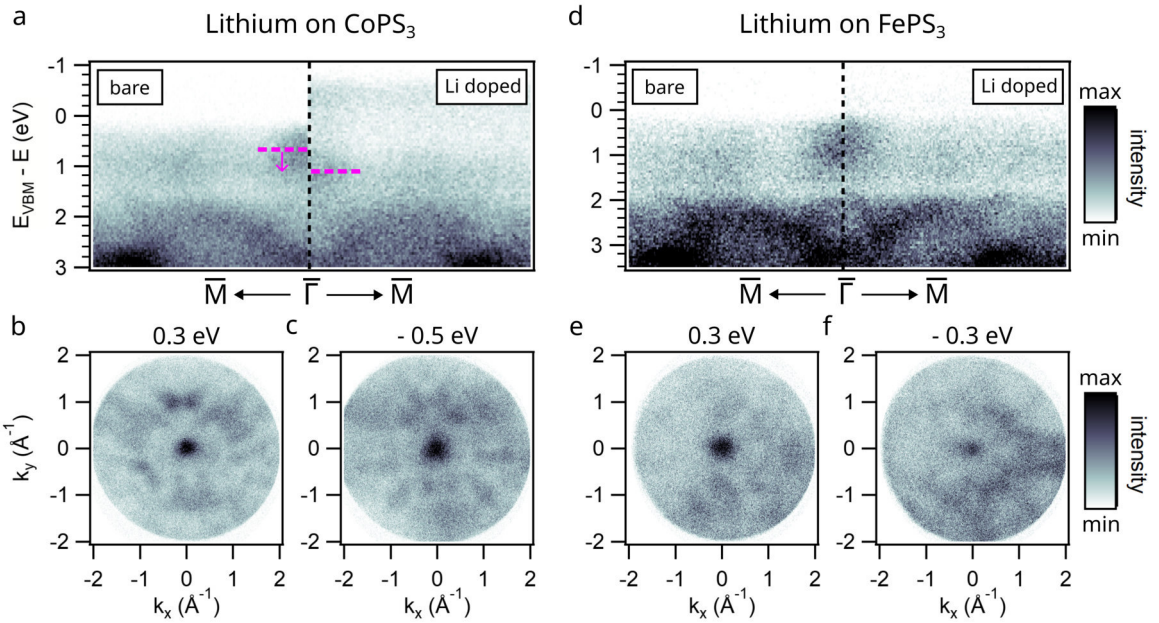

Figure 6.9: Lithium-induced modifications to the valence band structure of $CoPS_3$ and $FePS_3$. (a) Extracted band structure of Li-doped $CoPS_3$ along the $\overline{M}$ - $\overline{\Gamma}$ - $\overline{M}$ path, compared to the pristine surface. Pink markers indicate the shift of the feature near $\overline{\Gamma}$. (b) and (c) display momentum maps for Li-doped $CoPS_3$, extracted below and above the pristine VBM, respectively. (d), (e), and (f) show the corresponding band structure comparison and momentum maps for Li-doped $FePS_3$.

the parabolic band between 1.8 and 3 eV (marked with a blue dashed line). Based on the EDC and PDOS results, this shift is most likely related to modifications of bands originating from the Co 3*d* states.

In addition to changes in the pre-existing states, lithium deposition also induces new states above the pristine VBM, where a weak yet discernible momentum dependence is observed, with intensity concentrated near the $\overline{\Gamma}$ point. Taking advantage of the momentum-resolved capabilities of our analyzer, we can directly investigate whether this additional signal exhibits dispersion. The momentum map extracted at 0.5 eV above the pristine VBM for Li-doped $CoPS_3$ (Figure 6.9b) indeed reveals clear dispersive features. A comparison with the pristine Fermi surface indicates certain similarities, but also shows that the observed intensity is not simply a replica of existing states. A similar behaviour is found for Li-doped $FePS_3$, where the doped surface displays additional intensity above the pristine VBM (Figure 6.9d), though of significantly lower strength. Again, the momentum maps reveal dispersive features distinct from the bands near the Fermi level (Figure 6.9e and f).

To gain further insights into the observed modifications, particularly for $FePS_3$ and $CoPS_3$, we calculated the band structures for all four materials in their bare and lithium-doped states. The results, shown in Figure 6.10, confirm most of our experimental observations. First, $MnPS_3$ displays only a negligible shift in the valence band, with little to no modification upon lithium deposition. In contrast, $FePS_3$ and $NiPS_3$ exhibit a pronounced shift accompanied by a reduction in the band gap energy. When compared with the calculations on potassium-doped $NiPS_3$

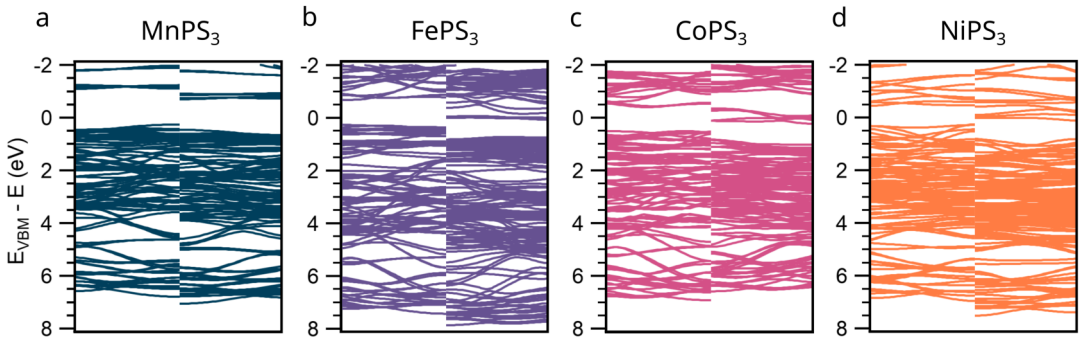

Figure 6.10: Comparison of the computational bandstructure for the bare and Li doped surface of (a) $MnPS_3$, (b) $FePS_3$, (c) $CoPS_3$, and (d) $NiPS_3$

presented by Cao *et al.* [233], our results differ from their findings for the highest potassium doping level reported. However, their work also shows that the modifications to the band structure depend strongly on the doping level, which could explain the deviations observed in our calculations. Additionally, for lithium-doped $FePS_3$, we observe a reduction of the band gap by 250 meV, suggesting that the dispersive states observed in the ARPES measurements could originate from occupation of the conduction band. Nevertheless, we do not observe metallic behaviour in the sample, in contrast to the predictions by Wu *et al.*, who reported a fully metallic state after lithium doping [80]. This discrepancy is most likely related to the different systems studied, as they focused exclusively on single-layer $FePS_3$.

The most pronounced modifications are again observed for $CoPS_3$. Pristine $CoPS_3$ exhibits semiconducting behaviour characterized by a finite band gap. Upon lithium doping, the Fermi level shifts upward, indicative of *n*-type doping. This shift closes the band gap and leads to the emergence of bands crossing the Fermi level, suggesting a transition from semiconducting to metallic behaviour. In line with experimental observations, the bands near the Fermi level display a pronounced dispersive character, pointing to enhanced electronic conductivity upon doping. This was further investigated experimentally by cooling the lithium-doped sample. As discussed at the beginning of this thesis, MPS_3 compounds are subject to strong charging effects when cooled, due to their semiconducting nature and low conductivity, which hinders measurements in the antiferromagnetic phase using photoelectron-based techniques. In contrast to the bare surface, the lithium-doped surfaces of $FePS_3$ allowed measurements at 80 K, where the bare surface already exhibited severe energy shifts that completely prevented spectral acquisition. However, no changes in the experimental band structure were observed, even though 80 K lies well below the Néel temperature of both materials. This could be related either to changes in the magnetic properties (as suggested in the literature, where electron doping can modify the Néel temperature [81]) or to the minor deviations expected for $FePS_3$ when crossing into the antiferromagnetic phase [227], which may be difficult to detect given the reduced sample quality after lithium deposition.

As mentioned earlier, the shift of the Co 3*d*-derived bands observed in the ARPES experiments and PDOS calculations showed a significant difference in intensity. We previously attributed this to a lower degree of electron doping in our experiments. To verify this, we repeated the

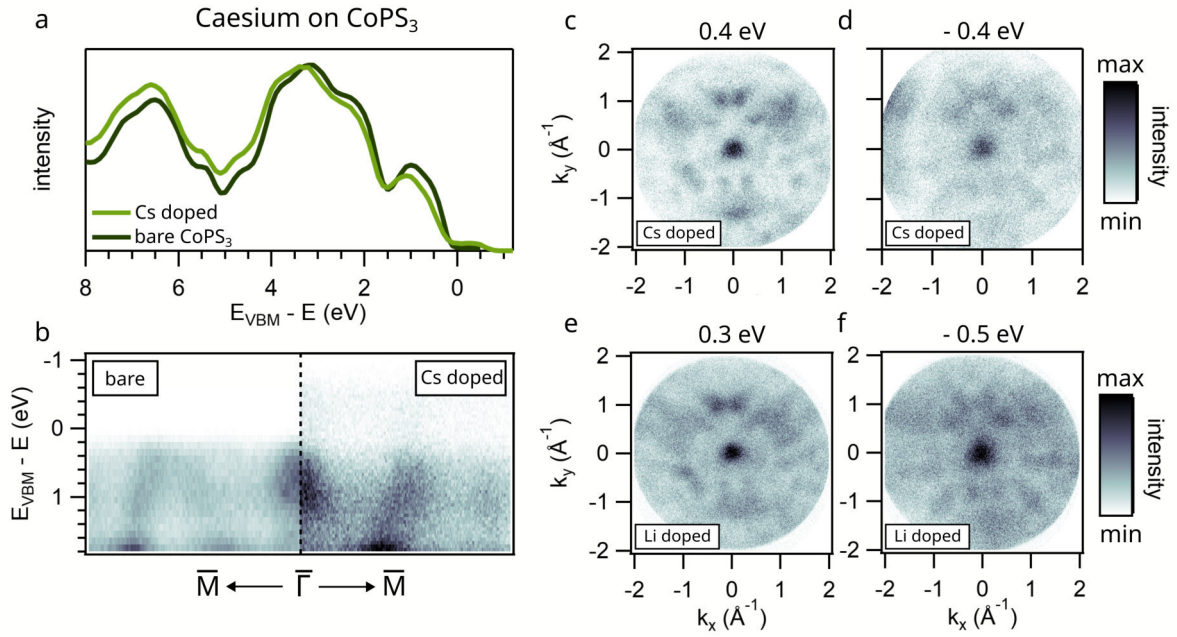

Figure 6.11: ARPES measurements on caesium doped $CoPS_3$. (a) and (b) show a comparison of the bare and lithium doped EDCs and extracted band structure, respectively. (c) and (d) present momentum maps extracted below and above the pristine VBM, showing a similar pattern as observed for the lithium doped system shown in (e) and (f).

experiment using caesium atoms, which are expected to introduce a smaller electron doping due to their larger atomic radius. Figure 6.11a displays the EDCs obtained for both surfaces, revealing a similar response to that observed under lithium doping: a slight shift of the peak closest to the VBM towards higher binding energies, accompanied by additional intensity above the pristine VBM. A comparable trend is also visible in the band structure cuts along the $\overline{\text{M}}$ - $\overline{\Gamma}$ - $\overline{\text{M}}$ path shown in Figure 6.11b, where the central feature around $\overline{\Gamma}$ is shifted by approximately 200 meV, while the features associated with S and P states (at the bottom of the image) remain at the same energy.

6.4 Conclusion

In this chapter, we presented a combined experimental and theoretical investigation of alkali metal doping effects, specifically via lithium and caesium, on various members of the MPS_3 compound family. Using XPS as a central analytical tool, we identified distinct doping behaviours across the different transition metal compositions. The M $2p$ spectra revealed that doping Fe-, Co-, and $NiPS_3$ results in a reduced spin-orbit splitting and the emergence of new lower-binding-energy components, indicating a change in oxidation state with the additional electrons localises in their $3d$-orbitals. Changes in satellite features, particularly their suppression in $NiPS_3$, further point to modifications in the final states and valence-band screening. In contrast, $MnPS_3$ shows no such transition-metal core-level shifts but exhibits a distinct change

in its S $2p$ spectrum, signalling preferential doping of the P_2S_6 ligands. This behaviour can be attributed to the stability conferred by the half-filled d^5 configuration of Mn^{2+}, highlighting the critical influence of the transition metal's electronic configuration on the doping process.

Further insights were obtained through ARPES measurements, where pronounced modifications to the valence band structure were observed upon doping for $FePS_3$, $CoPS_3$ and $NiPS_3$. Notably, the common rigid-band shift expected for alkali-metal doping in layered semiconductors was absent in all four compounds. Instead, $CoPS_3$ and $FePS_3$ developed momentum-dependent states above the pristine VBM, while $NiPS_3$ displayed only diffuse, non-dispersive additional intensity. Additionally, $CoPS_3$ experiences a modification of its states close to the VBM, with PDOS calculations indicating that this is caused by a reorganisation of the electronic states and a possible modification of magnetic exchange pathways In contrast, p-derived bands remained at the same binding energy, evidencing orbital-specific doping effects. The smaller shift of theses states observed by the deposition of caesium confirms the role of reduced electron donation due to the larger ionic size and could potentially explain the large shift observed in the computational band structure due to lower experimental doping level compared to the one-electron-per-cell model used in calculations. Additionally, these results indicate these modifications can be systematically tuned by adjusting the doping concentration.

In contrast, ARPES measurements on lithium doped $MnPS_3$ did not show strong changes besides a broadening of the observed peaks including a closing of the small gap around 1.5 eV below the VBM, which is also confirmed by computational band structure calculations.

To further elucidate the implications of these doping-induced modifications, particularly with respect to magnetic ordering, future studies employing element-specific magnetic probes such as XMCD will be essential. Additionally, time-resolved ARPES could provide valuable insight into the dynamics of excited states, with $FePS_3$ [237] serving as a representative case for exploring applications in ultrafast spintronic devices.

Overall, our findings demonstrate that alkali metal doping constitutes an effective and relatively non-invasive means of tuning the electronic structure of MPS_3 compounds. Without inducing substantial perturbations to the lattice or the baseline electronic states, this approach offers a versatile platform for engineering magnetic and electronic functionalities relevant to next-generation spintronic technologies [5, 30, 285].

7 | Summary and Outlook

In this work, we have undertaken a comprehensive investigation of the electronic structure, excitation dynamics, and tunability of layered antiferromagnetic semiconductors in the MPS_3 family, employing a combination of advanced photoelectron spectroscopy techniques and first-principles calculations. By systematically exploring these materials under different conditions, we have studied both their intrinsic electronic properties in the static and non-equilibrium regimes and the degree to which these properties can be externally modified

In **Figure 2.4**, X-ray photoelectron spectroscopy (XPS) and angle-resolved photoelectron spectroscopy (ARPES) revealed high-quality surfaces with minimal contamination and a complex valence band structure comprising both dispersive and flat bands in all four compounds. We identified three distinct energetic regions within the valence band (VB), with the upper $\approx 2\,\mathrm{eV}$ below the VB maximum showing the strongest material-dependent differences. Density function theory (DFT) calculations confirmed the orbital character of these regions, highlighting the dominant role of metal $3d$ states in $FePS_3$ and $MnPS_3$, and stronger hybridisation with S $2p$ states in $CoPS_3$ and $NiPS_3$. Momentum-resolved measurements further revealed intensity variations between central and neighbouring Brillouin zones, including additional features well reproduced by theory, as well as symmetry deviations likely linked to electronic correlations and local magnetic fluctuations. Shifting our focus to the intrinsic electron dynamics, we used time-resolved ARPES (trARPES) with momentum microscopy to identify and characterise two distinct d-d transitions in $FePS_3$, extracting their lifetimes and momentum-dependent fingerprints. The combination of experiment and nonequilibrium Green's function calculations confirmed the assignment of these excitations and revealed two different decay channels, an exchange-driven virtual hopping between neighbouring sites and spin-orbit-coupling (SOC)-mediated spin-flip process. These results extend the applicability of trARPES beyond exciton dynamics, demonstrating its capability to follow local multiplet excitations in momentum space.

In **Figure 2.4**, we studied the tunability with two different methods. First, the study of organic molecular adsorption by depositing pentacene on $FePS_3$ and $NiPS_3$ demonstrated the formation of well-ordered, physisorbed monolayers. Using photoemission orbital tomography, we identified multiple molecular orbitals. The good agreement between the observed patterns and energy separation with gas-phase calculations indicates the absence of significant charge transfer or hybridisation at the interface. While this limits direct interfacial electronic modulation for these systems, it establishes an essential baseline for future studies employing stronger donor or acceptor molecules. Using the deposition of alkali metals, we demonstrated that electron donation from lithium and caesium leads to distinct doping behaviours, depending on the

transition-metal ion. Using XPS, we observed oxidation-state changes in $FePS_3$, $CoPS_3$, and $NiPS_3$, with electrons localising in $3d$ orbitals, while $MnPS_3$ showed preferential ligand doping. Furthermore, ARPES and DFT calculations revealed doping-induced changes ranging from momentum-dependent in-gap states in $CoPS_3$ and $FePS_3$ to diffuse non-dispersive intensity in $NiPS_3$, while $MnPS_3$ remained largely unaffected. Notably, the commonly expected rigid-band shift was absent in all cases, with orbital- and momentum-specific effects dominating the response. Additional experiments involving caesium deposition confirmed the role of reduced electron donation, indicating the possibility for targeted tuning of the band structure by controlling the alkali metal dose.

Taken together, these results highlight the delicate interplay between the transition-metal electronic configuration, orbital hybridisation, and external perturbations in governing the electronic properties of MPS_3 compounds. They demonstrate that targeted modifications, whether through ultrafast optical excitation, molecular adsorption, or alkali-metal intercalation, can selectively influence orbital and momentum sectors of the band structure without necessarily disrupting the host lattice. This establishes MPS_3 as a versatile platform for exploring correlated-electron phenomena, interfacial coupling, and spin-dependent transport in two-dimensional magnets.

Building on these results, several promising research directions emerge. One possible avenue would be the investigation of influences from alkali-metal doping on the electron dynamics of *d-d* transitions in $FePS_3$. Since doping modifies the occupancy of the *d*-orbitals, such changes should also manifest in the trARPES signal. Furthermore, extending this approach to other systems could provide complementary insights into the role of transition-metal-specific electronic structures. For example, $CoPS_3$ exhibits comparable below-gap transitions but undergoes a more pronounced modification under electron doping. Complementary studies would further focus on the interplay between *d-d* transitions and other quasiparticles. In $FePS_3$, the investigated excitation is expected to couple to a phonon mode at low temperatures [53], which can also be detected with momentum microscopy. This study will become feasible with further improvements in sample preparation that allow the cooling of exfoliated MPS_3 samples without charging effects (see Ref [232]). Similarly, $NiPS_3$ offers an ideal opportunity to explore the connection between *d-d* transitions and exciton generation, as it exhibits two excitonic resonances energetically close to the absorption peak from a below-gap *d-d* transition [117]. Lastly, connecting the results under alkali metal deposition with the observation under molecular adsorption suggest $CoPS_3$ as a promising substrate for further studies involving strong donor molecules, highlighting the potential of combining chemical and molecular doping strategies for enhanced control over the electronic structure. Moving towards different experimental techniques, employing magnetic-sensitive probes such as XMCD in combination with time-resolved spectroscopies will be essential to unravel the coupling between doping, excitations, and magnetic order. Such approaches would not only deepen our understanding of the fundamental interactions in these materials, but advance their potential integration into functional architectures.

In conclusion, this work has presented a detailed study of the electronic ground state of four representative MPS_3 compounds, extended the application of trARPES to multiplet excitations by investigating electron dynamics in $FePS_3$, and provided first insights into targeted modification through molecular adsorption and alkali-metal intercalation. The results demonstrate the versatility of this material class, opening numerous avenues for future investigations and bringing the implementation of MPS_3 compounds in next-generation devices closer to reality.

List of Publications and Conference Contributions

Publications

As First author:

1. J. E. Nitschke, D. L. Esteras, M. Gutnikov, K. Schiller, S. Mañas-Valero, E. Coronado, M. Stupar, G. Zamborlini, S. Ponzoni, J. J. Baldoví, M. Cinchetti, "Valence band electronic structure of the van der Waals antiferromagnet $FePS_3$", *Mater. Today Electron.* 2023, 6, 100061
2. J. E. Nitschke, L. Sternemann, M. Gutnikov, K. Schiller, E. Coronado, A. Omar, G. Zamborlini, C. Saraceno, M. Stupar, A. M. Ruiz, D. L. Esteras, J. J. Baldoví, F. Anders, M. Cinchetti, "Tracing the ultrafast build up and decay of *d-d* transitions in $FePS_3$", *Newton* 2025, 100019
3. J. E. Nitschke, D. M. Janas, S. Ponzoni, M. Capra, E. Molteni, A. Picone, A. Giampietri, A. Ferretti, S. Ma, A. Brambilla, G. Zamborlini, G. Fratesi, M. Cinchetti, "Electronic and structural coupling of pentacene on NiO(001)", *Nanoscale*, 2025
4. J. E. Nitschke, P. Bhumla, T. Willershausen, P. Merisescu, D. Janas, L. Sternemann, M. Gutnikov, V. Mischke, M. Capra, M. Arndt, S. Botti, M.Cinchetti, "Electronic structure reorganization in MPS3 via d-shell-selective alkali metal doping", *ArXiV, under review in Adv. Science*, submitted 2025
5. J. E. Nitschke, L.Sternemann, M.Cinchetti, "Time resolved space charge modulation on Au111", manuscript under preparation

As Co-Author:

1. D. M. Janas, A. Windischbacher, M. S. Arndt, M. Gutnikov, L. Sternemann, D. Gutnikov, T. Willershausen, J. E. Nitschke, K. Schiller, D. Baranowski, V. Feyer, I. Cojocariu, K. Dave, P. Puschnig, M. Stupar, S. Ponzoni, M. Cinchetti, G. Zamborlini, "Metalloporphyrins on oxygen-passivated iron: Conformation and order beyond the first layer", *Inorg. Chim. Acta* 2023, 557, 121705.

2. K. J. Schiller, L. Sternemann, M. Stupar, A. Omar, M. Hoffmann, J. E. Nitschke, V. Mischke, D. M. Janas, S. Ponzoni, G. Zamborlini, C. J. Saraceno, M. Cinchetti, "Time-resolved momentum microscopy with fs-XUV photons at high repetition rates with flexible energy and time resolution", *Sci. Rep.* 2025, 15, 3611.

3. L. Sternemann, D.M. Janas, J.E. Nitschke, K. Schiller, T. Willershausen, L. Becker, A. Isaeva, G. Zamborlini, S. Tappertzhofen, M. Cinchetti, "Fabrication of large-area 2D magnetic semiconductor films for low-temperature ARPES", *2D Mater.* 12 (2025) 035008

4. D. M. Janas, M. S. Arndt, J. E. Nitschke, L. Sternemann, V. M. M. Mischke, V. Feyer, I. Cojocariu, D. Baranowski, A. Sala, A. Windischbacher, P. Puschnig, J. Dreiser, S. Ponzoni, G. Zamborlini, M. Cinchetti, "Interface engineering by design: atomic-scale oxygen control at crystalline MgO/Fe junctions", manuscript in preparation.

5. T. Biktagirov, W. G. Schmidt, K. Schiller, M. Capra, J. E. Nitschke, L. Sternemann, M. Cinchetti, "Intrinsic defects explain n-type conductivity in CrSBr", manuscript in preparation

Conference Contributions

1. ECMolS, **2022**, *Poster contribution*, "Characterization of the NiO/pentacene interface by angle-resolved photoelectron spectroscopy", J. E. Nitschke, D. Janas, M. Capra, A. Giampietri, A. Picone, A. Brambilla, G. Zamborlini, and M. Cinchetti

2. DPG Spring Meeting, **2022**, *Oral contribution*, "Molecular energy level alignment at the NiTPP/O/Cu(100) interface", J.E. Nitschke, H. Sturmeit, I. Cojocariu, V. Feyer, A. Sala, A. Windischbacher, P. <Puschnig, S. Ponzoni, G.<Zamborlini, and M.Cinchetti

3. WEH-Seminar on Spintronics, **2023**, *Poster contribution*, "Angle-resolved photoemission study of transition metal phosphorus trisulfides in the 2D limit", J. E. Nitschke, M. Gutnikov, S. Mañas-Valero, K. Schiller, M. Stupar, S. Ponzoni, G. Zamborlini, and M. Cinchetti

4. GRC on Spindynamics in Nanostructures, **2023**, *Poster contribution + Pitch talk*, "Angle-resolved photoemission study of organic molecules on 2D antiferromagnetic metal phosphorus trisulfides", J. E. Nitschke, D. L. Esteras, M. Gutnikov, S. Mañas-Valero, K. Schiller, M. Stupar, S. Ponzoni, G. Zamborlini, E. Coronado, J. J. Baldoví, and M. Cinchetti

5. WEH-Seminar on van der Waals materials, **2024**, *Oral contribution*, "Unveiling transient dynamics of *d-d* excitations in the van der Waals antiferromagnet $FePS_3$ via time-resolved ARPES", J. E. Nitschke, M. Gutnikov, K. Schiller, D. L. Esteras, J. J. Baldoví, S. Mañas-Valero, E. Coronado, G. Zamborlini, C. Saraceno, M. Stupar, and M. Cinchetti

6. Ultrafast Surface Dynamics, **2024**, *Poster contribution*, "Unveiling transient dynamics of *d-d* excitations in the van der Waals antiferromagnet $FePS_3$ via time-resolved ARPES", J. E. Nitschke, M. Gutnikov, K. Schiller, D. L. Esteras, J. J. Baldoví, S. Mañas-Valero, E. Coronado, G. Zamborlini, C. Saraceno, M. Stupar, F. Anders and M. Cinchetti

List of Abbreviations

1L	Monolayer
2D	Two-Dimensional
5A	Pentacene
AFM	Antiferromagnetic
AM	Alkali Metal
AMD	Alkali Metal Deposition
ARPES	Angle-Resolved Photoelectron Spectroscopy
BBO	Beta Barium Borate
BS	Beam Splitter
BZ	Brillouin Zone
CB	Conduction Band
CBM	Conduction Band Minimum
CEF	Crystal Electric Field
DFT	Density Functional Theory
DFT+U	DFT with Hubbard correction
DLD	Delay Line Detector
DOS	Density of States
EDC	Energy Distribution Curve
ELA	Energy Level Alignment
FM	Ferromagnetic
FT	Fourier Transformation
FWHM	Full Width at Half Maximum
GDD	Group Dispersion Delay
HHG	High-Harmonic Generation
HOMO	Highest Occupied Molecular Orbital
LUMO	Lowest Unoccupied Molecular Orbital

M ..... Transition Metal
MCP ..... Multi Channel Plate
MDC ..... Momentum Distribution Curve
ML ..... Multilayer
MM ..... Momentum Microscope
MO ..... Molecular Orbital
MPC ..... Multi Pass Cell
MPS_3 ..... Metal Phosphorus Trisulfides
OPA ..... Optical Parametric Amplifier
ORG ..... Organic Molecule
P ..... Phosphorus
POT ..... Photoemission Orbital Tomography
S ..... Sulphur
SC ..... Semiconductor
TDC ..... Time to Digital Converter
TMD ..... Transition Metal Dichalcogenide
ToF ..... Time-of-Flight
trARPES ..... Time-Resolved ARPES
UHV ..... Ultra High Vacuum
VB ..... Valence Band
VBM ..... Valence Band Maximum
vdW ..... van der Waals
XPS ..... X-Ray Photoelectron Spectroscopy
XUV ..... Extreme Ultraviolet Radiation

A | Appendix

A.1 XPS Fits of MPS_3 M $2p$ and M $3p$ spectra

Table A.1: Fit results for the $MnPS_3$ Mn $2p$ spectra.

Peak	Area	Binding Energy (eV)	FWHM (eV)	Origin
Peak 1	12 739	639.96	1.236	$2p_{3/2}$ Multiplet
Peak 2	9243	640.96	1.236	$2p_{3/2}$ Multiplet
Peak 3	4016	641.72	0.975	$2p_{3/2}$ Multiplet
Peak 4	3702	642.52	1.236	$2p_{3/2}$ Multiplet
Peak 5	18 840	644.98	3.851	Satellite
Peak 6	5290	651.76	1.643	$2p_{1/2}$ Multiplet
Peak 7	3898	653.02	1.643	$2p_{1/2}$ Multiplet
Peak 8	8026	657.53	4.958	Satellite

Table A.2: Fit results for the $MnPS_3$ Mn $3p$ spectra.

Peak	Area	Binding Energy (eV)	FWHM (eV)	Origin
Peak 1	7691	48.421	1.306	$2p_{3/2}$
Peak 2	3845	49.217	1.411	$2p_{1/2}$
Peak 3	9045	51.257	4.682	Satellite

Table A.3: Fit results for the $FePS_3$ Fe $2p$ spectra.

Peak	Area	Binding Energy (eV)	FWHM (eV)	Origin
Peak 1	30 750	708.51	1.828	$2p_{3/2}$ Multiplet
Peak 2	20 586	709.84	1.828	$2p_{3/2}$ Multiplet
Peak 3	5051	710.97	1.827	$2p_{3/2}$ Multiplet
Peak 4	63 589	713.85	6.489	Satellite
Peak 5	1769	717.4	1.828	$2p_{3/2}$ Multiplet
Peak 6	15 388	721.77	2.019	$2p_{1/2}$ Multiplet
Peak 7	10 688	723.1	2.018	$2p_{1/2}$ Multiplet
Peak 8	1854	724.24	2.021	$2p_{1/2}$ Multiplet
Peak 9	49 886	729.33	7.841	Satellite

Table A.4: Fit results for the $FePS_3$ Fe $3p$ spectra.

Peak	Area	Binding Energy (eV)	FWHM (eV)	Origin
Peak 1	26 961	54.243	2.29	$2p_{3/2}$
Peak 2	13 480	56.232	2.626	$2p_{1/2}$
Peak 3	11 310	58.726	4.109	Satellite

Table A.5: Fit results for the $CoPS_3$ Co $2p$ spectra.

Peak	Area	Binding Energy (eV)	FWHM (eV)	Origin
Peak 1	14 359	771.02	4.437	Auger
Peak 2	19 271	775.8	5.005	Auger
Peak 3	52 785	779.63	1.985	$2p_{3/2}$ Multiplet
Peak 4	19 373	781.26	1.985	$2p_{3/2}$ Multiplet
Peak 5	35 622	783.26	3.779	Satellite
Peak 6	52 490	787.19	5.593	Satellite
Peak 7	3631	793.02	2.341	$2p_{1/2}$ Multiplet
Peak 8	26 392	795.22	2.341	$2p_{1/2}$ Multiplet
Peak 9	9691	796.91	2.341	$2p_{1/2}$ Multiplet
Peak 10	28 951	800.21	5.005	Satellite
Peak 11	26 910	804.24	4.213	Satellite

Table A.6: Fit results for the $CoPS_3$ Co 3*p* spectra.

Peak	Area	Binding Energy (eV)	FWHM (eV)	Origin
Peak 1	6802	60.072	2.068	$2p_{3/2}$
Peak 2	3395	61.482	2.471	$2p_{1/2}$
Peak 3	6392	64.038	3.542	Satellite
Peak 4	1469	67.656	3.048	Satellite

Table A.7: Fit results for the $NiPS_3$ Ni 2*p* spectra.

Peak	Area	Binding Energy (eV)	FWHM (eV)	Origin
Peak 1	29 836	854.28	1.609	$2p_{3/2}$ Multiplet
Peak 2	7280	855.61	1.609	$2p_{3/2}$ Multiplet
Peak 3	2385	857.04	1.609	$2p_{3/2}$ Multiplet
Peak 4	16 414	859.39	2.83	Satellite
Peak 5	11 170	864.19	4.003	Satellite
Peak 6	1107	868.22	1.92	$2p_{1/2}$ Multiplet
Peak 7	12 512	871.55	1.941	$2p_{1/2}$ Multiplet
Peak 8	3817	872.88	1.941	$2p_{1/2}$ Multiplet
Peak 9	17 696	876.11	4.003	Satellite
Peak 10	11 887	881.84	3.617	Satellite

Table A.8: Fit results for the $NiPS_3$ Ni 3*p* spectra.

Peak	Area	Binding Energy (eV)	FWHM (eV)	Origin
Peak 1	5256	67.917	2.011	$2p_{3/2}$
Peak 2	2628	69.714	2.351	$2p_{1/2}$
Peak 3	2684	73.064	3.456	Satellite
Peak 4	1629	79.698	5.422	Satellite

A.2 XPS Fits of MPS_3 S and P $2p$ spectra

Table A.9: Fit results for the different MPS_3 P $2p$ and S $2p$ spectra. The area relation between both peaks was set to 2:1 regarding the $2p_{3/2}$ and $2p_{1/2}$ contribution, respectively.

Material	Peak	Binding Energy (eV)	FWHM (eV)
$MnPS_3$	P $2p_{3/2}$	132.1	0.72
	P $2p_{1/2}$	132.9	0.72
	S $2p_{3/2}$	162.4	0.81
	S $2p_{1/2}$	163.6	0.81
$FePS_3$	P $2p_{3/2}$	132.0	0.53
	P $2p_{1/2}$	132.8	0.53
	S $2p_{3/2}$	162.5	0.81
	S $2p_{1/2}$	163.7	0.81
$CoPS_3$	P $2p_{3/2}$	131.9	0.59
	P $2p_{1/2}$	132.7	0.59
	S $2p_{3/2}$	162.3	0.74
	S $2p_{1/2}$	163.5	0.74
$NiPS_3$	P $2p_{3/2}$	132.1	0.62
	P $2p_{1/2}$	133.0	0.62
	S $2p_{3/2}$	162.7	0.69
	S $2p_{1/2}$	163.9	0.69

A.3 Momentum Maps of Pentacene

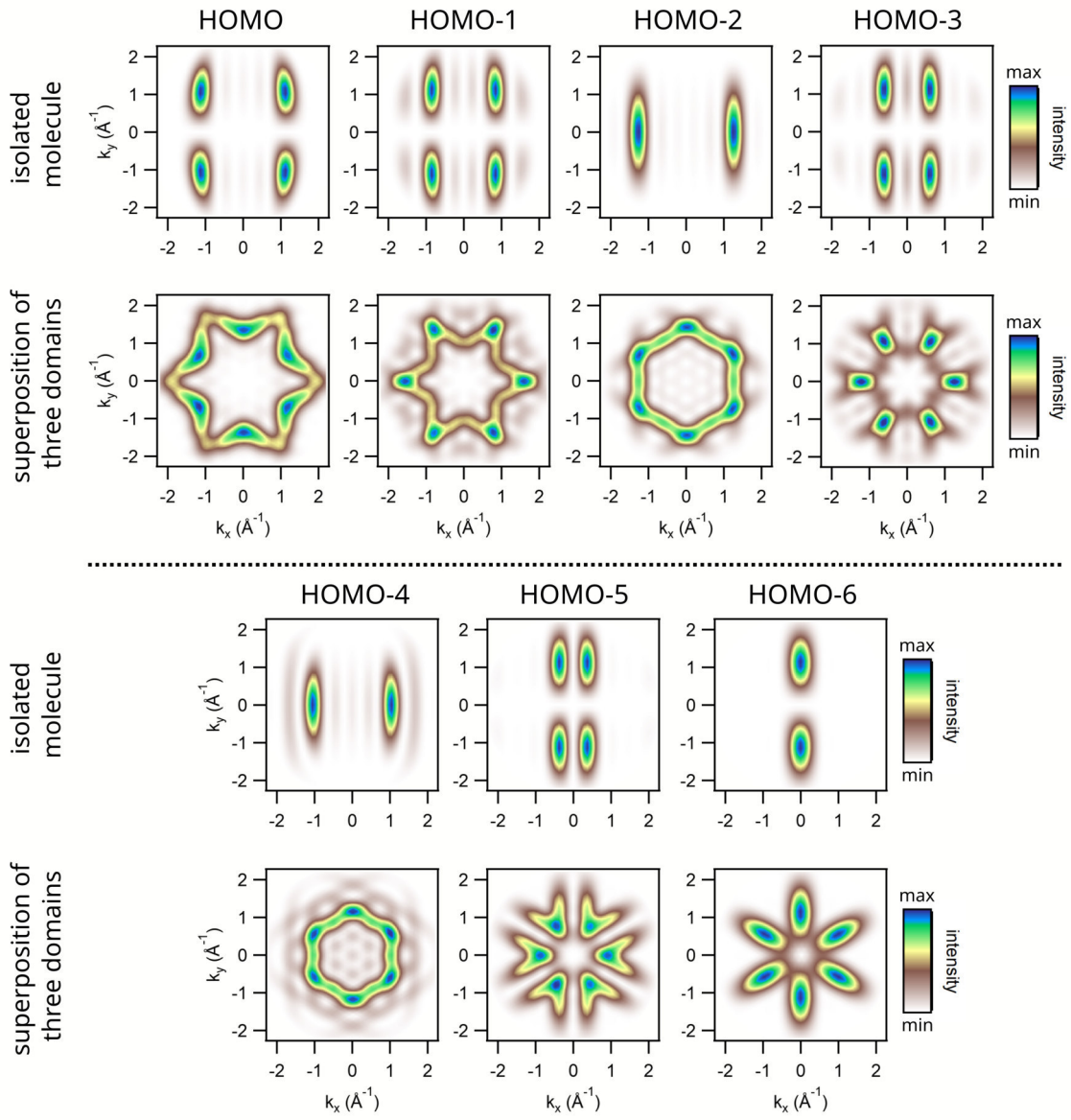

Figure A.1: Isoenergetic patterns for different molecular orbitals of pentacene. The top row visualises the photoemission intensity pattern for the isolated molecule. The bottom row visualises the pattern after applying a 3-fold symmetry, as used in chapter 5. The data for visualisation of the orbitals is taken from Ref [266].

A.4 XPS spectra of Li/MPS_3 S and P $2p$ peaks

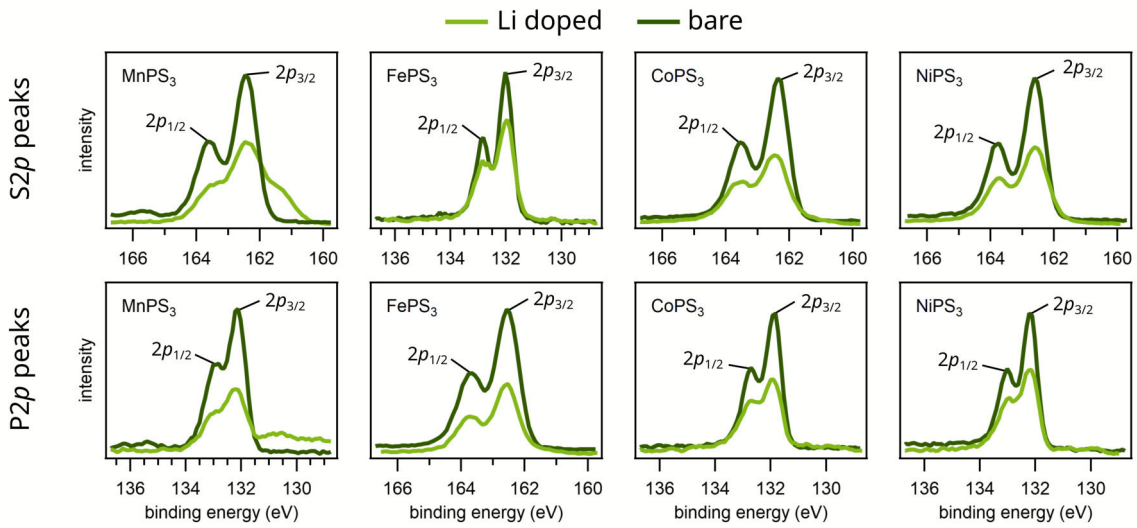

Figure A.2: XPS spectra before (dark green) and after (bright green) Li deposition for the S and P $2p$ peaks of all four MPS_3 compounds.

Bibliography

[1] Atsufumi Hirohata et al. "Review on spintronics: Principles and device applications". In: *Journal of Magnetism and Magnetic Materials* 509 (2020), p. 166711.
DOI: https://doi.org/10.1016/j.jmmm.2020.166711.

[2] A. V. Chumak et al. "Magnon spintronics". In: *Nature Physics* 11.6 (2015), pp. 453–461.
DOI: 10.1038/nphys3347.

[3] Matthias B. Jungfleisch, Wei Zhang, and Axel Hoffmann. "Perspectives of antiferromagnetic spintronics". In: *Physics Letters A* 382.13 (2018), pp. 865–871.
DOI: 10.1016/j.physleta.2018.01.008.

[4] Claude Chappert, Albert Fert, and Frédéric Nguyen Van Dau. "The emergence of spin electronics in data storage". In: *Nature Materials* 6.11 (2007), pp. 813–823.
DOI: 10.1038/nmat2024.

[5] Max C. Lemme et al. "2D materials for future heterogeneous electronics". In: *Nature Communications* 13.1 (2022), p. 1392.
DOI: 10.1038/s41467-022-29001-4.

[6] K. S. Novoselov et al. "Electric Field Effect in Atomically Thin Carbon Films". In: *Science* 306.5696 (2004), pp. 666–669.
DOI: 10.1126/science.1102896.

[7] A K Geim and I V Grigorieva. "Van der Waals heterostructures". In: *Nature* (July 2013), pp. 1–7.
DOI: 10.1038/nature12385.

[8] A. Chaves et al. "Bandgap engineering of two-dimensional semiconductor materials". In: *npj 2D Materials and Applications* 4.1 (2020), p. 29.
DOI: 10.1038/s41699-020-00162-4.

[9] Kenneth S. Burch, David Mandrus, and Je-Geun Park. "Magnetism in two-dimensional van der Waals materials". In: *Nature* 563.7729 (2018), pp. 47–52.
DOI: 10.1038/s41586-018-0631-z.

[10] M Gibertini et al. "Magnetic 2D materials and heterostructures". English. In: *Nature Nanotechnology* 14.5 (May 2019), pp. 1–12.
DOI: 10.1038/s41565-019-0438-6.

[11] Changhua Bao et al. “Light-induced emergent phenomena in 2D materials and topological materials”. In: *Nature Reviews Physics* 4.1 (2022), pp. 33–48.
DOI: 10.1038/s42254-021-00388-1.

[12] Yanping Liu et al. “Spintronics in Two-Dimensional Materials”. In: *Nano-Micro Letters* 12.1 (2020), p. 93.
DOI: 10.1007/s40820-020-00424-2.

[13] Ethan C. Ahn. “2D materials for spintronic devices”. In: *npj 2D Materials and Applications* 4.1 (2020), p. 17.
DOI: 10.1038/s41699-020-0152-0.

[14] Bevin Huang et al. “Electrical control of 2D magnetism in bilayer CrI3”. In: *Nature Nanotechnology* 13.7 (2018), pp. 544–548.
DOI: 10.1038/s41565-018-0121-3.

[15] Cheng Gong et al. “Discovery of intrinsic ferromagnetism in two-dimensional van der Waals crystals”. In: *Nature* 546.7657 (2017), pp. 265–269.
DOI: 10.1038/nature22060.

[16] Sarah Jenkins et al. “Breaking through the Mermin-Wagner limit in 2D van der Waals magnets”. In: *Nature Communications* 13.1 (2022), p. 6917.
DOI: 10.1038/s41467-022-34389-0.

[17] Ping Liu et al. “Recent advances in 2D van der Waals magnets: Detection, modulation, and applications”. In: *iScience* 26.9 (2023), p. 107584.
DOI: 10.1016/j.isci.2023.107584.

[18] David L. Cortie et al. “Two-Dimensional Magnets: Forgotten History and Recent Progress towards Spintronic Applications”. In: *Advanced Functional Materials* 30.18 (2020).
DOI: 10.1002/adfm.201901414.

[19] Youngjun Ahn et al. “Progress and prospects in two-dimensional magnetism of van der Waals materials”. In: *Progress in Quantum Electronics* 93 (2024), p. 100498.
DOI: 10.1016/j.pquantelec.2024.100498.

[20] Vertikasari P. Ningrum et al. “Recent Advances in Two-Dimensional Magnets: Physics and Devices towards Spintronic Applications”. In: *Research* 2020 (2020), p. 1768918.
DOI: 10.34133/2020/1768918.

[21] Michael E. Ziebel et al. “CrSBr: An Air-Stable, Two-Dimensional Magnetic Semiconductor”. In: *Nano Letters* 24.15 (2024), pp. 4319–4329.
DOI: 10.1021/acs.nanolett.4c00624.

[22] Dominika Majchrzak et al. “Experimental and theoretical band alignment study of MPS3 (M = Mn, Fe, Co, Ni) for designing tailored 2D heterostructures”. In: *npj 2D Materials and Applications* 9.1 (2025), p. 53.
DOI: 10.1038/s41699-025-00578-w.

[23] Raymond Brec. "Review on structural and chemical properties of transition metal phosphorous trisulfides MPS3". In: *Solid State Ionics* 22.1 (1986), pp. 3–30.
DOI: 10.1016/0167-2738(86)90055-x.

[24] Sharidya Rahman et al. "Temperature-Dependent Phase Variations in Van Der Waals CdPS3 Revealed by Raman Spectroscopy". In: *Symmetry* 16.2 (2024), p. 140.
DOI: 10.3390/sym16020140.

[25] Yue Sun et al. "Dipolar spin wave packet transport in a van der Waals antiferromagnet". In: *Nature Physics* (2024), pp. 1–7.
DOI: 10.1038/s41567-024-02387-2.

[26] Sergio M. Rezende, Antonio Azevedo, and Roberto L. Rodríguez-Suárez. "Introduction to antiferromagnetic magnons". In: *Journal of Applied Physics* 126.15 (2019), p. 151101.
DOI: 10.1063/1.5109132.

[27] Thomas Olsen. "Antiferromagnetism in two-dimensional materials: progress and computational challenges". In: *2D Materials* 11.3 (2024), p. 033005.
DOI: 10.1088/2053-1583/ad4ef1.

[28] Shuhao Wang et al. "Air Sensitivity and Degradation Evolution of Halide Solid State Electrolytes upon Exposure". In: *Advanced Functional Materials* 32.7 (2022), p. 2108805.
DOI: https://doi.org/10.1002/adfm.202108805.

[29] Qing Hua Wang et al. "The Magnetic Genome of Two-Dimensional van der Waals Materials". In: *ACS Nano* 16.5 (2022), pp. 6960–7079.
DOI: 10.1021/acsnano.1c09150.

[30] Xue Jiang et al. "Recent progress on 2D magnets: Fundamental mechanism, structural design and modification". In: *Applied Physics Reviews* 8.3 (2021), p. 031305.
DOI: 10.1063/5.0039979.

[31] Fengmei Wang et al. "New Frontiers on van der Waals Layered Metal Phosphorous Trichalcogenides". In: *Advanced Functional Materials* 28.37 (2018).
DOI: 10.1002/adfm.201802151.

[32] M. Piacentini et al. "X-ray photoemission and optical spectra of NiPS3, FePS3 and ZnPS3". In: *Chemical Physics* 72.1-2 (1982), pp. 61–71.
DOI: 10.1016/0301-0104(82)87066-3.

[33] M. Piacentini et al. "Optical transitions, XPS, electronic states in NiPS3". In: *Chemical Physics* 65.3 (1982), pp. 289–304.
DOI: 10.1016/0301-0104(82)85205-1.

[34] E. J. K. B. Banda. "Optical absorption of CoPs3 in the energy range 0.73 to 5.40 eV". In: *physica status solidi (b)* 135.1 (1986), K43–K47.
DOI: 10.1002/pssb.2221350153.

[35] M. Piacentini et al. “Study of the valence bands of FePS3 and NiPS3 by resonant-photoemission spectroscopy”. In: *Il Nuovo Cimento D* 4.5 (1984), pp. 444–452.
DOI: 10.1007/bf02450602.

[36] V. Grasso et al. “Optical-absorption spectra of crystal-field transitions in MnPS3 at low temperatures”. In: *Physical Review B* 44.20 (1991), pp. 11060–11066.
DOI: 10.1103/physrevb.44.11060.

[37] P. A. Joy and S. Vasudevan. “Optical-absorption spectra of the layered transition-metal thiophosphates MPS3 (M=Mn, Fe, and Ni)”. In: *Physical Review B* 46.9 (1992), pp. 5134–5141.
DOI: 10.1103/physrevb.46.5134.

[38] P. A. Joy and S. Vasudevan. “Magnetism in the layered transition-metal thiophosphates MPS3 (M=Mn, Fe, and Ni)”. In: *Physical Review B* 46.9 (1992), pp. 5425–5433.
DOI: 10.1103/physrevb.46.5425.

[39] Jae-Ung Lee et al. “Ising-Type Magnetic Ordering in Atomically Thin FePS3”. In: *Nano Letters* 16.12 (2016), pp. 7433–7438.
DOI: 10.1021/acs.nanolett.6b03052.

[40] M J Coak et al. “Tuning dimensionality in van-der-Waals antiferromagnetic Mott insulators TMPS3”. In: *Journal of Physics: Condensed Matter* 32.12 (2020), p. 124003.
DOI: 10.1088/1361-648x/ab5be8.

[41] Elena Voloshina, Yukun Jin, and Yuriy Dedkov. “ARPES studies of the ground state electronic properties of the van der Waals transition metal trichalcogenide CoPS 3”. In: *Chemical Physics Letters* 823 (2023), p. 140511.
DOI: 10.1016/j.cplett.2023.140511.

[42] Asish K. Kundu et al. “Valence band electronic structure of the van der Waals ferromagnetic insulators: VI3 and CrI3”. In: *Scientific Reports* 10.1 (2020), p. 15602.
DOI: 10.1038/s41598-020-72487-5.

[43] Fred A. Stevie and Carrie L. Donley. “Introduction to x-ray photoelectron spectroscopy”. In: *Journal of Vacuum Science & Technology A: Vacuum, Surfaces, and Films* 38.6 (2020), p. 063204.
DOI: 10.1116/6.0000412.

[44] Joshua W. Pinder et al. “Avoiding common errors in X-ray photoelectron spectroscopy data collection and analysis, and properly reporting instrument parameters”. In: *Applied Surface Science Advances* 19 (2024), p. 100534.
DOI: 10.1016/j.apsadv.2023.100534.

[45] Grzegorz Greczynski and Lars Hultman. “A step-by-step guide to perform x-ray photoelectron spectroscopy”. In: *Journal of Applied Physics* 132.1 (2022), p. 011101.
DOI: 10.1063/5.0086359.

[46] Jonathan A. Sobota, Yu He, and Zhi-Xun Shen. “Angle-resolved photoemission studies of quantum materials”. In: *Reviews of Modern Physics* 93.2 (2021), p. 025006.
DOI: 10.1103/revmodphys.93.025006.

[47] Chan-young Lim et al. "Recent technical advancements in ARPES: Unveiling quantum materials". In: *Current Applied Physics* 60 (2024), pp. 43–56.
DOI: 10.1016/j.cap.2024.01.010.

[48] Fabio Boschini, Marta Zonno, and Andrea Damascelli. "Time-resolved ARPES studies of quantum materials". In: *Reviews of Modern Physics* 96.1 (2024), p. 015003.
DOI: 10.1103/revmodphys.96.015003.

[49] MengXing Na, Arthur K. Mills, and David J. Jones. "Advancing time- and angle-resolved photoemission spectroscopy: The role of ultrafast laser development". In: *Physics Reports* 1036 (2023), pp. 1–47.
DOI: 10.1016/j.physrep.2023.09.005.

[50] Ouri Karni, Iliya Esin, and Keshav M. Dani. "Through the Lens of a Momentum Microscope: Viewing Light-Induced Quantum Phenomena in 2D Materials". In: *Advanced Materials* 35.27 (2023), e2204120.
DOI: 10.1002/adma.202204120.

[51] M. Puppin et al. "Excited-state band structure mapping". In: *Physical Review B* 105.7 (2022), p. 075417.
DOI: 10.1103/physrevb.105.075417.

[52] Adam K. Budniak et al. "Spectroscopy and Structural Investigation of Iron Phosphorus Trisulfide—FePS3". In: *Advanced Optical Materials* 10.7 (2022).
DOI: 10.1002/adom.202102489.

[53] Fabian Mertens et al. "Ultrafast Coherent THz Lattice Dynamics Coupled to Spins in the van der Waals Antiferromagnet FePS3". In: *Advanced Materials* 35.6 (2023), e2208355.
DOI: 10.1002/adma.202208355.

[54] Je-Geun Park. "Opportunities and challenges of 2D magnetic van der Waals materials: magnetic graphene?" In: *Journal of Physics: Condensed Matter* 28.30 (2016), p. 301001.
DOI: 10.1088/0953-8984/28/30/301001.

[55] Juan F. Sierra et al. "Van der Waals heterostructures for spintronics and opto-spintronics". In: *Nature Nanotechnology* 16.8 (2021), pp. 856–868.
DOI: 10.1038/s41565-021-00936-x.

[56] Jingxuan Zhou et al. "A cation-exchange approach to tunable magnetic intercalation superlattices". In: *Nature* 643.8072 (2025), pp. 683–690.
DOI: 10.1038/s41586-025-09147-z.

[57] Daniel Hashemi and Hideo Iizuka. "Magnetic properties of 3d transition metal (Sc–Ni) doped plumbene". In: *RSC Adv.* 10 (12 2020), pp. 6884–6892.
DOI: 10.1039/C9RA10337F.

[58] K. Sato et al. "First-principles theory of dilute magnetic semiconductors". In: *Rev. Mod. Phys.* 82 (2 May 2010), pp. 1633–1690.
DOI: 10.1103/RevModPhys.82.1633.

[59] Zhihao Lei et al. “Manipulation of ferromagnetism in intrinsic two-dimensional magnetic and nonmagnetic materials”. In: *Matter* 5.12 (2022), pp. 4212–4273.
DOI: https://doi.org/10.1016/j.matt.2022.11.017.

[60] Xiaoxu Zhao et al. “Engineering covalently bonded 2D layered materials by self-intercalation”. In: *Nature* 581.7807 (2020), pp. 171–177.
DOI: 10.1038/s41586-020-2241-9.

[61] Pim Witte, Annemijn M. van Koten, and Machteld E. Kamminga. “Tuning the magnetic properties of van der Waals materials by intercalation”. In: *Materials Advances* 5.17 (2024), pp. 6702–6718.
DOI: 10.1039/d4ma00539b.

[62] Yang Li et al. “Electrochemical Intercalation in Atomically Thin van der Waals Materials for Structural Phase Transition and Device Applications”. In: *Advanced Materials* 33.6 (2021), p. 2000581.
DOI: https://doi.org/10.1002/adma.202000581.

[63] Manthila Rajapakse et al. “Intercalation as a versatile tool for fabrication, property tuning, and phase transitions in 2D materials”. In: *npj 2D Materials and Applications* 5.1 (2021), p. 30.
DOI: 10.1038/s41699-021-00211-6.

[64] Nicolae Atodiresei et al. “Engineering the magnetic properties of hybrid organic-ferromagnetic interfaces by molecular chemical functionalization”. In: *Physical Review B* 84.17 (2011), p. 172402.
DOI: 10.1103/physrevb.84.172402.

[65] K. Bairagi et al. “Tuning the Magnetic Anisotropy at a Molecule-Metal Interface”. In: *Physical Review Letters* 114.24 (2015), p. 247203.
DOI: 10.1103/physrevlett.114.247203.

[66] Mirko Cinchetti, V Alek Dediu, and Luis E Hueso. “Activating the molecular spinterface”. In: *Nature Materials* 16.5 (May 2017), p. 507 515.
DOI: 10.1038/nmat4902.

[67] Adam R. Brill, Elad Koren, and Graham de Ruiter. “Molecular functionalization of 2D materials: from atomically planar 2D architectures to off-plane 3D functional materials”. In: *Journal of Materials Chemistry C* 9.35 (2021), pp. 11569–11587.
DOI: 10.1039/d1tc01534f.

[68] Cheng Tang, Lei Zhang, and Aijun Du. “Tunable magnetic anisotropy in 2D magnets via molecular adsorption”. In: *Journal of Materials Chemistry C* 8.42 (2020), pp. 14948–14953.
DOI: 10.1039/d0tc04049e.

[69] Kai Yang et al. “Tunable giant magnetoresistance in a single-molecule junction”. In: *Nature Communications* 10.1 (2019), p. 3599.
DOI: 10.1038/s41467-019-11587-x.

[70] Junhyeon Jo et al. “Exchange Bias in Molecule/Fe3GeTe2 van der Waals Heterostructures via Spinterface Effects”. In: *Advanced Materials* 34.21 (2022), p. 2200474.
DOI: https://doi.org/10.1002/adma.202200474.

[71] Jens Brede et al. “Long-range magnetic coupling between nanoscale organic–metal hybrids mediated by a nanoskyrmion lattice”. In: *Nature Nanotechnology* 9.12 (2014), pp. 1018–1023.
DOI: 10.1038/nnano.2014.235.

[72] Sebastian Jakobs et al. “Controlling the Spin Texture of Topological Insulators by Rational Design of Organic Molecules”. English. In: *Nano Letters* 15.9 (Sept. 2015), pp. 6022–6029.
DOI: 10.1021/acs.nanolett.5b02213.

[73] Rabindra Basnet and Jin” Hu. “Understanding and tuning magnetism in van der Waals-type metal thiophosphates””. In: *Nanoscale”* 16” (34” 2024”), 15851–15883”.
DOI: 10.1039/D4NR01577K".

[74] Cong Li et al. “Molecular intercalation in the van der Waals antiferromagnets FePS3 and NiPS3”. In: *Physical Review B* 109.18 (2024), p. 184407.
DOI: 10.1103/physrevb.109.184407.

[75] Adi Harchol et al. “Tuning magnetic and optical properties in Mn x Zn1−x PS3 single crystals by the alloying composition”. In: *2D Materials* 11.3 (2024), p. 035010.
DOI: 10.1088/2053-1583/ad3e07.

[76] Safe Khan et al. “Spin-Glass States Generated in a van der Waals Magnet by Alkali-Ion Intercalation”. In: *Advanced Materials* 36.36 (2024), p. 2400270.
DOI: https://doi.org/10.1002/adma.202400270.

[77] Cong Li et al. “Molecular intercalation in the van der Waals antiferromagnets FePS3 and NiPS3”. In: *Physical Review B* 109.18 (2024), p. 184407.
DOI: 10.1103/physrevb.109.184407.

[78] Peter Puschnig et al. “Reconstruction of Molecular Orbital Densities from Photoemission Data”. In: *Science* 326.5953 (2009), pp. 702–706.
DOI: 10.1126/science.1176105.

[79] Dong Chen et al. “Manipulating two-dimensional magnetism and electronic structure of van der Waals FePS3 bilayers via Li-ion intercalation”. In: *Materials Today Communications* 42 (2025), p. 111432.
DOI: 10.1016/j.mtcomm.2024.111432.

[80] Xiaoping Wu et al. “Tunable band gap and transition between antiferromagnetism and ferromagnetism by surface adsorption in single-layer FePS3”. In: *Journal of Materials Science: Materials in Electronics* 33.4 (2022), pp. 1871–1876.
DOI: 10.1007/s10854-021-07386-0.

[81] Dinesh Upreti et al. “Tuning magnetism in Ising-type van der Waals magnet FePS3 by lithium intercalation”. In: *Journal of Physics: Condensed Matter* 37.13 (2025), p. 135805.
DOI: 10.1088/1361-648x/adb232.

[82] Rabindra Basnet et al. “Emergence of ferrimagnetism in Li-intercalated NiPS3”. In: *Journal of Physics: Condensed Matter* 34.43 (2022), p. 434002.
DOI: 10.1088/1361-648x/ac8a81.

[83] Peter Y. Yu and Manuel Cardona. *Fundamentals of Semiconductors: Physics and Materials Properties*. 3rd ed. Berlin: Springer, 2005.

[84] Charles Kittel. *Introduction to Solid State Physics*. 8th ed. Hoboken, NJ: Wiley, 2005.

[85] Rudolf Gross and Achim Marx. *Festkoerperphysik*. 4, revised and extended. Berlin and Boston: De Gruyter Oldenbourg, 2022.
DOI: 10.1515/9783110782394.

[86] Aleksandr Rodin et al. "Collective excitations in 2D materials". In: *Nature Reviews Physics* 2.10 (2020), pp. 524–537.
DOI: 10.1038/s42254-020-0214-4.

[87] Alexey Chernikov et al. "Exciton Binding Energy and Nonhydrogenic Rydberg Series in Monolayer WS_2". In: *Phys. Rev. Lett.* 113 (7 Aug. 2014), p. 076802.
DOI: 10.1103/PhysRevLett.113.076802.

[88] Shane Smolenski et al. "Large exciton binding energy in a bulk van der Waals magnet from quasi-1D electronic localization". In: *Nature Communications* 16.1 (2025), p. 1134.
DOI: 10.1038/s41467-025-56457-x.

[89] Ziliang Ye et al. "Probing excitonic dark states in single-layer tungsten disulphide". In: *Nature* 513.7517 (2014), pp. 214–218.
DOI: 10.1038/nature13734.

[90] Yeongsu Cho, Samuel M. Greene, and Timothy C. Berkelbach. "Simulations of Trions and Biexcitons in Layered Hybrid Organic-Inorganic Lead Halide Perovskites". In: *Phys. Rev. Lett.* 126 (21 May 2021), p. 216402.
DOI: 10.1103/PhysRevLett.126.216402.

[91] Peter Q. Liu, John L. Reno, and Igal Brener. "Quenching of Infrared-Active Optical Phonons in Nanolayers of Crystalline Materials by Graphene Surface Plasmons". In: *ACS Photonics* 5.7 (2018), pp. 2706–2711.
DOI: 10.1021/acsphotonics.8b00421.

[92] Thomas P. Devereaux and Rudi Hackl. "Inelastic light scattering from correlated electrons". In: *Reviews of Modern Physics* 79.1 (2007), pp. 175–233.
DOI: 10.1103/revmodphys.79.175.

[93] R. Merlin. "Generating coherent THz phonons with light pulses". In: *Solid State Communications* 102.2-3 (1997), pp. 207–220.
DOI: 10.1016/s0038-1098(96)00721-1.

[94] Weijie Zhao et al. "Lattice dynamics in mono- and few-layer sheets of WS 2 and WSe 2". In: *Nanoscale* 5.20 (2013), pp. 9677–9683.
DOI: 10.1039/c3nr03052k.

[95] A. Molina-Sánchez and L. Wirtz. "Phonons in single-layer and few-layer MoS_2 and WS_2". In: *Phys. Rev. B* 84 (15 Oct. 2011), p. 155413.
DOI: 10.1103/PhysRevB.84.155413.

[96] Zhiying Bai et al. "Recent progress in electron–phonon interaction of two-dimensional materials". In: *Nano Select* 3.7 (2022), pp. 1112–1122.
DOI: 10.1002/nano.202100367.

[97] Youn Jue Bae et al. "Exciton-coupled coherent magnons in a 2D semiconductor". In: *Nature* 609.7926 (2022), pp. 282–286.
DOI: 10.1038/s41586-022-05024-1.

[98] F. Albert Cotton. *Chemical Applications of Group Theory*. 3rd. New York: Wiley-Interscience, 1990.

[99] R. V. Mikhaylovskiy et al. "Resonant Pumping of d-d Crystal Field Electronic Transitions as a Mechanism of Ultrafast Optical Control of the Exchange Interactions in Iron Oxides". In: *Physical Review Letters* 125.15 (2020), p. 157201.
DOI: 10.1103/physrevlett.125.157201.

[100] Chikara Sugiura, Atsushi Kamata, and Shun-ichi Nakai. "X-Ray Spectroscopic Investigation of the Valence-Band Structure of Layered Compounds MPS 3 (M = Mn, Fe, Ni, Zn, Mg)". In: *Journal of the Physical Society of Japan* 65.7 (1996), pp. 2152–2157.
DOI: 10.1143/jpsj.65.2152.

[101] Jonah Elias Nitschke et al. "Electronic structure reorganization in MPS3 via d-shell-selective alkali metal doping". In: *arXiv, under Review in Advanced Science* (2025).
DOI: 10.48550/arxiv.2506.01527.

[102] Ke-zhao Du et al. "Weak Van der Waals Stacking, Wide-Range Band Gap, and Raman Study on Ultrathin Layers of Metal Phosphorus Trichalcogenides". In: *ACS Nano* 10.2 (2016), pp. 1738–1743.
DOI: 10.1021/acsnano.5b05927.

[103] Juntao Yang et al. "Electronic, magnetic and optical properties of MnPX 3 (X = S, Se) monolayers with and without chalcogen defects: a first-principles study". In: *RSC Advances* 10.2 (2020), pp. 851–864.
DOI: 10.1039/c9ra09030d.

[104] Bheema Lingam Chittari et al. "Electronic and magnetic properties of single-layer MPX3 metal phosphorous trichalcogenides". In: *Physical Review B* 94.18 (2016), p. 184428.
DOI: 10.1103/physrevb.94.184428.

[105] Hüfner. *Photoelectron Spectroscopy (3rd Edition)*.

[106] J. Hubbard. "Electron correlations in narrow energy bands III. An improved solution". In: *Proceedings of the Royal Society of London. Series A. Mathematical and Physical Sciences* 281.1386 (1964), pp. 401–419.
DOI: 10.1098/rspa.1964.0190.

[107] N F Mott. "The Basis of the Electron Theory of Metals, with Special Reference to the Transition Metals". In: *Proceedings of the Physical Society. Section A* 62.7 (July 1949), p. 416.
DOI: 10.1088/0370-1298/62/7/303.

[108] J. Zaanen, G. A. Sawatzky, and J. W. Allen. "Band gaps and electronic structure of transition-metal compounds". In: *Phys. Rev. Lett.* 55 (4 July 1985), pp. 418–421.
DOI: 10.1103/PhysRevLett.55.418.

[109] Vladlen Zhukov, Santiago Alvarez, and Dmitrii Novikov. "Electronic band structure of the magnetic layered semiconductors MPS3 (M = Mn, Fe and Ni)". In: *Journal of Physics and Chemistry of Solids* 57.5 (1996), pp. 647–652.
DOI: 10.1016/0022-3697(95)00203-0.

[110] Yuriy Dedkov, Yefei Guo, and Elena Voloshina. "Progress in the studies of electronic and magnetic properties of layered MPX3 materials (M: transition metal, X: chalcogen)". In: *Electronic Structure* 5.4 (2023), p. 043001.
DOI: 10.1088/2516-1075/acfa4e.

[111] E. Ressouche et al. "Magnetoelectric MnPS3 as a candidate for ferrotoroidicity". In: *Physical Review B* 82.10 (2010), p. 100408.
DOI: 10.1103/physrevb.82.100408.

[112] Xingzhi Wang et al. "Electronic Raman scattering in the 2D antiferromagnet NiPS3". In: *Science Advances* 8.2 (2022), eabl7707.
DOI: 10.1126/sciadv.abl7707.

[113] Tae Yun Kim and Cheol-Hwan Park. "Magnetic Anisotropy and Magnetic Ordering of Transition-Metal Phosphorus Trisulfides". In: *Nano Letters* 21.23 (2021), pp. 10114–10121.
DOI: 10.1021/acs.nanolett.1c03992.

[114] Maria Ramos et al. "Photoluminescence Enhancement by Band Alignment Engineering in MoS2/FePS3 van der Waals Heterostructures". In: *ACS Applied Materials & Interfaces* 14.29 (2022), pp. 33482–33490.
DOI: 10.1021/acsami.2c05464.

[115] Qi Zhang et al. "Observation of Giant Optical Linear Dichroism in a Zigzag Antiferromagnet FePS3". In: *Nano Letters* 21.16 (2021), pp. 6938–6945.
DOI: 10.1021/acs.nanolett.1c02188.

[116] D. Khusyainov et al. "Ultrafast laser-induced spin–lattice dynamics in the van der Waals antiferromagnet CoPS3". In: *APL Materials* 11.7 (2023), p. 071104.
DOI: 10.1063/5.0146128.

[117] Ching-Hwa Ho, Tien-Yao Hsu, and Luthviyah Choirotul Muhimmah. "The band-edge excitons observed in few-layer NiPS3". In: *npj 2D Materials and Applications* 5.1 (2021), p. 8.
DOI: 10.1038/s41699-020-00188-8.

[118] Qishuo Tan et al. "Charge-transfer-enhanced d–d emission in antiferromagnetic NiPS3". In: *Applied Physics Reviews* 9.4 (2022), p. 041406.
DOI: 10.1063/5.0107065.

[119] Nashra Pistawala et al. "Probing electron–phonon coupling in magnetic van der Waals material NiPS3: A non-magnetic site-dilution study". In: *2D Materials* 11.2 (2024), p. 025035.
DOI: 10.1088/2053-1583/ad2f44.

[120] Slawomir Braun, William R. Salaneck, and Mats Fahlman. "Energy-Level Alignment at Organic/Metal and Organic/Organic Interfaces". In: *Advanced Materials* 21.14-15 (2009), pp. 1450–1472.
DOI: 10.1002/adma.200802893.

[121] Markus Clark Scharber and Niyazi Serdar Sariciftci. "Low Band Gap Conjugated Semiconducting Polymers". In: *Advanced Materials Technologies* 6.4 (2021), p. 2000857.
DOI: https://doi.org/10.1002/admt.202000857.

[122] James Ashenhurst. *Pi Molecular Orbitals of Butadiene and How to Draw Them*. Master Organic Chemistry (blog). Last updated December 18, 2024. Accessed August 7, 2025. 2024.

[123] OpenStax and Rice University. *Chemistry*. CC BY 4.0. BC Campus, Mar. 2015.

[124] J.P. Muscat and D.M. Newns. "Chemisorption on metals". In: *Progress in Surface Science* 9.1 (1978), pp. 1–43.
DOI: https://doi.org/10.1016/0079-6816(78)90005-9.

[125] Elizabeth Goiri et al. "Multi-Component Organic Layers on Metal Substrates". In: *Advanced Materials* 28.7 (2016), pp. 1340–1368.
DOI: 10.1002/adma.201503570.

[126] D. M. Newns. "Self-Consistent Model of Hydrogen Chemisorption". In: *Physical Review* 178.3 (1969), pp. 1123–1135.
DOI: 10.1103/physrev.178.1123.

[127] P. W. Anderson. "Localized Magnetic States in Metals". In: *Physical Review* 124.1 (1961), pp. 41–53.
DOI: 10.1103/physrev.124.41.

[128] Giovanni Zamborlini et al. "Multi-orbital charge transfer at highly oriented organic/metal interfaces". In: *Nature Communications* 8.1 (2017), p. 335.
DOI: 10.1038/s41467-017-00402-0.

[129] J K Norsko. "Chemisorption on metal surfaces". In: *Reports on Progress in Physics* 53.10 (1990), p. 1253.
DOI: 10.1088/0034-4885/53/10/001.

[130] Wiebke Bennecke et al. "Disentangling the multiorbital contributions of excitons by photoemission exciton tomography". In: *Nature Communications* 15.1 (2024), p. 1804.
DOI: 10.1038/s41467-024-45973-x.

[131] Yu Li Huang et al. "The organic–2D transition metal dichalcogenide heterointerface". In: *Chemical Society Reviews* 47.9 (2018), pp. 3241–3264.
DOI: 10.1039/c8cs00159f.

[132] Mark T. Greiner et al. “SI - Universal energy-level alignment of molecules on metal oxides”. In: *Nature Materials* (Nov. 2011).

[133] Jonah Elias Nitschke et al. “Electronic and structural coupling of pentacene on NiO(001)”. In: *Nanoscale* 17 (29 2025), pp. 17137–17145.
DOI: 10.1039/D5NR00700C.

[134] Mark T Greiner and Zheng-Hong Lu. “Thin-film metal oxides in organic semiconductor devices: their electronic structures, work functions and interfaces”. In: *NPG Asia Materials* 5.7 (2013), e55–e55.
DOI: 10.1038/am.2013.29.

[135] Raphael Schlesinger et al. “Controlling the work function of ZnO and the energy-level alignment at the interface to organic semiconductors with a molecular electron acceptor”. In: *Physical Review B* 87.15 (2012), p. 155311.
DOI: 10.1103/physrevb.87.155311.

[136] R. Schlesinger et al. “Efficient light emission from inorganic and organic semiconductor hybrid structures by energy-level tuning”. In: *Nature Communications* 6.1 (2015), p. 6754.
DOI: 10.1038/ncomms7754.

[137] Yong Xu et al. “Space-Charge Transfer in Hybrid Inorganic-Organic Systems”. In: *Phys. Rev. Lett.* 111 (22 Nov. 2013), p. 226802.
DOI: 10.1103/PhysRevLett.111.226802.

[138] Oliver T. Hofmann and Patrick Rinke. “Band Bending Engineering at Organic/Inorganic Interfaces Using Organic Self-Assembled Monolayers”. In: *Advanced Electronic Materials* 3.6 (2017), p. 1600373.
DOI: https://doi.org/10.1002/aelm.201600373.

[139] Xiaosheng Yang et al. “Momentum-selective orbital hybridisation”. In: *Nature Communications* 13.1 (2022), p. 5148.
DOI: 10.1038/s41467-022-32643-z.

[140] H. Vázquez et al. “Energy level alignment at metal/organic semiconductor interfaces: “Pillow” effect, induced density of interface states, and charge neutrality level”. In: *The Journal of Chemical Physics* 126.14 (Apr. 2007), p. 144703.
DOI: 10.1063/1.2717165.

[141] Wiebke Bennecke et al. “Hybrid Frenkel-Wannier excitons facilitate ultrafast energy transfer at a 2D-organic interface”. In: *arXiv* (2024).

[142] Shigemasa Suga, Akira Sekiyama, and Christian Tusche. “Photoelectron Spectroscopy, Bulk and Surface Electronic Structures”. In: *Springer Series in Surface Sciences* (2021), pp. 351–416.
DOI: 10.1007/978-3-030-64073-6_11.

[143] Ryan P. Day et al. “Computational framework chinook for angle-resolved photoemission spectroscopy”. In: *npj Quantum Materials* 4.1 (2019), p. 54.
DOI: 10.1038/s41535-019-0194-8.

[144] Hongyun Zhang et al. "Angle-resolved photoemission spectroscopy". In: *Nature Reviews Methods Primers* 2.1 (2022), p. 54.
DOI: 10.1038/s43586-022-00133-7.

[145] Qiyang Lu. "How to Correctly Analyze 2p X-ray Photoelectron Spectra of 3d Transition-Metal Oxides: Pitfalls and Principles". In: *ACS Nano* 18.22 (2024), pp. 13973–13982.
DOI: 10.1021/acsnano.4c03964.

[146] R. P. Gupta and S. K. Sen. "Calculation of multiplet structure of core p-vacancy levels". In: *Physical Review B* 10.1 (1974), pp. 71–77.
DOI: 10.1103/physrevb.10.71.

[147] R. P. Gupta and S. K. Sen. "Calculation of multiplet structure of core p -vacancy levels. II". In: *Physical Review B* 12.1 (1975), pp. 15–19.
DOI: 10.1103/physrevb.12.15.

[148] D.C. Frost, C.A. McDowell, and I.S. Woolsey. "Evidence for multiplet splitting of 2p photoelectron lines of transition metal complexes". In: *Chemical Physics Letters* 17.3 (1972), pp. 320–323.
DOI: 10.1016/0009-2614(72)87086-6.

[149] M. A. Isaacs, A. Graf, and D. J. Morgan. "XPS Insight Note: Multiplet Splitting in X-Ray Photoelectron Spectra". In: *Surface and Interface Analysis* 57.4 (2025), pp. 285–290.
DOI: 10.1002/sia.7383.

[150] Susumu Asada, Chikatoshi Satoko, and Satoru Sugano. "Multiplet Structure in X-Ray p-Shell Photoelectron and K-Emission Spectra of Nickel Compounds". In: *Journal of the Physical Society of Japan* 38.3 (1975), pp. 855–865.
DOI: 10.1143/jpsj.38.855.

[151] Marion A. Brisk and A.D. Baker. "Shake-up satellites in X-ray photoelectron spectroscopy". In: *Journal of Electron Spectroscopy and Related Phenomena* 7.3 (1975), pp. 197–213.
DOI: 10.1016/0368-2048(75)80061-2.

[152] Paul S. Bagus et al. "Origin of the complex main and satellite features in Fe 2p XPS of Fe 2 O 3". In: *Physical Chemistry Chemical Physics* 24.7 (2022), pp. 4562–4575.
DOI: 10.1039/d1cp04886d.

[153] Paul S. Bagus et al. "Main and Satellite Features in the Ni 2p XPS of NiO". In: *Inorganic Chemistry* 61.45 (2022), pp. 18077–18094.
DOI: 10.1021/acs.inorgchem.2c02549.

[154] B. Mayer, St. Uhlenbrock, and M. Neumann. "XPS satellites in transition metal oxides". In: *Journal of Electron Spectroscopy and Related Phenomena* 81.1 (1996), pp. 63–67.
DOI: 10.1016/0368-2048(96)03030-7.

[155] Mark C. Biesinger et al. "Resolving surface chemical states in XPS analysis of first row transition metals, oxides and hydroxides: Cr, Mn, Fe, Co and Ni". In: *Applied Surface Science* 257.7 (2011), pp. 2717–2730.
DOI: 10.1016/j.apsusc.2010.10.051.

[156] J. Sánchez-Barriga et al. "Subpicosecond spin dynamics of excited states in the topological insulator Bi2Te3". In: *Physical Review B* 95.12 (2017), p. 125405.
DOI: 10.1103/physrevb.95.125405.

[157] Christian Kern, Michael Zürch, and Christian Spielmann. "Limitations of Extreme Nonlinear Ultrafast Nanophotonics". In: *Nanophotonics* 4.3 (2015), pp. 303–323.
DOI: 10.1515/nanoph-2015-0013.

[158] Liran Hareli, Georgiy Shoulga, and Alon Bahabad. "Phase matching and quasi-phase matching of high-order harmonic generation—a tutorial". In: *Journal of Physics B: Atomic, Molecular and Optical Physics* 53.23 (Oct. 2020), p. 233001.
DOI: 10.1088/1361-6455/abb937.

[159] Fang Liu. "Time- and angle-resolved photoemission spectroscopy (TR-ARPES) of TMDC monolayers and bilayers". In: *Chemical Science* 14.4 (2022), pp. 736–750.
DOI: 10.1039/d2sc04124c.

[160] Alexandre Gauthier et al. "Tuning time and energy resolution in time-resolved photoemission spectroscopy with nonlinear crystals". In: *Journal of Applied Physics* 128.9 (2020), p. 093101.
DOI: 10.1063/5.0018834.

[161] H. Tanimura, J. Kanasaki, and K. Tanimura. "Ultrafast scattering processes of hot electrons in InSb studied by time- and angle-resolved photoemission spectroscopy". In: *Phys. Rev. B* 91 (4 Jan. 2015), p. 045201.
DOI: 10.1103/PhysRevB.91.045201.

[162] Antonija Grubišić Čabo et al. "Observation of Ultrafast Free Carrier Dynamics in Single Layer MoS2". In: *Nano Letters* 15.9 (2015), pp. 5883–5887.
DOI: 10.1021/acs.nanolett.5b01967.

[163] H Hedayat et al. "Non-equilibrium band broadening, gap renormalization and band inversion in black phosphorus". In: *2D Materials* 8.2 (2021), p. 025020.
DOI: 10.1088/2053-1583/abd89a.

[164] Søren Ulstrup et al. "Ultrafast Band Structure Control of a Two-Dimensional Heterostructure". In: *ACS Nano* 10.6 (2016), pp. 6315–6322.
DOI: 10.1021/acsnano.6b02622.

[165] Federico Andreatta et al. "Transient hot electron dynamics in single-layer TaS_2". In: *Phys. Rev. B* 99 (16 Apr. 2019), p. 165421.
DOI: 10.1103/PhysRevB.99.165421.

[166] Paulina Majchrzak et al. "Spectroscopic view of ultrafast charge carrier dynamics in single- and bilayer transition metal dichalcogenide semiconductors". In: *Journal of Electron Spectroscopy and Related Phenomena* 250 (2021), p. 147093.
DOI: https://doi.org/10.1016/j.elspec.2021.147093.

[167] Matthias Drüppel et al. “Diversity of trion states and substrate effects in the optical properties of an MoS2 monolayer”. In: *Nature Communications* 8.1 (2017), p. 2117.
DOI: 10.1038/s41467-017-02286-6.

[168] Daniela Marongiu et al. “The role of excitons in 3D and 2D lead halide perovskites”. In: *J. Mater. Chem. C* 7 (39 2019), pp. 12006–12018.
DOI: 10.1039/C9TC04292J.

[169] Dominik Christiansen et al. “Theory of exciton dynamics in time-resolved ARPES: Intra- and intervalley scattering in two-dimensional semiconductors”. In: *Phys. Rev. B* 100 (20 Nov. 2019), p. 205401.
DOI: 10.1103/PhysRevB.100.205401.

[170] Avinash Rustagi and Alexander F. Kemper. “Photoemission signature of excitons”. In: *Physical Review B* 97.23 (2018), p. 235310.
DOI: 10.1103/physrevb.97.235310.

[171] Julien Madéo et al. “Directly visualizing the momentum-forbidden dark excitons and their dynamics in atomically thin semiconductors”. In: *Science* 370.6521 (2020), pp. 1199–1204.
DOI: 10.1126/science.aba1029.

[172] Shuo Dong et al. “Direct measurement of key exciton properties: Energy, dynamics, and spatial distribution of the wave function”. In: *Natural Sciences* 1.1 (2021).
DOI: 10.1002/ntls.10010.

[173] Michael K. L. Man et al. “Experimental measurement of the intrinsic excitonic wave function”. In: *Science Advances* 7.17 (2021), eabg0192.
DOI: 10.1126/sciadv.abg0192.

[174] Emre Ergeçen et al. “Coherent detection of hidden spin–lattice coupling in a van der Waals antiferromagnet”. In: *Proceedings of the National Academy of Sciences* 120.12 (2023), e2208968120.
DOI: 10.1073/pnas.2208968120.

[175] H. J. Zeiger et al. “Theory for displacive excitation of coherent phonons”. In: *Phys. Rev. B* 45 (2 Jan. 1992), pp. 768–778.
DOI: 10.1103/PhysRevB.45.768.

[176] G. A. Garrett et al. “Coherent THz Phonons Driven by Light Pulses and the Sb Problem: What is the Mechanism?” In: *Phys. Rev. Lett.* 77 (17 Oct. 1996), pp. 3661–3664.
DOI: 10.1103/PhysRevLett.77.3661.

[177] J. A. Sobota et al. “Distinguishing Bulk and Surface Electron-Phonon Coupling in the Topological Insulator Bi2Se3 Using Time-Resolved Photoemission Spectroscopy”. In: *Physical Review Letters* 113.15 (2014), p. 157401.
DOI: 10.1103/physrevlett.113.157401.

[178] Yijing Huang et al. “Ultrafast Measurements of Mode-Specific Deformation Potentials of Bi2Te3 and Bi2Se3”. In: *Physical Review X* 13.4 (2023), p. 041050.
DOI: 10.1103/physrevx.13.041050.

[179] Umberto De Giovannini et al. "Direct Measurement of Electron-Phonon Coupling with Time-Resolved ARPES". In: *Physical Review Letters* 125.13 (2020), p. 136401.
DOI: 10.1103/physrevlett.125.136401.

[180] Petra Hein et al. "Mode-resolved reciprocal space mapping of electron-phonon interaction in the Weyl semimetal candidate Td-WTe2". In: *Nature Communications* 11.1 (2020), p. 2613.
DOI: 10.1038/s41467-020-16076-0.

[181] Fahad Mahmood et al. "Selective scattering between Floquet–Bloch and Volkov states in a topological insulator". In: *Nature Physics* 12.4 (2016), pp. 306–310.
DOI: 10.1038/nphys3609.

[182] Dongsung Choi et al. "Direct observation of Floquet-Bloch states in monolayer graphene". In: *arXiv* (2024).

[183] Marco Merboldt et al. "Observation of Floquet states in graphene". In: *Nature Physics* (2025), pp. 1–7.
DOI: 10.1038/s41567-025-02889-7.

[184] F. Schmitt et al. "Transient Electronic Structure and Melting of a Charge Density Wave in TbTe3". In: *Science* 321.5896 (2008), pp. 1649–1652.
DOI: 10.1126/science.1160778.

[185] Martin Schmid. *XPST – X-ray Photoelectron Spectroscopy Tools*. Accessed on 2025-08-04. 2025. URL: https://www.wavemetrics.com/project/XPStools (visited on 08/04/2025).

[186] Karl Jakob Schiller et al. "Time-resolved momentum microscopy with fs-XUV photons at high repetition rates with flexible energy and time resolution". In: *Scientific Reports* 15.1 (2025), p. 3611.
DOI: 10.1038/s41598-025-86660-1.

[187] Christopher G. Tarsitano and Christopher R. Webster. "Multilaser Herriott cell for planetary tunable laser spectrometers". In: *Appl. Opt.* 46.28 (Oct. 2007), pp. 6923–6935.
DOI: 10.1364/AO.46.006923.

[188] Fumihiko Matsui et al. "Photoelectron Momentum Microscope at BL6U of UVSOR-III synchrotron". In: *Japanese Journal of Applied Physics* 59.6 (May 2020), pp. 067001–10.
DOI: 10.35848/1347-4065/ab9184.

[189] B.P. Tonner. "Energy-filtered imaging with electrostatic optics for photoelectron microscopy". In: *Nuclear Instruments and Methods in Physics Research Section A: Accelerators, Spectrometers, Detectors and Associated Equipment* 291.1 (1990), pp. 60–66.
DOI: https://doi.org/10.1016/0168-9002(90)90034-4.

[190] Christian Tusche et al. "Imaging properties of hemispherical electrostatic energy analyzers for high resolution momentum microscopy". In: *Ultramicroscopy* 206 (2019), p. 112815.
DOI: https://doi.org/10.1016/j.ultramic.2019.112815.

[191] Christian Tusche, Alexander Krasyuk, and Jürgen Kirschner. "Spin resolved bandstructure imaging with a high resolution momentum microscope". In: *Ultramicroscopy* 159 (2015), pp. 520–529.
DOI: 10.1016/j.ultramic.2015.03.020.

[192] G. Schönhense et al. "Single-hemisphere photoelectron momentum microscope with time-of-flight recording". In: *Review of Scientific Instruments* 91.12 (Dec. 2020), p. 123110.
DOI: 10.1063/5.0024074.

[193] Surface Concept GmbH. *Surface Concept Delayline Detectors Catalogue*. Accessed: 2025-08-11. Surface Concept GmbH. 2011. URL: https://surface-concept.com/downloads/Surface_Concept_DLDs_Catalogue.pdf.

[194] G Schönhense et al. "Time-of-flight photoemission electron microscopy – a new way to chemical surface analysis". In: *Surface Science* 480.3 (2001), pp. 180–187.
DOI: 10.1016/s0039-6028(01)00833-0.

[195] B. Krömker et al. "Development of a momentum microscope for time resolved band structure imaging". In: *Review of Scientific Instruments* 79.5 (2008), p. 053702.
DOI: 10.1063/1.2918133.

[196] Jonah Elias Nitschke et al. "Valence band electronic structure of the van der Waals antiferromagnet FePS3". In: *Materials Today Electronics* 6 (2023), p. 100061.
DOI: 10.1016/j.mtelec.2023.100061.

[197] Qiyang Lu. "How to Correctly Analyze 2p X-ray Photoelectron Spectra of 3d Transition-Metal Oxides: Pitfalls and Principles". In: *ACS Nano* 18.22 (2024), pp. 13973–13982.
DOI: 10.1021/acsnano.4c03964.

[198] Fred A. Stevie and Carrie L. Donley. "Introduction to x-ray photoelectron spectroscopy". In: *Journal of Vacuum Science & Technology A: Vacuum, Surfaces, and Films* 38.6 (2020), p. 063204.
DOI: 10.1116/6.0000412.

[199] So Yeun Kim et al. "Charge-Spin Correlation in van der Waals Antiferromagnet NiPS3". In: *Physical Review Letters* 120.13 (2018), p. 136402.
DOI: 10.1103/physrevlett.120.136402.

[200] Neil G. Farr and Hans J. Griesser. "XPS excitation dependence of measured cobalt 2p32 peak intensity due to auger peak interference". In: *Journal of Electron Spectroscopy and Related Phenomena* 49.3 (1989), pp. 293–302.
DOI: 10.1016/0368-2048(89)85017-0.

[201] Isaac Brotons-Alcazár et al. "Molecular stabilization of chemically exfoliated bare MnPS3 layers". In: *ChemRxiv* (2021).
DOI: 10.26434/chemrxiv-2021-lph4p.

[202] A. P. Grosvenor et al. "Investigation of multiplet splitting of Fe 2p XPS spectra and bonding in iron compounds". In: *Surface and Interface Analysis* 36.12 (2004), pp. 1564–1574.
DOI: 10.1002/sia.1984.

[203] Eugene S. Ilton et al. "XPS determination of Mn oxidation states in Mn (hydr)oxides". In: *Applied Surface Science* 366 (2016), pp. 475–485.
DOI: 10.1016/j.apsusc.2015.12.159.

[204] Yu.G. Borod'ko et al. "Nature of satellites in x-ray photoelectron spectra XPS of paramagnetic cobalt (II) compounds". In: *Chemical Physics Letters* 42.2 (1976), pp. 264–267.
DOI: 10.1016/0009-2614(76)80360-0.

[205] Toru Yamashita and Peter Hayes. "Analysis of XPS spectra of Fe2+ and Fe3+ ions in oxide materials". In: *Applied Surface Science* 254.8 (2008), pp. 2441–2449.
DOI: 10.1016/j.apsusc.2007.09.063.

[206] T. Ivanova et al. "X-ray photoelectron spectra and electron structure of polynuclear cobalt complexes". In: *Journal of Electron Spectroscopy and Related Phenomena* 156 (2007), pp. 200–203.
DOI: 10.1016/j.elspec.2006.12.005.

[207] Mouhui Yan et al. "Electronic Correlations in Fe x Ni y PS3 Van der Waals Materials: Insights from Angle-Resolved Photoelectron Spectroscopy and DFT". In: *The Journal of Physical Chemistry Letters* 14.43 (2023), pp. 9774–9779.
DOI: 10.1021/acs.jpclett.3c02688.

[208] Yukun Jin et al. "Mixed Insulating State for van der Waals CoPS3". In: *The Journal of Physical Chemistry Letters* 13.45 (2022), pp. 10486–10493.
DOI: 10.1021/acs.jpclett.2c02992.

[209] Yichen Jin et al. "Mott–Hubbard insulating state for the layered van der Waals FePX3 (X: S, Se) as revealed by NEXAFS and resonant photoelectron spectroscopy". In: *Scientific Reports* 12.1 (2022), p. 735.
DOI: 10.1038/s41598-021-04557-1.

[210] T. Miyazaki et al. "UPS study of NiPS3 and FePS3 crystals using synchrotron radiation". In: *Chemical Physics* 201.2-3 (1995), pp. 539–546.
DOI: 10.1016/0301-0104(95)00319-3.

[211] Antoine Kahn. "Fermi level, work function and vacuum level". In: *Materials Horizons* 3.1 (2015), pp. 7–10.
DOI: 10.1039/c5mh00160a.

[212] Guosheng Shao. "Work Function and Electron Affinity of Semiconductors: Doping Effect and Complication due to Fermi Level Pinning". In: *Energy & Environmental Materials* 4.3 (2021), pp. 273–276.
DOI: 10.1002/eem2.12218.

[213] Jeff Strasdas et al. "Electronic Band Structure Changes across the Antiferromagnetic Phase Transition of Exfoliated MnPS3 Flakes Probed by μ-ARPES". In: *Nano Letters* 23.22 (2023), pp. 10342–10349.
DOI: 10.1021/acs.nanolett.3c02906.

[214] Maria Ramos et al. "Photoluminescence Enhancement by Band Alignment Engineering in MoS2/FePS3 van der Waals Heterostructures". In: *ACS Applied Materials & Interfaces* 14.29 (2022), pp. 33482–33490.
DOI: 10.1021/acsami.2c05464.

[215] Mouhui Yan et al. "Unveiling charge transport in monolayer and few-layer CoPS3/metal contact: Insight from C-AFM". In: *APL Materials* 12.8 (2024), p. 081121.
DOI: 10.1063/5.0222472.

[216] Lewis S. Hart et al. "Electronic bandstructure and van der Waals coupling of ReSe2 revealed by high-resolution angle-resolved photoemission spectroscopy". In: *Scientific Reports* 7.1 (2017), p. 5145.
DOI: 10.1038/s41598-017-05361-6.

[217] Simon Moser. "An experimentalist's guide to the matrix element in angle resolved photoemission". In: *Journal of Electron Spectroscopy and Related Phenomena* 214 (2017), pp. 29–52.
DOI: 10.1016/j.elspec.2016.11.007.

[218] Maciej Dendzik et al. "Reconstruction-induced trefoil knot Fermi contour of Au(111)". In: *Physical Review B* 94.20 (2016), p. 201401.
DOI: 10.1103/physrevb.94.201401.

[219] G. Kresse and J. Furthmüller. "Efficiency of ab-initio total energy calculations for metals and semiconductors using a plane-wave basis set". In: *Computational Materials Science* 6.1 (1996), pp. 15–50.
DOI: 10.1016/0927-0256(96)00008-0.

[220] G. Kresse and D. Joubert. "From ultrasoft pseudopotentials to the projector augmented-wave method". In: *Physical Review B* 59.3 (1998), pp. 1758–1775.
DOI: 10.1103/physrevb.59.1758.

[221] John P. Perdew, Kieron Burke, and Matthias Ernzerhof. "Generalized Gradient Approximation Made Simple". In: *Physical Review Letters* 77.18 (1996), pp. 3865–3868.
DOI: 10.1103/physrevlett.77.3865.

[222] Elliott H. Lieb. "Two theorems on the Hubbard model". In: *Physical Review Letters* 62.10 (1989), pp. 1201–1204.
DOI: 10.1103/physrevlett.62.1201.

[223] Qi Pei et al. "Superior Electronic Structure in Two-Dimensional MnPSe3/MoS2 van der Waals Heterostructures". In: *Scientific Reports* 7.1 (2017), p. 9504.
DOI: 10.1038/s41598-017-10145-z.

[224] Arash A. Mostofi et al. "wannier90: A tool for obtaining maximally-localised Wannier functions". In: *Computer Physics Communications* 178.9 (2008), pp. 685–699.
DOI: https://doi.org/10.1016/j.cpc.2007.11.016.

[225] QuanSheng Wu et al. "WannierTools: An open-source software package for novel topological materials". In: *Computer Physics Communications* 224 (2018), pp. 405–416.
DOI: https://doi.org/10.1016/j.cpc.2017.09.033.

[226] A. Koitzsch et al. "Intertwined electronic and magnetic structure of the van-der-Waals antiferromagnet Fe2P2S6". In: *npj Quantum Materials* 8.1 (2023), p. 27.
DOI: 10.1038/s41535-023-00560-z.

[227] Benjamin Pestka et al. “Identifying Band Structure Changes of FePS3 across the Antiferromagnetic Phase Transition”. In: *ACS Nano* (2024).
DOI: 10.1021/acsnano.4c12520.

[228] A M León et al. “Interlayer magnetic coupling in FePS3 and NiPS3 stacked bilayers from first principles”. In: *2D Materials* 12.2 (2025), p. 025023.
DOI: 10.1088/2053-1583/adb6ba.

[229] Mouhui Yan et al. “Correlations in the Electronic Structure of van der Waals NiPS3 Crystals: An X-ray Absorption and Resonant Photoelectron Spectroscopy Study”. In: *The Journal of Physical Chemistry Letters* 12.9 (2021), pp. 2400–2405.
DOI: 10.1021/acs.jpclett.1c00394.

[230] Marco Bianchi et al. “Paramagnetic electronic structure of CrSBr: Comparison between ab initio *GW* theory and angle-resolved photoemission spectroscopy”. In: *Phys. Rev. B* 107 (23 June 2023), p. 235107.
DOI: 10.1103/PhysRevB.107.235107.

[231] Yimeng Gu et al. “Lattice and magnetic structure in the van der Waals antiferromagnet VBr_3”. In: *Phys. Rev. B* 110 (6 Aug. 2024), p. 064403.
DOI: 10.1103/PhysRevB.110.064403.

[232] Lasse Sternemann et al. “Fabrication of large-area 2D magnetic semiconductor films for low-temperature ARPES”. In: *2D Materials* (2025).
DOI: 10.1088/2053-1583/add7ea.

[233] Yifeng Cao et al. “Revealing the Electronic Structure of $NiPS_3$ through Synchrotron-Based ARPES and Alkali Metal Dosing”. In: *arXiv* (2024).

[234] Benjamin Pestka et al. “Probing the band structure of the strongly correlated antiferromagnet NiPS3 across its phase transition”. In: *arXiv* (2025).
DOI: 10.48550/arxiv.2507.14890.

[235] David Schmitt et al. “Ultrafast nano-imaging of dark excitons”. In: *Nature Photonics* (2025), pp. 1–8.
DOI: 10.1038/s41566-024-01568-y.

[236] R. Wallauer et al. “Tracing orbital images on ultrafast time scales”. In: *Science* 371.6533 (2021), pp. 1056–1059.
DOI: 10.1126/science.abf3286.

[237] Jonah Elias Nitschke et al. “Tracing the ultrafast buildup and decay of d-d transitions in FePS3”. In: *Newton* (2025), p. 100019.
DOI: 10.1016/j.newton.2025.100019.

[238] Daniel Wilson et al. “On space charge effects in laboratory-based photoemission electron microscopy using compact gas discharge extreme ultraviolet sources”. In: *New Journal of Physics* 22.10 (2020), p. 103019.
DOI: 10.1088/1367-2630/abbc29.

[239] J. Maklar et al. "A quantitative comparison of time-of-flight momentum microscopes and hemispherical analyzers for time- and angle-resolved photoemission spectroscopy experiments". In: *Review of Scientific Instruments* 91.12 (2020), p. 123112.
DOI: 10.1063/5.0024493.

[240] B Schönhense et al. "Multidimensional photoemission spectroscopy—the space-charge limit". In: *New Journal of Physics* 20.3 (2018), p. 033004.
DOI: 10.1088/1367-2630/aaa262.

[241] Søren Ulstrup et al. "Ramifications of optical pumping on the interpretation of time-resolved photoemission experiments on graphene". In: *Journal of Electron Spectroscopy and Related Phenomena* 200 (2015), pp. 340–346.
DOI: 10.1016/j.elspec.2015.04.010.

[242] Anna Lévy et al. "Mitigating space charge in time-resolved photoelectron spectroscopy to study laser-heated copper dynamics in the high fluence regime". In: *Physical Review B* 109.17 (2024), p. 174311.
DOI: 10.1103/physrevb.109.174311.

[243] G. Schönhense et al. "Suppression of the vacuum space-charge effect in fs-photoemission by a retarding electrostatic front lens". In: *Review of Scientific Instruments* 92.5 (2021), p. 053703.
DOI: 10.1063/5.0046567.

[244] Jacob Pettine, Andrej Grubisic, and David J. Nesbitt. "Polarization-Controlled Directional Multiphoton Photoemission from Hot Spots on Single Au Nanoshells". In: *The Journal of Physical Chemistry C* 122.26 (2018), pp. 14805–14813.
DOI: 10.1021/acs.jpcc.8b03402.

[245] Herbert B. Michaelson. "The work function of the elements and its periodicity". In: *Journal of Applied Physics* 48.11 (Nov. 1977), pp. 4729–4733.
DOI: 10.1063/1.323539.

[246] G. Saathoff et al. "Laser-assisted photoemission from surfaces". In: *Physical Review A* 77.2 (2008), p. 022903.
DOI: 10.1103/physreva.77.022903.

[247] Marius Keunecke et al. "Electromagnetic dressing of the electron energy spectrum of Au(111) at high momenta". In: *Physical Review B* 102.16 (2020), p. 161403.
DOI: 10.1103/physrevb.102.161403.

[248] L. Miaja-Avila et al. "Laser-Assisted Photoelectric Effect from Surfaces". In: *Physical Review Letters* 97.11 (2006), p. 113604.
DOI: 10.1103/physrevlett.97.113604.

[249] Emre Ergeçen et al. "Magnetically brightened dark electron-phonon bound states in a van der Waals antiferromagnet". In: *Nature Communications* 13.1 (2022), p. 98.
DOI: 10.1038/s41467-021-27741-3.

[250] Dmytro Afanasiev et al. “Controlling the anisotropy of a van der Waals antiferromagnet with light”. In: *Science Advances* 7.23 (2021), eabf3096.
DOI: 10.1126/sciadv.abf3096.

[251] Thuc T. Mai et al. “Magnon-phonon hybridization in 2D antiferromagnet MnPSe3”. In: *Science Advances* 7.44 (2021), eabj3106.
DOI: 10.1126/sciadv.abj3106.

[252] D. Vaclavkova et al. “Magnon polarons in the van der Waals antiferromagnet FePS3”. In: *Physical Review B* 104.13 (2021), p. 134437.
DOI: 10.1103/physrevb.104.134437.

[253] Sheng Liu et al. “Direct Observation of Magnon-Phonon Strong Coupling in Two-Dimensional Antiferromagnet at High Magnetic Fields”. In: *Physical Review Letters* 127.9 (2021), p. 097401.
DOI: 10.1103/physrevlett.127.097401.

[254] E. J. K. B. Banda. “Optical Absorption of FePSe3 in the near Infrared, Visible, and near Ultraviolet Regions”. In: *physica status solidi (b)* 138.2 (1986), K125–K129.
DOI: 10.1002/pssb.2221380250.

[255] Denis Golež et al. “Unveiling the underlying interactions in Ta2NiSe5 from photoinduced lifetime change”. In: *Physical Review B* 106.12 (2022), p. L121106.
DOI: 10.1103/physrevb.106.l121106.

[256] M I Katsnelson and A I Lichtenstein. “Theory of optically forbidden d–d transitions in strongly correlated crystals”. In: *Journal of Physics: Condensed Matter* 22.38 (2010), p. 382201.
DOI: 10.1088/0953-8984/22/38/382201.

[257] A. I. Lichtenstein and M. I. Katsnelson. “Ab initio calculations of quasiparticle band structure in correlated systems: LDA++ approach”. In: *Phys. Rev. B* 57 (12 Mar. 1998), pp. 6884–6895.
DOI: 10.1103/PhysRevB.57.6884.

[258] Alexander Neef et al. “Orbital-resolved observation of singlet fission”. In: *Nature* 616.7956 (2023), pp. 275–279.
DOI: 10.1038/s41586-023-05814-1.

[259] Ouri Karni et al. “Structure of the moiré exciton captured by imaging its electron and hole”. In: *Nature* 603.7900 (2022), pp. 247–252.
DOI: 10.1038/s41586-021-04360-y.

[260] Rahul Rao et al. “Mode-Selective Spin–Phonon Coupling in van der Waals Antiferromagnets”. In: *Advanced Physics Research* (2024).
DOI: 10.1002/apxr.202300153.

[261] Z. H. Xiong et al. “Giant magnetoresistance in organic spin-valves”. In: *Nature* 427.6977 (2004), pp. 821–824.
DOI: 10.1038/nature02325.

[262] T. S. Santos et al. "Room-Temperature Tunnel Magnetoresistance and Spin-Polarized Tunneling through an Organic Semiconductor Barrier". In: *Physical Review Letters* 98.1 (2007), p. 016601.
DOI: 10.1103/physrevlett.98.016601.

[263] David Ciudad et al. "Sign Control of Magnetoresistance Through Chemically Engineered Interfaces". In: *Advanced Materials* 26.45 (2014), pp. 7561–7567.
DOI: 10.1002/adma.201401283.

[264] Jose Muñoz. "Rational Design of Stimuli-Responsive Inorganic 2D Materials via Molecular Engineering: Toward Molecule-Programmable Nanoelectronics". In: *Advanced Materials* 36.8 (2024), e2305546.
DOI: 10.1002/adma.202305546.

[265] Peter Puschnig. *Organic Molecule Database: A Database for Molecular Orbitals of π-Conjugated Organic Molecules Based on the Atomic Simulation Environment (ASE) and NWChem as the DFT Calculator*. 2025. URL: http://physikmdb.uni-graz.at:5001/default/row/98 (visited on 08/14/2025).

[266] Dominik Brandstetter et al. "kMap.py: A Python program for simulation and data analysis in photoemission tomography". In: *Computer Physics Communications* 263 (2021), p. 107905.
DOI: 10.1016/j.cpc.2021.107905.

[267] Anja Haags et al. "Tomographic identification of all molecular orbitals in a wide binding-energy range". In: *Physical Review B* 111.16 (2025), p. 165402.
DOI: 10.1103/physrevb.111.165402.

[268] David Maximilian Janas et al. "Metalloporphyrins on oxygen-passivated iron: Conformation and order beyond the first layer". In: *Inorganica Chimica Acta* 557 (2023), p. 121705.
DOI: 10.1016/j.ica.2023.121705.

[269] Wiebke Bennecke et al. "Table-top three-dimensional photoemission orbital tomography with a femtosecond extreme ultraviolet light source". In: *arXiv* (2025).
DOI: 10.48550/arxiv.2502.18269.

[270] Anja Haags et al. "Momentum space imaging of σ orbitals for chemical analysis". In: *Science Advances* 8.29 (2022), eabn0819.
DOI: 10.1126/sciadv.abn0819.

[271] E. Black, P. Kratzer, and J. M. Morbec. "Interaction between pentacene molecules and monolayer transition metal dichalcogenides". In: *Physical Chemistry Chemical Physics* 25.43 (2023), pp. 29444–29450.
DOI: 10.1039/d3cp01895d.

[272] Thorsten Schultz et al. "Work function and energy level alignment tuning at Ti3C2Tx MXene surfaces and interfaces using (metal-)organic donor/acceptor molecules". In: *Physical Review Materials* 7.4 (2023), p. 045002.
DOI: 10.1103/physrevmaterials.7.045002.

[273] T. Schultz et al. “Tuning the work function of GaN with organic molecular acceptors”. In: *Physical Review B* 93.12 (2016), p. 125309.
DOI: 10.1103/physrevb.93.125309.

[274] Ye Wang et al. “Doping of Monolayer Transition-Metal Dichalcogenides via Physisorption of Aromatic Solvent Molecules”. In: *The Journal of Physical Chemistry Letters* 10.3 (2019), pp. 540–547.
DOI: 10.1021/acs.jpclett.8b03697.

[275] B. M. Ludbrook et al. “Evidence for superconductivity in Li-decorated monolayer graphene”. In: *Proceedings of the National Academy of Sciences* 112.38 (2015), pp. 11795–11799.
DOI: 10.1073/pnas.1510435112.

[276] S. Ito et al. “Alkali-metal induced band structure deformation investigated by angle-resolved photoemission spectroscopy and first-principles calculations”. In: *Physical Review B* 97.15 (2018), p. 155423.
DOI: 10.1103/physrevb.97.155423.

[277] Wei Wen et al. “Alkali-metal induced electronic structure evolution in Sn4Sb3 studied by angle-resolved photoemission spectroscopy”. In: *Journal of Physics and Chemistry of Solids* 162 (2022), p. 110526.
DOI: 10.1016/j.jpcs.2021.110526.

[278] Iulia Cojocariu et al. “Distortion-driven spin switching in electron-doped metal porphyrins”. In: *Journal of Materials Chemistry C* 10.26 (2022), pp. 9748–9757.
DOI: 10.1039/d2tc01253g.

[279] SAES Industrial – Getters & Dispensers. *Alkali Metal Dispensers (AMD)*. Accessed: 2025-08-08. SAES Getters S.p.A. 2025. URL: https://www.saesgetters.com/industrial-getters-dispensers/solution/alkali-metal-dispensers-amd/.

[280] R. Eloirdi et al. “X-ray photoelectron spectroscopy study of the reduction and oxidation of uranium and cerium single oxide compared to (U-Ce) mixed oxide films”. In: *Applied Surface Science* 457 (2018), pp. 566–571.
DOI: https://doi.org/10.1016/j.apsusc.2018.06.148.

[281] G. K. Wertheim, S. Hüfner, and H. J. Guggenheim. “Systematics of Core-Electron Exchange Splitting in 3*d*-Group Transition-Metal Compounds”. In: *Phys. Rev. B* 7 (1 Jan. 1973), pp. 556–558.
DOI: 10.1103/PhysRevB.7.556.

[282] D.C. Frost, C.A. McDowell, and I.S. Woolsey. “X-ray photoelectron spectra of cobalt compounds”. In: *Molecular Physics* 27.6 (1974), pp. 1473–1489.
DOI: 10.1080/00268977400101251.

[283] Patrick Brant and Robert D. Feltham. “X-ray photoelectron spectra of iron complexes: Correlation of iron 2p satellite intensity with complex spin state”. In: *Journal of Electron Spectroscopy and Related Phenomena* 32.3 (1983), pp. 205–221.
DOI: 10.1016/0368-2048(83)85002-6.

[284] B. Reihl et al. “The bonding of alkali metals to semiconductor surfaces: a direct and inverse photoemission study”. In: *Applied Surface Science* 56-58 (1992), pp. 123–136.
DOI: https://doi.org/10.1016/0169-4332(92)90225-M.

[285] Han Zhong et al. “Integrating 2D magnets for quantum devices: from materials and characterization to future technology”. In: *Materials for Quantum Technology* 5.1 (2025), p. 012001.
DOI: 10.1088/2633-4356/adb474.

Declaration on the Use of Artificial Intelligence Tools

In the preparation of this thesis, I used artificial intelligence-based tools [DeepL, ChatGPT (OpenAI, GPT-4.5, 2025)] for the purposes of improving clarity, refining grammar, and suggesting alternative formulations in the English text. The use of these tools was limited to language editing and did not involve the generation of original content, research data, data analysis, or conceptual contributions. All scientific interpretations, analyses, and conclusions are my own, and I take full responsibility for the accuracy and integrity of the content presented herein. The unedited texts are available upon request.